TECHNICAL UNIVERSITY OF CRETE

DOCTORAL THESIS

Macroscopic Models Describing Lane-Free Movement of Automated Vehicles

Author:
Georgios TITAKIS

Supervisor:
Prof. Ioannis PAPAMICHAIL

A thesis submitted in fulfillment of the requirements for the degree of Doctor of Philosophy

in the

Dynamic Systems & Simulation Laboratory
School of Production, Engineering & Management

September, 2025

The present thesis is approved by the following jury:

Advisory Committee:

Ioannis Papamichail (Supervisor)
Professor, School of Production Engineering and Management
Technical University of Crete, Chania, Greece

Anargiros Delis (Member of committee in charge)
Professor, School of Production Engineering and Management
Technical University of Crete, Chania, Greece

Iasson Karafyllis (Member of committee in charge)
Professor, School of Applied Mathematics and Physical Sciences
National Technical University of Athens, Athens, Greece

Thesis Committee:

Markos Papageorgiou
Professor Emeritus, School of Production Engineering and Management
Technical University of Crete, Chania, Greece

Ioannis Nikolos
Professor, School of Production Engineering and Management
Technical University of Crete, Chania, Greece

Georgios Arampatzis
Associate Professor, School of Production Engineering and Management
Technical University of Crete, Chania, Greece

Claudio Roncoli
Associate Professor, Faculty of Engineering Science
KU Leuven, Belgium

ΕΠΤΑΜΕΛΗΣ ΕΞΕΤΑΣΤΙΚΗ ΕΠΙΤΡΟΠΗ

Τίτλος (ελληνικά/αγγλικά):

Μακροσκοπικά Μοντέλα για την Περιγραφή της Κίνησης Αυτόματων Οχημάτων σε Περιβάλλον Απαλλαγμένο από Λωρίδες

Macroscopic Models Describing Lane-Free Movement of Automated Vehicles

ΔΙΔΑΚΤΟΡΙΚΗ ΔΙΑΤΡΙΒΗ

(Ονοματεπώνυμο διδάκτορα)

Γεώργιος Τιτάκης

ΤΡΙΜΕΛΗΣ ΣΥΜΒΟΥΛΕΥΤΙΚΗ ΕΠΙΤΡΟΠΗ:

1. **Καθ. Ιωάννης Παπαμιχαήλ (Επιβλέπων)**
2. **Καθ. Ανάργυρος Δελής**
3. **Καθ. Ιάσων Καραφύλλης, ΕΜΠ**

Εγκρίθηκε από την επταμελή εξεταστική επιτροπή την: 15 / 09 / 2025

1. **Καθ. Ιωάννης Παπαμιχαήλ**
2. **Καθ. Ανάργυρος Δελής** A.Δ.Delis
3. **Καθ. Ιάσων Καραφύλλης, ΕΜΠ** Ι.Καραφύλλης
4. **Ομοτ. Καθ. Μάρκος Παπαγεωργίου**
5. **Καθ. Ιωάννης Νικολός**
6. **Αν. Καθ. Γεώργιος Αραμπατζής**
7. **As. Prof. Claudio Roncoli, Faculty of Engineering Science, KU Leuven** Claudio Roncoli

TECHNICAL UNIVERSITY OF CRETE

Abstract

School of Production, Engineering & Management

Doctor of Philosophy

Macroscopic Models Describing Lane-Free Movement of Automated Vehicles

by Georgios TITAKIS

Recent advances in technology have revolutionized vehicle automation with different kinds of driver support systems. In the era of connected automated vehicles (CAVs), new perspectives and principles have been suggested, where the vehicles can move on the two-dimensional surface of lane-free roads without abiding to lane discipline, something that may improve traffic flow and increase capacity of highways. Therefore, there is a need for cruise controllers that can operate in a lane-free environment. The cruise controllers under consideration are performed in microscopic models, i.e. models that consist of Ordinary Differential Equations (ODEs) and describe the dynamics of each individual vehicle.

Although several aspects of the cruise controllers, such as safety and passenger convenience, may be investigated at the microscopic level, it is also important to study their implications for the emerging traffic flow. To this end, macroscopic traffic flow models have been formally derived for the description of the traffic flow of CAVs under the effect of cruise controllers. The derived macroscopic models consist of two Partial Differential Equations (PDEs) (i.e a continuity equation and a speed equation) and they are similar to the equations of a viscous compressible fluid. The obtained macroscopic models have been formally derived using particle methods, in which the vehicles are considered as "self-driven" particles of a fluid ("the traffic fluid"). The particle methods provide the link between the macroscopic models and the cruise controllers, since certain relations between the microscopic quantities and the "traffic fluid" physical properties hold. Consequently, by changing the microscopic quantities of the cruise controllers we can determine the physical properties of the emerging traffic flow. Based on that, a specific selection for the functions included in the cruise controllers enabled a model reduction, which is completely analogous to the human-driven vehicles case, where the Aw-Rascle-Zhang (ARZ) model reduces to the well-known Lighthill-Whitham-Richards (LWR) model. Moreover, in contrast to conventional traffic, the proposed macroscopic models are isotropic since the vehicles react to both upstream and downstream vehicles. Isotropy, as well as the presence of "fluid-like" characteristics in the derived macroscopic models follow from the fact that lane-free movement and nudging are allowed by the cruise controllers.

In this thesis, numerical studies of the proposed macroscopic traffic flow models for CAVs are performed, where numerical experiments are conducted to study their properties and evaluate the performance of several numerical methods that are used to approximate their solutions. Moreover, the present work provides evidence that the proposed macroscopic models are successful for the description of the traffic flow in real complex traffic environments. More specifically, by considering traffic scenarios for which macroscopic traffic data are collected from microscopic simulations using the respective cruise controllers, it is shown that after calibrating one of the proposed macroscopic models for CAVs, all the traffic conditions that appear in the collected macroscopic traffic data are reproduced with high accuracy.

ΠΟΛΥΤΕΧΝΕΙΟ ΚΡΗΤΗΣ

Περίληψη

Σχολή Μηχανικών Παραγωγής και Διοίκησης

Doctor of Philosophy

Μακροσκοπικά Μοντέλα για την Περιγραφή της Κίνησης Αυτόματων Οχημάτων σε Περιβάλλον Απαλλαγμένο από Λωρίδες

Γεώργιος Τιτάκης

Πρόσφατες τεχνολογικές εξελίξεις έχουν φέρει επανάσταση στο χώρο των αυτόματων οχημάτων με την ύπαρξη διαφορετικών ειδών συστημάτων οδηγικής υποστήριξης. Στην εποχή των συνδεδεμένων αυτόματων οχημάτων (CAVs), νέες προοπτικές και θεμελιώδεις αρχές έχουν δημιουργηθεί, στις οποίες τα οχήματα μπορούν να κινηθούν στη δισδιάστατη επιφάνεια δρόμων χωρίς την ύπαρξη λωρίδων, γεγονός που μπορεί να βελτιώσει την κυκλοφοριακή ροή και να αυξήσει τη χωρητικότητα των αυτοκινητοδρόμων. Επομένως, υπάρχει ανάγκη για νέα συστήματα ελέγχου οχημάτων τα οποία να μπορούν να λειτουργήσουν σε δρόμους χωρίς λωρίδες. Αυτά τα συστήματα ελέγχου χρησιμοποιούνται σε μικροσκοπικά μοντέλα, δηλαδή μοντέλα τα οποία αποτελούνται από Συνήθεις Διαφορικές Εξισώσεις (ODEs) και περιγράφουν τη δυναμική κάθε οχήματος.

Παρόλο που αρκετές πτυχές αυτών των συστημάτων ελέγχου, όπως η ασφάλεια και η άνεση των επιβατών, μπορούν να διερευνηθούν σε μικροσκοπικό επίπεδο, είναι εξίσου σημαντική η μελέτη της κυκλοφοριακής ροής που απορρέει από τη χρήση τους. Για αυτόν τον σκοπό, έχουν παραχθεί μακροσκοπικά μοντέλα για την περιγραφή της κυκλοφοριακής ροής συνδεδεμένων αυτόματων οχημάτων υπό την επίδραση αυτών των συστημάτων ελέγχου. Τα μακροσκοπικά μοντέλα αποτελούνται από δύο Μερικές Διαφορικές Εξισώσεις (PDEs) (εξίσωση συνέχειας και εξίσωση ταχύτητας) και παρουσιάζουν ομοιότητες με τις εξισώσεις ενός ιξώδους συμπιεστού ρευστού. Αυτά τα μακροσκοπικά μοντέλα έχουν προκύψει χρησιμοποιώντας μεθόδους σωματιδίων, στις οποίες τα οχήματα θεωρούνται ως ¨αυτο-οδηγούμενα¨ σωματίδια ενός ρευστού (¨του κυκλοφοριακού ρευστού¨). Οι μέθοδοι σωματιδίων παρέχουν τη σύνδεση ανάμεσα στα μακροσκοπικά μοντέλα και τα συστήματα ελέγχου των οχημάτων, εφόσον υπάρχουν σχέσεις που συνδέουν τα μικροσκοπικά μεγέθη με τις φυσικές ιδιότητες του ¨κυκλοφοριακού ρευστού¨. Συνεπώς, αλλάζοντας τα μικροσκοπικά μεγέθη των συστημάτων ελέγχου μπορούμε να καθορίσουμε τις φυσικές ιδιότητες της αναδυόμενης κυκλοφοριακής ροής. Με βάση αυτό, μία συγκεκριμένη επιλογή των συναρτήσεων που περιέχονται στα συστήματα ελέγχου κατέστησε εφικτή μία απλοποίηση των προτεινόμενων μακροσκοπικών μοντέλων, η οποία είναι απολύτως ανάλογη με την περίπτωση των συμβατικών οχημάτων, όπου το (Aw-Rascle-Zhang) (ARZ) μοντέλο απλοποιείται στο ευρέως γνωστό (Lighthill-Whitham-Richards) (LWR) μοντέλο. Επιπλέον, σε αντίθεση με την κυκλοφοριακή ροή συμβατικών οχημάτων, τα προτεινόμενα μακροσκοπικά μοντέλα είναι ισοτροπικά αφού κάθε όχημα αλληλεπιδρά με οχήματα που βρίσκονται ανάντη και κατάντη του σημείου αναφοράς του. Η ισοτροπία, καθώς επίσης και η παρουσία χαρακτηριστικών που συναντώνται σε μοντέλα ρευστών βασίζονται στο γεγονός ότι η κίνηση σε δρόμους χωρίς λωρίδες και η ώθηση οχημάτων (nudging) επιτρέπονται από τα συστήματα ελέγχου των οχημάτων.

Η παρούσα διδακτορική διατριβή περιλαμβάνει αριθμητικές μελέτες των προτεινόμενων μακροσκοπικών μοντέλων, στις οποίες διεξάγονται αριθμητικά πειράματα με σκοπό τη μελέτη των ιδιοτήτων τους, καθώς και την αξιολόγηση αρκετών αριθμητικών μεθόδων που χρησιμοποιούνται για την προσέγγιση των λύσεών τους. Επιπλέον, παρέχονται ενδείξεις ότι τα προτεινόμενα μακροσκοπικά μοντέλα περιγράφουν επιτυχώς την κυκλοφοριακή ροή των οχημάτων κάτω από πραγματικές και πολύπλοκες κυκλοφοριακές συνθήκες. Πιο συγκεκριμένα, θεωρώντας σενάρια κυκλοφοριακής ροής, για τα οποία συλλέγουμε μακροσκοπικά δεδομένα από μικροσκοπικές προσομοιώσεις, χρησιμοποιώντας τα αντίστοιχα συστήματα ελέγχου των οχημάτων, διαπιστώνουμε ότι κατόπιν βαθμονόμησης ενός εκ των προτεινόμενων μακροσκοπικών μοντέλων, όλες οι κυκλοφοριακές συνθήκες που εμφανίζονται στα διαθέσιμα μακροσκοπικά δεδομένα μπορούν να αναπαραχθούν με μεγάλη ακρίβεια.

Acknowledgements

The path towards a PhD is always difficult, but also full of fulfilling moments. Having reached the end of this path, I would like to express my gratitude and appreciation to a group of people who have accompanied me along the way.

I would like to start with my advisors Prof. Papageorgiou, Prof. Karafyllis, and Prof. Papamichail. I am very grateful and fortunate to have these excellent advisors. Their academic excellence and constructive guidance, as well as their continuous support and patience, have been the most valuable ingredients for both my scientific work and my development as a researcher and as a person.

I would also like to extend my appreciation to all committee members for their thoughtful feedback valuable perspectives and for generously sharing their expertise and time. Of course, a heartfelt thank you goes to my colleagues and friends of the Dynamics Systems and Simulation Laboratory (DSSL) for their support and for the many interesting discussions over several topics and issues during this time. I am especially grateful to Dionysis and Vasilis, whose insightful counsel and unwavering encouragement have played a crucial role in the completion of this work.

Last but not least, I would like to thank my family for their enduring support, patience, and encouragement throughout this journey. Their unconditional love and unwavering belief in me is always the best motivation in my life.

This research received funding from the European Research Council under the European Union's Horizon 2020 Research and Innovation programme / ERC Grant Agreement n. [833915], project TrafficFluid.

Contents

List of Figures

List of Tables

List of Abbreviations

ARZ	**A**w **R**ascle **Z**hang
AV	**A**utomated **V**ehicle
CAV	**C**onnected **A**utomated **V**ehicle
CC	**C**ruise **C**ontroller
CFL	**C**ourant **F**riedrichs **L**ewy
GCC	**G**eneralized **C**ruise **C**ontroller
LWR	**L**ighthill **W**hitham **R**ichards
macro-NCC	**macro**scopic model for the **N**ewtonian **C**ruise **C**ontroller
macro-PRCC	**macro**scopic model for the **P**seudo **R**elativistic **C**ruise **C**ontroller
macro-GCC	**macro**scopic model for the **G**eneralized **C**ruise **C**ontroller
NCC	**N**ewtonian **C**ruise **C**ontroller
ODE	**O**rdinary **D**ifferential **E**quation
PDE	**P**artial **D**ifferential **E**quation

Notation

- $|x|$ denotes both the Euclidean norm of a vector $x \in \mathbb{R}^n$ and the absolute value of a scalar $x \in \mathbb{R}$.
- $\mathbb{R}_+ := [0, +\infty)$ denotes the set of non-negative real numbers.
- By x', the transpose of a vector $x \in \mathbb{R}^n$ is denoted. By $|x|_\infty = \max\{|x_i|, i = 1, ..., n\}$, the infinity norm of a vector $x = (x_1, x_2, ..., x_n)' \in \mathbb{R}^n$ is denoted.
- Let $A \subseteq \mathbb{R}^n$ be an open set. $C^0(A; \Omega)$ denotes the class of continuous functions on $A \subseteq \mathbb{R}^n$, which take values in $\Omega \subseteq \mathbb{R}^m$. $C^k(A; \Omega)$, where $k \geq 1$ is an integer, denotes the class of functions on $A \subseteq \mathbb{R}^n$ with continuous derivatives of order k, which take values in $\Omega \subseteq \mathbb{R}^m$. When $\Omega = \mathbb{R}$, the notation $C^0(A)$ or $C^k(A)$ is used.
- Let $I \subseteq \mathbb{R}$ be a given interval. For $p \in [1, \infty)$, $L^p(I)$ denotes the set of equivalence classes of Lebesgue measurable functions $f : I \to \mathbb{R}$ with $\|f\|_p := \left(\int_I |f(x)|^p dx\right)^{1/p} < +\infty$. $L^\infty(I)$ denotes the set of equivalence classes of measurable functions $f : I \to \mathbb{R}$ for which $\|f\|_\infty = ess \sup_{x \in I} \left(\left|f(x)\right|\right) < +\infty$.
- Let $u : \left(\bigcup_{t \geq 0} \{t\} \times I(t)\right) \to \mathbb{R}$ where $I(t) \subseteq \mathbb{R}$ is an open interval for each $t \geq 0$, be any function differentiable with respect to its arguments. The notation $u_t(t, x) = \frac{\partial u}{\partial t}(t, x)$ and $u_x(t, x) = \frac{\partial u}{\partial x}(t, x)$ is used for the partial derivatives of u with respect to t and x, respectively. The notation $u[t]$ is used to denote the profile at certain $t \geq 0$, $(u[t])[x] := u(t, x)$, for all $x \in I(t)$. The notation $u(t, x^-)$ and $u(t, x^+)$ is also used for the limits $u(t, x^-) = \lim_{s \to x^-} (u(t, s))$ and $u(t, x^+) = \lim_{s \to x^+} (u(t, s))$.

Chapter 1

Introduction

Vehicle automation is a research topic that started gathering broad interest in the 1990s with the concept of automated highway system (see Varaiya (1993)) and a plethora of related results (Ioannou and Chien (1993), Swaroop and Hedrick (1996)). During the last decade, there has been significant progress in developing and deploying a wide variety of vehicle automation and communication systems which revolutionize the capabilities of individual vehicles. Automated vehicles have already appeared on the same roads where conventional vehicles are present (see Kanagaraj and Treiber (2018), Yao et al. (2022), Li et al. (2023), Vranken and Schreckenberg (2022), Vranken et al. (2021)). The levels of vehicle automation can vary from relatively weak driver support, like the conventional cruise control, to more advanced driver assistance systems like the adaptive cruise control, or even fully automated driving (see Kerner (2023)). These driving automation systems may be further enhanced if vehicles are equipped with communication systems that enable real-time information exchange benefitting both safety and efficiency.

In this context, the TrafficFluid concept (Papageorgiou et al. (2021)) is a novel paradigm for vehicular traffic that applies at high levels of vehicle automation and communication, suggesting two combined principles: (a) Lane-free traffic, whereby the vehicles are not restricted to move on fixed traffic lanes but can drive anywhere on the 2-D surface, thus exploiting the road geometry in a better way compared to lane-based movement; and (b) Vehicle nudging, whereby the vehicles influence other vehicles not only behind, but also in front or on the sides of them. These principles improve on certain limitations of human driving. In particular, the use of traffic lanes in conventional traffic leads to reduced road capacity due to low lateral occupancy, and necessitates occasional lane-changes, which is a risky maneuver (see Artuñedo et al. (2024), Rahman et al. (2013)). Moreover, the traffic flow in conventional traffic is anisotropic due to the fact that human driving is influenced only by downstream vehicles, implying the lack of pressure at a macroscopic level. However, note that laneless driving is observed also with human driven vehicles (Agrawal et al. (2023)). In addition, the absence of lanes is adopted in several other aspects of living nature (see Ballerini et al. (2008), Parrish et al. (2002)), but also in some human activities (see Guo et al. (2021), Helbing et al. (1997)), while both isotropy and absence of lanes are met in the particles of fluids (liquids or gases).

Recently, the above principles have been adopted in various approaches to design safe and efficient vehicle movement strategies on lane-free roads, including optimal control (Yanumula et al. (2023)), nonlinear feedback control (Karafyllis et al. (2022a)), and multi-agent systems (Troullinos et al. (2021)). In this work, the traffic flow emerging from vehicle movement strategies based on nonlinear feedback control is studied. More specifically, by applying a Control Lyapunov methodology, a family of decentralized CCs (see Karafyllis et al. (2022d), Karafyllis et al. (2025a), Karafyllis et al. (2025b)) has been designed that can operate on lane-free roads and describe the two-dimensional movement of CAVs. The feedback design challenge for these CCs belongs to a unique category of control problems defined on sets that are not necessarily diffeomorphic to linear spaces. This complexity arises from constraints such as collision avoidance and the requirement for positive vehicle speeds, which confine the system of CAVs to an open set (see Karafyllis et al. (2022d), Karafyllis et al. (2025a), Karafyllis et al. (2025b)). Additionally, since CAVs governed by decentralized CCs cease to interact when sufficiently far apart, the resulting set of equilibrium points may be non-compact — a feature uncommon in most control problems. The CCs under consideration are developed through an algorithmic creation of artificial forces to direct vehicle movement in lane-free traffic, incorporating vehicle nudging. This approach rigorously ensures several desirable properties, including safety through collision avoidance and road boundary respect.

While safety and passenger convenience aspects of the employed CCs for CAVs may be investigated at the microscopic level, it is interesting and important to study their implications for the emerging traffic flow by spanning a bridge between the microscopic and macroscopic levels. In the macroscopic models, traffic flow may be viewed as a fluid with specific characteristics expressed with aggregate variables like vehicle density, flow, and mean speed of vehicles, and its evolution is described via PDEs (see Chapters 3, 4 in Ferrara et al. (2018)). Although the theoretical properties and numerical analysis of the macroscopic traffic flow models have been extensively studied in the literature, their rigorous derivation from microscopic models remains an issue.

Among the numerical methods used for fluid equations, the so-called "particle methods" (also known as "Smoothed Particle Hydrodynamics"; see Filho (2019), Price (2012), Violeau (2012) and references therein) provide a link between the macroscopic fluid model and the microscopic ODE model that describes the interaction between the fluid particles. Such a viewpoint is important (recall Hilbert's 6^{th} problem (Hilbert (2000))), even when the forces acting on the particles are fictitious. Recently, particle methods have been used for the proof of existence of entropy solutions for traffic flow problems (see Di Francesco and Rosini (2015), Holden and Risebro (2018a), Holden and Risebro (2018b)). Moreover, the actual convergence properties of particle methods were established in Karafyllis and Papageorgiou (2023) for 1-D fluid flows. It should be noted that while 1-D flows are not very common in the literature of fluids, they constitute the main paradigm for traffic flow theory.

In this thesis, macroscopic traffic flow models for CAVs, formally derived from the bicycle kinematic model (Polack et al. (2017), Rajamani (2012)) under the CCs proposed in Karafyllis et al. (2022d), Karafyllis et al. (2025a), are studied. The derivation is based on particle methods (see Karafyllis et al. (2022d),Karafyllis et al. (2025b)) by adopting a methodology that is inspired by Di Francesco and Rosini (2015), Holden and Risebro (2018a), Holden and Risebro (2018b). The particle methods provide the link between the macroscopic models and the respective microscopic CCs. More specifically, following the same derivation process that was first given in Karafyllis et al. (2022b) and neglecting the lateral movement of vehicles, the macroscopic traffic flow models presented in Section 1.2.1 (see also Karafyllis et al. (2022d), Karafyllis et al. (2025b)) are obtained. The formally derived macroscopic models are "fluid-like" models and they are isotropic, meaning that the vehicles react to both upstream and downstream vehicles. Isotropy, as well as several "fluid-like" characteristics that are present in the derived macroscopic models follow from the fact that lane-free movement and nudging are allowed by the respective CCs.

In the employed particle methods, the vehicles are considered as "self-driven" particles of a fluid ("the traffic fluid") and the corresponding macroscopic PDE models are similar to the equations of a viscous compressible fluid; (see Karafyllis et al. (2022d), Karafyllis et al. (2025b), Karafyllis et al. (2022b)). Based on that, specific selections for the functions included in the CCs enabled a model reduction in Theodosis et al. (2024), which is analogous to the human-driven vehicles case, where the ARZ model (Aw et al. (2002), Aw and Rascle (2000), Zhang (2002)) reduces to the well-known LWR model (see Li (2003)). The resulting reduced model consists of a single PDE that has the form of a nonlinear heat equation. The properties of the reduced model's solution are extensively studied in Chapter 2 by introducing the appropriate notion of a weak solution that requires certain entropy-like conditions.

Moreover, a first-order finite difference numerical scheme is constructed to approximate the solution of the nonlinear heat equation.

In Chapter 3, the performance of one of the particle methods used for the formal derivation of the proposed macroscopic models is evaluated. More specifically, a comparison with other numerical methods in the literature for compressible fluid models is provided, showing that the employed particle method, in addition to having much less computational cost, it performs better than the other numerical methods. It is also shown that the particle method under consideration preserves certain differential inequalities that hold for the macroscopic traffic flow model. Moreover, the obtained numerical solutions are compared with the corresponding numerical approximations provided for the solutions of the reduced model, verifying its high accuracy approximations.

The usefulness of the proposed macroscopic traffic flow models can be measured by means of empirical validation. Therefore, Chapter 4 attempts to give an answer to this question. Since the derivation of the macroscopic models is based on the assumption that the movement of vehicles is lane-based (1-D movement), the accurate description of the emerging traffic flow seems uncertain. However, Chapter 4 provides evidence that the proposed macroscopic traffic flow models for CAVs are successful even in very complex cases. More specifically, two distinct traffic scenarios are considered, each involving a different kind of bottleneck, for which macroscopic traffic data are collected from microscopic simulations using the respective CCs. It is shown that after calibrating one of the formally derived macroscopic traffic flow models for CAVs, all the traffic conditions that appear in the collected macroscopic traffic data are reproduced with high accuracy.

1.1 Macroscopic traffic flow models for human drivers

Before presenting the proposed macroscopic models for CAVs, it is important to highlight the most well-known macroscopic traffic flow models for human drivers. The first and most influential macroscopic traffic flow model was independently proposed by Lighthill and Whitham (1955) and Richards (1956) (LWR model). The well-known LWR model is a first-order model governed by one scalar hyperbolic PDE which is simply the continuity equation (conservation of mass)

$$\tilde{\rho}_\tau + (\tilde{\rho}\tilde{v})_\xi = 0 \tag{1.1}$$

where $\tilde{\rho} > 0$ is the vehicle density and $\tilde{v}$ is the mean speed, and both are combined with an algebraic equation that determines the vehicle speed as a function of the vehicle density

$$\tilde{v} = F(\tilde{\rho}) \tag{1.2}$$

where $F : \mathbb{R}_+ \to \mathbb{R}_+$ is a non-increasing function.

First-order traffic models, despite being widely studied, exhibit several shortcomings as they fail to capture key aspects of real-world traffic dynamics. For example, in the LWR model, vehicles are assumed to instantly adjust to a new equilibrium velocity following a change in traffic conditions, implying infinite acceleration. Additionally, the transition from free-flow to congested regimes occurs at a single critical density, without accounting for phenomena such as capacity drop or hysteresis. While some of these limitations can be mitigated through extensions of the LWR model (see Lebacque (2002), Leclercq (2007), Daganzo et al. (1997), Laval and Daganzo (2006)), researchers have proposed second-order models to achieve greater modeling fidelity, albeit at the cost of increased complexity due to an additional PDE.

The most prominent second-order model for human-driven traffic is the ARZ model (see Aw et al. (2002), Aw and Rascle (2000), Zhang (2002)), which comprises the continuity equation (1.1) and the following speed equation:

$$\tilde{v}_\tau + \left(\tilde{v} + \tilde{\rho}F'(\tilde{\rho})\right)\tilde{v}_\xi = -\tilde{\sigma}\left(\tilde{v} - F(\tilde{\rho})\right) \tag{1.3}$$

where $\tilde{\sigma} > 0$ is a constant.

A shared characteristic of both the LWR and ARZ models is their anisotropy — i.e., they respond solely to downstream traffic conditions (Daganzo (1995)) — unlike the proposed macroscopic models for CAVs. Another commonality is their hyperbolic nature and lack of viscosity (or diffusion) terms.

It is worth noting that the LWR model can be seen as a special case embedded within the ARZ model. Specifically, if the initial condition of the ARZ model satisfies the equilibrium condition (1.2) everywhere, the ARZ solution coincides with the LWR solution (see Goatin and Laurent-Brouty (2019), Li (2003)). This becomes evident by defining:

$$s = \tilde{v} - F(\tilde{\rho}) \tag{1.4}$$

which is a Riemann coordinate of the ARZ model and satisfies the equation

$$s_\tau + \tilde{v}s_\xi = -\tilde{\sigma}s. \tag{1.5}$$

Both LWR and ARZ models have been widely employed in traffic control research (see Bayen et al. (2022) – Yu et al. (2020)). Furthermore, the recent book by Yu and Krstic (2022) offers numerous extensions of the ARZ model, including adaptations for multi-lane traffic, multiple vehicle classes, and detailed designs of controllers and observers based on linearized versions of the model on bounded domains with input at the boundaries.

1.2 An overview of the proposed macroscopic traffic flow models for CAVs on lane-free roads

The CCs proposed in Karafyllis et al. (2022d) are constructed by means of Lyapunov functions (see Appendix A.1) expressed in terms of the mechanical energy of vehicles and additional penalty terms that guarantee that all vehicle orientations remain within certain bounds. For the construction of the Lyapunov functions, two main approaches are considered. The first one is based on Newtonian mechanics while the second one is inspired by relativistic mechanics, where the speed limits (± the speed of light) are replaced by the two speed limits for the vehicles (zero and the speed limit $v_{\max}$ of the road, respectively). Depending on the approach used for the construction of each Lyapunov function, the respective cruise controller is called NCC or PRCC. More specifically, the NCC (see Appendix A.2) is based on the Newtonian mechanical energy, while the PRCC (see Appendix A.3) is based on the pseudo-relativistic mechanical energy. The vehicle movement with the NCC and PRCC concerns roads of constant width and the same desired speed for all vehicles. For more complex driving situations, such as the consideration of variable-width roads, the potential to have different individual desired speeds for each vehicle, the possibility of each vehicle to move within its own corridor, and the presence of on-ramps and off-ramps, the generalized case of the above cruise controllers should be employed, i.e. the GCC. The construction of the GCC is based on a Lyapunov-like function which follows a pseudo-relativistic setting (see Karafyllis et al. (2025a), Karafyllis et al. (2025b) and Appendix A.1). However, it has many differences compared to the Lyapunov function used for the construction of the PRCC, since the general case is considered, where each vehicle has its own desired speed and its own corridor.

The performance of the NCC, PRCC, and GCC at the macroscopic level is evaluated by using formally derived macroscopic traffic flow models i.e the macro-NCC, the macro-PRCC, and the macro-GCC (see Karafyllis et al. (2025b)). The derived macroscopic models provide information about the implications of the respective cruise controllers for the emerging traffic flow. The present work is devoted to the study of the macro-PRCC and macro-GCC. The macro-PRCC is a system of quasi-linear PDEs (see Section 1.2.1) and therefore it is more manageable than the macro-NCC which is highly nonlinear (see Karafyllis et al. (2022d), Karafyllis et al. (2025b), and Appendix B). The macro-GCC is more applicable to real complex driving situations since it describes the traffic flow of vehicles under the effect of GCC. Both models consist of two PDEs: a continuity equation and a speed equation. However, a model reduction is possible for the macro-PRCC (see Section 1.2.2 and Chapter 2). The reduced model consists of a single PDE which has the form of a nonlinear heat equation. The forms of the macroscopic traffic flow models under consideration are given in the following Section 1.2.1.

1.2.1 The macroscopic traffic flow models

The macro-PRCC consists of the continuity equation (1.1) and the following speed equation

$$\tilde{q}(\tilde{v})\left(\tilde{v}_\tau+\tilde{v}\tilde{v}_\xi\right)+\frac{\tilde{P}'\left(\tilde{\rho}\right)}{\tilde{\rho}}\tilde{\rho}_\xi=\frac{1}{\tilde{\rho}}(\tilde{\mu}(\tilde{\rho})\tilde{g}'(\tilde{v})\tilde{v}_\xi)_\xi-\tilde{f}(\tilde{v}-v^*) \tag{1.6}$$

for $\tau>0$ and $\xi\in I(\tau)$, where $I(\tau)\subseteq\mathbb{R}$ is an appropriate interval that contains the vehicles for times $\tau>0$. The continuity equation (1.1) describes the mass (vehicle) conservation law while the speed equation (1.6) expresses the dynamics of mean speed. The macro-PRCC is to be considered with state constraints $\tilde{\rho}(\tau,\xi)\in(0,\rho_{\max})$, $\tilde{v}(\tau,\xi)\in(0,v_{\max})$ for all $\tau>0$, $\xi\in I(\tau)$, where $\tilde{\rho}(\tau,\xi)$, $\tilde{v}(\tau,\xi)$ are the traffic density and the mean speed, respectively, at position $\xi\in I(\tau)$ on a highway with $\rho_{\max}$ being the maximum density and $v_{\max}$ being the maximum speed limit of the road, while v^* is the speed set-point. Moreover, $\tilde{f}:\mathbb{R}\to\mathbb{R}$ is a C^1 function with $\tilde{f}(0)=0$ and $\xi\tilde{f}(\xi)>0$ for all $\xi\neq 0$, $\tilde{g}\in C^1(\mathbb{R})$ is an increasing function with $\tilde{g}'(\tilde{v})>0$ for all $\tilde{v}\in\mathbb{R}$, and $\tilde{q}(\tilde{v})$ is defined by

$$\tilde{q}(\tilde{v}):=v_{\max}^2\frac{v_{\max}\tilde{v}+\left(v_{\max}-2\tilde{v}\right)v^*}{2(v_{\max}-\tilde{v})^2\tilde{v}^2},\ \text{for all}\ \tilde{v}\in(0,v_{\max}). \tag{1.7}$$

The functions $\tilde{\mu}:(0,\rho_{\max})\to\mathbb{R}_+$, $\tilde{P}:(0,\rho_{\max})\to\mathbb{R}_+$ are $C^1\left((0,\rho_{\max})\right)$ and satisfy the following properties

$$\lim_{\tilde{\rho}\to\rho_{\max}^-}\tilde{P}(\tilde{\rho})=+\infty \tag{1.8}$$

$$\begin{aligned}&\tilde{\mu}(\tilde{\rho})=0,\ \tilde{P}(\tilde{\rho})=0,\ \text{for all}\ \tilde{\rho}\in(0,\bar{\rho}]\,,\ \text{and}\ \tilde{\mu}(\tilde{\rho})>0,\ \tilde{P}(\tilde{\rho})>0,\ \text{for all}\\&\tilde{\rho}\in(\bar{\rho},\rho_{\max})\end{aligned} \tag{1.9}$$

where the constant $\bar{\rho}\in(0,\rho_{\max})$ is called interaction density due to the fact that for all $\tilde{\rho}\in(0,\bar{\rho}]$ there is no interaction among vehicles (see (1.9)).

The form of the macro-GCC is given by the continuity equation (1.1) and the following speed equation

$$\tilde{Q}(\tilde{v},\tilde{r})\left(\tilde{v}_\tau+\tilde{v}\tilde{v}_\xi\right)+\frac{\tilde{P}'\left(\tilde{\rho}\right)}{\tilde{\rho}}\tilde{\rho}_\xi=-\frac{v_{\max}^2v^*\tilde{\sigma}'\left(\tilde{r}\right)}{\tilde{\rho}(v_{\max}-\tilde{v})\tilde{v}}\left(\tilde{\rho}\tilde{P}'\left(\tilde{\rho}\right)\tilde{v}_\xi\right)_\xi-\gamma\left(\tilde{v}-v^*\tilde{\sigma}\left(\tilde{r}\right)\right) \tag{1.10}$$

for $\tau > 0$ and $\xi \in I(\tau)$ ($I(\tau) \subseteq \mathbb{R}$ is an appropriate interval) where

$$\tilde{r} := \frac{\tilde{P}'(\tilde{\rho})}{\tilde{\rho}}\tilde{\rho}_\xi \tag{1.11}$$

and $\gamma > 0$ is a constant. The function $\tilde{P}(\tilde{\rho})$ satisfies the same properties as in the macro-PRCC, given by (1.8) and (1.9), while $\tilde{\sigma} : \mathbb{R} \to (0,1]$ is a non-increasing C^2 function that satisfies

$$\tilde{\sigma}(x) = 1 \text{ for } x \le \varepsilon \text{ and } \tilde{\sigma}(x)x \le M \text{ for } x \ge \varepsilon \tag{1.12}$$

$$\sup_{x\in\mathbb{R}} \left(|\tilde{\sigma}'(x)| + |\tilde{\sigma}''(x)|\right) < +\infty \tag{1.13}$$

where M and ε are positive constants. Finally, the function $\tilde{Q}(\tilde{v},\tilde{r})$ is given by

$$\tilde{Q}(\tilde{v},\tilde{r}) := v_{\max}^2 \frac{v_{\max}\tilde{v} + (v_{\max} - 2\tilde{v})\, v^*\tilde{\sigma}(\tilde{r})}{2(v_{\max} - \tilde{v})^2\tilde{v}^2}. \tag{1.14}$$

1.2.2 Analogy with traffic flow models for human drivers

Motivated by (1.5), a similar equation can be derived for the macro-PRCC by making specific selections for the functions included in the respective cruise controller. More specifically, the functions included in the PRCC (see Karafyllis et al. (2022d), Karafyllis et al. (2025b), and Appendix A.3) can be selected in such a way that the corresponding functions $\tilde{P}'(\tilde{\rho})$, $\tilde{\mu}(\tilde{\rho})$ $\tilde{g}(\tilde{v})$, $\tilde{f}(\tilde{v})$ of the macro-PRCC are given as follows

$$\tilde{P}'(\tilde{\rho}) = \tilde{\sigma}\tilde{\kappa}(\tilde{\rho}) \tag{1.15}$$

$$\tilde{\mu}(\tilde{\rho}) = \tilde{\rho}\tilde{\kappa}(\tilde{\rho}) \tag{1.16}$$

$$\tilde{g}(\tilde{v}) = \tilde{v} \tag{1.17}$$

$$\tilde{f}(\tilde{v} - v^*) = \tilde{\sigma}\tilde{\beta}(\tilde{v}) \tag{1.18}$$

where the function $\tilde{\kappa} : (0,\rho_{\max}) \to \mathbb{R}_+$ is $C^1\left((0,\rho_{\max})\right)$ and satisfies

$$\lim_{\tilde{\rho}\to\rho_{\max}^-} \tilde{\kappa}(\tilde{\rho}) = +\infty \tag{1.19}$$

$$\tilde{\kappa}(\tilde{\rho}) = 0 \;\text{ for all }\; \tilde{\rho} \in (0,\bar{\rho}] \;\text{ and }\; \tilde{\kappa}(\tilde{\rho}) > 0 \;\text{ for all }\; \tilde{\rho} \in (\bar{\rho},\rho_{\max}) \tag{1.20}$$

while the function $\tilde{\beta} : (0, v_{\max}) \to \mathbb{R}$ is given by means of the following formula (recall (1.7))

$$\tilde{\beta}(\tilde{v}) = \int_{v^*}^{\tilde{v}} \tilde{q}(s)ds, \text{ for all } \tilde{v} \in (0, v_{\max}). \tag{1.21}$$

If we define

$$\tilde{\varphi}(\tau,\xi) = \tilde{\beta}\left(\tilde{v}(\tau,\xi)\right) + \tilde{\kappa}(\tilde{\rho}(\tau,\xi))\tilde{\rho}^{-1}(\tau,\xi)\tilde{\rho}_\xi(\tau,\xi), \text{ for } \tau \ge 0 \text{ and } \xi \in \tilde{I}(\tau) \tag{1.22}$$

then, by virtue of (1.1), (1.6), (1.15), (1.16), (1.17), (1.18), and (1.21), we obtain the differential equation

$$\tilde{\varphi}_\tau + \tilde{v}\tilde{\varphi}_\xi = -\tilde{\sigma}\tilde{\varphi}. \tag{1.23}$$

The similarity of (1.5) and (1.23) is striking. Moreover, if the interval $I(\tau) \subseteq \mathbb{R}$ is given by the equation $I(\tau) = \left(\tilde{l}(\tau), \tilde{L}(\tau)\right)$ where

$$\frac{d}{d\tau}\tilde{l}(\tau) = \tilde{v}\left(\tau, \tilde{l}^+(\tau)\right) \tag{1.24}$$

$$\frac{d}{d\tau}\tilde{L}(\tau) = \tilde{v}\left(\tau, \tilde{L}^{-}(\tau)\right) \tag{1.25}$$

we can define the functional

$$\tilde{W}(\tau) = \frac{1}{2}\int_{\tilde{l}(\tau)}^{\tilde{L}(\tau)} \tilde{\rho}(\tau,\xi)\tilde{\varphi}^2(\tau,\xi)d\xi. \tag{1.26}$$

In addition, if a classical solution of (1.1), (1.6) satisfies

$$\tilde{\rho}\left(\tau, \tilde{l}^{+}(\tau)\right) \leq \bar{\rho}\,,\ \tilde{\rho}\left(\tau, \tilde{L}^{-}(\tau)\right) \leq \bar{\rho} \tag{1.27}$$

then, from (1.1), (1.23), (1.24), (1.25), (1.26), (1.27), it follows that

$$\dot{\tilde{W}}(\tau) = -2\tilde{\sigma}\tilde{W}(\tau) \Rightarrow \tilde{W}(\tau) = \exp(-2\tilde{\sigma}\tau)\tilde{W}(0) \text{ for } \tau > 0. \tag{1.28}$$

Therefore, it becomes clear that the subset of the state space where $\tilde{\varphi}(\tau,\xi) \equiv 0$ is invariant and exponentially attracting. On this invariant set, the solutions satisfy the following nonlinear heat equation (see Chapter 2 and Theodosis et al. (2024) for more details)

$$\tilde{\rho}_\tau + \left(\tilde{\rho}\tilde{\beta}^{-1}\left(-\tilde{\rho}^{-1}\tilde{\kappa}(\tilde{\rho})\tilde{\rho}_\xi\right)\right)_\xi = 0 \tag{1.29}$$

where $\tilde{\beta}^{-1} : \mathbb{R} \to (0, v_{\max})$ is the inverse function of $\tilde{\beta} : (0, v_{\max}) \to \mathbb{R}$ defined by (1.21). The solutions of (1.29) approximate the solutions of the macroscopic model given by (1.1), (1.6), (1.15), (1.16), (1.17), (1.18), (1.21).

The analogy with the traffic flow of human-driven vehicles is now clear. For human-driven vehicles, the ARZ model has an invariant and exponentially attracting set, on which the traffic flow is described by the LWR model. For CAVs, the macro-PRCC with the selections given by (1.15), (1.16), (1.17), (1.18), (1.21) has an invariant and exponentially attracting set. On this invariant set, the traffic flow is described by (1.29). Therefore, (1.29) is a reduced model for CAVs; loosely speaking, it is the "LWR model for CAVs".

1.2.3 Comparison with the 1-D Navier-Stokes equations

Both the macro-PRCC and macro-GCC can be classified as fluid-like models, as their respective speed equations — (1.6) and (1.10) — closely resemble the momentum equation found in the 1-D Navier-Stokes equations for a polytropic compressible fluid. In particular:

- The term $\frac{\tilde{P}'(\tilde{\rho})}{\tilde{\rho}}\tilde{\rho}_\xi$, present in both (1.6) and (1.10), acts analogously to the pressure term that appears in the Navier-Stokes equations.
- The term $\frac{1}{\tilde{\rho}}(\tilde{\mu}(\tilde{\rho})\tilde{g}'(\tilde{v})\tilde{v}_\xi)_\xi$ in (1.6) resembles the viscosity term $\frac{1}{\tilde{\rho}}(\tilde{\mu}(\tilde{\rho})\tilde{v}_\xi)_\xi$ that appears in Navier-Stokes equations. A similar role is played by the term $-\frac{v_{\max}^2 v^* \tilde{\sigma}'(\tilde{r})}{\tilde{\rho}(v_{\max}-\tilde{v})\tilde{v}}\left(\tilde{\rho}\tilde{P}'(\tilde{\rho})\tilde{v}_\xi\right)_\xi$ in (1.10), provided that $\tilde{P}'(\tilde{\rho}) \geq 0$ for all $\tilde{\rho} \in (0, \rho_{\max})$ (i.e. when $\tilde{P}(\tilde{\rho})$ is non-decreasing) . In this case, the term functions as a viscosity term — although it arises as a consequence of pressure and is not an independent property of the system.
- The terms $-\tilde{f}(\tilde{v}-v)$ and $-\gamma\left(\tilde{v}-v^*\tilde{\sigma}\left(\tilde{r}\right)\right)$ in (1.6) and (1.10), respectively, can be interpreted as friction or relaxation terms, comparable to $-\bar{\kappa}(\tilde{\rho},\tilde{v})\tilde{v}$ in the Navier-Stokes equations.

Table 1.1 outlines the structural similarities between the macro-PRCC, macro-GCC, and the 1-D Navier-Stokes equations for a compressible polytropic fluid. It highlights key components such as the continuity and speed equations, pressure and viscosity formulations, state variables, and model-specific parameters.

	macro-PRCC	**macro-GCC**	**1-D Navier-Stokes equations for a polytropic compressible fluid**
Continuity equation	$\tilde{\rho}_\tau + (\tilde{\rho}\tilde{v})_\xi = 0$		
Speed equation	$\tilde{Q}(\tilde{v},\tilde{r})\,(\tilde{v}_\tau + \tilde{v}\tilde{v}_\xi) = \tilde{G} - \tilde{J}\tilde{f}(\tilde{v} - \tilde{V}(\tilde{r}))$ $\tilde{r} = \tilde{\rho}^{-1}\tilde{P}'(\tilde{\rho})\,\tilde{\rho}_\xi$		
States	$\tilde{\rho} \in (0,\rho_{\max}),\ \tilde{v} \in (0, v_{\max})$		$\tilde{\rho} > 0,\ \tilde{v} \in \mathbb{R}$
Pressure	$\tilde{P} : (0,\rho_{\max}) \to \mathbb{R}_+,\ \lim\limits_{\tilde{\rho}\to\rho_{\max}^-} \tilde{P}(\tilde{\rho}) = +\infty,$ $\tilde{P}(\tilde{\rho}) = 0,\ \text{for } \tilde{\rho} \in (0,\bar{\rho}]$		$\tilde{P}(\tilde{\rho}) = B\tilde{\rho}^{\eta}$
Viscosity	$\tilde{\mu} : (0,\rho_{\max}) \to \mathbb{R}_+$, $\tilde{\mu}(\tilde{\rho}) = 0,\ \text{for } \tilde{\rho} \in (0,\bar{\rho}]$	$\tilde{\mu}(\tilde{\rho}) = \tilde{\rho}\tilde{P}'(\tilde{\rho})$	$\tilde{\mu} : (0,+\infty) \to$ $(0,+\infty)$ non-decreasing
Constants	$\rho_{\max}, v_{\max}, \gamma, \varepsilon, M > 0,\ v^* \in (0, v_{\max}),\ \bar{\rho} \in (0,\rho_{\max})$		$B > 0,\ \eta \in (1,2)$
$\tilde{Q}(\tilde{v},\tilde{r})$	$v_{\max}^2 \frac{v_{\max}\tilde{v}+(v_{\max}-2\tilde{v})v^*}{2(v_{\max}-\tilde{v})^2\tilde{v}^2}$	$v_{\max}^2 \frac{v_{\max}\tilde{v}+(v_{\max}-2\tilde{v})v^*\tilde{\sigma}(\tilde{r})}{2(v_{\max}-\tilde{v})^2\tilde{v}^2}$	1
$\tilde{G}$	$\tilde{\rho}^{-1}\tilde{S}(\tilde{v},\tilde{r})(\tilde{\mu}(\tilde{\rho})\tilde{g}'(\tilde{v})\tilde{v}_\xi)_\xi - \tilde{r}$		
$\tilde{S}(\tilde{v},\tilde{r})$	1	$-\frac{v_{\max}^2 v^*\tilde{\sigma}'(\tilde{r})}{\tilde{\rho}(v_{\max}-\tilde{v})\tilde{v}}$	1
$\tilde{J}$	1	γ	$\tilde{\kappa}(\tilde{\rho},\tilde{v})$
$\tilde{g}(\tilde{v})$	$\tilde{g} : \mathbb{R} \to \mathbb{R},$ $\tilde{g}'(\tilde{v}) > 0$ for $\tilde{v} \in \mathbb{R}$	$\tilde{v}$	$\tilde{v}$
$\tilde{V}(\tilde{r})$	v^*	$v^*\tilde{\sigma}(\tilde{r})$	0
$\tilde{f}(\tilde{v})$	$\tilde{f} : (-v^*, v_{\max} - v^*) \to \mathbb{R}$	$\tilde{v}$	$\tilde{v}$
Comments	$\tilde{v}\tilde{f}(\tilde{v}) > 0$ for $\tilde{v} \neq 0$	$\tilde{\sigma} : \mathbb{R} \to (0,1]$ is a non-increasing function that satisfies (1.12), (1.13)	$\tilde{\kappa} : (0,+\infty)\times\mathbb{R} \to \mathbb{R}_+$

Table 1.1: Macroscopic models for CAVs and 1-D compressible Navier-Stokes equations

Despite these analogies, there are several fundamental differences between the macroscopic models for CAVs (macro-PRCC and macro-GCC) and the classical 1-D Navier-Stokes equations:

- In compressible fluid flow, the density is only required to be positive, and the speed can assume any real value (Lions (1998)). In contrast, the macro-PRCC and macro-GCC models constrain the density to the interval $(0,\rho_{\max})$ and the speed to $(0, v_{\max})$ to reflect physical limitations on vehicle spacing and road speed limits.

- In compressible fluid flow, the friction term tends to bring the fluid speed to zero; while in the macro-PRCC and macro-GCC, the friction term tends to bring the speed to the given speed set-point $v^* \in (0, v_{\max})$.

- In compressible fluid flow, the pressure and viscosity terms are always present, and they never vanish; while in the derived macroscopic models, the pressure and viscosity terms vanish when the density is lower than a specific value (the interaction density) (see (1.9)).
- In the macro-PRCC and macro-GCC, the acceleration term $\tilde{v}_\tau + \tilde{v}\tilde{v}_\xi$ is scaled by a factor that blows up when the speed tends to zero or to the road speed limit. This factor originates from the pseudo-relativistic energy structure employed in the design of PRCC and GCC and is reminiscent of similar effects in relativistic fluid mechanics.

The similarities highlighted in Table 1.1 are not coincidental. They reflect the fact that traffic flow under PRCC and GCC exhibits isotropic behavior, where vehicles act as "self-driven" particles of a Newtonian fluid. Unlike conventional traffic models, where drivers only respond to downstream vehicles, these CAV models incorporate nudging effects, enabling vehicles to also respond to upstream vehicles.

1.3 Thesis outline

Chapter 2 is devoted to the study of the reduced model for CAVs. A concept of weak solution as well as certain entropy-like conditions that characterize physically meaningful solutions are defined for the reduced model. To approximate its solutions, a conservative finite difference numerical scheme is constructed that respects the entropy-like conditions, and certain links between the weak solution and the solutions of the numerical scheme are established. For the employed numerical scheme, a CFL-type condition is derived to ensure numerical stability. Moreover, the traffic flow of CAVs is compared with that of human-driven vehicles by considering a realistic traffic scenario and using the reduced model for CAVs and the LWR model.

In Chapter 3, the particle method, that was used to derive the macro-PRCC, is utilized as a numerical scheme for approximating its solutions. It is shown that the particle method preserves certain differential inequalities that hold for the macro-PRCC. To evaluate its performance, a comparison with other numerical methods for viscous compressible fluids is provided. The produced numerical solutions are compared with the corresponding numerical approximations provided for the solutions of the reduced model. In addition, a realistic traffic scenario is adopted to compare the traffic flow of CAVs with that of human-driven vehicles by using the macro-PRCC and the ARZ model.

Chapter 4 provides evidence that the proposed macroscopic models for the description of the traffic flow of vehicles under the effect of the respective CCs are successful even in very complex cases. More specifically, the macro-GCC is calibrated to fit traffic data collected from microscopic simulation using the GCC. The accuracy of the macro-GCC is evaluated by considering two independent traffic scenarios.

Finally, Chapter 5 concludes this thesis with some concluding remarks and future work.

1.4 Scientific work related to the PhD

The research conducted within the scope of this doctoral thesis has been published or is pending publication in the following journal and conference papers.

1.4.1 Journal papers

- Theodosis, D., Karafyllis, I., Titakis, G., Papamichail, I. and Papageorgiou, M. (2024). "A Nonlinear Heat Equation Arising from Macroscopic Automated-Vehicle Traffic Flow Models". *Journal of Computational and Applied Mathematics* 437, p.115443.

- Titakis, G., Karafyllis, I., Theodosis, D., Papamichail, I. and Papageorgiou, M. (2024). "A Comparative Study of Numerical Methods for Approximating the Solutions of a Macroscopic Automated-Vehicle Traffic Flow Model". *Computers and Mathematics with Applications* 176, pp. 469-490.

- Titakis, G., Papamichail, I., Karafyllis, I., Theodosis, D. and Papageorgiou, M. "Calibration of a Macroscopic Automated-Vehicle Traffic Flow Model for Lane-Free Traffic" (submitted to *Physical Review E*).

1.4.2 Conference papers

- Theodosis, D., Karafyllis, I., Titakis, G., Papamichail, I. and Papageorgiou, M. (2023). "Performance Evaluation of Cruise-Controlled Vehicles on a Macroscopic Scale". *31st Mediterranean Conference on Control and Automation (MED 2023).* IEEE, pp. 287-292.

- Titakis, G., Karafyllis, I., Theodosis, D., Papamichail, I. and Papageorgiou, M. (2023). "Numerical Approximations to a Macroscopic Automated-Vehicle Traffic Flow Model". *21st* International Conference of Numerical Analysis and Applied Mathematics (ICNAAM 2023). AIP Conf. Proc. 3315, pp. 400016 1-4.

- Titakis, G., Karafyllis, I., Theodosis, D., Papamichail, I. and Papageorgiou, M. (2024). "The Effects of Cruise-Controlled Vehicles on Traffic Density". *32nd Mediterranean Conference on Control and Automation (MED 2024).* IEEE, pp. 31-36.

Chapter 2

A nonlinear heat equation arising from the macro-PRCC

2.1 Abstract

In this chapter, a new nonlinear heat equation is studied that arises as a model of the collective behavior of automated vehicles. The properties of the solutions of this equation are studied by introducing the appropriate notion of a weak solution that requires certain entropy-like conditions. To obtain an approximation of the solutions of the nonlinear heat equation, a new conservative first-order finite difference numerical scheme is proposed that respects the entropy-like conditions, and certain links between the weak solution and the solutions of the numerical scheme are provided. Finally, a traffic simulation scenario and a comparison with the LWR model are provided, illustrating the benefits of the use of CAVs.

2.2 Introduction

The heat equation is a fundamental differential equation and among the most studied topics, (see for instance Nilssen et al. (2003), Ladyzhenskaya et al. (1968), Melo (2014), N'Gohisse and Boni (2011), Popovych and Ivanova (2005), Rodriguez and Vazquez (1995), Truong and Van Y (2016) and references therein). It describes the evolution of the density of some quantity, such as temperature or chemical concentration, and finds immediate application in a variety of topics such as financial mathematics, flow and pressure diffusion in porous media, image analysis and many others.

In this context, a novel nonlinear heat equation is considered, whose diffusion/viscosity coefficient depends on both the density and the spatial derivative of density (see also Nilssen et al. (2003), Ladyzhenskaya et al. (1968)), a feature that is rarely studied in the literature where typically the diffusion coefficient exclusively depends on the density (see for instance Melo (2014), N'Gohisse and Boni (2011), Popovych and Ivanova (2005), Rincon et al. (2006), Rodriguez and Vazquez (1995), Truong and Van Y (2016) and references therein). The nonlinear heat equation under consideration has been derived from the macro-PRCC (see Karafyllis et al. (2022d), Karafyllis et al. (2025b) and Section 1.1) by making specific selections for the functions included in the respective cruise controller, i.e. the PRCC.

In this chapter, it is shown that the solutions of the macro-PRCC can be approximated by the solutions of this particular nonlinear heat equation. Furthermore, inspired by the mechanical energy of the macro-PRCC, certain functionals are defined, providing entropy-like conditions that characterize physically meaningful solutions, (see Dafermos (2010), Smoller (1994)). In particular, the concept of a weak solution is defined for the problem at hand that is more demanding than the typical definition of weak solution (see Leveque (1992), Smoller (1994)), as it requires that certain entropy conditions hold and, in addition, the mass is conserved. Finally, it is shown that, under certain regularity assumptions, this type of weak solutions is equivalent to classical solutions (see Proposition 2.3.1).

The study of the nonlinear heat equation is inevitably related to numerical techniques in order to obtain an approximation of its solutions. More specifically, several finite-difference numerical methods have been proposed to study a variety of nonlinear heat equations (see for instance Baines and Sarahs (2018), Beale (2009), Buckmire et al. (2009), Cho (2013), Christou et al. (2008), Dratman (2013), Hajipour et al. (2018), Jovanovic et al. (2000), and references therein). In this paper, a new first-order explicit finite difference numerical scheme is proposed that, in addition to being conservative (Proposition 2.4.1), it also respects the corresponding entropy-like conditions (Proposition 2.4.2 and Proposition 2.4.4). Moreover, a condition on the step size is provided that is a nonlinear version of the CFL condition (Proposition 2.4.3). Finally, a link between the numerical solutions produced by the proposed numerical scheme and the corresponding weak solutions is provided (Proposition 2.4.5). To demonstrate the properties of the solutions of the nonlinear heat equation, two examples are presented: (i) an academic example, where the efficiency of the proposed numerical scheme is illustrated; and (ii) a realistic traffic simulation scenario showing that the mean flow produced by CAVs is much higher than that of the LWR (Lighthill and Whitham (1955) and Richards (1956)) model.

Therefore, the contribution of this chapter is summarized as follows:

- The study of a novel nonlinear heat equation that arises in traffic flow theory for CAVs;
- The construction of a first-order finite-difference numerical scheme that can be applied to nonlinear heat equations with an explicit condition for numerical stability;
- The study of the connection of the weak solutions of the nonlinear heat equation with the solutions produced by the proposed numerical scheme.

The structure of Chapter 2 is as follows. Section 2.3 is devoted to the derivation of the nonlinear heat equation. Section 2.4 presents the proposed numerical scheme and its properties. Section 2.5 presents the two aforementioned examples. Finally, some concluding remarks are given in Section 2.6. All proofs are provided in Section 2.7.

2.3 The nonlinear heat equation

2.3.1 Derivation of the nonlinear heat equation

When the domain is $\mathbb{R}$ (i.e. $\xi \in \mathbb{R}$), the macro-PRCC (1.1), (1.6) is given by the following PDEs for $\tau > 0$, $\xi \in \mathbb{R}$

$$\tilde{\rho}_\tau + (\tilde{\rho}\tilde{v})_\xi = 0 \tag{2.1}$$

$$\tilde{\rho}\tilde{q}(\tilde{v})\tilde{v}_\tau + \tilde{\rho}\tilde{q}(\tilde{v})\tilde{v}\tilde{v}_\xi + \tilde{P}'(\tilde{\rho})\tilde{\rho}_\xi = (\tilde{\mu}(\tilde{\rho})\tilde{g}'(\tilde{v})\tilde{v}_\xi)_\xi - \tilde{\rho}\tilde{f}(\tilde{v}-v^*) \tag{2.2}$$

with constraints $\tilde{\rho}(\tau,\xi) \in [0,\rho_{\max})$, $\tilde{v}(\tau,\xi) \in (0,v_{\max})$ for $\tau > 0$, $\xi \in \mathbb{R}$, where $\rho_{\max} > 0$, $v_{\max} > 0$, and $v^* \in (0,v_{\max})$ are constants. The states $\tilde{\rho}(\tau,\xi)$, $\tilde{v}(\tau,\xi)$ are the traffic density and mean speed, respectively, at time $\tau > 0$ and position $\xi \in \mathbb{R}$ on a highway, while the constants $\rho_{\max} > 0$, $v_{\max} > 0$, and $v^* \in (0,v_{\max})$ are the maximum density, the maximum speed, and the speed set-point, respectively. Moreover, $\tilde{f} : \mathbb{R} \to \mathbb{R}$ is a C^1 function with $\tilde{f}(0) = 0$ and $\xi\tilde{f}(\xi) > 0$ for all $\xi \neq 0$, $\tilde{g} \in C^1(\mathbb{R})$ is an increasing function with $\tilde{g}'(\tilde{v}) > 0$ for all $\tilde{v} \in \mathbb{R}$, and $\tilde{q}(\tilde{v})$ is defined by

$$\tilde{q}(\tilde{v}) := v_{\max}^2 \frac{v_{\max}\tilde{v} + (v_{\max} - 2\tilde{v})\,v^*}{2(v_{\max}-\tilde{v})^2\tilde{v}^2}, \text{ for all } \tilde{v} \in (0,v_{\max}). \tag{2.3}$$

Model (2.1), (2.2) is a fluid-like model where the term $\tilde{P}'(\tilde{\rho})\tilde{\rho}_\xi$ is a pressure term and expresses the tendency of vehicles to accelerate or decelerate based on the (local) density; while the term $(\tilde{\mu}(\tilde{\rho})\tilde{g}'(\tilde{v})\tilde{v}_\xi)_\xi$, is a viscosity term, by analogy with the theory of fluids, with $\tilde{\mu}(\tilde{\rho})$ playing the role of dynamic viscosity (see Karafyllis and Krstic (2022a), Lions (1998)). The functions $\tilde{\mu} : [0,\rho_{\max}) \to \mathbb{R}_+$, $\tilde{P} : [0,\rho_{\max}) \to \mathbb{R}_+$ are $C^1([0,\rho_{\max}))$ and satisfy the following properties

$$\lim_{\tilde{\rho}\to\rho_{\max}^-} \tilde{P}(\tilde{\rho}) = +\infty \tag{2.4}$$

$$\tilde{\mu}(\tilde{\rho}) = 0,\ \tilde{P}(\tilde{\rho}) = 0,\ \text{for all } \tilde{\rho} \in [0,\bar{\rho}],\ \text{ and } \tilde{\mu}(\tilde{\rho}) > 0,\ \tilde{P}(\tilde{\rho}) > 0,\ \text{ for all } \tilde{\rho} \in (\bar{\rho},\rho_{\max}) \tag{2.5}$$

where the constant $\bar{\rho} \in (0,\rho_{\max})$ is referred to as the interaction density due to the fact that for all $\rho \in [0,\bar{\rho}]$ there is no interaction among the vehicles (see (2.5)). The term $\tilde{f}(\tilde{v} - v^*)$ is a relaxation term that describes the tendency of vehicles to adjust their speed to the given speed set-point $v^* \in (0, v_{\max})$. The functions $\tilde{\mu}(\tilde{\rho})$, $\tilde{g}(\tilde{\rho})$, $\tilde{f}(\tilde{v} - v^*)$, $\tilde{P}(\tilde{\rho})$ are determined by the properties of the cruise controller of the vehicles (see Karafyllis et al. (2022d)).

Remarks: (i) Model (2.1), (2.2) does not include non-local terms and has certain characteristics from the kinematic theory of fluids. Traffic flow is isotropic, as in fluid flow, since the vehicles are autonomous and do not react to downstream vehicles only (as in conventional traffic), but also to upstream vehicles.
(ii) There are infinite equilibrium points, namely the points where $\tilde{v}(\xi) \equiv v^*$ and $\tilde{\rho}(\xi) \leq \bar{\rho}$ for all $\xi \in \mathbb{R}$.
(iii) The selection of $\tilde{\mu}(\tilde{\rho})$, $\tilde{g}(\tilde{\rho})$ has several implications on the characteristics of the traffic flow. The dynamic viscosity $\tilde{\mu}(\tilde{\rho})$ makes the "traffic fluid" act as a Newtonian fluid. However, in contrast to actual fluids, the dynamic viscosity also satisfies (2.5). For isentropic (or barotropic) flow of gases, the dynamic viscosity and the pressure are always increasing functions of the fluid density (see the discussion in Truong and Van Y (2016)). Thus, a traffic fluid can have very different physical properties from those of real compressible fluids.

Model (2.1), (2.2) is to be studied under the following conditions for all $\tau \geq 0$:

$$\lim_{\xi\to\pm\infty} \tilde{\rho}(\tau,\xi) = 0 \tag{2.6}$$

$$\lim_{\xi\to\pm\infty} \tilde{v}(\tau,\xi) = v^* \tag{2.7}$$

$$\int_{-\infty}^{+\infty} \tilde{\rho}(\tau,\xi)d\xi < +\infty. \tag{2.8}$$

Condition (2.6) expresses the fact that "far downstream and far upstream" the highway is "empty", i.e., there are no vehicles. Condition (2.8) expresses the fact that the total mass of the vehicles in the highway is finite. Let $r \in \mathbb{R}$ be a given constant length. Using the variable transformation $\xi = rx + v^*\tau$, $x \in \mathbb{R}$ and the dimensionless quantities $\tau = \frac{r}{v^*}t$, $b = \frac{v_{\max}-v^*}{v^*}$, $R = \frac{\rho_{\max}}{\bar{\rho}} > 1$, $w = \frac{\tilde{v}-v^*}{v^*}$, $\rho = \frac{\tilde{\rho}}{\bar{\rho}}$, we obtain the following dimensionless model for $t > 0$, $x \in \mathbb{R}$

$$\rho_t + (\rho w)_x = 0 \tag{2.9}$$

$$\rho q(w)w_t + \rho q(w)ww_x + P'(\rho)\rho_x = (\mu(\rho)g'(w)w_x)_x - \rho f(w) \tag{2.10}$$

with constraints $\rho(t,x) \in [0,R)$, $w(t,x) \in (-1,b)$ for $t > 0$, $x \in \mathbb{R}$, where $R > 1$, $b > 0$ are constants, $g \in C^1(\mathbb{R})$ is an increasing function with $g'(w) > 0$ for all $w \in (-1,b)$,

$f:\mathbb{R}\to\mathbb{R}$ with $f(0)=0$ is a C^1 function with $wf(w)>0$ for all $w\neq 0$, and

$$q(w)=(1+b)^2\frac{2b+(b-1)w}{2(b-w)^2(1+w)^2}\text{ for all } w\in(-1,b). \tag{2.11}$$

Moreover, the functions $\mu:[0,R)\to\mathbb{R}_+$, $P:[0,R)\to\mathbb{R}_+$ are $C^1([0,R))$ and satisfy the following properties:

$$\lim_{\rho\to R^-}P(\rho)=+\infty \tag{2.12}$$

$$\mu(\rho)=0,\ P(\rho)=0 \text{ for all } \rho\in[0,1], \text{ and } \mu(\rho)>0,\ P(\rho)>0 \text{ for all } \rho\in(1,R). \tag{2.13}$$

Model (2.9), (2.10) is studied under the following conditions for all $t\geq 0$:

$$\lim_{x\to\pm\infty}\rho(t,x)=0 \tag{2.14}$$

$$\lim_{x\to\pm\infty}w(t,x)=0 \tag{2.15}$$

$$\int_{-\infty}^{+\infty}\rho(t,x)dx<+\infty. \tag{2.16}$$

Let $\kappa:[0,R)\to\mathbb{R}_+$ be a function with

$$\kappa(\rho)=0 \text{ for all } \rho\in[0,1] \text{ and } \kappa(\rho)>0 \text{ for all } \rho\in(1,R). \tag{2.17}$$

Moreover, the function $\kappa:[0,R)\to\mathbb{R}_+$ is $C^1([0,R))$ and satisfies

$$\lim_{\rho\to R^-}\kappa(\rho)=+\infty. \tag{2.18}$$

If the functions of the PRCC that is applied to the vehicles are selected in such a way that

$$g(w)=w \text{ for all } w\in(-1,b) \tag{2.19}$$

$$P'(\rho)=\sigma\kappa(\rho) \tag{2.20}$$

$$\mu(\rho)=\rho\kappa(\rho) \tag{2.21}$$

$$\beta(w)=\int_0^w q(s)ds=\frac{b+1}{2}\left[\frac{w(b+1)}{(w+1)(b-w)}+\ln\left(\frac{b(w+1)}{b-w}\right)\right], \text{ for all } w\in(-1,b) \tag{2.22}$$

$$f(w)=\sigma\beta(w) \tag{2.23}$$

where $\sigma>0$ is a constant, then, using definitions (2.19), (2.20), (2.21), (2.22), (2.23), the PDE model (2.9), (2.10), becomes

$$\rho_t+(\rho w)_x=0 \tag{2.24}$$

$$\rho\beta'(w)w_t+\rho\beta'(w)ww_x+\sigma\kappa(\rho)\rho_x=(\rho\kappa(\rho)w_x)_x-\sigma\rho\beta(w) \tag{2.25}$$

with $t>0$, $x\in\mathbb{R}$.

Remark: **(i)** The selections (2.18), (2.19), (2.20), (2.21), (2.23) in addition to simplifying the original model (2.9), (2.10), provides a straightforward methodology to approximate the solutions of (2.24), (2.25) by the solutions of a single PDE (see the analysis below) . Moreover, this particular selection is inspired by fluid flow models, since the resulting model (2.24), (2.25) is very similar to isentropic compressible fluid flow models for Newtonian fluids (see Lions (1998) and Smoller (1994)). Condition (2.18) makes the fluid behave like a solid when

density tends to the maximum density R, while definition (2.19) is met in real fluid flows in non-porous media (see Aronson (1986)).
(ii) By changing the functions and the parameters of the PRCC, it is possible to determine the physical properties of the "traffic fluid" via the functions P, μ, g, f, and design an artificial fluid that approximates the emerging traffic flow. An alternative selection of the aforementioned functions will lead to a new model with a variety of properties.

Assume now that $\rho(t,x) > 0$ for $t > 0$, $x \in \mathbb{R}$ and that (2.14), (2.15), and (2.16) hold. Define

$$\varphi(t,x) = \rho(t,x)\beta\left(w(t,x)\right) + \kappa(\rho(t,x))\rho_x(t,x), \text{ for all } t > 0 \text{ and } x \in \mathbb{R} \tag{2.26}$$

where $\beta(w)$ is given by (2.22). Equations (2.24), (2.25) and definition (2.26) imply the following equation for $t > 0$, $x \in \mathbb{R}$:

$$\varphi_t + (w\varphi)_x = -\sigma\varphi. \tag{2.27}$$

Next, define

$$g(t,x) = \frac{\varphi(t,x)}{\rho(t,x)} \exp(\sigma t), \text{ for all } t > 0 \text{ and } x \in \mathbb{R}. \tag{2.28}$$

Thus, we get from (2.24), (2.25), (2.27), and (2.28) that

$$g_t + wg_x = 0. \tag{2.29}$$

It follows from (2.29) that $\left\|g[t]\right\|_\infty \leq \left\|g[0]\right\|_\infty$ for all $t \geq 0$, which, combined with (2.28), implies that the following estimate holds:

$$\left\|\frac{\varphi[t]}{\rho[t]}\right\|_\infty \leq \exp(-\sigma t)\left\|\frac{\varphi[0]}{\rho[0]}\right\|_\infty \text{ for all } t \geq 0. \tag{2.30}$$

Inequality (2.30) and definition (2.26) imply that for all $x \in \mathbb{R}$:

$$\lim_{t\to+\infty}\left(\beta\left(w(t,x)\right) + \rho^{-1}(t,x)\kappa(\rho(t,x))\rho_x(t,x)\right) = 0. \tag{2.31}$$

Since $\beta\left((-1,b)\right) = \mathbb{R}$, we can define the inverse function $h : \mathbb{R} \to (-1,b)$ with $h(0) = 0$ and $h'(s) > 0$ for all $s \in \mathbb{R}$. Thus, we get from (2.31) for all $x \in \mathbb{R}$:

$$\lim_{t\to+\infty}\left(w(t,x) - h\left(-\rho^{-1}(t,x)\kappa(\rho(t,x))\rho_x(t,x)\right)\right) = 0. \tag{2.32}$$

Inequality (2.30) and equation (2.32) imply that the manifold described by the equation $w(t,x) = h\left(-\rho^{-1}(t,x)\kappa(\rho(t,x))\rho_x(t,x)\right)$ is exponentially attracting.

Consequently, the solutions of (2.9), (2.10) are approximated by the solutions of the following PDE that holds for $t > 0$, $x \in \mathbb{R}$

$$\rho_t + \left(\rho h\left(-\theta(\rho)\rho_x\right)\right)_x = 0$$

where

$$\theta\left(\rho\right) := \rho^{-1}\kappa(\rho) \text{ for } \rho \in (0,R)\,. \tag{2.33}$$

Notice that due to definition (2.33) and (2.17), it follows that $\theta(\rho) = 0$ for all $\rho \in (0,1]$ and $\theta(\rho) > 0$ for all $\rho \in (1,R)$.

2.3.2 The model and its properties

Motivated by the analysis of Section (2.3.1), we study hereafter the following model and its properties

$$\rho_t + \left(\rho h\left(-\theta(\rho)\rho_x\right)\right)_x = 0,\ t > 0,\ x \in \mathbb{R} \tag{2.34}$$

where $\theta \in C^1\left([0,R);\mathbb{R}_+\right)$ with $\theta(\rho) = 0$ for all $\rho \in [0,1]$ and $\theta(\rho) > 0$ for all $\rho \in (1,R)$, and $h \in C^1\left(\mathbb{R};(-1,b)\right)$ with $h' \in L^\infty\left(\mathbb{R}\right)$ and satisfies $h(0) = 0$ and $h'(s) > 0$ for all $s \in \mathbb{R}$. In addition, the PDE (2.34) is studied under the condition:

$$\lim_{x\to\pm\infty}\left(\rho(t,x)\right) = 0, \text{ for all } t > 0 \tag{2.35}$$

with state constraint $\rho(t,x) \in [0,R)$ for all $t > 0$ and $x \in \mathbb{R}$, and $\int_{-\infty}^{+\infty} \rho(t,x)dx < +\infty$ for all $t \geq 0$.

We notice that :

• There are infinite equilibrium points, namely the points where $\rho(x) \leq 1$ for all $x \in \mathbb{R}$.

• The nonlinear PDE (2.34) is not hyperbolic and is not parabolic. When $\rho(t,x) \leq 1$, we get $\rho_t(t,x) = 0$ (a zero-speed hyperbolic PDE) with the propagation speed being zero; and when $\rho(t,x) > 1$, we get the following nonlinear heat equation

$$\rho_t + h\left(-\theta(\rho)\rho_x\right)\rho_x - \rho h'\left(-\theta(\rho)\rho_x\right)\theta'(\rho)\rho_x^2 = \rho h'\left(-\theta(\rho)\rho_x\right)\theta(\rho)\rho_{xx}. \tag{2.36}$$

• The PDE (2.34) (see also (2.36)) is a nonlinear heat equation with the diffusion coefficient depending on both the density ρ and the spatial derivative of the density ρ_x. This feature is rarely studied in the literature, where the diffusion coefficient exclusively depends on the density ρ (see for instance Melo (2014), N'Gohisse and Boni (2011), Popovych and Ivanova (2005), Rincon et al. (2006), Rodriguez and Vazquez (1995), Truong and Van Y (2016) and references therein). Notable exceptions are Ladyzhenskaya et al. (1968), Nilssen et al. (2003), where the viscosity also depends on the spatial derivative of the state.

Define the set

$$X = \left\{\rho \in L^1\left(\mathbb{R}\right) \cap L^\infty\left(\mathbb{R}\right) : \inf_{x\in\mathbb{R}}\left(\rho(x)\right) = 0,\ \sup_{x\in\mathbb{R}}\left(\rho(x)\right) < R,\ \lim_{x\to\pm\infty}\left(\rho(x)\right) = 0\right\}. \tag{2.37}$$

Using (2.34), it can be shown that for every classical solution $\rho \in C^1\left(\mathbb{R}_+ \times \mathbb{R}; [0,R)\right) \cap C^2\left((0,+\infty) \times \mathbb{R}\right)$ of (2.34), (2.35) with $\rho[t] \in X$ for all $t \geq 0$, it holds that

$$\dot{m}(t) = 0 \text{ for } t > 0 \tag{2.38}$$

where $m(t)$ is the total mass

$$m(t) = \int_{-\infty}^{+\infty} \rho(t,x)dx. \tag{2.39}$$

Therefore, the total mass remains constant. The fact that mass is conserved is of great importance, since it characterizes physically admissible solutions.

For any classical solution $\rho \in C^1\left(\mathbb{R}_+ \times \mathbb{R}; [0,R)\right) \cap C^2\left((0,+\infty) \times \mathbb{R}\right)$ of (2.34), (2.35) with $\rho[t] \in X$ for all $t \geq 0$, we can define the following functionals

$$E_1(t) = \int_{-\infty}^{+\infty} \rho(t,x)H\left(-\theta(\rho(t,x))\rho_x(t,x)\right)dx \tag{2.40}$$

$$E_2(t) = \int_{-\infty}^{+\infty} Q(\rho(t,x))dx \tag{2.41}$$

where

$$H(w) := \int_0^w h(s)ds \text{ for all } w \in (-1, b) \tag{2.42}$$

$$Q(\rho) := \int_1^\rho (\rho - \tau)\,\theta(\tau)\,d\tau \text{ for all } \rho \in [0, R)\,. \tag{2.43}$$

The above functionals are inspired by the mechanical energy of the original model (2.24), (2.25), with the functional E_1 in (2.40) expressing the kinetic energy and the functional E_2 in (2.41) expressing the potential energy. A direct consequence of (2.34) and the functionals defined by (2.40) and (2.41) are the following inequalities that hold for all classical solutions $\rho \in C^1(\mathbb{R}_+ \times \mathbb{R}; [0, R)) \cap C^2((0, +\infty) \times \mathbb{R})$ of (2.34), (2.35) with $\rho[t] \in X$ for all $t \geq 0$:

$$\dot{E}_1(t) = -\int_{-\infty}^{+\infty} \rho^2(t,x)\theta(\rho(t,x))\left(h(-\theta(\rho(t,x))\rho_x(t,x))\right)_x^2 dx \leq 0, \text{ for } t > 0 \tag{2.44}$$

$$\dot{E}_2(t) = \int_{-\infty}^{+\infty} \rho(t,x)\theta(\rho(t,x))\rho_x(t,x)h(-\theta(\rho(t,x))\rho_x(t,x))\,dx \leq 0, \text{ for } t > 0. \tag{2.45}$$

Inequalities (2.44), (2.45) show us that both functionals (2.40), (2.41) are decreasing along the classical solutions of (2.34). Inequality (2.45) gives an entropy-like condition (see (2.50)) that characterizes physically meaningful solutions, (see Dafermos (2010), Smoller (1994)).

Let the initial condition

$$\rho[0] = \rho_0 \in X \tag{2.46}$$

be given. Next, the concept of a weak solution is given for the initial-value problem (2.34), (2.35), (2.46).

Definition 2.3.1 *A pair of maps $\rho, w : \mathbb{R}_+ \to L^1(\mathbb{R}) \cap L^\infty(\mathbb{R})$ with*

$$\inf_{x\in\mathbb{R}}(\rho(t,x)) = 0 \textit{ for all } t \geq 0, \quad \sup_{x\in\mathbb{R}, t\geq 0}(\rho(t,x)) < R \tag{2.47}$$

$$-1 < \inf_{x\in\mathbb{R}, t\geq 0}(w(t,x)) \leq \sup_{x\in\mathbb{R}, t\geq 0}(w(t,x)) < b \tag{2.48}$$

$$\int_{-\infty}^{+\infty} \rho(t,x)dx = \int_{-\infty}^{+\infty} \rho_0(x)dx, \textit{ for all } t \geq 0 \tag{2.49}$$

$$\int_{-\infty}^{+\infty} Q(\rho(t,x))\,dx \leq \int_{-\infty}^{+\infty} Q(\rho_0(x))\,dx, \textit{ for all } t \geq 0 \tag{2.50}$$

for which (2.35) holds, is a weak solution of the initial-value problem (2.34), (2.35), (2.46), if, for every function $\phi \in C^2(\mathbb{R}_+ \times \mathbb{R})$ of compact support, the following equations are satisfied:

$$-\int_{-\infty}^{+\infty} \phi(0,x)\rho_0(x)dx = \int_0^{+\infty}\int_{-\infty}^{+\infty} \rho(t,x)\left(w(t,x)\phi_x(t,x) + \phi_t(t,x)\right)dxdt \tag{2.51}$$

$$\int_0^{+\infty}\int_{-\infty}^{+\infty} \left(\phi(t,x)\beta(w(t,x)) - \phi_x(t,x)\,Q'(\rho(t,x))\right)dxdt = 0. \tag{2.52}$$

Definition 2.3.1 is more demanding than the typical definition of weak solution (see for instance Leveque (1992), Smoller (1994)) since, in addition to (2.51) and (2.52), it also requires that the mass is conserved (see (2.49)) and the entropy-like condition (2.50) also holds.

Proposition 2.3.1 *Suppose that $\rho \in C^1(\mathbb{R}_+ \times \mathbb{R};\ [0,R)) \cap C^2((0,+\infty) \times \mathbb{R})$ is a classical solution of the initial-value problem (2.34), (2.35), (2.46), that satisfies (2.47) and*

$$\theta(\rho)\rho_x \in L^\infty(\mathbb{R}_+ \times \mathbb{R}) \tag{2.53}$$

$$\rho[t] \in X, \text{ for all } t \geq 0. \tag{2.54}$$

Then, the pair ρ, w is also a weak solution of (2.34), (2.35), (2.46), where w is given by

$$w = h(-\theta(\rho)\rho_x). \tag{2.55}$$

Moreover, if the pair ρ, w is a weak solution of the initial-value problem (2.34), (2.35), (2.46) with $\rho \in C^1(\mathbb{R}_+ \times \mathbb{R};\ [0,R)) \cap C^2((0,+\infty) \times \mathbb{R})$, then ρ is also a classical solution of the initial-value problem (2.34), (2.35), (2.46) that satisfies (2.53), (2.47), and (2.54).

2.4 A numerical scheme and its properties

Using finite-differences for (2.34) with time-step $\delta t > 0$ and spatial discretization $\delta x > 0$, we next study the following explicit numerical scheme

$$\rho_i^{k+1} = \rho_i^k + \frac{\delta t}{\delta x}\left(G_{i-1}^k - G_i^k\right),\ i \in \mathbb{Z},\ k \in \mathbb{Z},\ k \geq 0 \tag{2.56}$$

where

$$G_i^k = \rho_i^k w_i^k = \rho_i^k h\left(-q_i^k\right),\ i \in \mathbb{Z},\ k \in \mathbb{Z},\ k \geq 0 \tag{2.57}$$

$$q_i^k = -\beta(w_i^k) = \frac{Q'(\rho_{i+1}^k) - Q'(\rho_i^k)}{\delta x},\ i \in \mathbb{Z},\ k \in \mathbb{Z},\ k \geq 0 \tag{2.58}$$

with $\rho_i^k \in [0,R)$ for $i \in \mathbb{Z}$, $k \in \mathbb{Z}$, $k \geq 0$ and $M = \sup_{i,k \in \mathbb{Z}} \left(\rho_i^k\right) < R$ be given and $\beta : (-1,b) \to \mathbb{R}$ being the inverse of $h : \mathbb{R} \to (-1,b)$. Here ρ_i is the numerical value of density at the point $x = i\delta x$ and at time $t \geq 0$, while ρ_i^k is the numerical value of density at the point $x = i\delta x$ and at time $t = k\delta t$. The numerical scheme (2.56)-(2.58) is a first-order accurate discretization and is appropriately designed to respect the entropy-like condition (2.45), for sufficiently small time-step δt, and to satisfy certain very important properties, such as conservation of mass, that are discussed in detail below.

A direct consequence of the discretization (2.56)-(2.58) above, is that the mass $m(t)$ remains constant showing that the numerical scheme is conservative, (see Leveque (1992)). Indeed, this becomes clear in Proposition 2.4.1.

Proposition 2.4.1 *For every sequence $\rho_i^k \in [0,R)$, $i \in \mathbb{Z}$, $k \in \mathbb{Z}$, $k \geq 0$ with $\sum_{i\in\mathbb{Z}} \rho_i^k < +\infty$, it holds that $\sum_{i\in\mathbb{Z}} \rho_i^{k+1} = \sum_{i\in\mathbb{Z}} \rho_i^k$.*

Notice that Proposition 2.4.1 implies that $\lim_{t\to\pm\infty}(\rho_i^{k+1}) = \inf_{i\in\mathbb{Z}}(\rho_i^{k+1}) = 0$ for every sequence $\rho_i^k \in [0,R)$, $i \in \mathbb{Z}$, $k \in \mathbb{Z}$, $k \geq 0$ with $\sum_{i\in\mathbb{Z}} \rho_i^k < +\infty$. The proof of Proposition 2.4.1 is trivial and is omitted. To complete the discretization of model (2.34), the above scheme has to be supplemented with a suitable time-step for certain properties to be preserved. In the following propositions, an upper bound on the time discretization step δt is obtained, for a given space discretization δx, which guarantees that the functional E_2 defined by (2.41) is non-increasing (in a discretized sense) and that (2.45) holds (again in discretized sense). In particular, it is proved that, in addition to the numerical scheme being conservative, it respects the entropy condition (2.45).

Proposition 2.4.2 *Define* $f(\delta t) = \delta x \sum_{i\in\mathbb{Z}} Q(\rho_i^{k+1})$ *for all* $\delta t \geq 0$. *Then, it holds that* $\frac{df}{d\delta t}(0) = \delta x \sum_{i\in\mathbb{Z}} \rho_i^k q_i^k h\left(-q_i^k\right) \leq 0$.

Proposition 2.4.3 *Suppose that* $1 \geq \frac{\delta t}{\delta x}\left(b + 2\frac{M\|h'\|_\infty}{\delta x} \max_{0\leq\rho\leq M} (\theta(\rho))\right)$. *Then* $\rho_i^{k+1} \in [0, M]$ *for all* $i \in \mathbb{Z},\ k \in \mathbb{Z},\ k \geq 0$, *where* $M = \sup_{i\in\mathbb{Z}} \left(\rho_i^k\right) < R$.

For given δx, the bound on the time-step provided in Proposition 2.4.3, establishes that ρ_i^k is non-negative and remains bounded by $M = \sup_{i\in\mathbb{Z}} \left(\rho_i^k\right) < R$ for all $i \in \mathbb{Z},\ k \in \mathbb{Z},\ k \geq 0$. It should be noted that the condition on the time-step is an analogous nonlinear version of the well-known CFL condition, (see Thomas (1995)). Finally, under the same bounds on time-step δt, as in Proposition 2.4.3, it is shown next that the functional E_2 in (2.41) is non-increasing in a discretized sense.

Proposition 2.4.4 *Suppose that* $1 \geq \frac{\delta t}{\delta x}\left(b + 2\frac{M\|h'\|_\infty}{\delta x} \max_{0\leq\rho\leq M} (\theta(\rho))\right)$. *Then*

$$\begin{aligned}
&\textstyle\sum_{i\in\mathbb{Z}} Q(\rho_i^{k+1}) \leq \sum_{i\in\mathbb{Z}} Q(\rho_i^k) + \delta t \left(1 - \delta t\frac{4M\|h'\|_\infty}{(\delta x)^2} \max_{0\leq\rho\leq M} (\theta(\rho))\right) \sum_{i\in\mathbb{Z}} \rho_i^k q_i^k h\left(-q_i^k\right)\\
&= \textstyle\sum_{i\in\mathbb{Z}} Q(\rho_i^k) - \delta t \left(1 - \delta t\frac{4M\|h'\|_\infty}{(\delta x)^2} \max_{0\leq\rho\leq M} (\theta(\rho))\right) \sum_{i\in\mathbb{Z}} \rho_i^k w_i^k \beta\left(w_i^k\right)\\
&\leq \textstyle\sum_{i\in\mathbb{Z}} Q(\rho_i^k).
\end{aligned} \tag{2.59}$$

The following proposition provides the link between the numerical solution produced by the numerical scheme (2.56)-(2.58) and the corresponding weak solution of (2.34), (2.35), (2.46).

Proposition 2.4.5 *Let* $\rho_0 \in X$ *be given. Let* $\delta x, \delta t > 0$ *be given constants. Consider the sequence* $\{\rho_i^k :\ i, k \in \mathbb{Z},\ k \geq 0\}$ *defined by the recursive formula*

$$\rho_i^{k+1} = \rho_i^k + \frac{\delta t}{\delta x}\left(\rho_{i-1}^k h\left(\frac{Q'(\rho_{i-1}^k) - Q'(\rho_i^k)}{\delta x}\right) - \rho_i^k h\left(\frac{Q'(\rho_i^k) - Q'(\rho_{i+1}^k)}{\delta x}\right)\right) \tag{2.60}$$

for all $i, k \in \mathbb{Z}$, $k \geq 0$ *with*

$$\rho_i^0 = \frac{1}{\delta x}\int_{i\delta x}^{(i+1)\delta x} \rho_0(s)ds, \text{ for } i \in \mathbb{Z}. \tag{2.61}$$

Define the functions $\rho_{\delta x,\delta t}, w_{\delta x,\delta t} : \mathbb{R}_+ \times \mathbb{R} \to \mathbb{R}$ *by means of the formulas:*

$$\begin{aligned}
\rho_{\delta x,\delta t}(t,x) &= \rho_i^k\\
w_{\delta x,\delta t}(t,x) &= w_i^k = h\left(\frac{Q'(\rho_i^k) - Q'(\rho_{i+1}^k)}{\delta x}\right)
\end{aligned} \tag{2.62}$$

for $x \in [i\delta x, (i+1)\delta x)$, $t \in [k\delta t, (k+1)\delta t)$, $i, k \in \mathbb{Z}$, $k \geq 0$. *Then for every function* $\phi \in C^2(\mathbb{R}_+ \times \mathbb{R})$ *of compact support, the following equations hold:*

$$\int_{-\infty}^{+\infty} \rho_{\delta x,\delta t}(t,x)dx = \int_{-\infty}^{+\infty} \rho_0(x)dx, \text{ for all } t \geq 0 \tag{2.63}$$

$$-\int_{-\infty}^{+\infty} \phi(0,x)\rho_0(x)dx = \int_0^{+\infty}\int_{-\infty}^{+\infty} \rho_{\delta x,\delta t}(t,x)\left(w_{\delta x,\delta t}(t,x)\phi_x(t,x) + \phi_t(t,x)\right)dxdt$$

$$+P_1 \tag{2.64}$$

$$\int_0^{+\infty}\int_{-\infty}^{+\infty}\left(\phi\left(t,x\right)\beta\left(w_{\delta x,\delta t}(t,x)\right)-\phi_x\left(t,x\right)Q'\left(\rho_{\delta x,\delta t}(t,x)\right)\right)dxdt=P_2 \tag{2.65}$$

where

$$\begin{aligned}P_1(t,x) :=& -\sum_{i\in\mathbb{Z}}\int_0^{\delta t}\int_{i\delta x}^{(i+1)\delta x}\phi_t(0,i\delta x)\rho_{\delta x,\delta t}(t,x)dxdt\\
&+\delta t\sum_{k\geq 0}\sum_{i\in\mathbb{Z}}\rho_{i-1}^k w_{i-1}^k\int_{(i-1)\delta x}^{i\delta x}\int_{(i-1)\delta x}^{\xi}\phi_{xx}(k\delta t,s)dsd\xi\\
&+\delta x\sum_{k\geq 0}\sum_{i\in\mathbb{Z}}\rho_i^{k+1}\int_{k\delta t}^{(k+1)\delta t}\int_{k\delta t}^{\tau}\phi_{tt}(l,i\delta x)dld\tau-\sum_{i\in\mathbb{Z}}\int_{i\delta x}^{(i+1)\delta x}\int_{i\delta x}^{x}\rho_0(x)\phi_x(0,l)dldx\\
&-\sum_{k\geq 0}\sum_{i\in\mathbb{Z}}\int_{k\delta t}^{(k+1)\delta t}\int_{i\delta x}^{(i+1)\delta x}\left(\int_{i\delta x}^{x}\phi_{tx}(t,s)ds+\int_{k\delta t}^{t}\phi_{tt}(\tau,i\delta x)d\tau\right)\rho_{\delta x,\delta t}(t,x)dxdt\\
&-\sum_{k\geq 0}\sum_{i\in\mathbb{Z}}\int_{k\delta t}^{(k+1)\delta t}\int_{(i-1)\delta x}^{i\delta x}\left(\int_{(i-1)\delta x}^{x}\phi_{xx}(t,s)ds+\int_{k\delta t}^{t}\phi_{xt}(\tau,(i-1)\delta x)d\tau\right)\\
&\times\rho_{\delta x,\delta t}(t,x)w_{\delta x,\delta t}(t,x)dxdt\\
&-\sum_{k\geq 0}\sum_{i\in\mathbb{Z}}\int_{(k+1)\delta t}^{(k+2)\delta t}\int_{i\delta x}^{(i+1)\delta x}\left(\int_{k\delta x}^{(k+1)\delta t}\phi_{tt}(\tau,i\delta x)d\tau\right)\end{aligned} \tag{2.66}$$

and

$$\begin{aligned}P_2(t,x) :=& -\sum_{k\geq 0}\sum_{i\in\mathbb{Z}}\int_{k\delta t}^{(k+1)\delta t}\int_{i\delta x}^{(i+1)\delta x}\left(\int_{i\delta x}^{x}\phi_{xx}(t,s)ds\right)Q^{'}\left(\rho_{\delta x,\delta t}(t,x)\right)dxdt\\
&+\sum_{k\geq 0}\sum_{i\in\mathbb{Z}}\int_{k\delta t}^{(k+1)\delta t}\int_{i\delta x}^{(i+1)\delta x}\left(\int_{k\delta t}^{t}\phi_t(\tau,i\delta x)d\tau+\int_{i\delta x}^{x}\phi_x(t,i\xi)d\xi\right)\beta(w_{\delta x,\delta t}(t,x))dxdt\\
&-\sum_{k\geq 0}\sum_{i\in\mathbb{Z}}\int_{k\delta t}^{(k+1)\delta t}\int_{(i+1)\delta x}^{(i+2)\delta x}\left(\int_{i\delta x}^{(i+1)\delta x}\phi_{xx}(t,s)ds+\int_{k\delta t}^{t}\phi_{xt}(\tau,i\delta x)d\tau\right)\\
&\times Q^{'}\left(\rho_{\delta x,\delta t}(t,x)\right)dxdt\\
&+\delta t\sum_{k\geq 0}\sum_{i\in\mathbb{Z}}Q^{'}\left(\rho_{i+1}^k\right)\int_{i\delta x}^{(i+1)\delta x}\int_{i\delta x}^{\xi}\phi_{xx}(k\delta t,s)dsd\xi.\end{aligned} \tag{2.67}$$

Furthermore, if $1\geq\frac{\delta t}{\delta x}\left(b+2\frac{\|\rho_0\|_\infty\|h'\|_\infty}{\delta x}\max_{0\leq\rho\leq\|\rho_0\|_\infty}(\theta(\rho))\right)$ *and* $1\geq\delta t\frac{4\|\rho_0\|_\infty\|h'\|_\infty}{(\delta x)^2}\max_{0\leq\rho\leq\|\rho_0\|_\infty}(\theta(\rho))$ *then we also have for all* $t\geq 0$*:*

$$\int_{-\infty}^{+\infty}Q\left(\rho_{\delta x,\delta t}(t,x)\right)dx\leq\int_{-\infty}^{+\infty}Q\left(\rho_0(x)\right)dx \tag{2.68}$$

$$0=\inf_{x\in\mathbb{R}}\left(\rho_{\delta x,\delta t}(t,x)\right)\leq\sup_{x\in\mathbb{R}}\left(\rho_{\delta x,\delta t}(t,x)\right)\leq\|\rho_0\|_\infty \tag{2.69}$$

Proposition 2.4.5 is not adequate to guarantee existence of weak solutions in the sense of Definition 2.3.1. To be able to show existence of a weak solution using Proposition 2.4.5, we need to show additional properties. For instance, we may need to show the existence of two sequences: a sequence $\left\{(\delta x)_q>0:q\in\mathbb{N}\right\}$ which converges to zero and a sequence $\left\{(\delta t)_q > 0 : q \in \mathbb{N}\right\}$ satisfying $1 \geq \frac{(\delta t)_q}{(\delta x)_q}\left(b + 2\frac{\|\rho_0\|_\infty \|h'\|_\infty}{(\delta x)_q} \max_{0\leq\rho\leq\|\rho_0\|_\infty}(\theta(\rho))\right)$ and $1 \geq (\delta t)_q \frac{4\|\rho_0\|_\infty \|h'\|_\infty}{(\delta x)_q^2} \max_{0\leq\rho\leq\|\rho_0\|_\infty}(\theta(\rho))$ for all $q \in \mathbb{N}$ for which there exists a constant $L > 0$ (independent from $(\delta t)_q$ and $(\delta x)_q$) such that the corresponding numerical solution with $\delta t = (\delta t)_q$ and $\delta x = (\delta x)_q$ satisfies

$$\left|Q'(\rho_{i+1}^k) - Q'(\rho_i^k)\right| \leq L\delta x, \text{ for } i,\, k \in \mathbb{Z},\, k > 0. \tag{2.70}$$

Finally, the following proposition, shows the asymptotic behavior of the numerical scheme. It also shows that the possibility of an inequality like (2.70) to be satisfied by the computed numerical solution is large.

Proposition 2.4.6 *Suppose that the inequalities* $1 \geq \frac{\delta t}{\delta x}\left(b + 2\frac{\|\rho_0\|_\infty \|h'\|_\infty}{\delta x} \max_{0\leq\rho\leq\|\rho_0\|_\infty}(\theta(\rho))\right)$ *and* $1 > \delta t \frac{4\|\rho_0\|_\infty \|h'\|_\infty}{(\delta x)^2} \max_{0\leq\rho\leq\|\rho_0\|_\infty}(\theta(\rho))$ *hold. Then*

$$\lim_{k\to+\infty}\left(\rho_i^k \left|Q'(\rho_i^k) - Q'(\rho_{i+1}^k)\right|\right) = 0, \textit{ for all } i \in \mathbb{Z}. \tag{2.71}$$

2.5 Numerical experiments

2.5.1 An academic example

The aim of this example is to demonstrate the numerical solutions of model (2.34) and the convergence of the functionals defined by (2.40) and (2.41). In order to apply the numerical scheme (2.56)-(2.58), the interval $[-1, 3]$ and the following functions are used:

$$h(s) = \tanh(s),\ s \in \mathbb{R} \tag{2.72}$$

$$\theta(\rho) = \begin{cases} 0 & ,0 \leq \rho \leq 1 \\ c\dfrac{(\rho-1)^2}{R-\rho} & ,1 < \rho < R \end{cases}. \tag{2.73}$$

The constant $c > 0$ is a parameter that allows to increase or decrease the viscosity. Notice also that: (i) $h(0) = 0$, $h' \in L^\infty(\mathbb{R})$ and $h'(s) > 0$ for all $s \in \mathbb{R}$; and (ii) the function $\theta(\rho)$, defined by (2.73), is a C^1 function with $\theta(\rho) = 0$ for all $\rho \in [0, 1]$, $\theta(\rho) > 0$ for all $\rho \in (1, R)$ and $\lim_{\rho\to R^-}(\theta(\rho)) = +\infty$.

Using (2.73) and definition (2.43) it follows that

$$Q(\rho) = c\begin{cases} 0 & ,0 \leq \rho \leq 1 \\ (\rho-1)\left(\dfrac{\rho^2+\rho+1}{3} + (R-\rho)\dfrac{\rho+2R+1}{2} + \rho - 2R\right) & \\ \qquad +(R-1)^2(\rho-R)ln\left(\dfrac{R-1}{R-\rho}\right) & ,1 < \rho < R \end{cases} \tag{2.74}$$

Let $M = 1.4$, where $M = \sup_{i\in\mathbb{Z}}(\rho_i) < R$ (recall Proposition 2.4.3), spatial-step $\delta x = 0.04$ ($n = 100$) and consider the initial condition:

$$\rho[0] = \begin{cases} 0.25(x-\varepsilon_1)^2(x-\varepsilon_2)^2 & ,\varepsilon_1 < x < \varepsilon_2 \\ 0 & \text{otherwise} \end{cases}$$

where $\varepsilon_1 = -0.52$ and $\varepsilon_2 = 2.52$. Using $R = 2$, $b = 1$, due to definition (2.72) and the fact that $\theta(\rho)$ in (2.73) is an increasing function, it follows that $\max_{0\leq\rho\leq M}(\theta(\rho)) = \theta(M)$ and

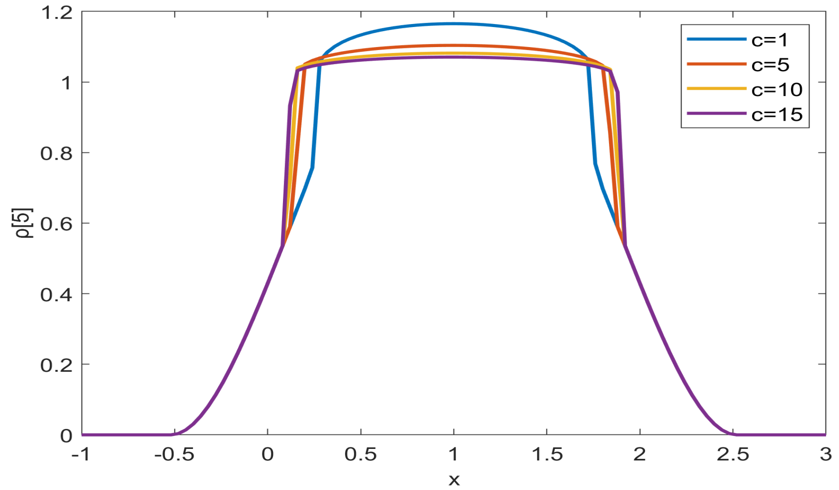

Figure 2.1: The density profile $\rho[5]$ for different values of the constant c.

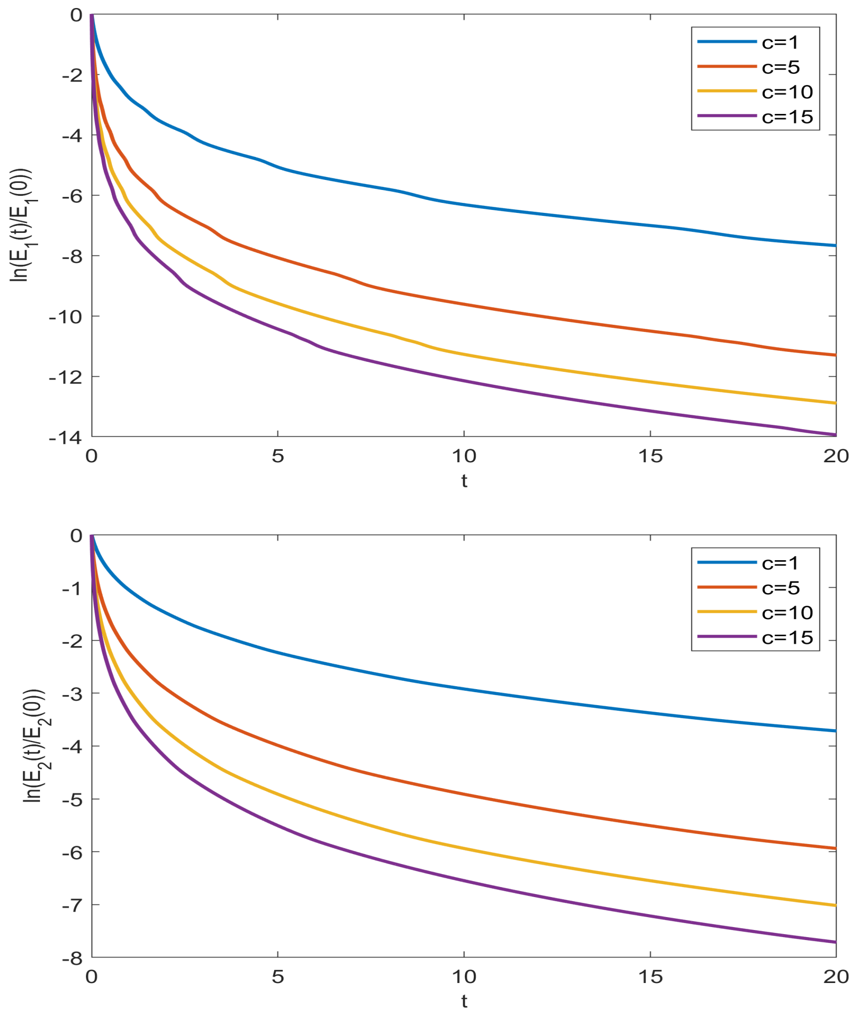

Figure 2.2: Time-evolution of $\ln(E_1(t)/E_1(0))$ (top) and $\ln(E_2(t)/E_2(0))$ (bottom) for different values of constant c.

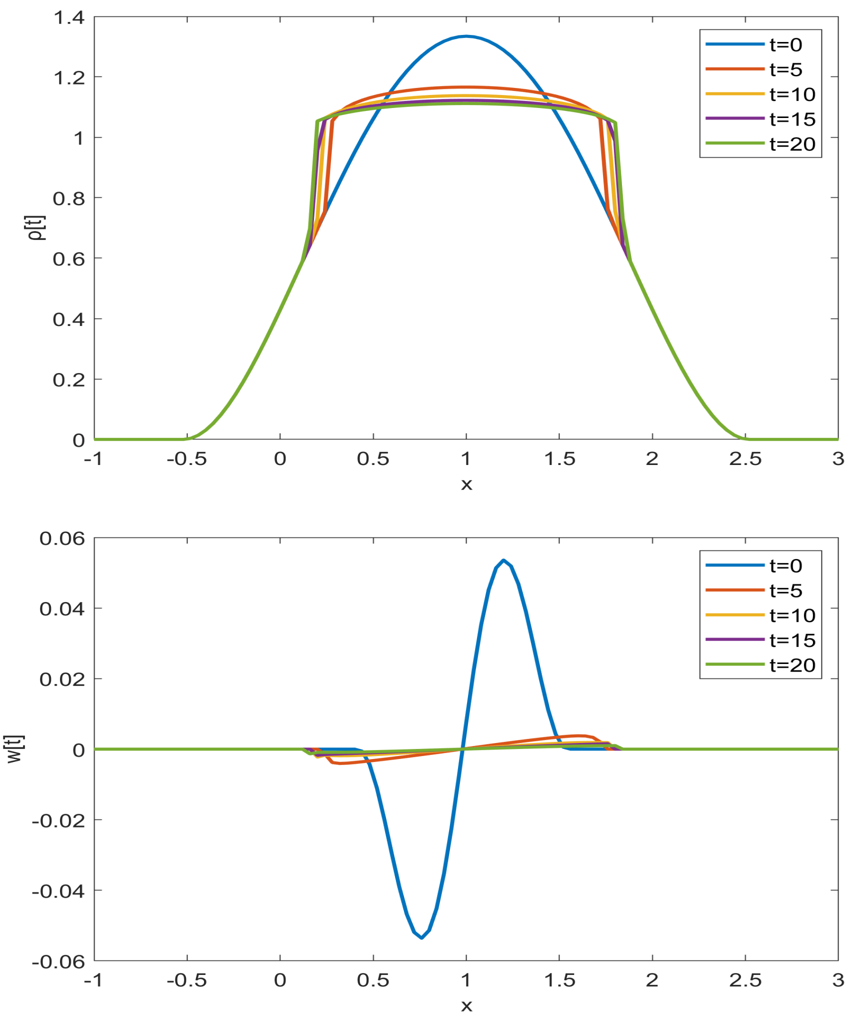

Figure 2.3: The profiles $\rho[t]$ (top) and $w[t]$ (bottom) for $c = 1$.

$\|h'\|_\infty = 1$. It is also used that $\delta t = 10^{-4}$, which satisfies

$$\delta t \leq \frac{\delta x^2}{\delta x b + 2M \|h'\|_\infty \theta(M)} \tag{2.75}$$

for all values of $c \in \{1, 5, 10, 15\}$. Figure 2.1 displays the density profile for different values of constant c. By increasing the value of the constant c, the convergence rate of the numerical solution to an equilibrium $\rho(x) \leq 1$, $w(x) \equiv 0$ is faster. This is also illustrated in Figure 2.2 that shows the convergence of the logarithm of the functionals $E_1(t)/E_1(0)$ and $E_2(t)/E_1(0)$.

In addition, Figure 2.3 shows the profiles $\rho[t]$ and $w[t]$ for $c = 1$ and $\delta x = 0.04$, $\delta t = 10^{-3}$ at different times indicating the convergence to an equilibrium $\rho \leq 1$, $w = 0$, where $w(t,x) = h(-\theta(\rho(t,x))\rho_x(t,x))$. Note that the highest resolution of the solutions produced by the numerical scheme (2.56)-(2.58) can be achieved by obtaining grid-independent solutions. However, in order to achieve grid-independence a fine grid of a large number of grid-points should be used. As you can see in Figure 2.4, even by using 2000 grid-points, the solution is not still grid-independent. Although a fine grid achieves higher resolution of the solution, the increase in the number of grid-points has an impact on the value of the time-step and as a result can also affect the CPU time. More specifically, as the number of

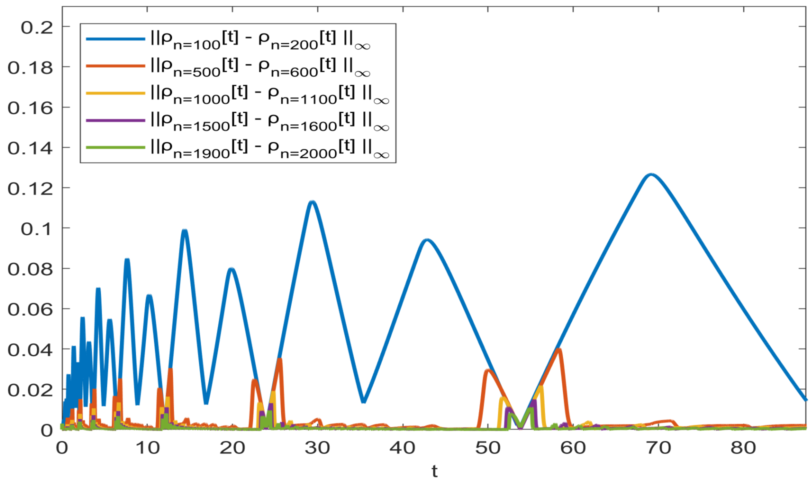

Figure 2.4: Sup-norm of the difference between the density solutions obtained by using a gradually increasing number of grid-points and $\delta t = 10^{-5}$.

the grid-points is increased, the value of the time-step should be decreased significantly to satisfy the time-step condition provided by Propositions 2.4.3 and 2.4.4 and consequently more CPU time is required. Therefore, in order to achieve grid-independent solutions, an extremely small time-step should be used, given that the profile solutions in Figure 2.3 have been obtained by using $\delta t = 10^{-3}$ and $n = 100$ grid points. In Figure 2.4, the sup-norm of the difference between the density solutions obtained by using a gradually increasing number of grid-points and $\delta t = 10^{-5}$ is illustrated.

The numerical scheme (2.56)-(2.58) is explicit and is supplemented with a suitable time-step for the preservation of certain properties (recall Propositions 2.4.3 and 2.4.4). This restriction in the size of the time-step can be removed when implicit finite-difference schemes are used. To this purpose, it is interesting to compare the solution of the explicit numerical scheme (2.56)-(2.58) with the solution of an implicit numerical scheme. The implicit analogue of numerical scheme (2.56)-(2.58) is the following:

$$\rho_i^{k+1} = \rho_i^k + \frac{\delta t}{\delta x}\left(G_{i-1}^{k+1} - G_i^{k+1}\right), i \in \mathbb{Z}, k \in \mathbb{Z}, k \geq 0 \tag{2.76}$$

where

$$G_i^{k+1} = \rho_i^{k+1} w_i^{k+1} = \rho_i^{k+1} h\left(-q_i^{k+1}\right), i \in \mathbb{Z}, k \in \mathbb{Z}, k \geq 0 \tag{2.77}$$

$$q_i^{k+1} = -\beta(w_i^{k+1}) = \frac{Q'(\rho_{i+1}^{k+1}) - Q'(\rho_i^{k+1})}{\delta x}, i \in \mathbb{Z}, k \in \mathbb{Z}, k \geq 0. \tag{2.78}$$

In Figure 2.5, the sup-norm of the difference between the solution of the implicit scheme (2.76)-(2.78) and the solution of the explicit scheme (2.56)-(2.58) is illustrated. By increasing the time-step of the implicit scheme, which is represented in the horizontal axis, and using time-step $\delta t = 10^{-4}$ for the explicit scheme, the sup-norm of the difference between the solution of the implicit and the explicit schemes is also increased. Furthermore, it is obvious that $\lim_{t\to\infty} \left\|\rho_{imp}[t] - \rho_{\exp}[t]\right\|_\infty = 0$ and $\lim_{t\to\infty} \left\|w_{imp}[t] - w_{\exp}[t]\right\|_\infty = 0$, indicating that the solutions of the two schemes coincide as they converge to the equilibrium $\rho(x) \leq 1$, $w(x) \equiv 0$. This is also illustrated in Figure 2.6 which shows the sup-norm of the difference between the solution of the implicit scheme (2.76)-(2.78) using time-step $\delta t = 10^{-2}$ and the solution of the explicit scheme (2.56)-(2.58) using time-step $\delta t = 10^{-4}$.

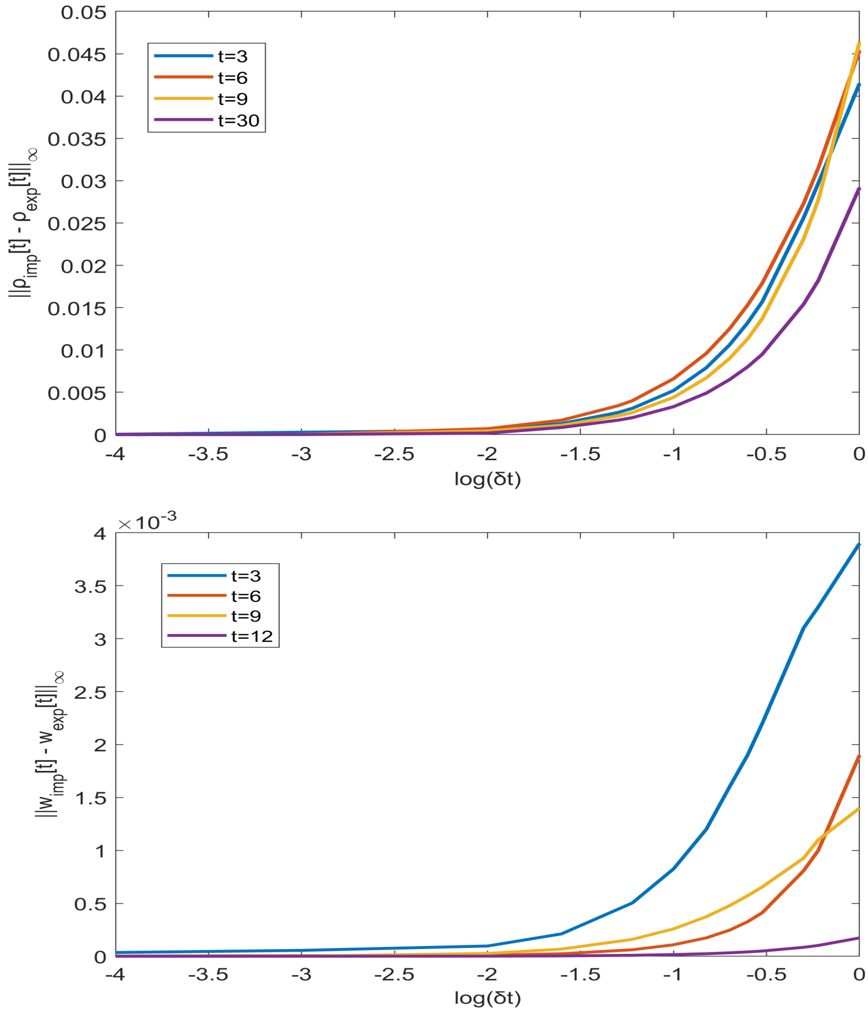

Figure 2.5: Time-evolution of $\left\|\rho_{imp}[t]-\rho_{\exp}[t]\right\|_{\infty}$ (top) and $\left\|w_{imp}[t]-w_{\exp}[t]\right\|_{\infty}$ (bottom) using time-step $\delta t = 10^{-4}$ for the explicit scheme and different time-steps for the implicit scheme.

2.5.2 A realistic traffic scenario and comparison with the LWR

In this section, a traffic scenario is considered to compare the density and flow of (2.34) with one of the most well-known traffic flow models for human drivers, the so-called LWR model (Lighthill and Whitham (1955), Richards (1956))

$$\tilde{\rho}_{\tau} + (\tilde{\rho}\tilde{v})_{\xi} = 0, \tau > 0,\ \xi \in \mathbb{R} \tag{2.79}$$

with the speed $\tilde{v}$ given by

$$\tilde{v}(\tau,\xi) = v_f \exp\left(-\frac{1}{a}\left(\frac{\tilde{\rho}(\tau,\xi)}{\rho_c}\right)^{a}\right) \tag{2.80}$$

where $v_f > 0$ is the free-flow speed, ρ_c is the critical density, and $a > 0$ is a parameter.

Our model (2.34), in the original variables $\tau > 0,\ \xi \in \mathbb{R}$, is given by equation (2.79) with the speed $\tilde{v}$ defined by

$$\tilde{v}(\tau,\xi) = v^{*}\left(1 + h\left(-\theta\left(\frac{\tilde{\rho}(\tau,\xi)}{\bar{\rho}}\right)\frac{\tilde{\rho}_{\xi}(\tau,\xi)}{\bar{\rho}}\right)\right) \tag{2.81}$$

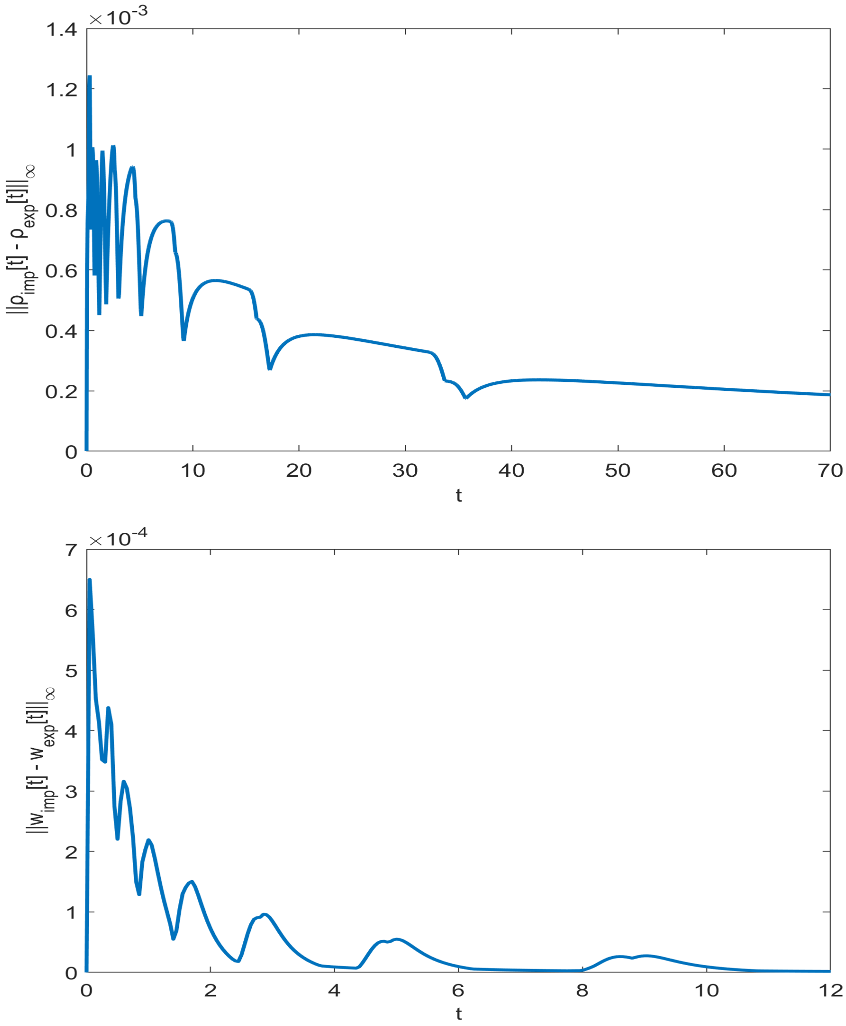

Figure 2.6: Time-evolution of $\left\|\rho_{imp}[t]-\rho_{\exp}[t]\right\|_{\infty}$ (top) and $\left\|w_{imp}[t]-w_{\exp}[t]\right\|_{\infty}$ (bottom) using time-step $\delta t = 10^{-2}$ for the implicit scheme and $\delta t = 10^{-4}$ for the explicit scheme.

(recall the transformation $\xi = rx + v^{*}\tau$, $x \in \mathbb{R}$ and the quantities $\tau = \frac{r}{v^{*}}t$, $w = \frac{\tilde{v}-v^{*}}{v^{*}}$, $\rho = \frac{\tilde{\rho}}{\bar{\rho}}$, with $r = 1$), where

$$h(s) = \beta^{-1}(s), s \in \mathbb{R} \tag{2.82}$$

with $\beta(w)$ defined by (2.22), and $\theta(\rho)$ given by

$$\theta(\rho) = \begin{cases} 0 & , 0 \le \rho \le 1 \\ c\frac{(\rho-1)^2}{\rho^2(R-\rho)} & , 1 < \rho < R \end{cases} \tag{2.83}$$

where $c > 0$ is parameter. Model (2.79), (2.81), is a CAV model.

A single-lane motorway is considered with $v_f = 102$ (km/h), $\rho_{\max} = 180$ (veh/km), $\rho_c = 33.3$ (veh/km), and $a = 2.34$ that were estimated in Kotsialos et al. (2002) based on real data from a part of the Amsterdam A10 motorway. In this scenario, it is assumed that the initial density on the road is characterized by a congestion belt in the interval $[1.5, 2.75]$ (km) as shown in Figure 2.7 with $\tilde{\rho}_0(\xi) = 0$ for $\xi < 0$ and $\xi > 0$. Note also that outside the congested area, the density is below the critical density ρ_c.

For the parameters of the CAV model (2.79), (2.81), the speed set-point has been selected

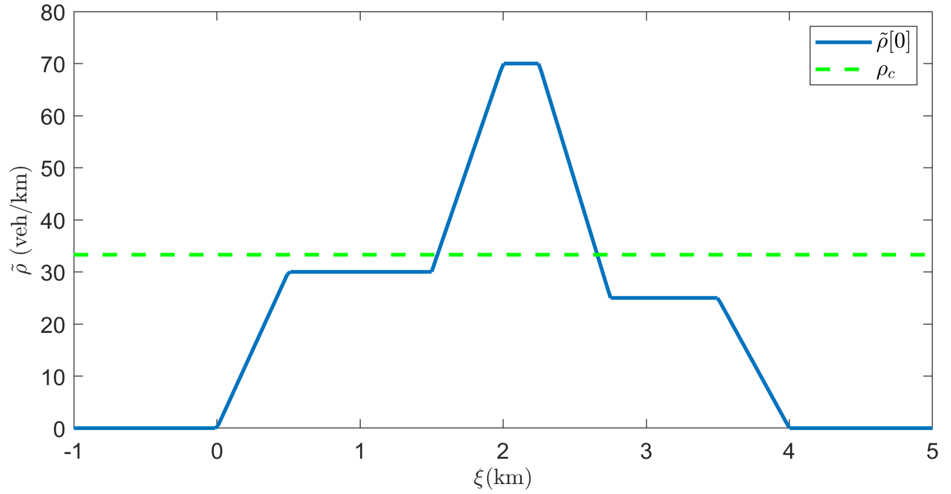

Figure 2.7: Initial density $\tilde{\rho}_0(\xi)$.

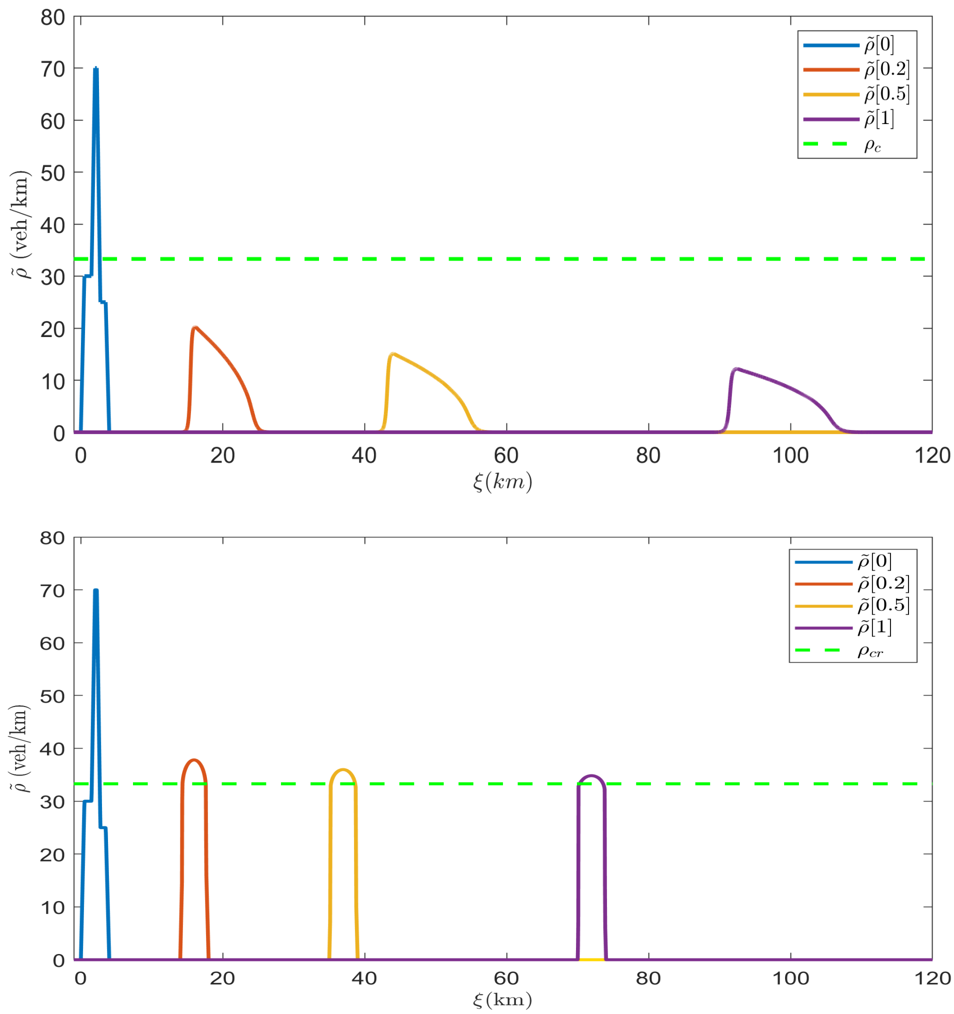

Figure 2.8: Density profiles for the LWR (top), and density profiles of AV model (bottom).

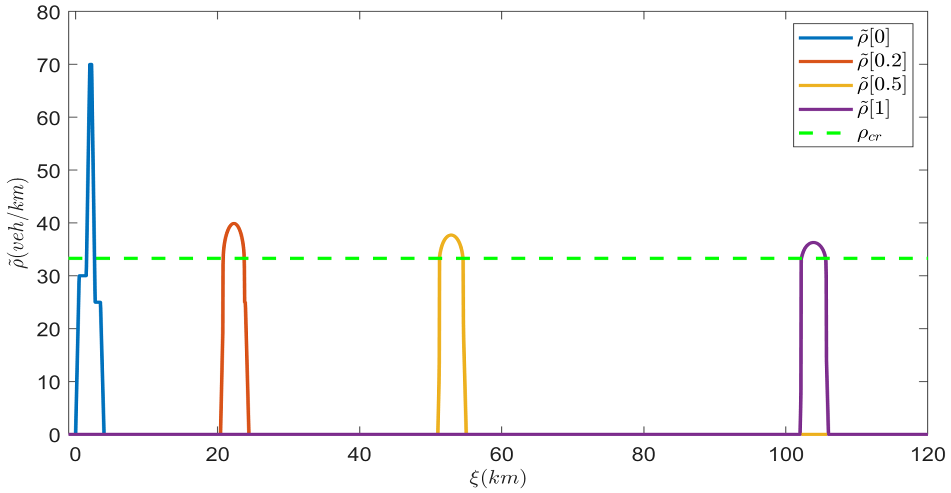

Figure 2.9: Density profiles of the AV model with $v^* = 102$ (km/h).

to be $v^* = 70$ (km/h) (significantly smaller than the speed limit), the viscosity constant $c = 40$, the interaction density $\bar{\rho} = 31$, the speed limit $v_{\max} = 110$ (km/h) and recall that the quantities R and b are given by $R = \frac{\rho_{\max}}{\bar{\rho}} > 1$ and $b = \frac{v_{\max} - v^*}{v^*}$, respectively. For the CAV model, the explicit scheme (2.56)-(2.58) is used, since the numerical solution obtained from the implicit scheme has only minor differences, recall Figure 2.6. For the LWR model, the interval $[0, 120]$ is considered and the Godunov's method is used to obtain its solution:

$$\tilde{\rho}_i^{k+1} = \tilde{\rho}_i^k - \frac{\delta t}{\delta x}\left(\min\left(F\left(\min(\tilde{\rho}_i^k, \rho_c)\right), F\left(\max(\tilde{\rho}_{i+1}^k, \rho_c)\right)\right)\right)$$
$$+ \frac{\delta t}{\delta x}\left(\min\left(F\left(\min(\tilde{\rho}_{i-1}^k, \rho_c)\right), F\left(\max(\tilde{\rho}_i^k, \rho_c)\right)\right)\right).$$

Note that the above formula of the Godunov's scheme follows immediately from Leveque (1992) and the fact that flux $F(\tilde{\rho}) := \tilde{\rho}\tilde{v}$, with $\tilde{v}$ defined by (2.80) is strictly increasing on $[0, \rho_c]$ and strictly decreasing on $[\rho_c, +\infty)$. For both schemes, $\delta x = 0.04$ is used, which corresponds to $n = 3025$ grid points on the interval $[-1, 120]$ and $\delta t = 10^{-6}$.

The density profiles for both models over a simulation time of $1h$ are shown in Figure 2.8. It is shown that the density of both models dissipates along the road. However, for the LWR model the dissipation is much stronger and the density is spread over a large road interval for increasing $\tau > 0$. More specifically, for $\tau = 1$ (h), the density is non-zero over the interval $[90, 106]$ (km), which implies that the vehicles retain large inter-vehicle distances while the maximum density is equal to $\max\limits_{\xi \in [90,106]} (\tilde{\rho}[1]) = 11.8$ (veh/km). On the other hand, for the CAV model, the density dissipates at a lower rate but the vehicles remain in a $4km$ stretch of the road ($\xi \in [70, 74]$ (km)), since the desired speed is $v^* = 70$ (km/h)), as was the case in the initial density, and with maximum density $\max\limits_{\xi \in [70,74]} (\tilde{\rho}[1]) = 34.83$ (veh/km) (near the critical density ρ_c). However, note that the travel time of the CAV model is higher since the vehicles are moving with a significantly lower speed ($v^* = 70$ (km/h)). Note also that the density for the CAV model converges towards an equilibrium where $\tilde{v}(\xi) \equiv v^*$ and $\tilde{\rho}(\xi) \leq \bar{\rho} < \rho_c$.

Moreover, the case where the speed set-point is equal to the free-flow speed $v^* = v_f = 102$ (km/h) is also considered. The density profiles of the CAV model with $v^* = 102$ (km/h) are shown in Figure 2.9. Note that when vehicles are moving with free-flow speed $v^* = 102$ (km/h), the overall travel time is lower with the CAV model, since, for $\tau = 1$ (h), the vehicles

	CAV model (2.79), (2.81) with $v^* = 70$ (km/h)	CAV model (2.79), (2.81) with $v^* = 102$ (km/h)	LWR
Mean Flow	2232 (veh/h)	3201 (veh/h)	926 (veh/h)

Table 2.1: Mean flow

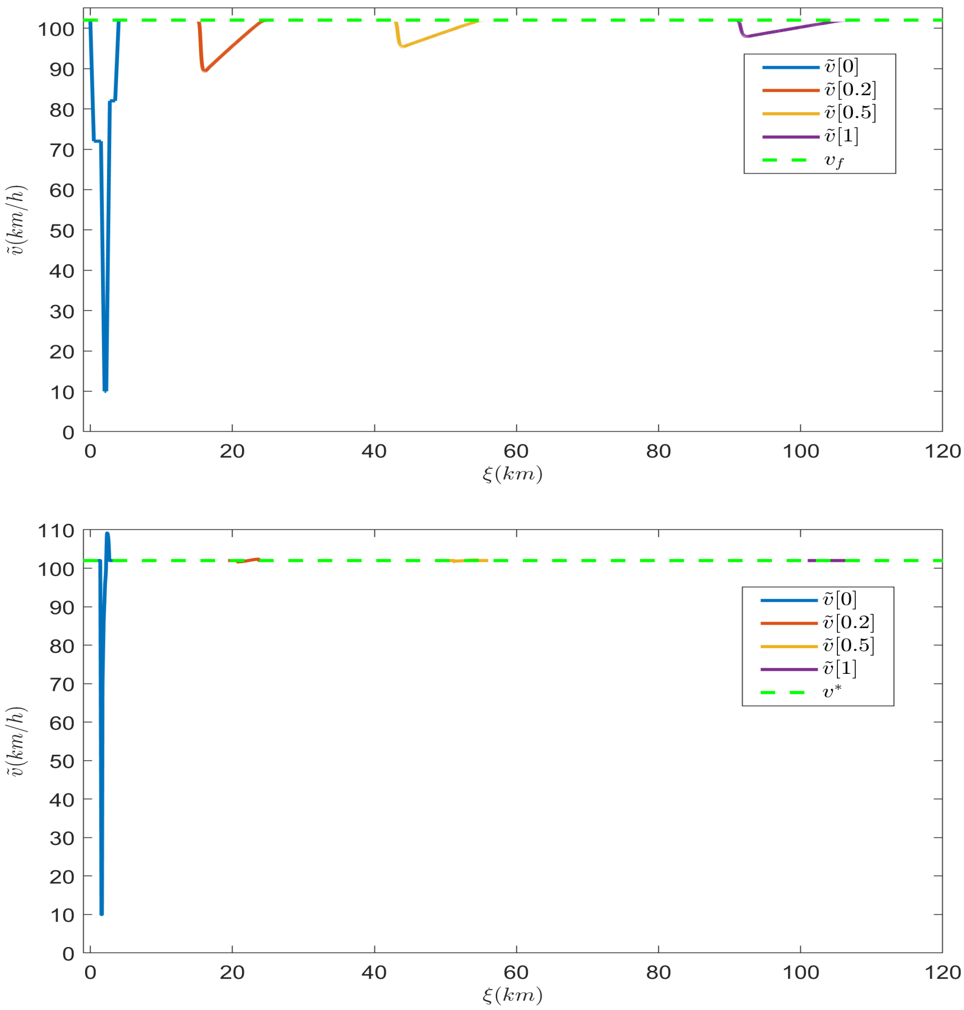

Figure 2.10: Speed profiles for the LWR (top), and the speed profiles of AV model(bottom) with $v^* = 102$ (km/h).

are in the interval $(102, 106)$ (km), whereas with the LWR, the vehicles are in the interval $(90, 106)$ (km), compare with Figure 2.8 (top).

The speed profiles for both models are shown in Figure 2.10. It is obvious that with the CAV model (2.79), (2.81), the mean speed converges to the speed set-point v^* much faster than that of the LWR to the free-flow speed v_f, causing a decrease in the overall travel time for model (2.79), (2.81), as also observed in Figure 2.9.

Since with the CAV model (2.79), (2.81) the density converges towards an equilibrium near the critical density, while vehicles are spread in a small space interval (recall Figures 2.8, 2.9) it is expected that the flow $q = \tilde{\rho}\tilde{v}$ of the CAV model is much higher than the flow of the LWR model. Equivalently, vehicles equipped with the PRCC proposed in Karafyllis et al. (2022d) will retain smaller inter-vehicle distances (higher density) than human-driven vehicles. Indeed, to compare the mean flow for each model, we define

$$\text{Mean Flow } = \frac{1}{T}\int_0^T \int_{a(t)}^{b(t)} \frac{\tilde{\rho}(t,x)\tilde{v}(t,x)}{b(t)-a(t)}dxdt$$

where $T > 0$ denotes the maximum time and $[a(\tau), b(\tau)]$ denotes the interval where $\tilde{\rho}(\tau,\xi) \neq 0$ for $\xi \in [a(\tau), b(\tau)]$ at each time instant $\tau \geq 0$. The following cases are considered: (i) $v^* = 70$ (km/h) - the speed set-point is much lower than the free-flow speed; and (ii) $v^* = 102$ (km/h) - the speed set-point is equal to the free flow speed v_f. The mean flow for both models and $T = 1$ (h) is shown in Table 2.1. In both cases, the mean flow for the CAV model is much higher than the mean flow of the LWR. In particular, when the vehicles are moving with free-flow speed, the mean flow of the CAV model is 346% higher than the mean flow of the LWR model.

Finally, it should be noticed that the macroscopic model (2.79), (2.81) follows directly from the corresponding CCs in Karafyllis et al. (2022d), whose design has many degrees of freedom and can influence the characteristics of (2.79), (2.81). For instance, just by increasing (or decreasing) the value of the viscosity constant $c > 0$, we can influence the dissipation rate of the density $\tilde{\rho}$ and speed $\tilde{v}$ to an equilibrium (recall Figure 2.1).

2.6 Conclusions

A nonlinear heat equation arising from the macro-PRCC has been presented showing that its solutions approximate the solutions of the macro-PRCC. Moreover, a concept of weak solution was defined and certain entropy-like conditions were derived. A conservative finite difference scheme was also proposed that respects the corresponding entropy conditions and certain links between the weak solution and the numerical scheme were provided. Finally, a traffic simulation scenario and a comparison with the LWR model were provided, illustrating the benefits of the proposed macroscopic traffic model.

2.7 Proofs

Proof of Proposition 2.3.1 We first show that if $\rho \in C^1(\mathbb{R}_+ \times \mathbb{R}; [0,R)) \cap C^2((0,+\infty) \times \mathbb{R})$ is a classical solution of (2.34), (2.35), (2.46) that satisfies (2.53), (2.47), and (2.54), then the pair ρ, w with w defined by (2.55), is also a weak solution of the initial-value problem (2.34), (2.35), (2.46). First notice that by virtue of (2.51), (2.35), (2.34), (2.41) and (2.45), it follows that (2.49), (2.50) hold. Furthermore, it follows from (2.53), definition (2.55) and the fact that $h(\mathbb{R}) = (-1, b)$, $\theta(\rho)\rho_x \in L^\infty(\mathbb{R}_+ \times \mathbb{R})$ that (2.48) holds. Equation (2.35) is a direct consequence of (2.54) and definition (2.39).

Let $\phi \in C^2(\mathbb{R}_+ \times \mathbb{R})$ be a function with compact support in $\Omega := [0,T] \times [-a,a]$, for $T, a > 0$ sufficiently large. Multiplying (2.34) by ϕ and using (2.55), we obtain

$$\int_0^{+\infty}\int_{-\infty}^{+\infty} \phi(t,x)\left(\rho_t(t,x) + (w(t,x)\rho(t,x))_x\right)dxdt = 0. \tag{2.84}$$

Integrating by parts (2.84) and using (2.47), (2.48), Fubini's Theorem, (2.46) and that ϕ has compact support in Ω we obtain

$$\begin{aligned} 0 &= \int_0^{+\infty}\int_{-\infty}^{+\infty} \phi(t,x)\left(\rho_t(t,x) + (w(t,x)\rho(t,x))_x\right)dtdx \\ &= \int_{-\infty}^{+\infty} \rho(t,x)\phi(t,x)\Big|_{t=0}^{t=+\infty} dx - \int_{-\infty}^{+\infty}\int_0^{+\infty} \phi_t(t,x)\rho(t,x)dtdx \end{aligned}$$

$$+\int_0^{+\infty}\left(\phi(t,x)w(t,x)\rho(t,x)\big|_{x=-\infty}^{x=+\infty}\right)dt-\int_0^{+\infty}\int_{-\infty}^{+\infty}\rho(t,x)w(t,x)\phi_x(t,x)dxdt$$
$$=-\int_{-\infty}^{+\infty}\phi(0,x)\rho_0(x)dx-\int_0^{+\infty}\int_{-\infty}^{+\infty}\left(\rho(t,x)w(t,x)\phi_x(t,x)\right)dxdt$$
$$-\int_0^{+\infty}\int_{-\infty}^{+\infty}\phi_t(t,x)\rho(t,x)dxdt \tag{2.85}$$

which implies (2.51). Notice that due to definition (2.43), and the fact that β is the inverse of h, (2.55) is written as follows:

$$\beta\left(w(t,x)\right)+\left(Q'\left(\rho(t,x)\right)\right)_x=0. \tag{2.86}$$

Using (2.86) and integrating by parts the equation

$$\int_0^{+\infty}\int_{-\infty}^{+\infty}\phi(t,x)\left(\beta(w(t,x))+\left(Q'(\rho(t,x))\right)_x\right)dxdt=0 \tag{2.87}$$

we obtain

$$\int_0^{+\infty}\int_{-\infty}^{+\infty}\phi(t,x)\beta(w(t,x))-\phi_x(t,x)Q'(\rho(t,x))dxdt+\int_0^{+\infty}\phi(t,x)Q'(\rho(t,x))\Big|_{x=-\infty}^{x=+\infty}dt$$
$$=0$$

and due to the fact that ϕ has compact support in Ω, equation (2.52) follows, establishing that the pair ρ, w is a weak solution.

Conversely, suppose that the pair ρ, w is a weak solution of (2.34), (2.35), (2.46) as per Definition 2.3.1. Since $\rho \in C^1\left(\mathbb{R}_+\times\mathbb{R};[0,R)\right)\cap C^2\left((0,+\infty)\times\mathbb{R}\right)$, it follows by definition (2.43) that $Q'(\rho)\in C^1(\mathbb{R}_+\times\mathbb{R})$.
Let arbitrary $T, a>0$ be given. Define

$$\Omega := (0,T)\times(-a,a). \tag{2.88}$$

Let an arbitrary function $\phi \in C^2\left(\mathbb{R}_+\times\mathbb{R}\right)$ with compact support in Ω. From (2.55) and using integration by parts we obtain the following equation

$$0=\iint_\Omega\left(\phi\left(t,x\right)\beta\left(w(t,x)\right)-\phi_x\left(t,x\right)Q'\left(\rho(t,x)\right)\right)dxdt$$
$$=\iint_\Omega\phi(t,x)\left(\beta(w(t,x))+\left(Q'(\rho(t,x))\right)_x\right)dxdt+\int_0^T\phi(t,x)Q'(\rho(t,x))\Big|_{x=-a}^{x=a}dt$$
$$=\iint_\Omega\phi(t,x)\left(\beta(w(t,x))+\left(Q'(\rho(t,x))\right)_x\right)dxdt. \tag{2.89}$$

Moreover, compactness of $\bar{\Omega}$ and (2.48) (which imply that $\beta(w)\in L^\infty(\Omega)\subseteq L^2(\Omega)$), definition (2.43) (which implies that $\left(Q'(\rho)\right)_x=\theta(\rho)\rho_x$) and (2.53) (which implies that $\left(Q'(\rho)\right)_x\in L^\infty(\Omega)\subseteq L^1(\Omega)$) give that $\beta(w)+\left(Q'(\rho)\right)_x\in L^1(\Omega)$. Corollary 4.24 on page 110 in Brezis (2010) gives that

$$\beta(w(t,x))+\left(Q'(\rho(t,x))\right)_x=0 \text{ a.e. in } \Omega$$

or (using (2.43))

$$w(t,x)=h\left(-\theta(\rho(t,x))\rho_x(t,x)\right)\ \text{a.e. in } \Omega$$

where h is the inverse of β. Finally, due to continuity of $h\left(-\kappa(\rho)\rho_x\right)$, we get that $w \in C^0\left(\bar{\Omega}\right)$ and using (2.88) we get

$$w(t,x) = h\left(-\theta(\rho(t,x))\rho_x(t,x)\right) \text{ in } \bar{\Omega} = [0,T] \times [-a,a]. \tag{2.90}$$

Since $\rho \in C^1\left(\mathbb{R}_+ \times \mathbb{R};\, [0,R)\right) \cap C^2\left((0,+\infty) \times \mathbb{R}\right)$ and since $T, a > 0$ are arbitrary, we obtain that $w \in C^0\left(\mathbb{R}_+ \times \mathbb{R}; (-1,b)\right) \cap C^1\left((0,+\infty) \times \mathbb{R}\right)$ and (2.55) holds for all $(t,x) \in \mathbb{R}_+ \times \mathbb{R}$.

Let arbitrary $a > 0$, $T > t_0 > 0$ be given. Define

$$\Omega := (t_0, T) \times (-a, a). \tag{2.91}$$

Next, let arbitrary function $\phi \in C^2\left(\mathbb{R}_+ \times \mathbb{R}\right)$ with compact support in Ω be given. Since $\rho \in C^1\left(\mathbb{R}_+ \times \mathbb{R};\, [0,R)\right) \cap C^2\left((0,+\infty) \times \mathbb{R}\right)$, $w \in C^0\left(\mathbb{R}_+ \times \mathbb{R}; (-1,b)\right) \cap C^1\left((0,+\infty) \times \mathbb{R}\right)$ and since ϕ has compact support in Ω, it follows from equations (2.51) and (2.55) by direct integration by parts that the following equation holds

$$\iint_{\Omega} \phi(t,x)\left(\rho_t(t,x) + \left(\rho(t,x)w(t,x)\right)_x\right) dxdt = 0. \tag{2.92}$$

Since $\rho_t + (\rho w)_x \in C^0\left(\bar{\Omega}\right) \subset L^1\left(\Omega\right)$, Corollary 4.24 on page 110 in Brezis (2010) gives that

$$\rho_t(t,x) + (\rho w)_x(t,x) = 0 \text{ a.e. in } \Omega.$$

Since $\rho_t + (\rho w)_x \in C^0\left(\bar{\Omega}\right)$, we get from (2.91):

$$\rho_t(t,x) + (\rho w)_x(t,x) = 0 \text{ in } \bar{\Omega} = [t_0, T] \times [-a,a].$$

Since $a > 0$, $T > t_0 > 0$ are arbitrary we obtain that $\rho_t + (\rho w)_x = 0$ for all $t > 0$ and $x \in \mathbb{R}$. Consequently, using (2.55) we conclude that (2.34) holds for all $t > 0$ and $x \in \mathbb{R}$.

Inclusion (2.53) is a direct consequence of (2.48) and (2.55). Inclusion (2.54) is a direct consequence of definition (2.40), (2.47), (2.35) and (2.49).

We complete the proof by showing that (2.46) holds. Using (2.51), Fubini's theorem, integration by parts and the fact that $\rho_t + (\rho w)_x = 0$ for all $t > 0$ and $x \in \mathbb{R}$, we get for every function $\phi \in C^2\left(\mathbb{R}_+ \times \mathbb{R}\right)$ of compact support:

$$\begin{aligned}
&-\int_{-\infty}^{+\infty} \phi(0,x)\rho_0(x)dx = \int_0^{+\infty}\int_{-\infty}^{+\infty} \rho(t,x)\left(w(t,x)\phi_x(t,x) + \phi_t(t,x)\right) dxdt \\
&= \int_{-\infty}^{+\infty}\int_0^{+\infty} \rho(t,x)\phi_t(t,x)\, dtdx + \int_0^{+\infty}\int_{-\infty}^{+\infty} \rho(t,x)w(t,x)\phi_x(t,x)\, dxdt \\
&= -\int_{-\infty}^{+\infty} \rho(0,x)\phi(0,x)\, dx - \int_{-\infty}^{+\infty}\int_0^{+\infty} \rho_t(t,x)\phi(t,x)\, dtdx \\
&-\int_0^{+\infty}\int_{-\infty}^{+\infty} \left(\rho(t,x)w(t,x)\right)_x \phi(t,x)\, dxdt \\
&= -\int_{-\infty}^{+\infty} \rho(0,x)\phi(0,x)\, dx - \int_0^{+\infty}\int_{-\infty}^{+\infty} \left(\rho_t(t,x) + \left(\rho(t,x)w(t,x)\right)_x\right)\phi(t,x)\, dxdt \\
&= -\int_{-\infty}^{+\infty} \rho(0,x)\phi(0,x)\, dx.
\end{aligned}$$

Thus, we conclude that for every function $\phi \in C^2\left(\mathbb{R}\right)$ of compact support it holds that:

$$\int_{-\infty}^{+\infty} \phi(x)\,(\rho(0,x)-\rho_0(x))\,dx = 0. \tag{2.93}$$

Using (2.93), Corollary 4.24 on page 110 in Brezis (2010), the fact that $\rho_0 \in X \subset L^1(\mathbb{R}) \cap L^\infty(\mathbb{R})$ and the fact that $\rho[0] \in X \subset L^1(\mathbb{R}) \cap L^\infty(\mathbb{R})$ we get that $\rho(0,x) = \rho_0(x)$ for $x \in \mathbb{R}$ a.e.. Since $\rho[0] \in C^1(\mathbb{R})$, it follows that $\rho_0 \in C^1(\mathbb{R})$ and that $\rho(0,x) = \rho_0(x)$ for all $x \in \mathbb{R}$. Therefore, (2.46) holds. The proof is complete. $\triangleleft$

Proof of Proposition 2.4.2: Notice first that from (2.56) we have that

$$\frac{d\rho_i^{k+1}}{d\,\delta t} = \frac{G_{i-1}^k - G_i^k}{\delta x},\ i \in \mathbb{Z},\ k \in \mathbb{Z},\ k \geq 0. \tag{2.94}$$

Using (2.56) and (2.94) and definition of f we get

$$\begin{aligned}
\frac{df}{d\,\delta t}(\delta t) &= \delta x \sum_{i\in\mathbb{Z}} Q'(\rho_i^{k+1}) \frac{d\rho_i^{k+1}}{d\,\delta t} = \sum_{i\in\mathbb{Z}} Q'(\rho_i^{k+1}) \left(G_{i-1}^k - G_i^k\right) \\
&= \sum_{i\in\mathbb{Z}} Q'(\rho_{i+1}^{k+1}) G_i^k - \sum_{i\in\mathbb{Z}} Q'(\rho_i^{k+1}) G_i^k \\
&= \sum_{i\in\mathbb{Z}} \left(Q'(\rho_{i+1}^{k+1}) - Q'(\rho_i^{k+1})\right) G_i^k \\
&= \delta x \sum_{i\in\mathbb{Z}} \rho_i^k \frac{Q'(\rho_{i+1}^{k+1}) - Q'(\rho_i^{k+1})}{\delta x} h\left(-q_i^k\right).
\end{aligned} \tag{2.95}$$

The desired inequality is a direct consequence of (2.95), definitions (2.57), (2.58), and the fact that $h(\cdot)$ is increasing with $h(0) = 0$. This completes the proof. $\triangleleft$

Proof of Proposition 2.4.3: From (2.56) and definitions (2.57) and (2.58) we have for $i \in \mathbb{Z}, k \in \mathbb{Z}, k \geq 0$

$$\rho_i^{k+1} = \rho_i^k + \frac{\delta t}{\delta x}\left(\rho_{i-1}^k h\left(\frac{Q'(\rho_{i-1}^k) - Q'(\rho_i^k)}{\delta x}\right) - \rho_i^k h\left(\frac{Q'(\rho_i^k) - Q'(\rho_{i+1}^k)}{\delta x}\right)\right). \tag{2.96}$$

It follows from (2.43), (2.96), the facts that $M = \sup\limits_{i\in\mathbb{Z}}\left(\rho_i^k\right)$ and $h' \in L^\infty(\mathbb{R})$, and assumption $1 \geq \frac{\delta t}{\delta x}\left(b + 2\frac{M\|h'\|_\infty}{\delta x}\max\limits_{0\leq\rho\leq M}(\theta(\rho))\right)$ that

$$\begin{aligned}
\frac{\partial \rho_i^{k+1}}{\partial \rho_i^k} &= 1 - \frac{\delta t}{\delta x} h\left(\frac{Q'(\rho_i^k) - Q'(\rho_{i+1}^k)}{\delta x}\right) \\
&\quad - \frac{\delta t}{\delta x}\frac{\theta(\rho_i^k)}{\delta x}\left(\rho_{i-1}^k h'\left(\frac{Q'(\rho_{i-1}^k) - Q'(\rho_i^k)}{\delta x}\right) + \rho_i^k h'\left(\frac{Q'(\rho_i^k) - Q'(\rho_{i+1}^k)}{\delta x}\right)\right) \\
&\geq 1 - \frac{\delta t}{\delta x} b - \delta t \frac{\theta(\rho_i)}{(\delta x)^2}\left(\rho_{i-1}^k h'\left(\frac{Q'(\rho_{i-1}^k) - Q'(\rho_i^k)}{\delta x}\right) + \rho_i h'\left(\frac{Q'(\rho_i^k) - Q'(\rho_{i+1}^k)}{\delta x}\right)\right) \\
&\geq 1 - \frac{\delta t}{\delta x} b - 2\delta t \frac{M\|h'\|_\infty}{(\delta x)^2} \max_{0\leq\rho\leq M}(\theta(\rho)) \geq 0.
\end{aligned} \tag{2.97}$$

Inequality (2.97) implies that ρ_i^{k+1} is increasing with respect to ρ_i^k. Therefore, by the definition of M and (2.96) we get that the following inequalities hold for $i \in \mathbb{Z}, k \in \mathbb{Z}, k \geq 0$

$$\rho_i^{k+1} \leq M + \frac{\delta t}{\delta x}\left(\rho_{i-1}^k h\left(\frac{Q'(\rho_{i-1}^k) - Q'(M)}{\delta x}\right) - Mh\left(\frac{Q'(M) - Q'(\rho_{i+1}^k)}{\delta x}\right)\right) \tag{2.98}$$

$$\rho_i^{k+1} \geq \frac{\delta t}{\delta x}\rho_{i-1}^k h\left(\frac{Q'(\rho_{i-1}^k)}{\delta x}\right). \tag{2.99}$$

Since Q' is a non-decreasing function (recall definition (2.43)) and since $\rho_{i-1}^k \leq M$, it follows that $Q'(\rho_{i-1}^k) \leq Q'(M)$ and consequently $h\left(\frac{Q'(\rho_{i-1}^k)-Q'(M)}{\delta x}\right) \leq 0$. Moreover, since $\rho_{i+1}^k \leq M$, it follows that $Q'(\rho_{i+1}^k) \leq Q'(M)$ and consequently $h\left(\frac{Q'(M)-Q'(\rho_{i+1}^k)}{\delta x}\right) \geq 0$. Thus, (2.98) implies that $\rho_i^{k+1} \leq M$. Moreover, $Q'(\rho_{i-1}^k) \geq 0$ and consequently, $h\left(\frac{Q'(\rho_{i-1}^k)}{2\delta x}\right) \geq 0$. Hence, from (2.99) we get $\rho_i^{k+1} \geq 0$. This completes the proof. ◂

Proof of Proposition 2.4.4: Recall that $f(\delta t) = \delta x \sum_{i\in\mathbb{Z}} Q(\rho_i^{k+1})$. Using definitions (2.6), (2.56), (2.57), equation (2.94), and inequality $\rho_i^k \leq M$, $i \in \mathbb{Z}$, $k \in \mathbb{Z}$, $k \geq 0$ we obtain

$$\begin{aligned}
\frac{d^2 f}{d(\delta t)^2}(\delta t) &= \sum_{i\in\mathbb{Z}} \rho_i^k \theta(\rho_{i+1}^{k+1}) h\left(-q_i^k\right) \frac{d\rho_{i+1}^{k+1}}{d\,\delta t} - \sum_{i\in\mathbb{Z}} \rho_i^k \theta(\rho_i^{k+1}) h\left(-q_i^k\right) \frac{d\rho_i^{k+1}}{d\,\delta t} \\
&= \sum_{i\in\mathbb{Z}} \rho_i^k \theta(\rho_{i+1}^{k+1}) h\left(-q_i^k\right) \frac{G_i^k - G_{i+1}^k}{\delta x} - \sum_{i\in\mathbb{Z}} \rho_i^k \theta(\rho_i^{k+1}) h\left(-q_i^k\right) \frac{G_{i-1}^k - G_i^k}{\delta x} \\
&= \sum_{i\in\mathbb{Z}} \theta(\rho_i^{k+1}) \frac{G_{i-1}^k - G_i^k}{\delta x} \left(\rho_{i-1}^k h\left(-q_{i-1}^k\right) - \rho_i^k h\left(-q_i^k\right)\right) \\
&= \frac{1}{\delta x} \sum_{i\in\mathbb{Z}} \theta(\rho_i^{k+1}) \left(G_{i-1}^k - G_i^k\right)^2 \leq \frac{1}{\delta x} \max_{0\leq\rho\leq M} (\theta(\rho)) \sum_{i\in\mathbb{Z}} \left(G_{i-1}^k - G_i^k\right)^2 \\
&\leq \frac{4}{\delta x} \max_{0\leq\rho\leq M} (\theta(\rho)) \sum_{i\in\mathbb{Z}} \left(G_i^k\right)^2 = \frac{4}{\delta x} \max_{0\leq\rho\leq M} (\theta(\rho)) \sum_{i\in\mathbb{Z}} \left(\rho_i^k\right)^2 h^2\left(-q_i^k\right) \\
&\leq \frac{4M}{\delta x} \max_{0\leq\rho\leq M} (\theta(\rho)) \sum_{i\in\mathbb{Z}} \rho_i^k h^2\left(-q_i^k\right) \leq \frac{4M\,\|h'\|_\infty}{\delta x} \max_{0\leq\rho\leq M} (\theta(\rho)) \sum_{i\in\mathbb{Z}} \rho_i^k \left|q_i^k\right| \left|h\left(-q_i^k\right)\right| \\
&= \frac{4M\,\|h'\|_\infty}{\delta x} \max_{0\leq\rho\leq M} (\theta(\rho)) \sum_{i\in\mathbb{Z}} \rho_i^k \left(-q_i^k\right) h\left(-q_i^k\right) \\
&= -\frac{4M\,\|h'\|_\infty}{\delta x} \max_{0\leq\rho\leq M} (\theta(\rho)) \sum_{i\in\mathbb{Z}} \rho_i^k q_i^k h\left(-q_i^k\right).
\end{aligned} \tag{2.100}$$

From Proposition 2.4.2 and equation (2.100) we finally obtain

$$f(\delta t) \leq f(0) + \delta t \left(1 - \delta t \frac{4M\,\|h'\|_\infty}{(\delta x)^2} \max_{0\leq\rho\leq M} (\theta(\rho))\right) \delta x \sum_{i\in\mathbb{Z}} \rho_i^k q_i^k h\left(-q_i^k\right)$$

which implies inequality (2.59). The proof is complete. ◂

Proof of Proposition 2.4.5: For any $\phi \in C^2(\mathbb{R}_+ \times \mathbb{R})$ with compact support, define $\phi_i^k = \phi(k\delta t, i\delta x)$ for $i, k \in \mathbb{Z}$, $k \geq 0$. We have from (2.60) and definition (2.61) after adding and subtracting terms that

$$-\sum_{i\in\mathbb{Z}}\frac{\rho_i^0\phi_i^0}{\delta t}=\sum_{k\geq 0}\sum_{i\in\mathbb{Z}}\frac{\rho_{i-1}^k w_{i-1}^k}{\delta x}\left(\phi_i^k-\phi_{i-1}^k\right)+\sum_{k\geq 0}\sum_{i\in\mathbb{Z}}\rho_i^{k+1}\frac{\phi_i^{k+1}-\phi_i^k}{\delta t}. \tag{2.101}$$

Moreover, from (2.101), (2.61), and (2.62) we obtain

$$\begin{aligned}-\sum_{i\in\mathbb{Z}}\phi_i^0\int_{i\delta x}^{(i+1)\delta x}\rho_0(s)ds&=\sum_{i\in\mathbb{Z}}\frac{\phi_i^k-\phi_{i-1}^k}{\delta x}\int_{k\delta t}^{(k+1)\delta t}\int_{(i-1)\delta x}^{i\delta x}\rho_{\delta x,\delta t}(t,x)w_{\delta x,\delta t}(t,x)dxdt\\&+\sum_{i\in\mathbb{Z}}\frac{\phi_i^{k+1}-\phi_i^k}{\delta t}\int_{(k+1)\delta t}^{(k+2)\delta t}\int_{i\delta x}^{(i+1)\delta x}\rho_{\delta x,\delta t}(t,x)dxdt.\end{aligned} \tag{2.102}$$

Notice that since $\phi\in C^2(\mathbb{R}_+\times\mathbb{R})$ we have that the following equations hold for k, $i\in\mathbb{Z}$, $k>0$

$$\begin{aligned}\frac{\phi_i^{k+1}-\phi_i^k}{\delta t}&=\phi_t(k\delta t,i\delta x)+\frac{1}{\delta t}\int_{k\delta t}^{(k+1)\delta t}\int_{k\delta t}^{\tau}\phi_{tt}(l,i\delta x)dld\tau\\\frac{\phi_i^k-\phi_{i-1}^k}{\delta x}&=\phi_x(k\delta t,(i-1)\delta x)+\frac{1}{\delta x}\int_{(i-1)\delta x}^{i\delta x}\int_{(i-1)\delta x}^{\xi}\phi_{xx}(k\delta t,s)dsd\xi.\end{aligned} \tag{2.103}$$

Combining (2.103) with (2.102) we get

$$\begin{aligned}&-\sum_{i\in\mathbb{Z}}\int_{i\delta x}^{(i+1)\delta x}\phi(0,x)\rho_0(x)dx\\&=\sum_{i\in\mathbb{Z}}\int_{k\delta t}^{(k+1)\delta t}\int_{(i-1)\delta x}^{i\delta x}\phi_x(t,(i-1)\delta x)\rho_{\delta x,\delta t}(t,x)w_{\delta x,\delta t}(t,x)dxdt\\&+\sum_{i\in\mathbb{Z}}\int_{k\delta t}^{(k+1)\delta t}\int_{i\delta x}^{(i+1)\delta x}\phi_t(k\delta t,i\delta x)\rho_{\delta x,\delta t}(t,x)dxdt\\&-\sum_{i\in\mathbb{Z}}\int_0^{\delta t}\int_{i\delta x}^{(i+1)\delta x}\phi_t(0,i\delta x)\rho_{\delta x,\delta t}(t,x)dxdt\\&+\delta t\sum_{i\in\mathbb{Z}}\rho_{i-1}^k w_{i-1}^k\int_{(i-1)\delta x}^{i\delta x}\int_{(i-1)\delta x}^{\xi}\phi_{xx}(k\delta t,s)dsd\xi+\delta x\sum_{i\in\mathbb{Z}}\rho_i^{k+1}\int_{k\delta t}^{(k+1)\delta t}\int_{k\delta t}^{\tau}\phi_{tt}(l,i\delta x)dld\tau\\&-\sum_{i\in\mathbb{Z}}\int_{i\delta x}^{(i+1)\delta x}\int_{i\delta x}^{x}\rho_0(x)\phi_x(0,l)dldx\\&-\sum_{i\in\mathbb{Z}}\int_{k\delta t}^{(k+1)\delta t}\int_{(i-1)\delta x}^{i\delta x}\left(\int_{k\delta t}^{t}\phi_{xt}(\tau,(i-1)\delta x)\,d\tau\right)\rho_{\delta x,\delta t}(t,x)w_{\delta x,\delta t}(t,x)dxdt\\&+\sum_{i\in\mathbb{Z}}\int_{(k+1)\delta t}^{(k+2)\delta t}\int_{i\delta x}^{(i+1)\delta x}\left(\phi_t(k\delta t,i\delta x)-\phi_t((k+1)\delta t,i\delta x)\right)\rho_{\delta x,\delta t}(t,x)dxdt.\end{aligned} \tag{2.104}$$

Using (2.104) it is straightforward to obtain (2.64) with P_1 defined by (2.66). Notice next that definition (2.58) implies that

$$\sum_{i\in\mathbb{Z}}\beta\left(w_i^k\right)\phi_i^k=\sum_{i\in\mathbb{Z}}Q'(\rho_{i+1}^k)\frac{\phi_{i+1}^k-\phi_i^k}{\delta x} \tag{2.105}$$

and due to (2.103) we obtain that

$$
\begin{aligned}
&\sum_{i\in\mathbb{Z}}\int_{k\delta t}^{(k+1)\delta t}\int_{i\delta x}^{(i+1)\delta x}\phi\left(k\delta t,i\delta x\right)\beta\left(w_{\delta x,\delta t}(t,x)\right)dxdt\\
&=\sum_{i\in\mathbb{Z}}\int_{k\delta t}^{(k+1)\delta t}\int_{(i+1)\delta x}^{(i+2)\delta x}\phi_x\left(k\delta t,i\delta x\right)Q'\left(\rho_{\delta x,\delta t}(t,x)\right)dxdt\\
&+\delta t\sum_{i\in\mathbb{Z}}Q'\left(\rho_{i+1}^{k}\right)\int_{i\delta x}^{(i+1)\delta x}\int_{i\delta x}^{\xi}\phi_{xx}(k\delta t,s)dsd\xi.
\end{aligned}
\tag{2.106}
$$

From (2.106) and expanding the integrals $\int_{k\delta t}^{t}\phi_t\left(\tau,i\delta x\right)d\tau$ and $\int_{i\delta x}^{x}\phi_x(t,\xi)d\xi$ we can obtain the following equation

$$
\begin{aligned}
&\sum_{i\in\mathbb{Z}}\int_{k\delta t}^{(k+1)\delta t}\int_{i\delta x}^{(i+1)\delta x}\phi\left(t,x\right)\beta\left(w_{\delta x,\delta t}(t,x)\right)dxdt\\
&-\sum_{i\in\mathbb{Z}}\int_{k\delta t}^{(k+1)\delta t}\int_{i\delta x}^{(i+1)\delta x}\left(\int_{i\delta x}^{x}\phi_x(t,\xi)d\xi\right)\beta\left(w_{\delta x,\delta t}(t,x)\right)dxdt\\
&-\sum_{i\in\mathbb{Z}}\int_{k\delta t}^{(k+1)\delta t}\int_{i\delta x}^{(i+1)\delta x}\left(\int_{k\delta t}^{t}\phi_t\left(\tau,i\delta x\right)d\tau\right)\beta\left(w_{\delta x,\delta t}(t,x)\right)dxdt\\
&=\sum_{i\in\mathbb{Z}}\int_{k\delta t}^{(k+1)\delta t}\int_{i\delta x}^{(i+1)\delta x}\phi_x\left(t,i\delta x\right)Q'\left(\rho_{\delta x,\delta t}(t,x)\right)dxdt\\
&-\sum_{i\in\mathbb{Z}}\int_{k\delta t}^{(k+1)\delta t}\int_{(i+1)\delta x}^{(i+2)\delta x}\left(\phi_x\left(t,(i+1)\delta x\right)-\phi_x\left(t,i\delta x\right)\right)Q'\left(\rho_{\delta x,\delta t}(t,x)\right)dxdt\\
&+\delta t\sum_{i\in\mathbb{Z}}Q'\left(\rho_{i+1}^{k}\right)\int_{i\delta x}^{(i+1)\delta x}\int_{i\delta x}^{\xi}\phi_{xx}(k\delta t,s)dsd\xi\\
&-\sum_{i\in\mathbb{Z}}\int_{k\delta t}^{(k+1)\delta t}\int_{(i+1)\delta x}^{(i+2)\delta x}\left(\int_{k\delta t}^{t}\phi_{xt}\left(\tau,i\delta x\right)d\tau\right)Q'\left(\rho_{\delta x,\delta t}(t,x)\right)dxdt.
\end{aligned}
\tag{2.107}
$$

Equation (2.107) implies (2.65) with P_2 defined by (2.67). Finally, inequalities (2.68) and (2.69) are a direct consequence of Proposition 2.4.2 and Proposition 2.4.3. The proof is complete. ◁

Proof of Proposition 2.4.6: Define

$$V_k=\sum_{i\in\mathbb{Z}}Q(\rho_i^k) \tag{2.108}$$

$$W_k=\sum_{i\in\mathbb{Z}}\rho_i^k w_i^k\beta\left(w_i^k\right) \tag{2.109}$$

and notice that due to definitions (2.22) and (2.46), $V_k\geq 0$ and $W_k\geq 0$ for all $k\geq 0$. Moreover, let

$$c=1-\delta t\frac{4\left\|\rho_0\right\|_\infty\left\|h'\right\|_\infty}{(\delta x)^2}\max_{0\leq\rho\leq\|\rho_0\|_\infty}\left(\theta(\rho)\right)>0. \tag{2.110}$$

Definitions (2.108), (2.109), (2.110) and inequality (2.59) imply the following estimate

$$V_{k+1}\leq V_k-c\,\delta t\,W_k$$

which recursively gives that

$$V_k \leq V_0 - c\,\delta t \sum_{j=0}^{k-1} W_j. \tag{2.111}$$

Since $V_k \geq 0$, we obtain from (2.111) the following implication

$$\sum_{j=0}^{+\infty} W_j \leq \frac{1}{c\,\delta t} V_0 \Rightarrow \lim_{k\to+\infty}\left(\sum_{i\in\mathbb{Z}} \rho_i^k w_i^k \beta\left(w_i^k\right)\right) = 0 \Rightarrow \lim_{k\to+\infty}\left(\rho_i^k w_i^k \beta\left(w_i^k\right)\right) = 0. \tag{2.112}$$

Suppose that $\lim_{k\to+\infty}\left(\rho_i^k \left|w_i^k\right|\right) = 0$ is not true for some $i \in \mathbb{Z}$. Then there exists $\varepsilon \in \left(0, \frac{\min(1,b)}{R}\right)$ and an increasing sequence $\{k_n : n = 1, 2, ...\}$ with $\rho_i^{k_n}\left|w_i^{k_n}\right| \geq \varepsilon$ for all $n = 1, 2, ...$ It follows that $\left|w_i^{k_n}\right| \geq \frac{\varepsilon}{R}$ and $\rho_i^{k_n} \geq \frac{\varepsilon}{\max(1,b)}$ for all $n = 1, 2, ...$ Since β is increasing with $\beta(0) = 0$ we get that $w_i^{k_n}\beta\left(w_i^{k_n}\right) \geq \min\left(\frac{\varepsilon}{R}\beta\left(\frac{\varepsilon}{R}\right), -\frac{\varepsilon}{R}\beta\left(-\frac{\varepsilon}{R}\right)\right)$ for all $n = 1, 2, ...$ Consequently, we have $\rho_i^{k_n} w_i^{k_n}\beta\left(w_i^{k_n}\right) \geq \frac{\varepsilon}{\max(1,b)} \min\left(\frac{\varepsilon}{R}\beta\left(\frac{\varepsilon}{R}\right), -\frac{\varepsilon}{R}\beta\left(-\frac{\varepsilon}{R}\right)\right)$ for all $n = 1, 2, ...,$ which contradicts the fact that $\lim_{k\to+\infty}\left(\rho_i^k w_i^k \beta\left(w_i^k\right)\right) = 0$. Therefore, $\lim_{k\to+\infty}\left(\rho_i^k \left|w_i^k\right|\right) = 0$ for some $i \in \mathbb{Z}$.

Suppose that $\lim_{k\to+\infty}\left(\rho_i^k \left|Q'(\rho_i^k) - Q'(\rho_{i+1}^k)\right|\right) = 0$ is not true for some $i \in \mathbb{Z}$. Clearly, this cannot happen if $\|\rho_0\|_\infty \leq 1$. Consequently, $\|\rho_0\|_\infty > 1$. Then there exists $\varepsilon > 0$ and an increasing sequence $\{k_n : n = 1, 2, ...\}$ with $\rho_i^{k_n}\left|Q'(\rho_i^{k_n}) - Q'(\rho_{i+1}^{k_n})\right| \geq \varepsilon$ for all $n = 1, 2, ...$ It follows that $\left|Q'(\rho_i^{k_n}) - Q'(\rho_{i+1}^{k_n})\right| \geq \frac{\varepsilon}{R}$ and $\rho_i^{k_n} \geq \frac{\varepsilon}{Q'(\|\rho_0\|_\infty)}$ for all $n = 1, 2, ...$ Since h is increasing with $h(0) = 0$ and since $w_i^k = h\left(\frac{Q'(\rho_i^k) - Q'(\rho_{i+1}^k)}{\delta x}\right)$ we get that $\left|w_i^{k_n}\right| \geq \min\left(h\left(\frac{\varepsilon}{R\delta x}\right), -h\left(-\frac{\varepsilon}{R\delta x}\right)\right)$ for all $n = 1, 2, ...$ Consequently, we have $\rho_i^{k_n}\left|w_i^{k_n}\right| \geq \frac{\varepsilon}{Q'(\|\rho_0\|_\infty)} \min\left(h\left(\frac{\varepsilon}{R\delta x}\right), -h\left(-\frac{\varepsilon}{R\delta x}\right)\right)$ for all $n = 1, 2, ...,$ which contradicts the fact that $\lim_{k\to+\infty}\left(\rho_i^k \left|w_i^k\right|\right) = 0$. Therefore, $\lim_{k\to+\infty}\left(\rho_i^k \left|Q'(\rho_i^k) - Q'(\rho_{i+1}^k)\right|\right) = 0$ for some $i \in \mathbb{Z}$. The proof is complete. ◃

Chapter 3

A comparative study of numerical methods for approximating the solutions of the macro-PRCC

3.1 Abstract

In this chapter, a particle method is used to approximate the solutions of the macro-PRCC. It is shown that this method preserves certain differential inequalities that hold for the macroscopic traffic model: mass is preserved, the mechanical energy is decaying and an energy functional is also decaying. To demonstrate the advantages of the particle method under consideration, a comparison with other numerical methods for viscous compressible fluid models is provided. Since the solutions of the macro-PRCC can be approximated by the solutions of its reduced model (Chapter 2), the numerical solutions produced by the particle method are also compared with the corresponding numerical approximations provided for the solutions of the reduced model. Finally, a traffic simulation scenario and a comparison with the ARZ model are provided.

3.2 Introduction

In contrast to traffic flow models for human drivers, the macro-PRCC derived in Karafyllis et al. (2022d) via the design of a bidirectional cruise controller for CAVs is isotropic, as in other fluids, with the principle that vehicles react to both upstream and downstream vehicles. Isotropy, as well as many other characteristics of the compressible fluid flow that are present in the macro-PRCC, follow from the fact that nudging and lane-free vehicle movement are allowed by the respective CC. Moreover, a link with the underlying microscopic CC (i.e. the PRCC) is provided in Karafyllis et al. (2022d), which allows to determine the physical properties of the "traffic fluid" by changing the functions or the parameter values included in the PRCC.

This chapter deals with the approximation of the solutions of the macro-PRCC which follows from certain selections of the functions involved in the PRCC (see Theodosis et al. (2024) and Chapter 2). These selections, in addition to providing more "fluid-like" characteristics, enable a model reduction (Chapter 2). This fact is analogous to the human-driven vehicles case, where the ARZ model reduces to the LWR model (Li (2003)). For the derivation of the macro-PRCC, a particle method was proposed in Karafyllis et al. (2022d), in which the vehicles are considered as "self-driven" particles of a fluid. This method is a modified version of the particle method presented in Karafyllis and Papageorgiou (2023) for compressible fluids, and it is used for approximating the solutions of the macro-PRCC. It is shown that all differential inequalities that hold for the macroscopic model (described in Section 3.3) are preserved by the particle method (see Proposition 3.3.1 and Proposition 3.3.3 below). It is noted that, to the best of our knowledge, a numerical study of the particle method and comparison with other numerical methods has never been performed in the literature for viscous compressible fluid models. Therefore, a main goal of this chapter is the numerical study of the particle scheme and the derivation of important conclusions about its effectiveness.

Although many numerical methods have been used for compressible fluid models with constant viscosity (see for example Al-Taki et al. (2021), Ansanay-Alex et al. (2011), Gallouët et al. (2019), Haack et al. (2012), Hošek and She (2018), Karper (2013) and references therein), there are very few articles that cover the case of density-dependent viscosity (see Bresch et al. (2007), Caggio and Donatelli (2021), Gunawan (2014), Guo and Zhu (2010), Karafyllis and Papageorgiou (2023), Katsaounis and Simeoni (2002), Nishida (1986)) and most of them utilize an approximation scheme for proving existence of solutions. Since the macro-PRCC is similar to compressible fluids with density-dependent viscosity (see Section 3.3), the particle method proposed in Karafyllis and Papageorgiou (2023), Karafyllis et al. (2022d) is compared with the so-called "method of lines" used in Guo and Zhu, 2010, Nishida (1986) for proving existence of solutions for compressible fluid models with density-dependent viscosity, as well as with the numerical method used in Gunawan (2014) for approximating the solutions of the viscous Saint-Venant equations.

A common characteristic between the method of lines (Guo and Zhu (2010), Nishida (1986)) and the particle method proposed in Karafyllis and Papageorgiou (2023), Karafyllis et al. (2022d) is that in both methods the solutions of the macroscopic model are approximated by solving a system of ODEs. However, with the method of lines, the solutions are approximated at fixed grid-points in Lagrangian coordinates, and, as a result, the actual coordinates of the vehicles remain unknown. Therefore, a variable transformation is required to obtain the solutions in Eulerian coordinates, which, in addition to having an impact on the computational cost, (see Section 3.5), may create an additional error in the approximation of the solutions. On the other hand, the approximation of the solutions with the particle method proposed in Karafyllis and Papageorgiou (2023), Karafyllis et al. (2022d) is given directly in Eulerian coordinates, and the computational cost, in terms of CPU time, is much less compared to the method of lines and the numerical method used in Gunawan (2014).

To demonstrate the advantages of the particle method as well as the properties of the macro-PRCC, two examples are presented. The first example focuses on evaluating the performance of the proposed particle method, while the second example includes also a realistic traffic simulation scenario for comparing the macro-PRCC with the ARZ model. In both examples, the particle method is compared with the method of lines (Guo and Zhu (2010), Nishida (1986)) and the numerical method used for the viscous Saint-Venant equations (see Gunawan (2014)) showing that, although the difference between the numerical solutions is small, higher accuracy approximations are provided by the proposed particle method, since it better preserves a differential inequality that holds for the macro-PRCC and indicates energy conservation. Comparisons with the numerical solutions of the reduced model (see Theodosis et al. (2024) and Chapter 2) are also provided for both examples, indicating the latter's high accuracy approximations.

The contribution of this chapter is summarized as follows:

- The study of the macro-PRCC under specific selections for the functions included in the PRCC;

- The use of a particle method for approximating the solutions of the macro-PRCC and a comparison with other numerical methods in the literature for compressible fluid models, showing that the employed particle method, in addition to having much less computational cost, it provides better approximations compared to the other numerical methods;

- The numerical approximations provided for the solutions of the macro-PRCC are compared with those provided for the solutions of its reduced model, derived in Chapter 2, showing that the reduced model provides high accuracy approximations.

The structure of Chapter 3 is as follows. Section 3.3 presents the particle method used for approximating the solutions of the macro-PRCC. Section 3.4 is devoted to the presentation of some numerical methods used in the literature for approximating the solutions of viscous compressible fluid models. Section 3.5 presents the two aforementioned examples. Finally, Section 3.6 gives the concluding remarks of the present work. All proofs are provided in Section 3.7.

3.3 A particle method for the macro-PRCC

3.3.1 The macro-PRCC

The macro-PRCC (1.1), (1.6) under the selections (1.15)-(1.18), (1.21) is given by the following equations for all $\tau > 0$, $\xi \in \left(\tilde{l}(\tau), \tilde{L}(\tau)\right)$:

$$\tilde{\rho}_\tau + (\tilde{\rho}\tilde{v})_\xi = 0 \tag{3.1}$$

$$\tilde{\rho}\tilde{\beta}'(\tilde{v})\tilde{v}_\tau + \tilde{\rho}\tilde{\beta}'(\tilde{v})\tilde{v}\tilde{v}_\xi + \tilde{\sigma}\tilde{\kappa}(\tilde{\rho})\tilde{\rho}_\xi = (\tilde{\rho}\tilde{\kappa}(\tilde{\rho})\tilde{v}_\xi)_\xi - \tilde{\sigma}\tilde{\rho}\tilde{\beta}(\tilde{v}) \tag{3.2}$$

$$\frac{d}{d\tau}\tilde{l}(\tau) = \tilde{v}\left(\tau, \tilde{l}^+(\tau)\right) \tag{3.3}$$

$$\frac{d}{d\tau}\tilde{L}(\tau) = \tilde{v}\left(\tau, \tilde{L}^-(\tau)\right). \tag{3.4}$$

The states $\tilde{l}(\tau), \tilde{L}(\tau) \in \mathbb{R}$ yield the interval $\left(\tilde{l}(\tau), \tilde{L}(\tau)\right)$ that contains the vehicles for times $\tau > 0$; $\tilde{\rho}(\tau, \xi) \in (0, \rho_{\max})$, $\tilde{v}(\tau, \xi) \in (0, v_{\max})$ are the traffic density and mean speed, respectively, at position $\xi \in \left(\tilde{l}(\tau), \tilde{L}(\tau)\right)$ on a highway, with $\rho_{\max} > 0$, $v_{\max} > 0$ being the maximum density and speed limits, respectively; $v^* \in (0, v_{\max})$ is the speed set-point and $\tilde{\sigma} > 0$ is a constant. Moreover, the function $\tilde{\beta}(\tilde{v})$ is defined by (1.21) and $\tilde{\kappa} : (0, \rho_{\max}) \to \mathbb{R}_+$ is a function of class $C^1((0, \rho_{\max}))$ that satisfies (1.19), (1.20). It should be noted that outside the interval $\left(\tilde{l}(\tau), \tilde{L}(\tau)\right)$ the highway is "empty" and therefore:

$$\tilde{\rho}(\tau, \xi) = 0 \text{ for } \xi \leq \tilde{l}(\tau) \text{ and } \xi \geq \tilde{L}(\tau),\ \tau > 0. \tag{3.5}$$

As shown in Chapter 2, it is possible to approximate the solutions of (3.1)-(3.4) by the solutions of a reduced model that consists of the following single nonlinear heat-type PDE:

$$\tilde{\rho}_\tau + (\tilde{\rho}\tilde{\beta}^{-1}(-\tilde{\rho}^{-1}\tilde{\kappa}(\tilde{\rho})\tilde{\rho}_\xi))_\xi = 0. \tag{3.6}$$

Moreover, notice that the speed PDE (3.2) is strongly reminiscent of the momentum equation for 1-D polytropic compressible fluid flow since it contains a viscosity term with density-dependent viscosity $(\tilde{\rho}\tilde{\kappa}(\tilde{\rho})\tilde{v}_\xi)_\xi$, a pressure term $\tilde{\sigma}\tilde{\kappa}(\tilde{\rho})\tilde{\rho}_\xi$ and a friction term $-\tilde{\sigma}\tilde{\rho}\tilde{\beta}(\tilde{v})$ (by analogy with the relaxation term involved in the macroscopic traffic flow models for human drivers, Aw and Rascle (2000), Zhang (2002)). The pressure term $\tilde{\sigma}\tilde{\kappa}(\tilde{\rho})\tilde{\rho}_\xi$ describes the tendency of vehicles to accelerate or decelerate based on the (local) density, the term $(\tilde{\rho}\tilde{\kappa}(\tilde{\rho})\tilde{v}_\xi)_\xi$ is a viscosity term with $\tilde{\rho}\tilde{\kappa}(\tilde{\rho})$ playing the role of viscosity and making the "traffic fluid" act as a Newtonian fluid, while the friction term $-\tilde{\sigma}\tilde{\rho}\tilde{\beta}(\tilde{v})$ expresses the tendency of vehicles to adjust their speed to the given speed set-point.

Remarks: (i) In contrast to conventional traffic, the traffic flow for model (3.1)-(3.4) is isotropic, as in fluid flow, since the vehicles are automated and react to both upstream and downstream vehicles.
(ii) The selection of $\tilde{\kappa}(\tilde{\rho})$ to satisfy condition (1.19) has the effect of making the fluid behave like a solid when the density tends to the maximum density $\rho_{\max}$.

Assume that $r > 0$ is a given constant length. Using the variable transformation $\xi = rx + v^*\tau$, $x \in (l(t), L(t))$ where $l(t) = \frac{\tilde{l}(\tau)-v^*\tau}{r}$, $L(t) = \frac{\tilde{L}(\tau)-v^*\tau}{r}$ and the dimensionless quantities $\tau = \frac{r}{v^*}t$, $b = \frac{v_{\max}-v^*}{v^*}$, $R = \frac{\rho_{\max}}{\bar{\rho}} > 1$, $w = \frac{\tilde{v}-v^*}{v^*}$, $\rho = \frac{\tilde{\rho}}{\bar{\rho}}$, $\sigma = \frac{r}{v^*}\tilde{\sigma}$, we obtain the following dimensionless model for all $t > 0$, $x \in (l(t), L(t))$:

$$\rho_t + (\rho w)_x = 0 \tag{3.7}$$

$$\rho\beta'(w)w_t + \rho\beta'(w)ww_x + \sigma\kappa(\rho)\rho_x = (\rho\kappa(\rho)w_x)_x - \sigma\rho\beta(w) \tag{3.8}$$

$$\frac{d}{dt}l(t) = w\left(t, l^+(t)\right) \tag{3.9}$$

$$\frac{d}{dt}L(t) = w\left(t, L^-(t)\right) \tag{3.10}$$

with state-constraints $\rho(t,x) \in (0,R)$, $w(t,x) \in (-1,b)$ for $t > 0$, $x \in (l(t), L(t))$, where $R > 1$, $b > 0$, $\sigma > 0$ are constants. The function $\beta(w)$ is defined by (2.22) and $\kappa : (0,R) \to \mathbb{R}_+$ is a function of class $C^1((0,R))$ that satisfies the following properties:

$$\lim_{\rho \to R^-} \kappa(\rho) = +\infty \tag{3.11}$$

$$\kappa(\rho) = 0 \text{ for all } \rho \in (0,1] \text{ and } \kappa(\rho) > 0 \text{ for all } \rho \in (1,R). \tag{3.12}$$

Notice that outside the interval $(l(t), L(t))$ it holds that:

$$\rho(t,x) = 0 \text{ for } x \le l(t) \text{ and } x \ge L(t), \quad t > 0. \tag{3.13}$$

The solutions of (3.7)-(3.10) can be approximated by the solutions of the following dimensionless reduced model (see Section 2.3.1):

$$\rho_t + (\rho\beta^{-1}(-\rho^{-1}\kappa(\rho)\rho_x))_x = 0. \tag{3.14}$$

The relations between the functions β, κ of the dimensionless model (3.7)-(3.10) and the functions $\tilde{\beta}, \tilde{\kappa}$ of the original model (3.1)-(3.4) are given in Table 3.1.

Dimensionless model (3.7)-(3.10)	**Original model** (3.1)-(3.4)
$\beta(w)$	$\frac{1}{v^*}\tilde{\beta}(v^*(w+1))$
$\kappa(\rho)$	$\frac{1}{rv^*}\tilde{\kappa}(\rho\bar{\rho})$

Table 3.1: Relations between the functions β, κ of the dimensionless model (3.7)-(3.10) and the functions $\tilde{\beta}, \tilde{\kappa}$ of the original model (3.1)-(3.4).

For any classical solution of model (3.7)-(3.10) we can define the following functionals:

$$m(t) = \int_{l(t)}^{L(t)} \rho(t,x)dx \tag{3.15}$$

$$E(t) = \int_{l(t)}^{L(t)} \rho(t,x)H(w(t,x))dx + \int_{l(t)}^{L(t)} Q(\rho(t,x))dx \tag{3.16}$$

$$W(t) = \frac{1}{2}\int_{l(t)}^{L(t)} \frac{1}{\rho(t,x)}\left(\rho(t,x)\beta(w(t,x)) + \sigma^{-1}\left(P(\rho(t,x))\right)_x\right)^2 dx \tag{3.17}$$

where

$$H(w) = \int_0^w s\beta'(s)ds = \frac{w^2(b+1)^2}{2(w+1)(b-w)}, \text{ for all } w \in (-1,b) \tag{3.18}$$

$$Q(\rho) = \rho\int_1^\rho \tau^{-2}P(\tau)\,d\tau, \text{ for all } \rho \in (0,R) \tag{3.19}$$

$$P(\rho) = \sigma\int_1^\rho \kappa(\tau)d\tau, \text{ for all } \rho \in (0,R)\,. \tag{3.20}$$

Notice that definitions (3.19), (3.20) in conjunction with (3.12) imply that $Q(\rho) \geq 0$, $P(\rho) \geq 0$ for all $\rho \in (0,R)$. The functional (3.15) expresses the total mass and the functional (3.16) is inspired by the mechanical energy of model (3.7)-(3.10) where $\int_{l(t)}^{L(t)} \rho(t,x)H(w(t,x))dx$ denotes the kinetic energy and $\int_{l(t)}^{L(t)} Q(\rho(t,x))dx$ the potential energy. Moreover, the functional (3.17) is an energy functional that has been constructed using the following transformation

$$\varphi(t,x) = \rho(t,x)\beta(w(t,x)) + \sigma^{-1}\left(P(\rho(t,x))\right)_x. \tag{3.21}$$

The transformation (3.21) has been used in the literature of isentropic, compressible fluid flow (see Karafyllis and Krstic (2022b), Karafyllis and Krstic (2022c), Karafyllis et al. (2022c), Karafyllis et al. (2023), Kazhikhov and Shelukhin (1977), Shelukhin (1977), Shelukhin (1978), Smoller (1994)) and has the effect of making the viscosity disappear from equation (3.8), which then becomes

$$\varphi_t + (w\varphi)_x + (P(\rho))_x = -\sigma\rho\beta(w). \tag{3.22}$$

If a classical solution of (3.7)-(3.10) satisfies

$$\rho\left(t,l^+(t)\right) \leq 1\,,\ \rho\left(t,L^-(t)\right) \leq 1 \tag{3.23}$$

then using (3.15)-(3.20), (3.7)-(3.10) and (3.23) we get the following estimates:

$$\dot{m}(t) = 0 \tag{3.24}$$

$$\begin{aligned}\dot{E}(t) = &-\int_{l(t)}^{L(t)} \rho(t,x)\kappa\left(\rho(t,x)\right)w_x^2(t,x)dx \\ &-\sigma\int_{l(t)}^{L(t)} \rho(t,x)w(t,x)\beta\left(w(t,x)\right)dx \leq 0\end{aligned} \tag{3.25}$$

$$\dot{W}(t) = -\sigma\int_{l(t)}^{L(t)} \frac{1}{\rho(t,x)}\left(\rho(t,x)\beta(w(t,x)) + \sigma^{-1}\left(P(\rho(t,x))\right)_x\right)^2 dx \leq 0 \tag{3.26}$$

which hold for all $t > 0$. Definition (3.24) implies that the total mass, defined by (3.15), remains constant while (3.25), (3.26) show that the functionals defined by (3.16), (3.17) are non-increasing.

3.3.2 The particle method

Several particle methods in the literature have been used for the numerical solution of partial differential equations (see for example Chertock and Levy (2001), Y. and Seibold (2009)). Here, a particle method is considered that was initially proposed in Karafyllis et al. (2022d) to derive model (3.7)-(3.11) by designing a cruise controller on a microscopic scale. A similar particle method (without a friction term) was also recently presented in Karafyllis and Papageorgiou (2023), that provided approximations that converge to a weak solution of the Navier-Stokes equations for the 1-D flow of a viscous compressible fluid. The particle method follows by considering n vehicles/particles with coordinates $L^{(n)}(t) = x_1(t) > x_2(t) > .... > x_n(t) = l^{(n)}(t)$ which move according to the following equations (recall that $b > 0, \sigma > 0, R > 1$):

$$s_i = x_{i-1} - x_i,\ \ i = 2, ..., n \tag{3.27}$$

$$\dot{x}_i = w_i,\ \ i = 1, ..., n \tag{3.28}$$

$$\beta'(w_1)\dot{w}_1 = -\sigma\beta(w_1) - na\,\Phi'\left(nas_2\right) + n^2 aK\left(nas_2\right)\left(w_2 - w_1\right) \tag{3.29}$$

$$\begin{aligned}\beta'(w_i)\dot{w}_i =& -\sigma\beta(w_i) + na\,\Phi'\left(nas_i\right) - na\,\Phi'\left(nas_{i+1}\right) + n^2 aK\left(nas_i\right)\left(w_{i-1} - w_i\right) \\ &+ n^2 aK\left(nas_{i+1}\right)\left(w_{i+1} - w_i\right),\ \ i = 2, ..., n-1\end{aligned} \tag{3.30}$$

$$\beta'(w_n)\dot{w}_n = -\sigma\beta(w_n) + na\,\Phi'\left(nas_n\right) + n^2 aK\left(nas_n\right)\left(w_{n-1} - w_n\right) \tag{3.31}$$

with state-space

$$\Omega_n = \{\,(x_1, ..., x_n, w_1, ..., w_n) \in \mathbb{R}^n \times (-1, b)^n\ :\ na(x_{i-1} - x_i) > 1/R,\ \ i = 2, ..., n\} \tag{3.32}$$

where a is a positive constant and $\beta(w)$ is defined by (2.22). The functions $\Phi : \left(\frac{1}{R}, +\infty\right) \to \mathbb{R}_+$, $K : \left(\frac{1}{R}, +\infty\right) \to \mathbb{R}_+$, $\Phi \in C^2$, $K \in C^2$ satisfy the following equations for all $s \in \left(\frac{1}{R}, +\infty\right)$:

$$K(s) = \frac{a}{s^2}\kappa\left(\frac{1}{s}\right) \tag{3.33}$$

$$\Phi(s) = sQ\left(\frac{1}{s}\right). \tag{3.34}$$

It follows from (3.12), (3.19), (3.20), (3.33), and (3.34) that

$$K(s), \Phi(s) > 0 \text{ for all } s \in \left(\frac{1}{R}, 1\right) \text{ and } K(s) = \Phi(s) = 0 \text{ for all } s \geq 1. \tag{3.35}$$

Moreover, by virtue of (3.34), (3.19) and (3.20) we get that:

$$\lim_{d \to (1/R)^+} \left(\Phi(d)\right) = +\infty \tag{3.36}$$

and

$$\Phi'(s) = -\sigma \int_1^{1/s} \kappa(\tau) d\tau \text{ for all } s \in \left(\frac{1}{R}, +\infty\right). \tag{3.37}$$

Notice that equations (3.33), (3.37) provide a link between the function $\kappa(\rho)$ used in the macroscopic model (3.7)-(3.10) and the functions $K(s)$, $\Phi'(s)$ used in the particle method (3.27)-(3.32). This fact implies that by changing the functions $K(s), \Phi(s)$ we can determine the physical properties of the "traffic fluid" through the function $\kappa(\rho)$.

We next define the following functions:

$$E_n(t) = \frac{1}{na}\sum_{i=1}^{n} H(w_i(t)) + \frac{1}{na}\sum_{i=2}^{n}\Phi(nas_i(t)) \tag{3.38}$$

$$W_n(t) = \frac{1}{2na}\sum_{i=2}^{n-1}\varphi_i^2(t) \tag{3.39}$$

where

$$\varphi_i(t) = \beta(w_i(t)) + \sigma^{-1}na\left(\Phi'\left(nas_{i+1}(t)\right) - \Phi'\left(nas_i(t)\right)\right). \tag{3.40}$$

For the parameterized family of finite-dimensional systems (3.27)-(3.31) defined on Ω_n (recall (3.32)) with initial conditions $(x_1(0),...,x_n(0),w_1(0),...,w_n(0))$ in Ω_n, the following propositions hold.

Proposition 3.3.1 *For every solution of* (3.32)-(3.36) *the following equation holds*

$$\dot{E}_n(t) = -n\sum_{i=2}^{n} K(nas_i(t))(w_{i-1}(t) - w_i(t))^2 - \frac{\sigma}{na}\sum_{i=1}^{n} w_i(t)\beta(w_i(t)) \le 0 \tag{3.41}$$

as long as the solution of (3.27)-(3.31) *is defined.*

Inequality (3.41) is the discretized version of inequality (3.25) and shows that the discretized mechanical energy E_n is not increasing.

Proposition 3.3.2 *Every solution of* (3.27)-(3.31) *is defined for all* $t \ge 0$.

Proposition 3.3.3 *For every solution of* (3.27)-(3.31) *the following equation holds for all* $t \ge 0$

$$\dot{W}_n(t) = -\frac{\sigma}{na}\sum_{i=2}^{n-1}\varphi_i^2(t) \le 0. \tag{3.42}$$

Inequality (3.42) is the discretized version of inequality (3.26) and shows that the discretized energy functional W_n is not increasing.

Let a solution $(x_i(t), w_i(t)),\ i = 1,...,n$ of (3.27)-(3.31), defined for $t \ge 0$, be given. We define for all $t \ge 0$:

$$\rho_i(t) = \frac{1}{na(x_{i-1}(t) - x_i(t))},\ i = 2,...,n \tag{3.43}$$

$$\rho_1(t) = \rho_2(t) = \frac{1}{na(x_1(t) - x_2(t))} \tag{3.44}$$

$$\begin{aligned}&\rho^{(n)}(t,x) = \rho_i(t) + (\rho_{i-1}(t) - \rho_i(t))\left(\tfrac{x - x_i(t)}{x_{i-1}(t) - x_i(t)}\right),\\ &x \in [x_i(t), x_{i-1}(t)),\ i = 2,...,n-1\end{aligned} \tag{3.45}$$

$$\begin{aligned}&w^{(n)}(t,x) = w_i(t) + (w_{i-1}(t) - w_i(t))\left(\tfrac{x - x_i(t)}{x_{i-1}(t) - x_i(t)}\right),\\ &x \in [x_i(t), x_{i-1}(t)),\ i = 2,...,n-1\end{aligned} \tag{3.46}$$

$$\rho^{(n)}(t,x) = \rho_n(t) + (\rho_{n-1}(t) - \rho_n(t))\left(\frac{x - x_n(t)}{x_{n-1}(t) - x_n(t)}\right),\ x \in (x_n(t), x_{n-1}(t)) \tag{3.47}$$

$$w^{(n)}(t,x) = w_n(t) + (w_{n-1}(t) - w_n(t))\left(\frac{x - x_n(t)}{x_{n-1}(t) - x_n(t)}\right),\ x \in (x_n(t), x_{n-1}(t)) \tag{3.48}$$

$$\begin{aligned} l^{(n)}(t) &= x_n(t) \\ L^{(n)}(t) &= x_1(t). \end{aligned} \tag{3.49}$$

The functions $\rho^{(n)} : \bigcup_{t\geq 0}\{t\}\times(x_n(t), x_1(t)) \to (0,R)$, $w^{(n)} : \bigcup_{t\geq 0}\{t\}\times(x_n(t), x_1(t)) \to (-1,b)$ are C^1 on the set $\bigcup_{t\geq 0}\{(t,x) : x\in(x_n(t),x_1(t)),\ x\neq x_i(t),\ i=2,...,n-1\}$ and can be used to approximate the solutions of (3.7)-(3.10). In Karafyllis and Papageorgiou (2023), it was proved that similar approximations converge to a weak solution of the Navier-Stokes equations for the 1-D flow of a viscous compressible fluid.

It should be noted that the particle method (3.27)-(3.32) is a mesh-free method, uses only special discretization that depends entirely on the spacing s_i of the vehicles/particles, may be non-uniform and varies with time. Moreover, the particle method consists of a set of $2n$ ODEs whose accuracy and numerical stability is influenced by the choice of the time integration method, (see Hairer et al. (1993)). The solution of the particle method is based on the interactions between particles, via the functions Φ and K, while the equations (3.43)-(3.49) are used to approximate the solutions of model (3.7)-(3.10).

3.4 Numerical methods for viscous compressible fluids

To evaluate the performance of the proposed particle method (2.32)-(2.37), it is of great importance to compare it with other numerical methods in the literature that are used for the numerical approximation of viscous compressible fluid models with density-dependent viscosity. Equation (3.8) can be written in the following form for all $t>0$ and $x\in(l(t),L(t))$:

$$(\rho\beta(w))_t + (\rho w\beta(w) + P(\rho))_x = (\rho\kappa(\rho)w_x)_x - \sigma\rho\beta(w) \tag{3.50}$$

where $\beta(w)$, $P(\rho)$ are defined by (2.22), (3.20), respectively. Equation (3.50) is similar to the momentum equation of the 1-D compressible Navier-Stokes equations with density-dependent viscosity (see Guo and Zhu (2010), Karafyllis and Papageorgiou (2023)). Therefore, it is interesting to compare the particle method under consideration with the so-called "method of lines" used in Guo and Zhu (2010) for proving existence of global weak solutions to the 1-D compressible Navier-Stokes equations, as well as with the numerical method used in Gunawan (2014) for the numerical approximation of the viscous Saint-Venant equations. However, there are crucial differences between the momentum equations used in Gunawan (2014), Guo and Zhu (2010) and equation (3.50) related to the functions $\beta(w)$, $P(\rho)$, $\mu(\rho)$ and the friction term (see Table 3.2). Therefore, appropriate modifications should be made to compare the proposed particle method with the aforementioned numerical methods. Note that apart from the differences described in Table 3.2, the momentum equation used in Gunawan (2014) includes also an additional term $g\rho z_x$, where z is the topography of the fluid and g is the acceleration of gravity (used also in the pressure function (see Table 3.2)).

To obtain a numerical approximation of the solutions of model (3.7)-(3.10), the numerical method used in Gunawan (2014) is modified by omitting the additional term $g\rho z_x$ from the momentum equation and substituting the functions $\beta(w)$, $P(\rho)$, $\mu(\rho)$ as well as the friction term with the corresponding functions of equation (3.50) (see Table 3.2). Thus, the modified version of the numerical method discussed in Gunawan (2014) reads as follows:

$$\rho_i^0 = \frac{1}{\delta x}\int_{x_{i-1/2}}^{x_{i+1/2}} \rho(0,x)dx,\ i\in\mathbb{Z} \tag{3.51}$$

$$w_{i+1/2}^0 = \frac{1}{\delta x}\int_{x_i}^{x_{i+1}} w(0,x)dx,\ i\in\mathbb{Z} \tag{3.52}$$

	Equation (3.50)	**Momentum equation used in Gunawan (2014)**	**Momentum equation used in Guo and Zhu (2010)**
	$\beta(w) = \frac{b+1}{2}\left[\frac{w(b+1)}{(w+1)(b-w)} + \ln\left(\frac{b(w+1)}{b-w}\right)\right]$	$\beta(w) = w$	$\beta(w) = w$
Pressure	$P(\rho) = \sigma \int_1^\rho \kappa(\tau)d\tau$ $\sigma > 0$	$P(\rho) = \sigma\rho^2$ $\sigma = \frac{1}{2}g,\ g > 0$	$P(\rho) = \sigma\rho^\gamma, \gamma > 1$ $\sigma = 1$
Viscosity	$\mu(\rho) = \rho\kappa(\rho)$	$\mu(\rho) = \mu\rho$ $\mu > 0$	$\mu(\rho) = \mu(\theta\rho^\theta + \varepsilon\eta\rho^\eta)$ $\theta, \varepsilon > 0,\ \eta \in (0,1)$ $\mu = 1$
Friction Term	$-\sigma\rho\beta(w)$	$-\frac{\kappa}{1+\frac{\kappa\rho}{3\mu}}w$ $\kappa, \mu > 0$	No friction term

Table 3.2: Differences between equation (3.50) and the momentum equations used in Gunawan (2014), Guo and Zhu (2010).

$$w^0_{i-1/2} = \frac{1}{\delta x}\int_{x_{i-1}}^{x_i} w(0,x)dx,\ i \in \mathbb{Z} \tag{3.53}$$

$$\rho_i^{k+1} = \rho_i^k + \frac{\delta t}{\delta x}\left(G^k_{i-1/2} - G^k_{i+1/2}\right),\ i \in \mathbb{Z},\ k \in \mathbb{Z},\ k \geq 0 \tag{3.54}$$

$$G^k_{i+1/2} = \frac{w^k_{i+1/2} + \left|w^k_{i+1/2}\right|}{2}\rho_i^k + \frac{w^k_{i+1/2} - \left|w^k_{i+1/2}\right|}{2}\rho^k_{i+1},\ i \in \mathbb{Z},\ k \in \mathbb{Z},\ k \geq 0 \tag{3.55}$$

$$G^k_{i-1/2} = \frac{w^k_{i-1/2} + \left|w^k_{i-1/2}\right|}{2}\rho^k_{i-1} + \frac{w^k_{i-1/2} - \left|w^k_{i-1/2}\right|}{2}\rho^k_i,\ i \in \mathbb{Z},\ k \in \mathbb{Z},\ k \geq 0 \tag{3.56}$$

$$G_i^k = \frac{1}{2}\left(G^k_{i-1/2} + G^k_{i+1/2}\right),\ i \in \mathbb{Z},\ k \in \mathbb{Z},\ k \geq 0 \tag{3.57}$$

$$\rho^{k+1}_{i+1/2} = \frac{1}{2}\left(\rho_i^{k+1} + \rho^{k+1}_{i+1}\right),\ i \in \mathbb{Z},\ k \in \mathbb{Z},\ k \geq 0 \tag{3.58}$$

$$\hat{\beta}_i^k = \beta(\hat{w}_i^k) = \begin{cases} \beta(w^k_{i-1/2}), G_i^k \geq 0 \\ \beta(w^k_{i+1/2}), G_i^k < 0 \end{cases},\ i \in \mathbb{Z},\ k \in \mathbb{Z},\ k \geq 0 \tag{3.59}$$

$$\beta^k_{i+1/2} = \beta\left(w^k_{i+1/2}\right),\ i \in \mathbb{Z},\ k \in \mathbb{Z},\ k \geq 0 \tag{3.60}$$

$$\beta_{i+1/2}^{k+1} = \beta\left(w_{i+1/2}^{k+1}\right), \; i \in \mathbb{Z}, \; k \in \mathbb{Z}, \; k \geq 0 \tag{3.61}$$

$$\begin{aligned}\rho_{i+1/2}^{k+1}\beta_{i+1/2}^{k+1} &= \tfrac{1}{1+\sigma\delta t}\left(\tfrac{\rho_i^k+\rho_{i+1}^k}{2}\beta_{i+1/2}^k + \tfrac{\delta t}{\delta x}\left(P(\rho_i^{k+1}) - P(\rho_{i+1}^{k+1}) + G_i^k\hat{\beta}_i^k - G_{i+1}^k\hat{\beta}_{i+1}^k\right)\right.\\ &+\left.\tfrac{\delta t}{\delta x}\left(\rho_{i+1}^{k+1}\kappa(\rho_{i+1}^{k+1})\tfrac{w_{i+3/2}^k-w_{i+1/2}^k}{\delta x} \; -\rho_i^{k+1}\kappa(\rho_i^{k+1})\tfrac{w_{i+1/2}^k-w_{i-1/2}^k}{\delta x}\right)\right), \; i \in \mathbb{Z}, \; k \in \mathbb{Z}, \; k \geq 0\end{aligned} \tag{3.62}$$

with δt, $\delta x > 0$ being the time-step and spatial discretization step and the functions $\beta(w)$, $P(\rho)$ being given by (2.22), (3.20), respectively. Moreover, ρ_i^k , $\rho_{i+1/2}^k$, w_i^k, $w_{i+1/2}^k$ are the numerical values at the points $x_i = i\delta x$, $x_{i+1/2} = (i+1/2)\delta x$ and at time $t_k = k\delta t$ while ρ_i^{k+1}, $\rho_{i+1/2}^{k+1}$, w_i^{k+1}, $w_{i+1/2}^{k+1}$ are the numerical values at the points $x_i = i\delta x$, $x_{i+1/2} = (i+1/2)\delta x$, and at time $t_{k+1} = (k+1)\delta t$.

The next numerical method used, is the so-called "method of lines" (see Guo and Zhu (2010), Nishida (1986)). In this method, the states (density and mean speed) are approximated at fixed grid points in Lagrangian coordinates. Therefore, in order to use this numerical method, it is required to transform equations (3.1), (3.2) into Lagrangian coordinates by making the following transformation (see also Guo and Zhu (2010)):

$$s = \int_{\tilde{l}(\tau)}^{\xi} \tilde{\rho}(\tau, z)dz, \; h = \tau. \tag{3.63}$$

Thus, in the Lagrangian coordinates, equations (3.1), (3.2) become

$$\tilde{\rho}_h + \tilde{\rho}^2\tilde{v}_s = 0 \tag{3.64}$$

$$(\tilde{\beta}(\tilde{v}))_h + (\tilde{P}(\tilde{\rho}))_s = (\tilde{\rho}^2\tilde{\kappa}(\tilde{\rho})\tilde{v}_s)_s - \tilde{\sigma}\tilde{\beta}(\tilde{v}) \tag{3.65}$$

for all $h > 0$ and $0 < s < \tilde{m}$ where $\tilde{m} = \int_{\tilde{l}(\tau)}^{\tilde{L}(\tau)} \tilde{\rho}(\tau, z)dz$, $\tilde{P}(\tilde{\rho}) = \tilde{\sigma}\int_{\tilde{\rho}}^{\tilde{\rho}} \tilde{\kappa}(\tau)d\tau$ for all $\tilde{\rho} \in (0, \rho_{\max})$ and $\tilde{\beta}(\tilde{v})$ defined by (1.21). Model (3.64), (3.65) is studied under the following boundary conditions:

$$\tilde{\rho}(h,0) = \tilde{\rho}(h,\tilde{m}) = 0. \tag{3.66}$$

The "method of lines" is applied by discretizing the spatial derivatives of model (3.64), (3.65) with respect to s and leaving the time variable continuous. Therefore, the following system of $2n$ ordinary differential equations is obtained:

$$\frac{d}{dh}\tilde{\rho}_{2i}(h) + \{\tilde{\rho}_{2i}(h)\}^2\frac{\tilde{v}_{2i+1}(h) - \tilde{v}_{2i-1}(h)}{\delta s} = 0 \tag{3.67}$$

$$\begin{aligned}\tfrac{d}{dh}\tilde{\beta}(\tilde{v}_{2i}(h)) + \tfrac{\tilde{P}(\tilde{\rho}_{2i}(h))-\tilde{P}(\tilde{\rho}_{2i-2}(h))}{\delta s} &= \tfrac{1}{(\delta s)^2}\{G_{2i}(h)(\tilde{v}_{2i+1}(h) - \tilde{v}_{2i-1}(h))\\ -G_{2i-2}(h)(\tilde{v}_{2i-1}(h) - \tilde{v}_{2i-3}(h))\} - \tilde{\sigma}\tilde{\beta}(\tilde{v}_{2i-1}(h))\end{aligned} \tag{3.68}$$

with boundary conditions

$$\tilde{\rho}_0(h) = \tilde{\rho}_{2n}(h) = 0 \tag{3.69}$$

and initial data

$$\tilde{\rho}_{2i}(0) = \tilde{\rho}_0\left(2i\frac{\delta s}{2}\right), \tilde{v}_{2i-1}(0) = \tilde{v}_0\left((2i-1)\frac{\delta s}{2}\right) \tag{3.70}$$

where $i = 1, 2, ..., n$, $G_{2i}(h) = \tilde{\rho}_{2i}^2(h)\tilde{\kappa}(\tilde{\rho}_{2i}(h))$, $\tilde{v}_{-1}(h) = \tilde{v}_{2n+1}(h) = v^*$ and $\delta s = \frac{\tilde{m}}{n}$ for a given number n of grid-points.

3.5 Numerical experiments

3.5.1 Academic example

In this example, the particle method (3.27)-(3.32) is applied, and the equations (3.43)-(3.49) are used to approximate the solutions of model (3.7)-(3.10). Moreover, the numerical solutions obtained by applying the proposed particle method are compared with the numerical solutions of the modified numerical methods presented in Section 3.4. Finally, a comparison with the numerical approximations provided for the solutions of the reduced model (3.14) is included, indicating the effectiveness of the employed particle method as well as the high-accuracy approximations of the reduced model.

In order to approximate the solutions of the ODE systems (3.27)-(3.32) and (3.67)-(3.70) involved in the particle method and the method of lines, respectively, an adaptive step size numerical scheme is used (see Hairer et al. (1993), pages 167-169) consisting of the explicit Euler and Heun schemes. For these schemes, the new step size is given by the formula:

$$\delta t_{new} = \delta t \min\left\{p, 0.9\sqrt{\frac{1}{err}}\right\} \tag{3.71}$$

where

$$err = \sqrt{\frac{1}{2n}\sum_{i=1}^{n}\left(\frac{x_{i,Euler}-x_{i,Heun}}{sc_{x,i}}\right)^2 + \frac{1}{2n}\sum_{i=1}^{n}\left(\frac{y_{i,Euler}-y_{i,Heun}}{sc_{y,i}}\right)^2} \tag{3.72}$$

and

$$sc_{x,i} = Atol + Rtol\max\left\{|x_i|, |x_{i,Heun}|\right\}, i = 1, ..., n \tag{3.73}$$

$$sc_{y,i} = Atol + Rtol\max\left\{|y_i|, |y_{i,Heun}|\right\}, i = 1, ..., n \tag{3.74}$$

for a given number n of state variables.

The constant $Atol > 0$ denotes the tolerance for absolute errors, $Rtol > 0$ is the tolerance for relative errors, and $p \geq 1$ is a constant factor which determines the magnitude of a possible increase of the step size. In addition, $x_{i,Euler}$, $y_{i,Euler}$ and $x_{i,Heun}$, $y_{i,Heun}$, $i = 1, ..., n$ are the components of the solution by the respective schemes, where $(x_i, y_i) = (x_i, w_i)$, $i = 1, ..., n$ for the ODE system (3.27)-(3.32) and $(x_i, y_i) = (\tilde{\rho}_{2i}, \tilde{v}_{2i})$, $i = 1, ..., n$ for the ODE system (3.67)-(3.70). For the particle method, (3.27)-(3.32) the aforementioned adaptive numerical method with $A_{tol} = R_{tol} = 10^{-4}$, $p = 2$, and the parameters of Table 3.3 are used.

	n	b	R	σ	a
Particle method (3.27)-(3.32)	225	0.0606	1.9	30	0.4653

Table 3.3: Parameters of the Particle Method (3.27)-(3.32).

The functions $\Phi'(s)$ and $K(s)$ are obtained by using (3.33), (3.37) and the function

$$\kappa(\rho) = \begin{cases} 0, 0 < \rho \leq 1 \\ \frac{(\rho-1)^2}{\rho(R-\rho)}, 1 < \rho < R \end{cases} \tag{3.75}$$

for the state-dependent viscosity term in (3.7)-(3.10). Finally, the approximations of the solutions of (3.7)-(3.10) are obtained by using the equations (3.43)-(3.49) and the initial condition:

$$\begin{aligned} \rho[0] &= \begin{cases} 0.25\,(x-l(0))^2\,(x-L(0))^2\,,\; l(0) < x < L(0) \\ 0,\; otherwise \end{cases} \\ w[0] &= \begin{cases} -0.158\,(x-0.5)^2\,(x-1.5)^2\,,\; 0.5 < x < 1.5 \\ 0,\; x \in (l(0), 0.5] \cup [1.5, L(0)) \end{cases} \end{aligned} \tag{3.76}$$

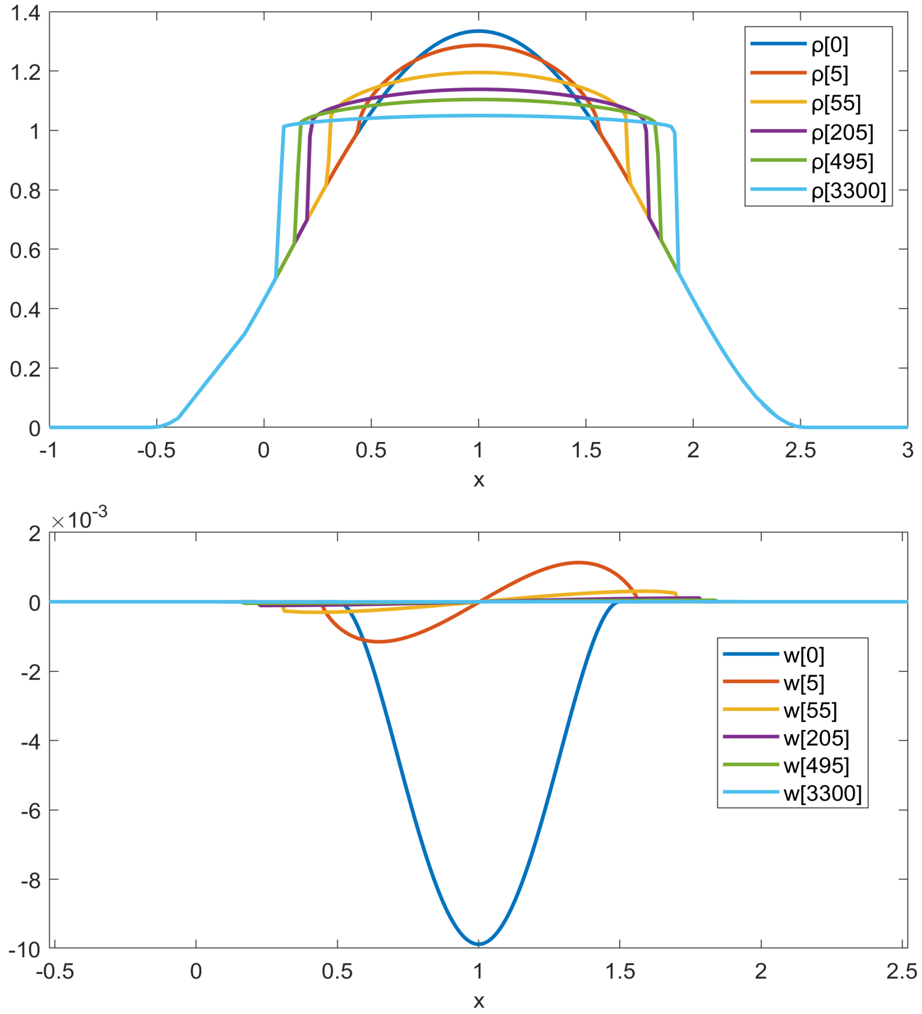

Figure 3.1: Solution profiles of model (3.7)-(3.10) produced by applying the particle method (3.27)-(3.32).

	n	δt	δx	σ
Numerical method 1 (NM1) (3.51)-(3.62)	225	0.0033	0.0178	30

Table 3.4: Parameters of the numerical method (3.51)-(3.62) (NM1).

where $l(0) = -0.52$ and $L(0) = 2.52$.

Figure 3.1, shows the solution profiles and their convergence to an equilibrium point (ρ, w) with $0 \leq \rho(x) \leq 1$ and $w(x) = 0$ for all $x \in (l(t), L(t))$ as time increases. Figure 3.2 and Figure 3.3 illustrate the time evolution of the discretized functionals defined by (3.38), (3.39). Notice that both functionals E_n, W_n are not increasing, showing that the differential inequalities (3.41), (3.42) are preserved.

Next, the numerical solutions produced by applying the proposed particle method are compared with those of the numerical method (3.51)-(3.62) (NM1) and the method of lines (3.67)-(3.70) (NM2). For the numerical method (3.51)-(3.62) (NM1), the parameters of Table 3.4 are used.

To compare the solutions of the particle method with the solutions of the method of lines (3.67)-(3.70) (NM2), the solution of (3.67)-(3.70) is transformed from Lagrangian to Eulerian coordinates and its physical dimensions are removed through the variable transformation

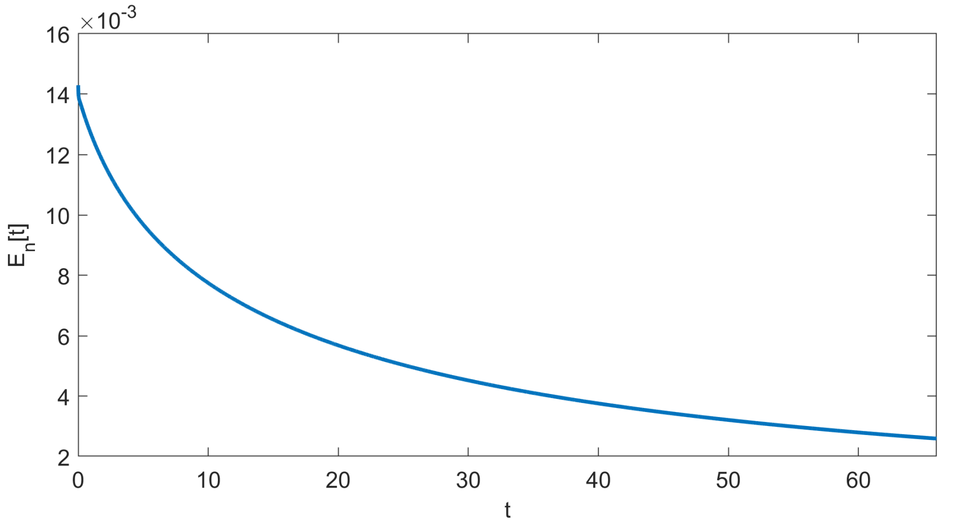

Figure 3.2: Time-evolution of the discretized functional E_n defined by (3.38) obtained by using the particle method (3.27)-(3.32).

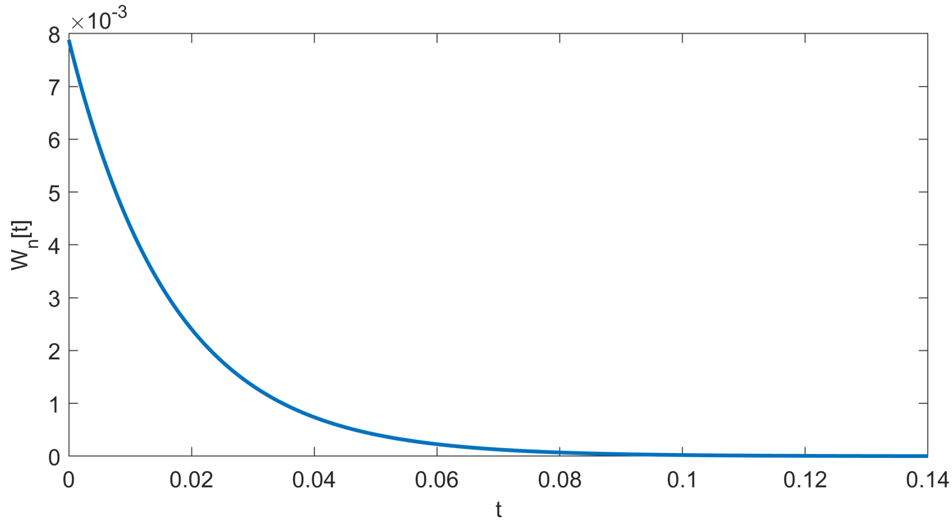

Figure 3.3: Time-evolution of the discretized functional W_n defined by (3.39) obtained by using the particle method (3.27)-(3.32).

	n	$\tilde{\sigma}$	δs	v^*	r	$\bar{\rho}$	$\rho_{\max}$	$v_{\max}$
Numerical Method 2 (NM2) (Method of lines) (3.67)-(3.70)	225	990	1.3665	33	1	63.1579	120	35

Table 3.5: Parameters of the numerical method (3.67)-(3.70) (NM2).

$\xi = rx + v^*\tau$ and the dimensionless quantities $\tau = \frac{r}{v^*}t$, $b = \frac{v_{\max}-v^*}{v^*}$, $R = \frac{\rho_{\max}}{\bar{\rho}} > 1$, $w = \frac{\tilde{v}-v^*}{v^*}$, $\rho = \frac{\tilde{\rho}}{\bar{\rho}}$, $\sigma = \frac{r}{v^*}\tilde{\sigma}$, where the values of $\tilde{\sigma}$, v^*, r , $\bar{\rho}$, $\rho_{\max}$, $v_{\max}$ are given in Table 3.5. Note that the transformation was made by integrating the differential equation $\dot{\xi}_i = \tilde{v}_{2i}$, $i = 1, ..., n$, using the trapezoidal rule.

To obtain the numerical solution of (3.67)-(3.70), the aforementioned adaptive step size scheme with $A_{tol} = R_{tol} = 10^{-4}$, $p = 2$, is used again. Note also that the expressions of the functions $\tilde{\beta}(\tilde{v})$, $\tilde{P}(\tilde{\rho})$, $\tilde{\kappa}(\tilde{\rho})$ used in the ODE system (3.67)-(3.70) can be found by using

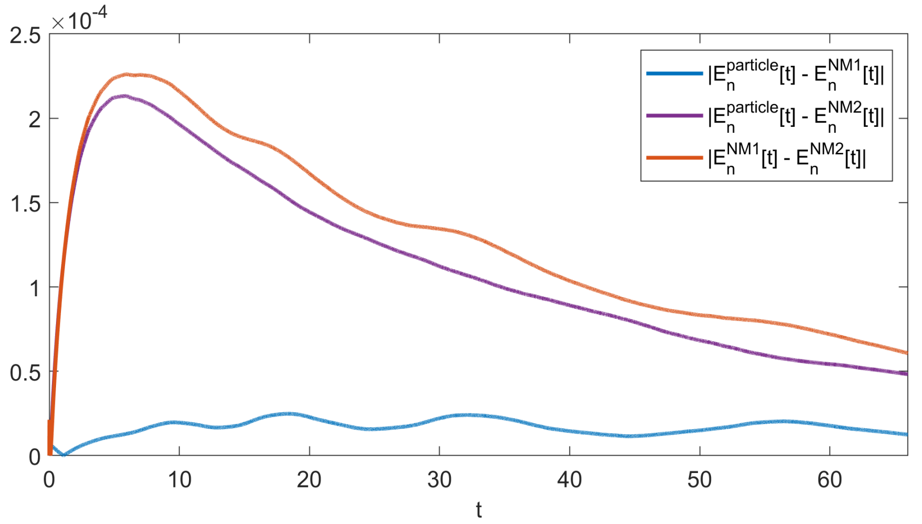

Figure 3.4: Time-evolution of the quantities $\left|E_n^{particle}[t]-E_n^{NM1}[t]\right|$, $\left|E_n^{particle}[t]-E_n^{NM2}[t]\right|$, and $\left|E_n^{NM1}[t]-E_n^{NM2}[t]\right|$.

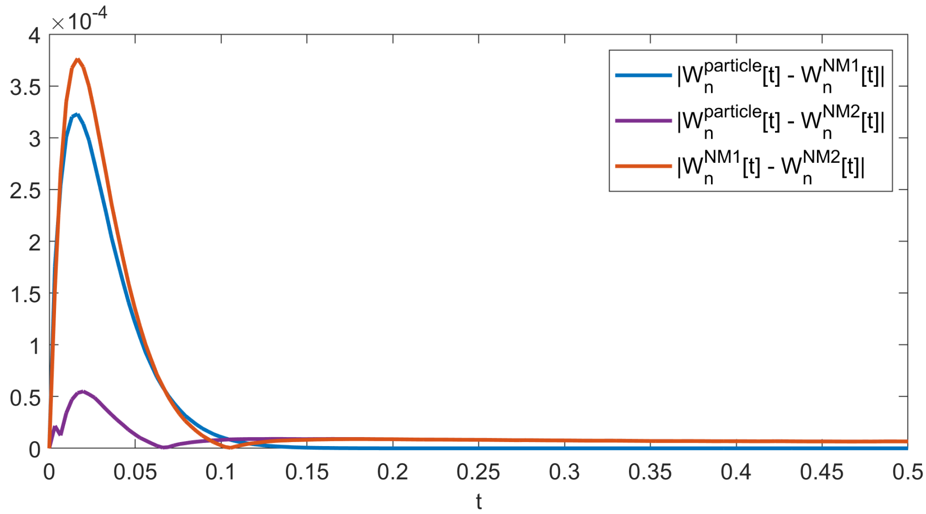

Figure 3.5: Time-evolution of the quantities $\left|W_n^{particle}[t]-W_n^{NM1}[t]\right|$, $\left|W_n^{particle}[t]-W_n^{NM2}[t]\right|$, $\left|W_n^{NM1}[t]-W_n^{NM2}[t]\right|$.

the function $\tilde{P}(\tilde{\rho}) = \tilde{\sigma}\int_{\bar{\rho}}^{\tilde{\rho}}\tilde{\kappa}(\tau)d\tau$, for all $\tilde{\rho}\in(0,\rho_{\max})$, the definitions (3.75), (2.22) and the relations of Table 3.1.

Figures 3.4 and 3.5 illustrate the small difference between the discretized functionals $E_n[t]$, $W_n[t]$ obtained by applying the proposed particle method (3.27)-(3.32) and the numerical methods (3.51)-(3.62) (NM1), (3.67)-(3.70) (NM2). Moreover, the sup-norms of the difference between the numerical solutions for the states ρ, w are depicted in Figures 3.6, 3.7. It is obvious that as time increases, and the solution converges to the equilibrium point where $0 \le \rho(x) \le 1$, $w(x) = 0$, the difference between the numerical solutions becomes even smaller.

Notice that (3.42) along with (3.39) imply the differential equation $\dot{W}_n(t) = -2\sigma W_n(t)$ with analytical solution $W_n(t) = W_n(0)\exp(-2\sigma t)$. Figure 3.8 shows that the discretized energy functional W_n obtained by using the particle method is closer to the analytical solution of the differential equation $\dot{W}_n(t) = -2\sigma W_n(t)$. Indeed, by plotting the time evolution

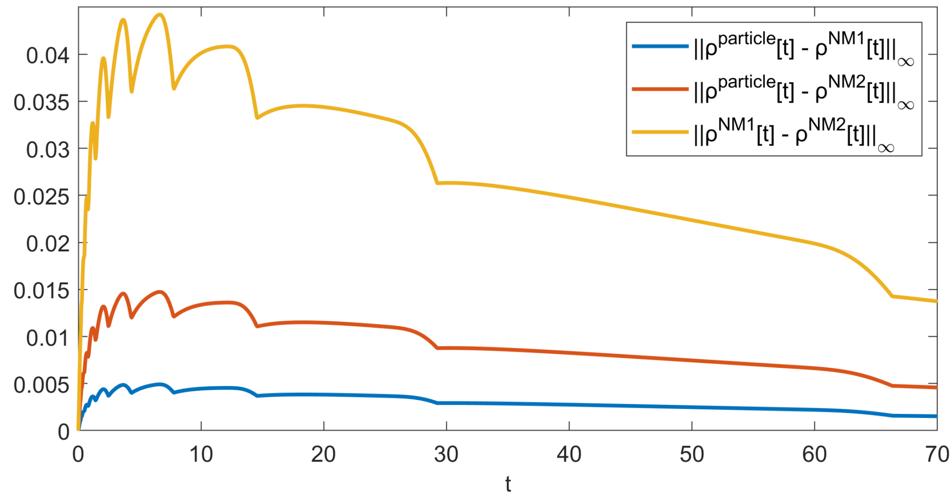

Figure 3.6: Time-evolution of the quantities $\left\|\rho^{particle}[t]-\rho^{NM1}[t]\right\|_{\infty}$, $\left\|\rho^{particle}[t]-\rho^{NM2}[t]\right\|_{\infty}$, and $\left\|\rho^{NM1}[t]-\rho^{NM2}[t]\right\|_{\infty}$.

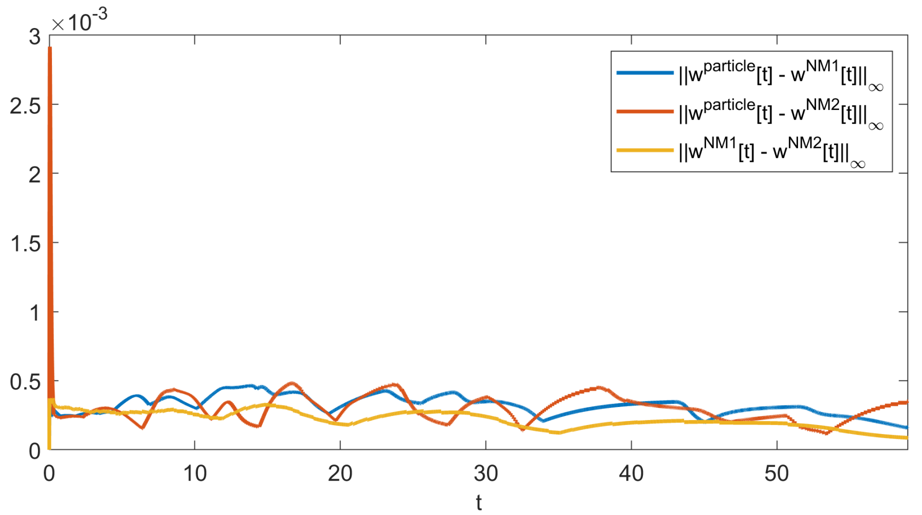

Figure 3.7: Time-evolution of the quantities $\left\|w^{particle}[t]-w^{NM1}[t]\right\|_{\infty}$, $\left\|w^{particle}[t]-w^{NM2}[t]\right\|_{\infty}$, and $\left\|w^{NM1}[t]-w^{NM2}[t]\right\|_{\infty}$.

of $\ln(W_n(t)/W_n(0))$ in Figure 3.9, it is shown that when the values of W_n become very small, the discretized functional W_n produced by applying the particle method (3.27)-(3.32) remains closer to the analytical solution $W_n(t) = W_n(0)\exp(-2\sigma t)$ compared to the discretized functionals of the numerical methods (3.51)-(3.62) (NM1), (3.67)-(3.70) (NM2), which diverge. This fact implies that the differential inequality (3.26) is better preserved by the particle method. Note also that a better approximation of the solution can be achieved with the particle method by using smaller values for the tolerances *Atol*, *Rtol*.

However, the number of particles used, affects significantly the performance of the particle method with respect to the energy conservation. As shown in Figure 3.10, the differential inequality (3.26), which indicates energy conservation, is better preserved with an increased number of particles. More specifically, Figure 3.10 shows that for $n = 225$ particles, the discretized energy functional W_n, produced by the particle method, almost coincides with the analytical solution of the differential equation $\dot{W}_n(t) = -2\sigma W_n(t)$ compared to the discretized energy functionals produced with smaller number of particles.

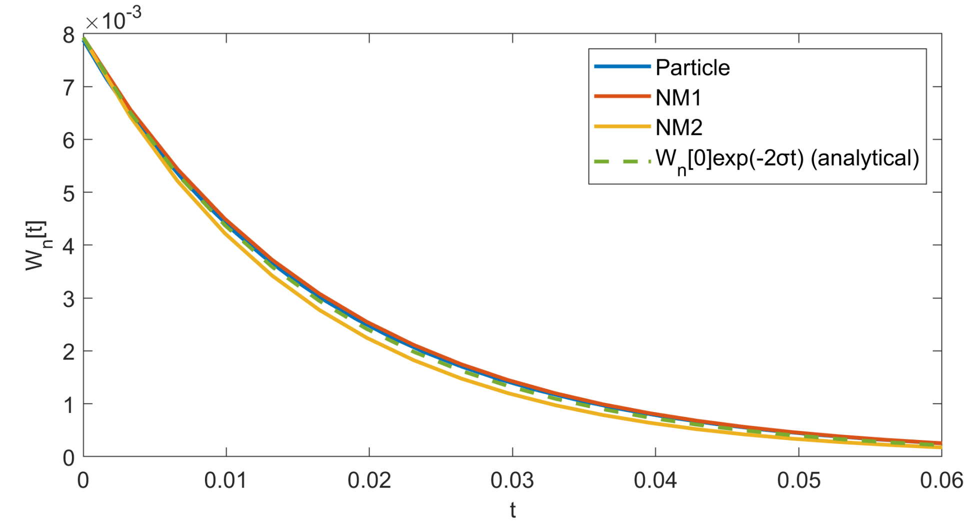

Figure 3.8: Time-evolution of $W_n^{particle}[t]$, $W_n^{NM1}[t]$, and $W_n^{NM2}[t]$.

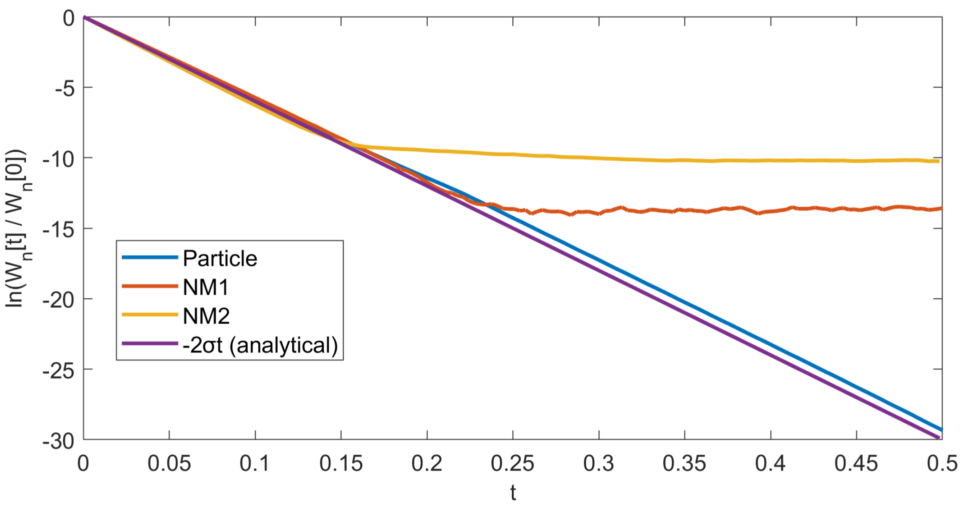

Figure 3.9: Time-evolution of the quantities $\ln(W_n^{particle}[t]/W_n[0])$, $\ln(W_n^{NM1}[t]/W_n[0])$, and $\ln(W_n^{NM2}[t]/W_n[0])$.

In addition, the computational cost for each numerical method is compared by means of CPU time needed. Table 3.6 shows the corresponding results for the overall simulation time $t_{\max}$ of 33 time units, demonstrating that the CPU time needed for the proposed particle method is significantly less than the corresponding CPU times of the numerical methods (3.51)-(3.62) (NM1), (3.67)-(3.70) (NM2). It should be mentioned, that even in the case of smaller tolerances $(A_{tol} = R_{tol} = 10^{-8})$ for the particle method, its execution time was no more than 20 seconds. On the other hand, NM2 failed to give a result even after 2h. The simulations were performed on Matlab R2021a and a laptop with Intel(R) Core(TM) i7-7700HQ CPU 2.80GHz.

Finally, the numerical solution of model (3.7)-(3.10) produced by applying the particle method (3.27)-(3.32) is compared with the numerical solutions of the reduced model (3.15) obtained by using the numerical scheme (2.56)-(2.58) proposed in Theodosis et al. (2024) with time-step $\delta t = 0.0033$ and spatial discretization step $\delta x = 0.0178$. Figure 3.11 and Figure 3.12 show that the selection of the constant σ plays an important role in the deviation between the numerical solutions of the two models.

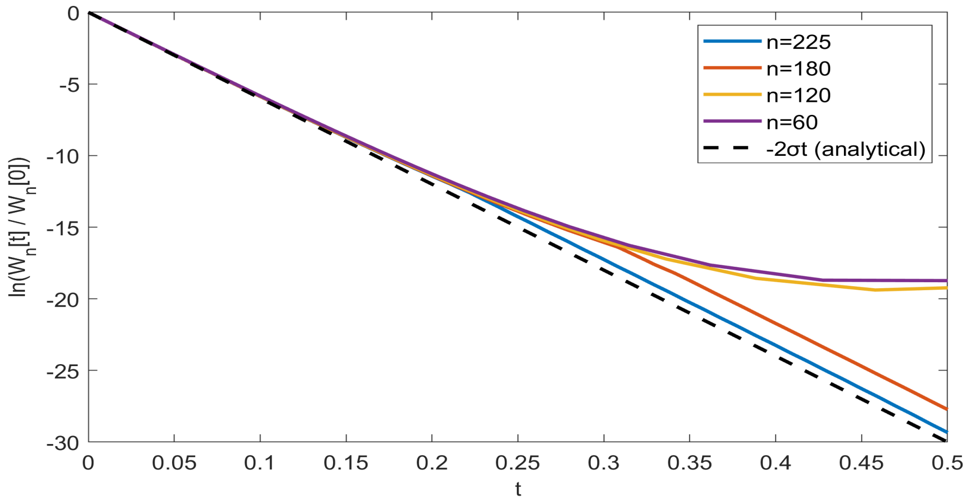

Figure 3.10: Time-evolution of $\ln(W_n^{particle}[t]/W_n[0])$, for $n = 225$, $n = 180$, $n = 120$, and $n = 60$ particles.

Numerical Method	**CPU time (sec)**
Particle Method (3.27)-(3.32)	18.65
NM1: (3.51)-(3.62)	274.52
NM2: (3.67)-(3.70)	171.97

Table 3.6: CPU times needed for the proposed particle method (3.27)-(3.32) and the numerical methods (3.51)-(3.62), (3.67)-(3.70) with $t_{\max} = 33$ time units.

As the value of constant σ increases, the convergence of the solution of model (3.7)-(3.10) to the solution of the reduced model becomes faster and therefore the difference between the numerical solutions is faster suppressed. Figure 3.13 illustrates the small difference between the numerical solution of model (3.7)-(3.10) and the numerical solution of the reduced model (3.15). Although a different initial condition $w[0]$ is given for each model, it is

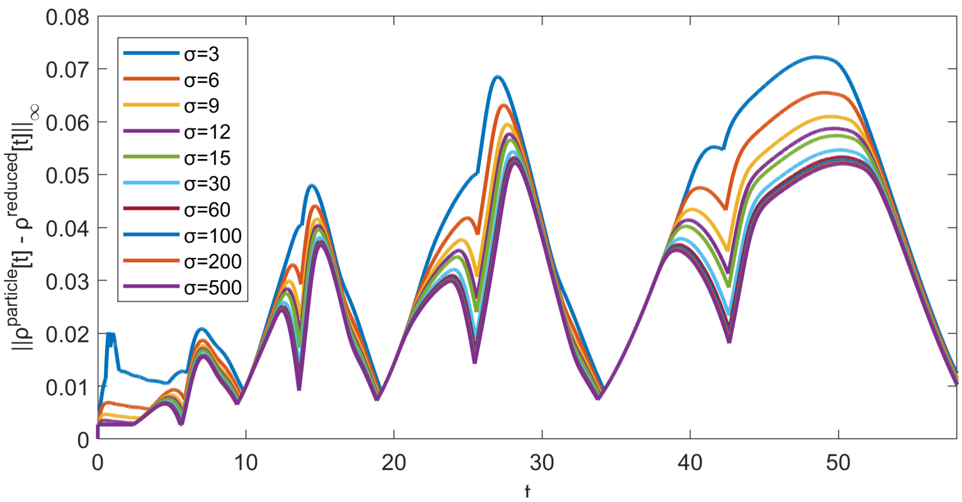

Figure 3.11: Time-evolution of $\left\|\rho^{particle}[t] - \rho^{reduced}[t]\right\|_\infty$ for a range of σ values.

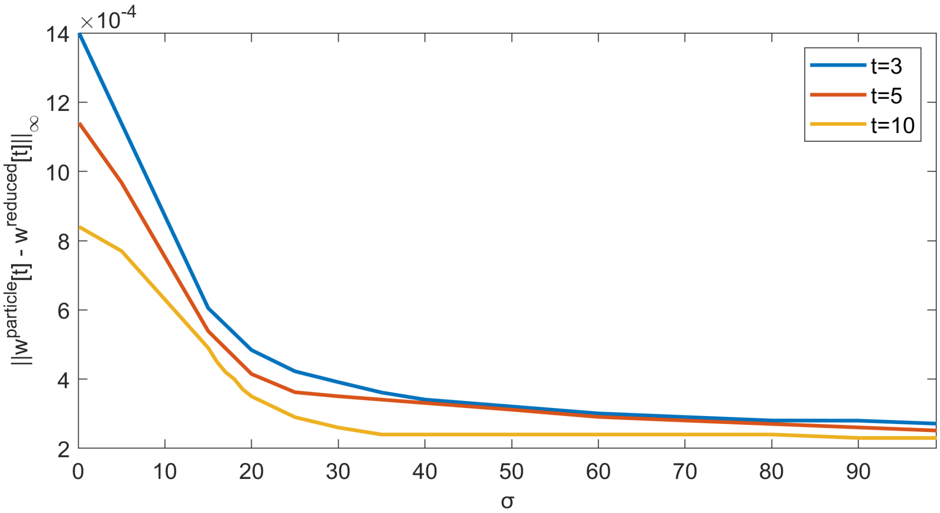

Figure 3.12: Profiles of $\left\|w^{particle}[t] - w^{reduced}[t]\right\|_{\infty}$ for a range of σ values.

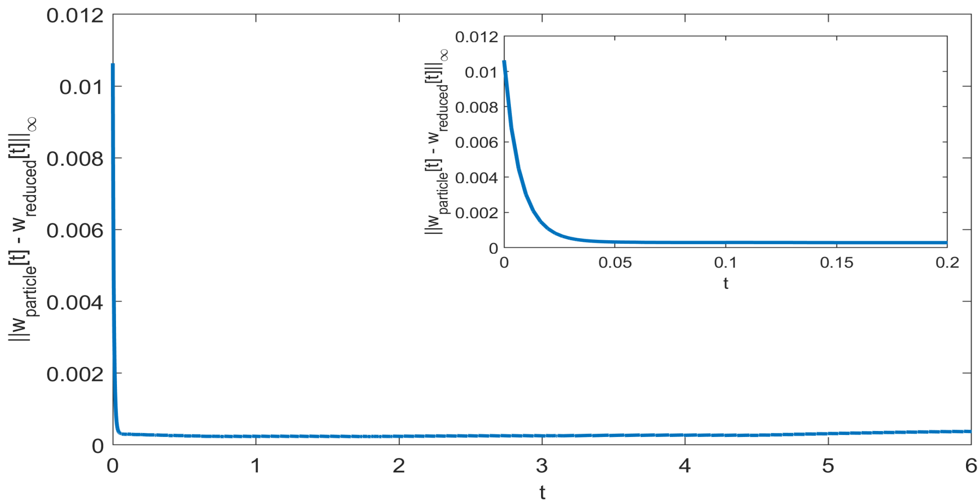

Figure 3.13: Time evolution of $\left\|w^{particle}[t] - w^{reduced}[t]\right\|_{\infty}$.

obvious that the sup-norm of the difference between the numerical solutions becomes small very fast, indicating the high accuracy provided by the reduced model.

3.5.2 A realistic traffic scenario and comparison with the ARZ

In this section, a traffic scenario is considered to compare the density, mean speed, acceleration, and flow of the macro-PRCC (3.1)-(3.4) with a well-known second-order macroscopic traffic flow model for human drivers, the so-called ARZ model (see Aw and Rascle (2000), Zhang (2002)). For this scenario, the numerical solutions produced by applying the particle method (3.27)-(3.32) are also compared with the numerical solutions of (3.51)-(3.62) (NM1), (3.67)-(3.70) (NM2) and the numerical solutions of the reduced model (3.6). Note that this example is an analogue of the traffic application presented in Section 2.5.2, where the reduced model (3.6) was compared with a first-order traffic flow model for human drivers, the so-called LWR model (see Lighthill and Whitham (1955), Richards (1956)). Using the Riemann coordinate $s = \tilde{v} - F(\tilde{\rho})$ (see (1.4), (1.5)), the ARZ model (1.1), (1.3) with $\tilde{\sigma} = \frac{1}{\delta}$, $\delta > 0$, can be written in the following form:

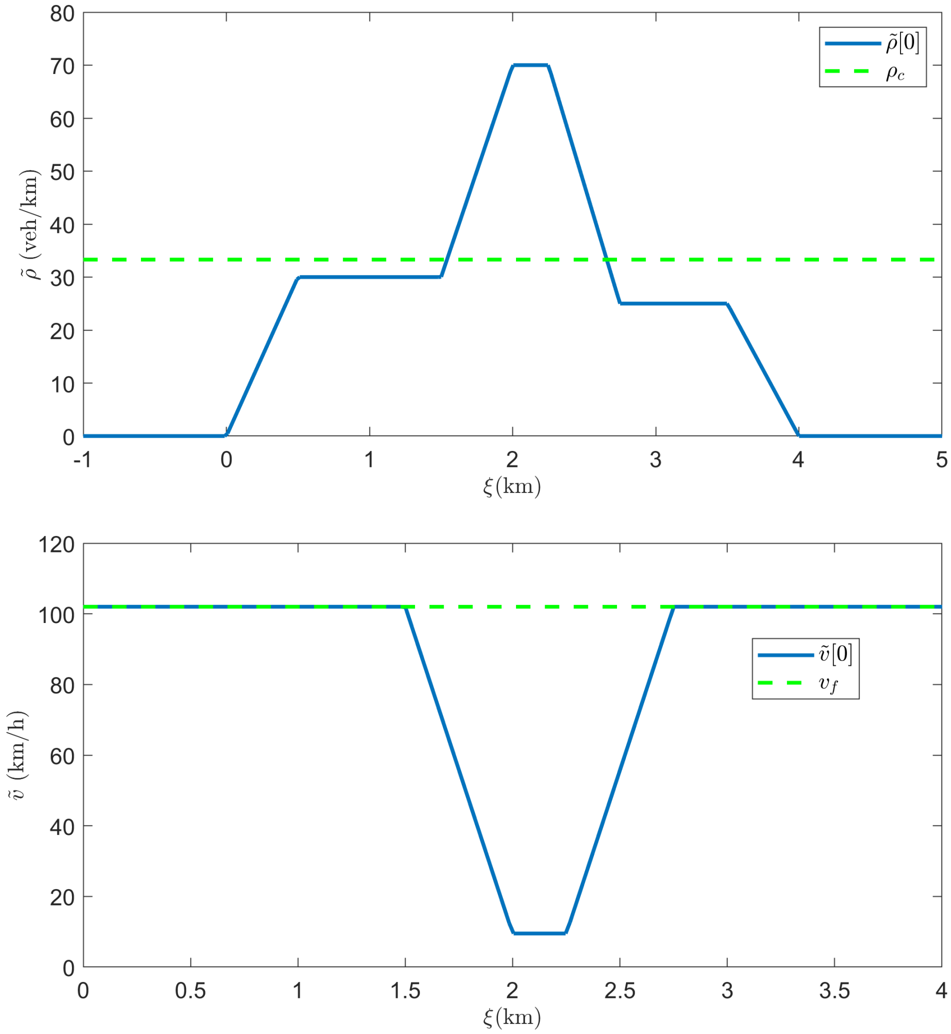

Figure 3.14: Initial density $\tilde{\rho}_0(\xi)$ (top) and speed $\tilde{v}_0(\xi)$ (bottom).

$$\tilde{\rho}_\tau + (y + \tilde{\rho}F(\tilde{\rho}))_\xi = 0 \tag{3.77}$$

$$y_\tau + (y^2/\tilde{\rho} + yF(\tilde{\rho}))_\xi = -\frac{y}{\delta} \tag{3.78}$$

where $y = \tilde{\rho}s$ and $F(\tilde{\rho})$ is the equilibrium speed profile given by the expression:

$$F(\tilde{\rho}) = v_f \exp\left(-\frac{1}{d}\left(\frac{\tilde{\rho}}{\rho_c}\right)^d\right). \tag{3.79}$$

Note that d is a positive constant, ρ_c is the critical density, v_f is the free-flow speed and δ is the relaxation time. In this scenario, a single-lane motorway is considered with $v_f = 102$ (km/h), $\rho_{\max} = 180$ (veh/km), $d = 2.34$ and $\rho_c = 33.3$ (veh/km) that were estimated in Kotsialos et al. (2002) based on real data from a part of the Amsterdam A10 motorway. The initial condition used for this scenario is illustrated in Figure 3.14. Notice that the initial density on the road is characterized by a congestion belt in the interval $[1.5, 2.75]$ (km) with $\tilde{\rho}_0(\xi) = 0$ for $\xi \leq \tilde{l}(0) = 0$ and $\xi \geq \tilde{L}(0) = 4$. Moreover, the density has been selected to be lower than the critical density ρ_c outside the congested area. For the macro-PRCC (3.1)-(3.4), the particle method (3.27)-(3.32) is applied by using the adaptive step size numerical scheme discussed in Section 3.5.1 with $p = 2$ and tolerances $Atol = Rtol = 10^{-5}$. The following function is also used:

$$\kappa(\rho) = c\begin{cases} 0, 0 < \rho \leq 1 \\ \frac{(\rho-1)^2}{\rho(R-\rho)}, 1 < \rho < R \end{cases} \tag{3.80}$$

where $c > 0$ is a constant that is used to increase or decrease the viscosity. For the comparison with the ARZ, the value $c = 40$ is used. Note that the functions $K(s), \Phi'(s)$ are given by means of (3.80) and (3.33), (3.37), while the expressions of the functions $\tilde{\beta}(\tilde{v})$, $\tilde{\kappa}(\tilde{\rho})$ involved in the macro-PRCC (3.1)-(3.4) can be found by using (3.80), (2.22) and the relations of Table 3.1. Moreover, the parameters $v^* = 102\ (km/h)$ (equal to the free-flow speed v_f), $\bar{\rho} = 31\ (veh/km)$, $r = 1\ (km)$, $\tilde{\sigma} = 3060\ (1/h)$ are used, and recall that the quantities R, b, and σ are given by $R = \frac{\rho_{\max}}{\bar{\rho}} > 1$, $b = \frac{v_{\max}-v^*}{v^*}$, and $\sigma = \frac{r}{v^*}\tilde{\sigma}$, respectively.

To approximate the solutions of the ARZ model (3.77)-(3.79), a second-order central scheme for balance laws described in Liotta et al. (2000) is used, which is the extension of the Nessyahu-Tadmor scheme for conservation laws proposed in Nessyahu and Tadmor (1990). By expressing the ARZ model (3.77)-(3.79) in the following conservative form:

$$U_\tau + (f(U))_\xi = R(U) \tag{3.81}$$

where $U = \begin{bmatrix} \tilde{\rho} \\ y \end{bmatrix}$, $f(U) = \begin{bmatrix} y + \tilde{\rho}F(\tilde{\rho}) \\ y^2/\tilde{\rho} + yF(\tilde{\rho}) \end{bmatrix}$, and $R(U) = \begin{bmatrix} 0 \\ -y/\delta \end{bmatrix}$, the scheme reads as follows:

$$\begin{aligned} U_{i+1/2}^{k+1} = &\frac{1}{2}(U_i^k + U_{i+1}^k) + \frac{1}{8}(U_i' - U_{i+1}') - \frac{\delta\tau}{\delta\xi}(f(U_{i+1}^{k+1/2}) - f(U_i^{k+1/2})) \\ &+\delta\tau\left(\frac{3}{8}R(U_i^{k+1/3}) + \frac{3}{8}R(U_{i+1}^{k+1/3}) + \frac{1}{4}R(U_{i+1/2}^{k+1})\right) \end{aligned} \tag{3.82}$$

where

$$U_i' = \min\operatorname{mod}(U_{i+1}^k - U_i^k, U_i^k - U_{i-1}^k) \tag{3.83}$$

$$U_i^{k+1/2} = U_i^k + \frac{\delta\tau}{2}\left(R(U_i^{k+1/2}) - \frac{f_i'}{\delta\xi}\right) \tag{3.84}$$

$$U_i^{k+1/3} = U_i^k + \frac{\delta\tau}{3}\left(R(U_i^{k+1/3}) - \frac{f_i'}{\delta\xi}\right) \tag{3.85}$$

$$f_i' = \min\operatorname{mod}(f(U_{i+1}^k) - f(U_i^k), f(U_i^k) - f(U_{i-1}^k)) \tag{3.86}$$

and

$$\min\operatorname{mod}(x,y) = \begin{cases} sgn(x)\min(|x|,|y|), & if\ \ sgn(x) = sgn(y) \\ 0, & otherwise \end{cases} \tag{3.87}$$

with $\delta\tau$, $\delta\xi > 0$ being the time-step and the spatial discretization step. Moreover, U_i^k, $U_{i+1/2}^{k+1}$ are the numerical values at the points $\xi_i = i\delta\xi$, $\xi_{i+1/2} = (i+1/2)\delta\xi$ and at times $t_k = k\delta\tau$, $t_{k+1} = (k+1)\delta\tau$, while $U_i^{k+1/2}$, $U_i^{k+1/3}$ are the numerical values at the point $\xi_i = i\delta\xi$ and at times $t_{k+1/2} = (k+1/2)\delta\tau$, $t_{k+1/3} = (k+1/3)\delta\tau$, respectively.

By selecting $\delta = 20\,(s)$, $\delta\xi = 0.04$, $\delta\tau = 10^{-6}$ for the numerical scheme (3.82)-(3.87) and $a = 0.2411$, $n = 226$ particles/vehicles on the interval $(\tilde{l}(0), \tilde{L}(0))\ (km)$ for the particle method, the density and speed profiles illustrated in Figure 3.15 and Figure 3.16 are obtained. Figure 3.15 shows that the dissipation of density is much stronger for the ARZ model while the density is spread over a large road interval for increasing $\tau > 0$. More specifically, for $\tau = 1\,(h)$, the density is non-zero over the interval $(90, 106)\ (km)$, which implies that the vehicles retain large inter-vehicle distances. Notice also that the density for the macro-PRCC model converges towards an equilibrium where $\tilde{v}(\xi) = v^*$, $\tilde{\rho}(\xi) \leq \bar{\rho} < \rho_{cr}$ and the travel

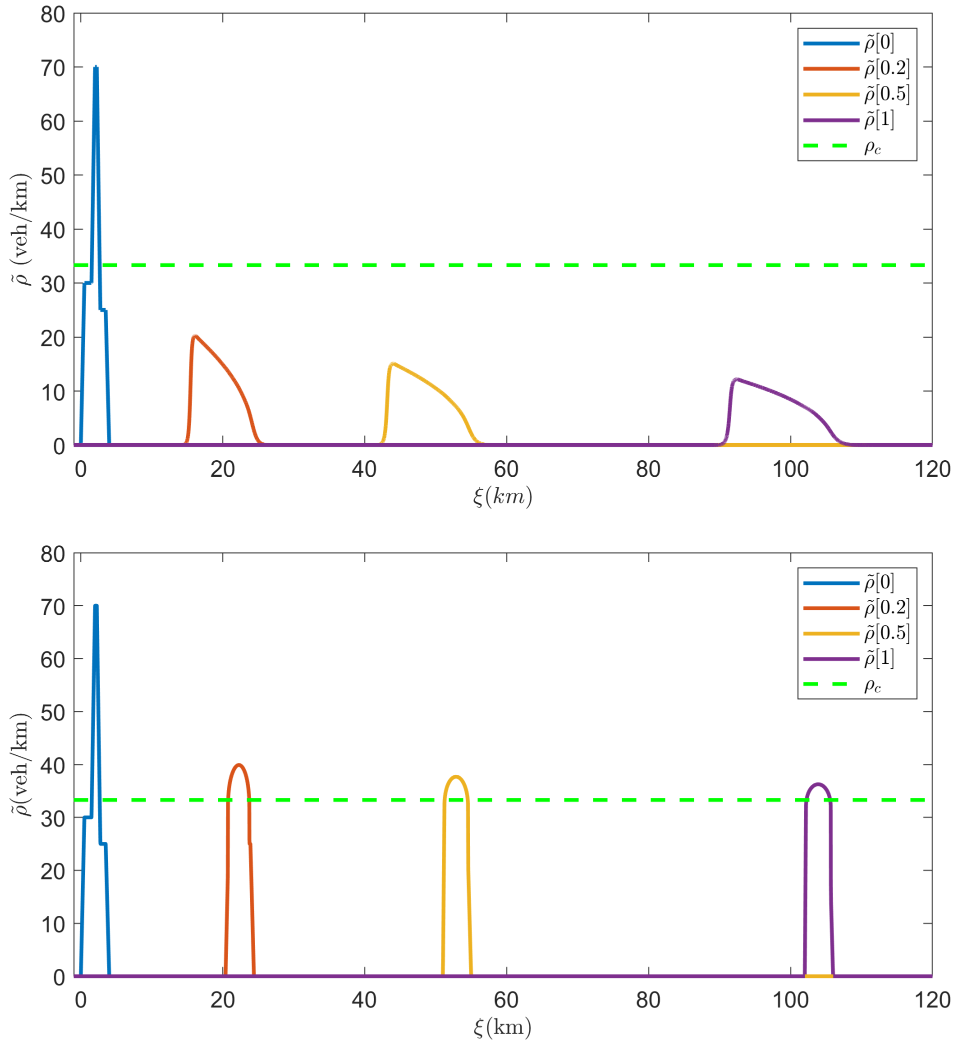

Figure 3.15: Density profiles for the ARZ model obtained by using $\delta = 20\,(s)$ (top), and density profiles of the macro-PRCC (3.1)-(3.4) with $v^* = 102\ (km/h)$ (bottom).

time is lower using the macro-PRCC, since, for $\tau = 1\ (h)$, vehicles are in the interval $(102, 106)\ (km)$, while with the ARZ model, vehicles are in the interval $(90, 106)\ (km)$.

Due to the fact that the use of the macro-PRCC (3.1)-(3.4) causes the convergence of density towards an equilibrium near the critical density, while vehicles are spread in a small space interval (see Figure 3.15), it is expected that the flow $q = \tilde{\rho}\tilde{v}$ is much higher for the macro-PRCC compared to the ARZ. Indeed, this can be noticed in Table 3.7 where the mean flow for each model is compared using the definition:

$$Mean\ \ Flow = \frac{1}{T}\int_0^T \int_{a(t)}^{b(t)} \frac{\tilde{\rho}(t,x)\tilde{v}(t,x)}{b(t)-a(t)}dxdt$$

where $T > 0$ denotes the time horizon and $[a(\tau), b(\tau)]$ denotes the interval where $\tilde{\rho}(\tau, \xi) \neq 0$ for $\xi \in [a(\tau), b(\tau)]$ at each time instant $\tau \geq 0$. Notice that the mean flow obtained with the ARZ model is achieved with the macro-PRCC (3.1)-(3.4) by using a significantly smaller desired speed $v^* = 30.8\ (km/h)$ than the free-flow speed $v_f = 102\ (km/h)$ of the ARZ.

Figure 3.17 displays the sup-norms of the accelerations by using the ARZ and the macro-PRCC (3.1)-(3.4). Since the vehicles with the macro-PRCC obtain the desired speed v^* faster

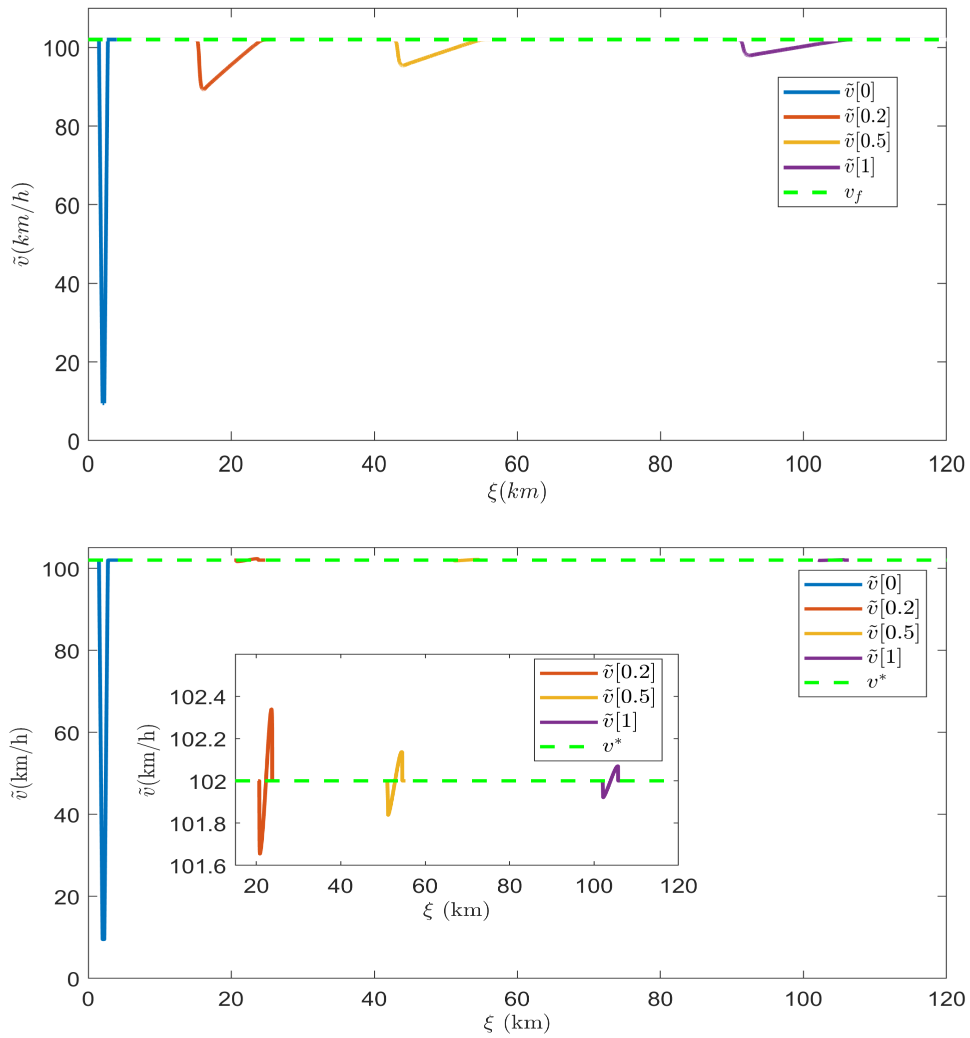

Figure 3.16: Speed profiles for the ARZ model obtained by using $\delta = 20\,(s)$ (top), and speed profiles of the macro-PRCC (3.1)-(3.4) with $v^* = 102\ (km/h)$ (bottom)

.

	macro-PRCC (3.1)-(3.4) with $v^* = 102\ (km/h)$	macro-PRCC (3.1)-(3.4) with $v^* = 70\ (km/h)$	macro-PRCC (3.1)-(3.4) with $v^* = 30.8\ (km/h)$	ARZ using $\delta = 20\,(s)$ and $v_f = 102\ (km/h)$
Mean Flow	3388 (veh/h)	2229 (veh/h)	963 (veh/h)	963 (veh/h)

Table 3.7: Mean Flow.

compared to the ARZ (see Figure 3.16), the maximum accelerations of the vehicles using the macro-PRCC (3.1)-(3.4) are decreasing faster compared to those of the ARZ model, which fluctuate at the first time instants and then converge to lower values. Notice also that the acceleration of the macro-PRCC (3.1)-(3.4) is close to the acceleration of the ARZ model. This occurs due to the selection of the parameter $\tilde{\sigma}$ which appears on the friction term $-\tilde{\sigma}\tilde{\rho}\tilde{\beta}(\tilde{v})$ of the speed PDE (3.2). The constant $\tilde{\sigma}$ has the potential to affect the tendency of vehicles to adjust their speed to the speed set-point v^*. Consequently, by changing the value of the parameter $\tilde{\sigma}$ we can increase or decrease the acceleration of vehicles.

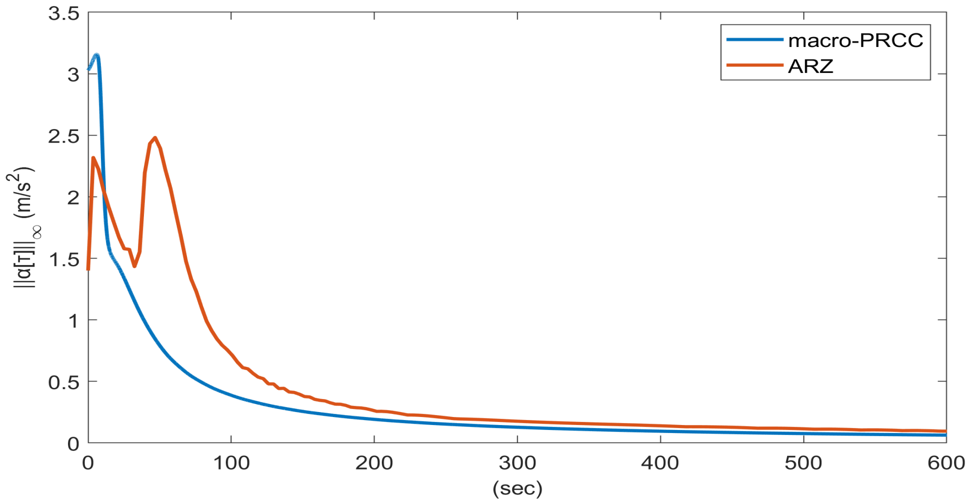

Figure 3.17: Sup-norm of the acceleration of the ARZ model and the macro-PRCC.

Numerical Method	CPU time (sec)
Particle Method (3.27)-(3.32)	391.32
NM1: (3.51)-(3.62)	2034.76
NM2: (3.67)-(3.70)	1602.21
numerical scheme (2.56)-(2.58)	2104.13

Table 3.8: CPU times needed for the proposed particle method (3.27)-(3.32), the numerical methods (3.51)-(3.62) (NM1), (3.67)-(3.70) (NM2) and the numerical method presented in Chapter 2 for the reduced model (3.6).

Next, the numerical solutions produced by applying the particle method (3.27)-(3.32) are compared with the numerical solutions of (3.51)-(3.62) (NM1), (3.67)-(3.70) (NM2) and the numerical solutions of the reduced model (3.6) produced by using the numerical scheme (2.56)-(2.58). Figures 3.18, 3.19 illustrate the profile solutions of the macro-PRCC (3.1)-(3.4) produced by applying each one of the aforementioned numerical methods. It is obvious that the difference between the numerical solutions is very small and it tends to be even smaller as time increases and the solutions converge to the equilibrium point $\tilde{v}(\xi) \equiv v^*$, $\tilde{\rho}(\xi) \leq \bar{\rho}$, $\xi \in \left(\tilde{l}(\tau), \tilde{L}(\tau)\right)$.

The computational cost of each numerical method, in terms of CPU time needed, is given in Table 3.8 for the overall simulation time of $t_{\max} = 0.1\ (h)$. Again, the CPU time needed for the proposed particle method is significantly less than the corresponding CPU times of NM1 (3.51)-(3.62), NM2 (3.67)-(3.70) and the numerical method presented in Chapter 2 for the numerical approximation of the reduced model (3.6). The simulations were performed on Matlab R2021a and a laptop with Intel(R) Core(TM) i7-7700HQ CPU 2.80GHz.

Moreover, the proposed particle method (3.27)-(3.32) provides higher accuracy approximations compared to the numerical methods (3.51)-(3.62) (NM1), (3.67)-(3.70) (NM2) with respect to the discretized energy functional W_n defined by (3.39) preserving the inequality (3.42). This conclusion can be reached by plotting the time evolution of $\ln(W_n(t)/W_n(0))$ in Figure 3.20. It is shown that the discretized functional W_n obtained by using the particle method coincides with the analytical solution of the differential equation $\dot{W}_n(t) = -2\sigma W_n(t)$ while the discretized functionals produced by applying the methods (3.51)-(3.62) (NM1), (3.67)-(3.70) (NM2) diverge. This fact implies that the differential inequality (3.26) is strongly preserved by the particle method.

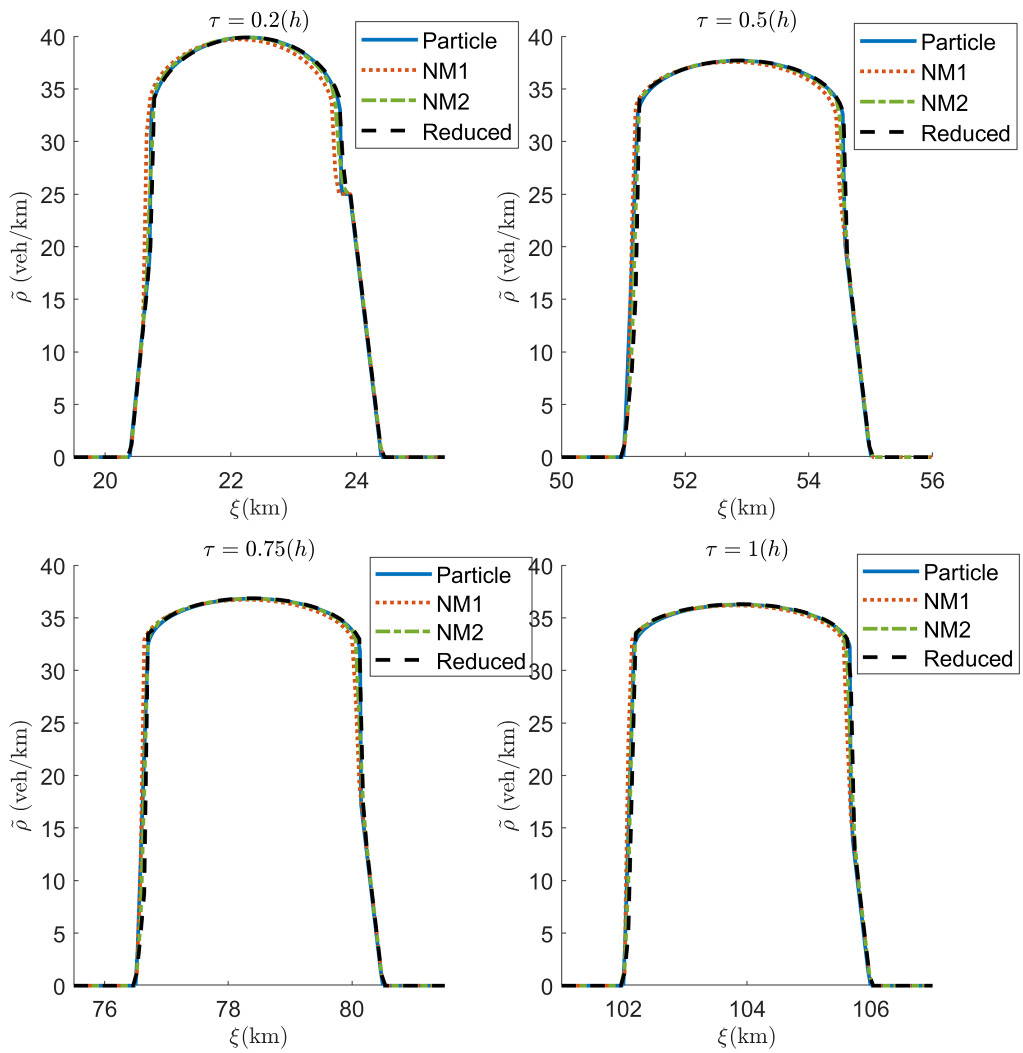

Figure 3.18: Density profiles of the macro-PRCC (3.1)-(3.4) at $\tau = 0.2\ (h)$, $\tau = 0.5\ (h)$, $\tau = 0.75\ (h)$, and $\tau = 1\ (h)$.

It should be noted that the solutions of the macro-PRCC (3.1)-(3.4) can be influenced by increasing (or decreasing) the viscosity function (3.80) through the constant c or replacing the entire function with a different one. For instance, the use of a variety of c values for the viscosity function (3.80) yields the density profiles illustrated in Figure 3.21. It is shown that the convergence rate of density becomes faster by increasing viscosity through the constant c. Since the density decreases faster by increasing viscosity (Fig. 3.21), by replacing the function (3.80) with the following

$$\kappa(\rho) = \begin{cases} 0, 0 < \rho \leq 1 \\ c\frac{(\rho-1)^2}{\rho(R-\rho)}, 1 < \rho < r_1 \\ c\frac{(\rho-1)^2}{\rho(R-\rho)} + A(r_2-\rho)^3(\rho-r_1)^3, r_1 \leq \rho \leq r_2 \\ c\frac{(\rho-1)^2}{\rho(R-\rho)}, r_2 < \rho < R \end{cases} \tag{3.88}$$

where $A = 27 \times 10^2$, $r_1 = 1.3$, $r_2 = 1.9$, the highly congested parts of the highway can be relieved of congestion. By using $c = 1$ for both functions (3.80), (3.88), Fig. 3.22 shows that the dissipation of density along the congestion belt is stronger with the use of (3.88). More specifically, at $\tau = 0.005(h)$ (see Fig. 3.22 (top)), the density obtained by using (3.88)

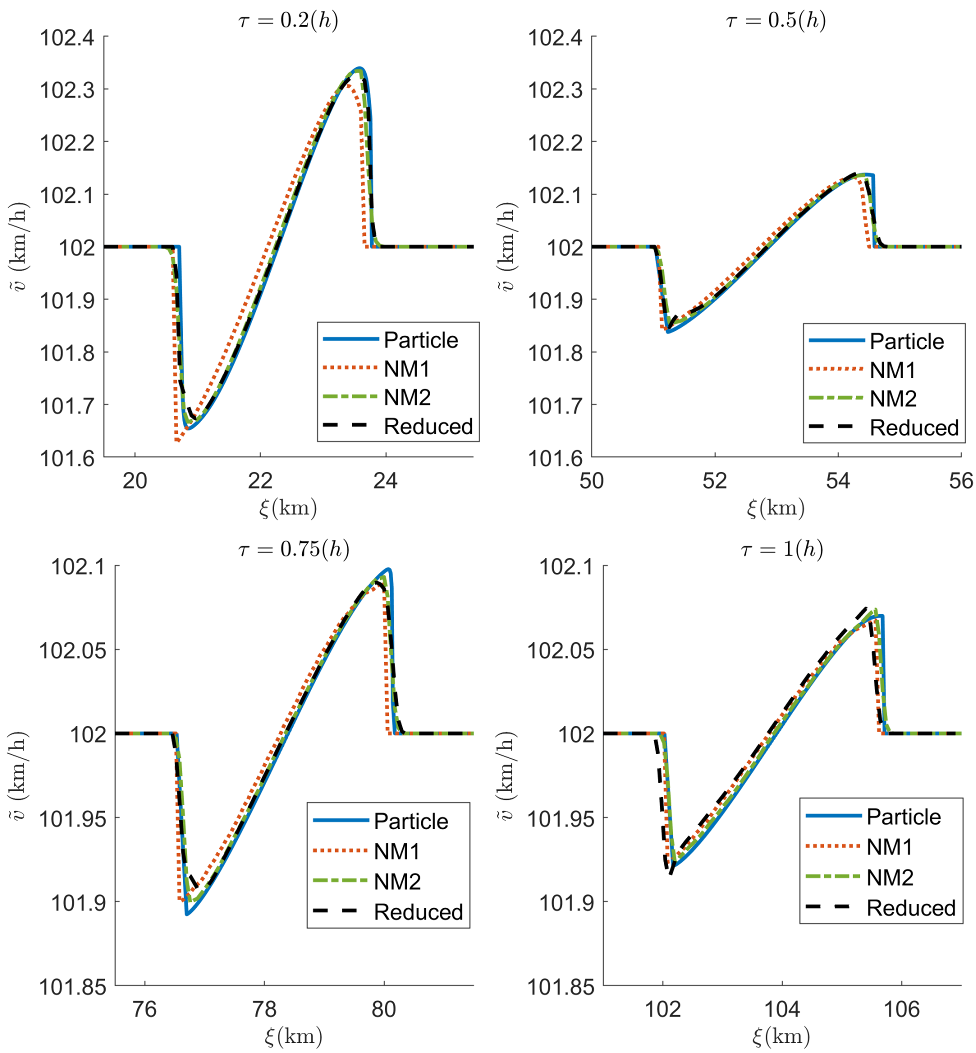

Figure 3.19: Speed profiles of the macro-PRCC (3.1)-(3.4) at $\tau = 0.2\ (h)$, $\tau = 0.5\ (h)$, $\tau = 0.75\ (h)$, and $\tau = 1\ (h)$.

achieves roughly the same level of maximum density with that produced by using (3.80), while the vehicles are spread over a large road interval. At $\tau = 0.5(h)$ (see Fig. 3.22 (middle)), the maximum density obtained by using (3.88) is significantly less than that of (3.80), while at $\tau = 5(h)$ (see Fig. 3.22 (bottom)), the level of maximum density achieved with both functions (3.80), (3.88) is almost the same.

3.6 Conclusions

A particle method for approximating the solutions of the macro-PRCC has been presented. This method preserves all the differential inequalities that hold for the macroscopic traffic model: mass is preserved, the mechanical energy is decaying and an energy functional is also decaying. To evaluate the performance of the employed particle method, a comparison with other numerical methods for viscous compressible fluid models is provided. It is shown that although the difference between the numerical solutions is small, the proposed particle method produces sharper accuracy in the numerical solutions, as it better preserves a certain differential inequality for energy conservation that holds for the macroscopic traffic model. Moreover, the particle method under consideration has much less computational

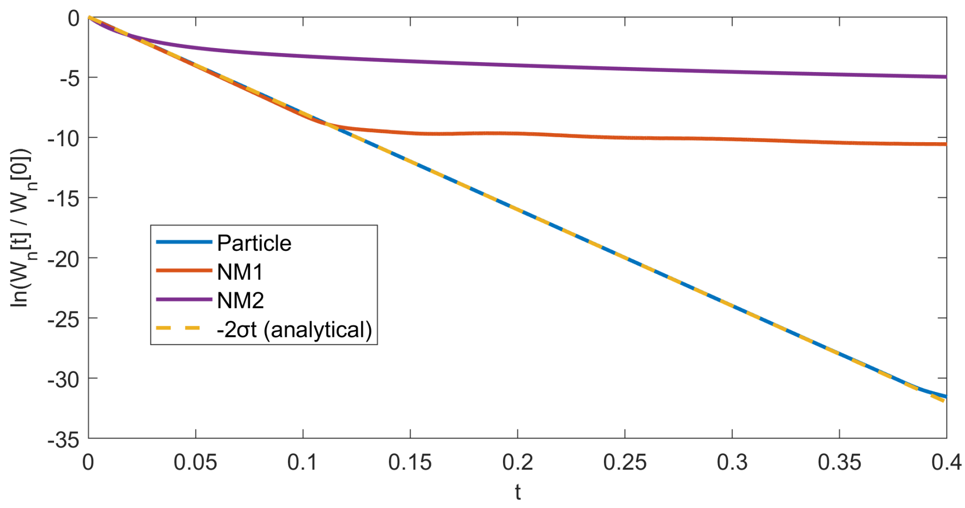

Figure 3.20: Time-evolution of the quantities $\ln(W_n^{particle}[t]/W_n[0])$, $\ln(W_n^{NM1}[t]/W_n[0])$, and $\ln(W_n^{NM2}[t]/W_n[0])$.

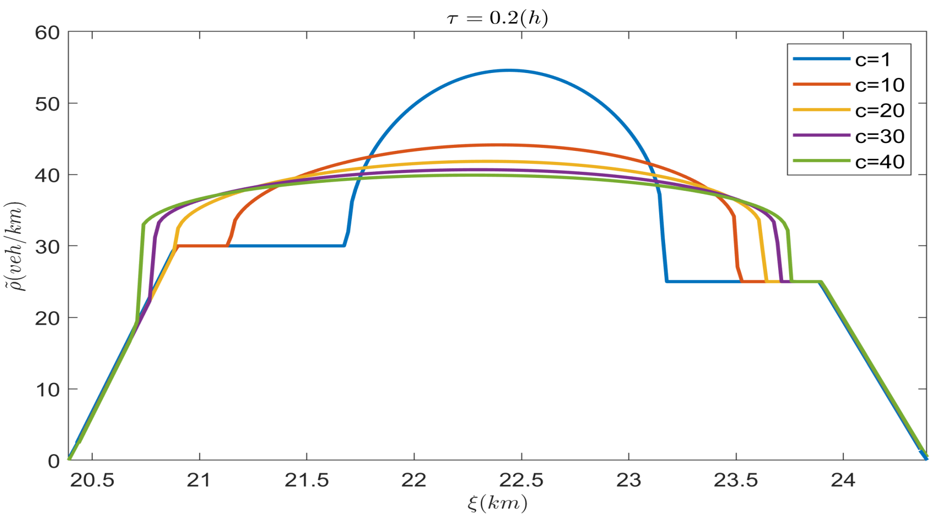

Figure 3.21: Density profiles of the macro-PRCC (3.1)-(3.4) for a variety of c values.

cost, in terms of CPU time, compared to the numerical methods used for viscous compressible fluid models, since both the fixed time step used in the numerical method (3.51)-(3.62) (NM1) and the transformation from Lagrangian to Eulerian coordinates required in the numerical method (3.67)-(3.70) (NM2), affect significantly the CPU time. On the contrary, both the fact that the solution of the ODE system involved in the particle method is approximated by using an adaptive step size numerical scheme, and the fact that the approximation of the macro-PRCC's solution is given directly in Eulerian coordinates, lead to lower CPU times. In addition, since the solutions of the macroscopic traffic model are approximated by the solutions of a reduced model consisting of a single nonlinear heat-type partial differential equation, the numerical solutions produced by the proposed particle method are also compared with the numerical solutions provided for the reduced model, verifying its high accuracy approximations. Finally, the properties of the macro-PRCC model are demonstrated by applying a traffic simulation scenario. In this scenario, the macro-PRCC is compared with the ARZ model showing that the mean flow is much higher with the use of CAVs and the

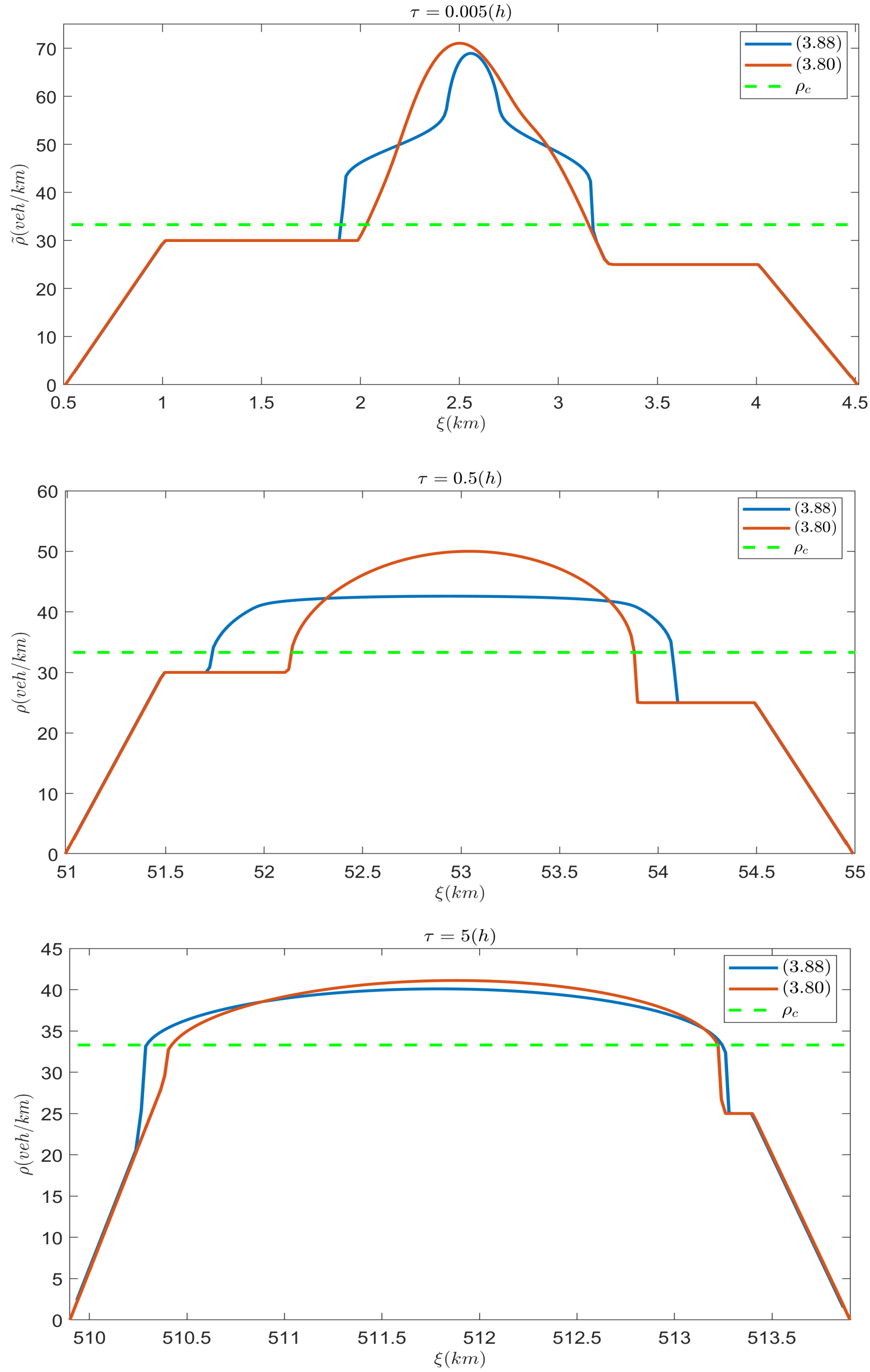

Figure 3.22: Density profiles of the macro-PRCC at $\tau = 0.005(h)$ (top), $\tau = 0.5(h)$ (middle), and $\tau = 5(h)$ (bottom) using the functions (3.80), (3.88).

acceleration remains close to the acceleration produced by the ARZ model.

3.7 Proofs

Proof of Proposition 3.3.1: Using (3.38), (3.27), (3.28) and (3.18) we get:

$$\begin{aligned}\dot{E}_n(t) &= \frac{1}{na}\sum_{i=1}^{n} H'(w_i(t))\dot{w}_i(t) + \sum_{i=2}^{n} \Phi'(nas_i(t))\dot{s}_i(t)\\ &= \frac{1}{na}\sum_{i=1}^{n} w_i(t)\beta'(w_i(t))\dot{w}_i(t) + \sum_{i=2}^{n} \Phi'(nas_i(t))(w_{i-1}(t)-w_i(t))\\ &= \frac{1}{na}w_1(t)\beta'(w_1(t))\dot{w}_1(t) + \frac{1}{na}w_n(t)\beta'(w_n(t))\dot{w}_n(t)\\ &+ \frac{1}{na}\sum_{i=2}^{n-1} w_i(t)\beta'(w_i(t))\dot{w}_i(t) + \sum_{i=2}^{n} \Phi'(nas_i(t))(w_{i-1}(t)-w_i(t)) \end{aligned} \tag{3.89}$$

Moreover, using (3.29), (3.30), (3.31) we get from (3.89) that:

$$\begin{aligned}\dot{E}_n(t) &= -\frac{\sigma}{na}w_1(t)\beta(w_1(t)) - w_1(t)\Phi'(nas_2(t)) + nw_1(t)K(nas_2(t))(w_2(t)-w_1(t))\\ &- \frac{\sigma}{na}w_n(t)\beta(w_n(t)) + w_n(t)\Phi'(nas_n(t)) + nw_n(t)K(nas_n(t))(w_{n-1}(t)-w_n(t))\\ &- \frac{\sigma}{na}\sum_{i=2}^{n-1} w_i(t)\beta(w_i(t)) + \sum_{i=2}^{n-1} w_i(t)\Phi'(nas_i(t)) - \sum_{i=2}^{n-1} w_i(t)\Phi'(nas_{i+1}(t))\\ &+ n\sum_{i=2}^{n-1} w_i(t)K\left(nas_i(t)\right)\left(w_{i-1}(t)-w_i(t)\right) + n\sum_{i=2}^{n-1} w_i(t)K\left(nas_{i+1}(t)\right)\left(w_{i+1}(t)-w_i(t)\right)\\ &+ \sum_{i=2}^{n} \Phi'(nas_i(t))(w_{i-1}(t)-w_i(t)) \end{aligned} \tag{3.90}$$

Since $\sum_{i=1}^{n-1} w_i(t)\Phi'(nas_{i+1}(t)) = \sum_{i=2}^{n} w_{i-1}\Phi'(nas_i(t))$, it follows by rearranging terms in (3.90) that:

$$\begin{aligned}\dot{E}_n(t) &= -nw_1(t)K(nas_2(t))(w_1(t)-w_2(t))^2 - nw_n(t)K(nas_n(t))(w_{n-1}(t)-w_n(t))^2\\ &+ n\sum_{i=3}^{n-1} w_i(t)K\left(nas_i(t)\right)\left(w_{i-1}(t)-w_i(t)\right) + n\sum_{i=2}^{n-2} w_i(t)K\left(nas_{i+1}(t)\right)\left(w_{i+1}(t)-w_i(t)\right)\\ &- \frac{\sigma}{na}\sum_{i=1}^{n} w_i(t)\beta(w_i(t)) = -n\sum_{i=2}^{n} K(nas_i(t))(w_{i-1}(t)-w_i(t))^2 - \frac{\sigma}{na}\sum_{i=1}^{n} w_i(t)\beta(w_i(t)) \end{aligned} \tag{3.91}$$

Recall that from (3.35), $K(s) \geq 0$ for all $s \in \left(\frac{1}{R}, +\infty\right)$. Therefore, it holds that $\sum_{i=2}^{n} K(nas_i(t))(w_{i-1}(t)-w_i(t))^2 \geq 0$. Moreover, the fact that $\sum_{i=1}^{n} w_i(t)\beta(w_i(t)) \geq 0$ is a direct consequence of the fact that $\beta(0) = 0$ and the fact that $\beta'(w) = q(w) = (1+b)^2\frac{2b+(b-1)w}{2(b-w)^2(1+w)^2} > 0$ for all $w \in (-1, b)$, which implies that the function $\beta(w)$ defined by (2.22) is increasing. Consequently, we obtain from (3.91) that:

$$\dot{E}_n(t) = -n\sum_{i=2}^{n} K(nas_i(t))(w_{i-1}(t)-w_i(t))^2 - \frac{\sigma}{na}\sum_{i=1}^{n} w_i(t)\beta(w_i(t)) \leq 0.$$

The proof is complete. ◂

Proof of Proposition 3.3.2: A direct consequence of Proposition 3.3.1 is the following inequality:

$$\begin{aligned}E_n(t) &= \frac{1}{na}\sum_{i=1}^{n} H(w_i(t)) + \frac{1}{na}\sum_{i=2}^{n}\Phi(nas_i(t))\\ &\leq E_n(0) = \frac{1}{na}\sum_{i=1}^{n} H(w_i(0)) + \frac{1}{na}\sum_{i=2}^{n}\Phi(nas_i(0))\end{aligned} \tag{3.92}$$

as long as the solution of (3.27)-(3.31) is defined. Using the fact that $H(w) \geq 0$ for all $w \in (-1, b)$ (see (3.18)) and the fact that $\Phi(s) \geq 0$ for all $s \in \left(\frac{1}{R}, +\infty\right)$ (a consequence of (3.35)), we get from (3.92) that:

$$\Phi(nas_i(t)) \leq \sum_{j=1}^{n} H(w_j(0)) + \sum_{j=2}^{n}\Phi(nas_j(0)),\ \text{for } i = 2, ..., n \tag{3.93}$$

$$H(w_i(t)) \leq \sum_{j=1}^{n} H(w_j(0)) + \sum_{j=2}^{n}\Phi(nas_j(0)),\ \text{for } i = 1, ..., n. \tag{3.94}$$

Using the fact that $\lim_{w\to(-1)^+} H(w) = \lim_{w\to b^-} H(w) = +\infty$ and (3.94) we conclude that there exist constants $-1 < w_{\min} < w_{\max} < b$ such that $w_i(t) \in [w_{\min}, w_{\max}]$ for $i = 1, ..., n$ as long as the solution of (3.27)-(3.32) is defined. Using (3.36) and (3.93) we also conclude that there exists a constant $s_{\min} > \frac{1}{naR}$ such that $s_i(t) \geq s_{\min}$ for $i = 2, ..., n$ as long as the solution of (3.27)-(3.31) exists. Notice that boundedness of $w_i(t) \in [w_{\min}, w_{\max}]$, for $i = 1, ..., n$ as long as the solution of (2.27)-(3.31) is defined, implies that $\dot{s}_i(t)$ are bounded for all $i = 2, ..., n$. Moreover, by virtue of (3.35) and since $s_i(t) \geq s_{\min}$ we also obtain boundedness of $\Phi'(s_i)$ and $K(s_i)$, which in conjunction with continuity of $\beta'(w)$ and the fact that $w_i(t) \in [w_{\min}, w_{\max}]$, for $i = 1, ..., n$, as long as the solution of (3.27)-(3.31) is defined, implies that $\dot{w}_i(t)$, are bounded for all $i = 1, ..., n$. The latter, in conjunction with (3.41) of Proposition 3.3.1, and Theorem 1 in Karafyllis et al. (2025a), implies that every solution of (3.27)-(3.31) is defined for all $t \geq 0$. ◂

Proof of Proposition 3.3.3: Using (3.37) we obtain

$$\Phi''(s) = \frac{\sigma}{s^2}\kappa\left(\frac{1}{s}\right)$$

which due to definition (3.33) implies that

$$\Phi''(s) = \frac{\sigma}{a}K(s)\,. \tag{3.95}$$

Combining definition (3.40) and (3.95) we get that for $i = 2, ..., n-1$

$$\begin{aligned}\dot{\varphi}_i(t) &= \beta'(w_i(t))\dot{w}_i(t) + n^2 aK\left(nas_{i+1}(t)\right)\left(w_i(t) - w_{i+1}(t)\right)\\ &\quad - n^2 aK\left(nas_i(t)\right)\left(w_{i-1}(t) - w_i(t)\right).\end{aligned} \tag{3.96}$$

Next, using (3.30), (3.39), (3.40), and (3.96) we get:

$$\dot{W}_n(t) = \frac{1}{na}\sum_{i=2}^{n-1}\varphi_i(t)\dot{\varphi}_i(t)$$

$$
\begin{aligned}
&= \frac{1}{na}\sum_{i=2}^{n-1}\varphi_i(t)\beta'\left(w_i(t)\right)\dot{w}_i(t) + n\sum_{i=2}^{n-1}\varphi_i(t)K(nas_{i+1}(t))(w_i(t)-w_{i+1}(t))\\
&- n\sum_{i=2}^{n-1}\varphi_i(t)K(nas_i(t))(w_{i-1}(t)-w_i(t))\\
&= \frac{1}{na}\sum_{i=2}^{n-1}\varphi_i(t)\left(-\sigma\beta(w_i(t)) + na\,\Phi'\left(nas_i(t)\right) - na\,\Phi'\left(nas_{i+1}(t)\right)\right.\\
&\left.+n^2aK\left(nas_i(t)\right)\left(w_{i-1}(t)-w_i(t)\right) + n^2aK\left(nas_{i+1}(t)\right)\left(w_{i+1}(t)-w_i(t)\right)\right)\\
&+ n\sum_{i=2}^{n-1}\varphi_i(t)K(nas_{i+1}(t))(w_i(t)-w_{i+1}(t)) - n\sum_{i=2}^{n-1}\varphi_i(t)K(nas_i(t))(w_{i-1}(t)-w_i(t))\\
&= -\frac{\sigma}{na}\sum_{i=2}^{n-1}\varphi_i(t)\left(\beta(w_i(t)) + \sigma^{-1}na\left(\Phi'\left(nas_{i+1}(t)\right) - \Phi'\left(nas_i(t)\right)\right)\right).
\end{aligned}
\tag{3.97}
$$

Using again definition (3.40), we get from (3.97) that

$$
\dot{W}_n(t) = -\frac{\sigma}{na}\sum_{i=2}^{n-1}\varphi_i^2(t) \leq 0.
$$

This completes the proof. ◂

Chapter 4

Calibration of the macro-GCC

4.1 Abstract

This chapter provides evidence that the proposed macroscopic models for the description of the traffic flow of vehicles under the effect of CCs are successful even in very complex cases. More specifically, the macro-GCC is calibrated to fit traffic data collected from the microscopic simulation with a lane-free vehicle movement strategy. The considered macroscopic model was formally derived - using a particle method - from the particular microscopic movement strategy. To evaluate the accuracy of the calibrated macro-GCC, two traffic scenarios are considered. In the first scenario, a highway stretch with an off-ramp and an on-ramp is used, while in the second scenario a funnel-like narrowing of the road is considered. In both cases, it is shown that the calibrated macro-GCC reproduces with high accuracy all the dynamically changing traffic conditions that appear in the microscopically produced traffic data.

4.2 Introduction

In the previous chapters, a specific selection of the functions involved in the PRCC enabled a model reduction for the formally derived macroscopic model i.e. the macro-PRCC. The theoretical properties of the reduced model's solutions were studied in Chapter 2 and a numerical scheme was constructed to approximate its solutions. In Chapter 3, several numerical methods were compared to approximate the solutions of the macro-PRCC. However, the most crucial issue is the performance evaluation of the proposed macroscopic models in complex driving situations. At first glance, the answer to this question seems uncertain since the macroscopic models under consideration have been formally derived from the respective CCs under the assumption that the movement of vehicles is lane-based (see Karafyllis et al. (2022d)) (i.e., it is 1-D movement). Therefore, when the vehicles are allowed to change lanes or even move in a lane-free road and when there are on-ramps, off-ramps and changes in the road width then one cannot be sure that the macroscopic models will describe accurately the traffic flow. The present work is the first attempt to give an answer to this question.

This chapter provides evidence that the proposed macroscopic models for the description of the traffic flow of vehicles under the effect of CCs are successful even in very complex cases. Indeed, two distinct traffic scenarios are studied, each involving a different kind of traffic bottleneck, for which macroscopic traffic data are collected from microscopic simulations using the GCC (Karafyllis et al. (2025b)). The GCC is the generalized case of the CCs proposed in Karafyllis et al. (2022d) and allows the consideration of many real complex driving situations, including the presence of on-ramps and off-ramps, the consideration of variable-width roads, the possibility of each vehicle to move within its own corridor, and the potential to have different individual desired speeds for each vehicle. The first scenario deals with a highway stretch that includes an on-ramp and an off-ramp. In the second scenario, a highway with a width-reducing funnel is employed. In both cases, each of the vehicles involved has its own desired speed, which leads to a realistic traffic environment with vivid overtakes. Also, in both cases the vehicle speed reduces, and congestion is formed at the respective bottleneck, i.e. at the on-ramp merge area and at the width-narrowing funnel. By calibrating the formally derived macroscopic model (i.e. the macro-GCC), it is shown that all the traffic conditions appearing in the microscopically produced data are reproduced with high accuracy. Moreover, all formulas that link the CC parameters and the "traffic fluid" physical properties (see Table 4.1 below) are verified. In addition, the calibrated macro-GCC model estimates properly the congestion spillback, the acceleration of vehicles downstream of the congestion area as well as the capacity drop and the hysteresis phenomena observed in the microscopic data in both scenarios (see Section 4.6 below).

In summary, the structure of this Chapter is as follows. Section 4.3 presents the continuous-time and the derived discrete-time microscopic models, the latter used for simulation to produce macroscopic traffic data. Section 4.4 is devoted to the presentation of the continuous and the discretized macro-GCC models to be calibrated. The calibration procedure is described in Section 4.5. Section 4.6 presents the two traffic scenarios and calibration results. Finally, Section 4.7 gives the concluding remarks of the present work.

4.3 Microscopic model

4.3.1 Continuous-time model

In this context, the microscopic model that is employed to describe the vehicle movement is the bicycle kinematic model. This model has been widely used in the literature (Polack et al. (2017), Rajamani (2012)) and is given by the following set of ODEs (Ordinary Differential Equations), where subscript i refers to vehicle #i:

$$\begin{aligned}\dot{x}_i &= v_i \cos(\theta_i)\\ \dot{y}_i &= v_i \sin(\theta_i)\\ \dot{\theta}_i &= \sigma_i^{-1} v_i \tan(\delta_i)\\ \dot{v}_i &= F_i\end{aligned} \tag{4.1}$$

for $i = 1, ..., n$. The variables of model (4.1) are visualized in Fig. 4.1, where (x_i, y_i) is the vehicle's reference point which is placed at the midpoint of the rear axle, with x_i being the longitudinal position and y_i being the lateral position of the vehicle in an inertial frame with Cartesian coordinates (X, Y); $v_i > 0$ is the vehicle speed at the point (x_i, y_i), $\theta_i \in \left(-\frac{\pi}{2}, \frac{\pi}{2}\right)$ is the vehicle orientation with respect to the X-axis, and $\sigma_i > 0$ is the vehicle length. Finally, δ_i and F_i are the control inputs of the i-th vehicle, where δ_i is the steering angle of the front wheels relative to the orientation θ_i and F_i is the acceleration.

Let $v_{\max} > 0$ be the road speed limit and $\varphi \in \left(0, \frac{\pi}{2}\right)$ be an angle that satisfies:

$$\cos(\varphi) > \max\left\{\frac{\max\limits_{i=1,\ldots,n}\left\{v_i^*\right\}}{v_{\max}}, \frac{1}{3}\right\} \tag{4.2}$$

where $v_i^* \in (0, v_{\max})$ is the speed set-point of each vehicle $i = 1, ..., n$. Inequality (4.2) is a technical condition that ensures that the maximum orientation angle of the vehicles is restricted, i.e. $\theta_i \in (-\varphi, \varphi)$. This mild restriction is necessary for the safe movement of vehicles. Moreover, it is assumed that each vehicle $i = 1, ..., n$ follows a path which is contained in the set (corridor)

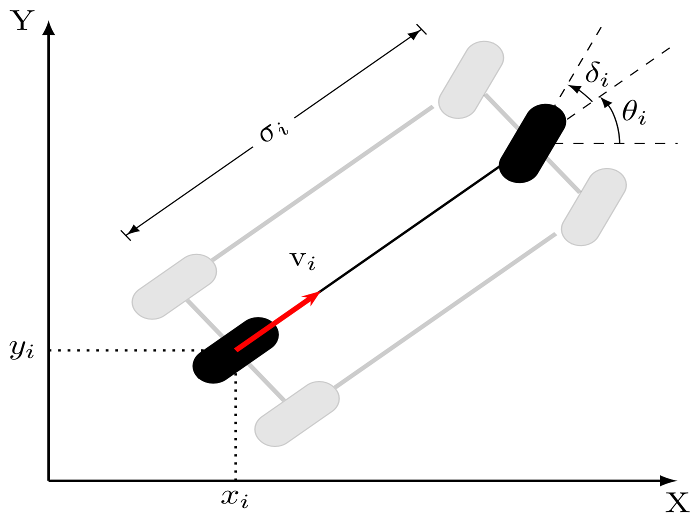

Figure 4.1: The bicycle kinematic model.

$$Y_i = \{(x,y) : x \in \mathbb{R},\ \alpha_i(x) < y < \beta_i(x)\} \tag{4.3}$$

with $\alpha_i : \mathbb{R} \to \mathbb{R}$ and $\beta_i : \mathbb{R} \to \mathbb{R}$ being C^2 functions (the corridor boundaries), for which there exist constants $r_{\max} > r_{\min} > 0$ and $\gamma_{\max}, \gamma_{\min} \in \mathbb{R}$ with $\gamma_{\max} > \gamma_{\min}$ such that the following hold for all $x \in \mathbb{R}$, $i = 1, ..., n$:

$$\gamma_{\max} \geq \beta_i(x), \alpha_i(x) \geq \gamma_{\min} \tag{4.4}$$

$$r_{\max} \geq \beta_i(x) - \alpha_i(x) \geq r_{\min} > 0 \tag{4.5}$$

$$\max\left(\sup_{\xi\in\mathbb{R}} (|\alpha_i'(x)|), \sup_{\xi\in\mathbb{R}} (|\beta_i'(x)|)\right) < \tan(\varphi) \tag{4.6}$$

$$\sup_{x\in\mathbb{R}} (|\alpha_i''(x)| + |\beta_i''(x)|) < +\infty. \tag{4.7}$$

Inequalities (4.5) specify the maximum and minimum width of each corridor Y_i, $i = 1, ..., n$. The boundedness of the corridor boundaries in (4.4) is not only a technical requirement but also shows that if $\gamma_{\max}$ is small and $\gamma_{\min}$ is large, then, due to (4.5) the width of the corridor (4.3) would also be small. In addition, inequalities (4.6) are used to ensure that the rate of change of each corridor boundary will not exceed the maximum orientation angle of each vehicle. It should be noted that it is possible for a corridor Y_i not to have common points with a corridor Y_j (with $j \neq i$) of a different vehicle. In the case that all vehicles share the same corridor, i.e. $\alpha_i(x) = \alpha(x)$ and $\beta_i(x) = \beta(x)$, then the functions $\alpha(x)$ and $\beta(x)$ constitute the boundaries of the road.

In what follows, the distance between vehicles is defined by

$$d_{i,j} := \sqrt{(x_i - x_j)^2 + p\,(y_i - y_j)^2} \text{ for } i, j = 1, ..., n \tag{4.8}$$

where $p > 0$ is a constant that is used to adapt the distance metric to the rectangular shape of the vehicles.

Let

$$\tilde{w} = (x_1, ..., x_n, y_1, ..., y_n, \theta_1, ..., \theta_n, v_1, ..., v_n)' \in \mathbb{R}^{4n}. \tag{4.9}$$

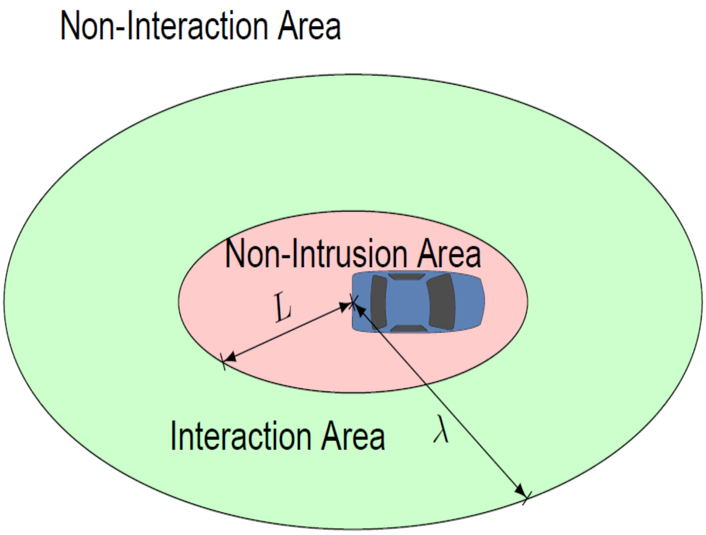

Figure 4.2: Interaction and non-intrusion areas around a vehicle.

Define also the set

$$\Omega := \left\{ \tilde{w} \in \mathbb{R}^{4n} : \begin{array}{c} (x_i, y_i) \in Y_i,\ i = 1, ..., n \\ v_i \in (0, v_{\max}),\ |\theta_i| < \varphi,\ i = 1, ..., n \\ d_{i,j} > L,\ i, j = 1, ..., n\,,\ j \neq i \end{array} \right\} \tag{4.10}$$

where $L > 0$ (Fig. 4.2) is a safety distance that prevents collisions (non-intrusion area). The set Ω describes all possible states of a system of n vehicles. More specifically, the vehicles should stay within the corridor boundaries, i.e. $(x_i, y_i) \in Y_i$, no vehicle can move backwards or exceed the road speed limit, i.e. $v_i \in (0, v_{\max})$, the vehicles should not be able to turn perpendicular to the road, i.e. $|\theta_i| < \varphi$, and the minimum intervehicle distance should always be greater than L to avoid collisions, i.e. $d_{i,j} > L$.

Next, a potential function V is defined, which will be used to create repulsion forces among vehicles depending on their distance. Let $V : (L, +\infty) \to \mathbb{R}_+$ be a C^2 function that satisfies the following properties

$$\lim_{d \to L^+} (V(d)) = +\infty \tag{4.11}$$

$$V(d) = 0,\ \text{for all } d \geq \lambda \tag{4.12}$$

where $\lambda > L$ is a constant which determines the required real-time information zone around each vehicle (Fig. 4.2) (interaction area). In the case that the intervehicle distance $d_{i,j}$ becomes greater than λ, the condition (4.12) implies that there is no repulsion, hence no information exchange between the vehicles.

A potential function to account for repulsion from the corridor boundaries is also considered. This is the C^2 function $U : (-1, 1) \to \mathbb{R}_+$ that satisfies

$$U(0) = 0 \tag{4.13}$$

$$\lim_{s \to (-1)^+} (U(s)) = +\infty,\ \lim_{s \to 1^-} (U(s)) = +\infty. \tag{4.14}$$

The potential functions V and U have been extensively used in the literature for avoiding collisions and road boundary violation, respectively (see Karafyllis et al. (2022d), Wolf and Burdick (2008)).

It should be noted that in Karafyllis et al. (2025b), where the GCC was initially proposed, the constant p involved in (4.8), the safety distance L, as well as the potential function V were defined for pairs of vehicles, i.e. $p_{i,j}$, $L_{i,j}$, $V_{i,j}$, $i, j = 1, ..., n$, $i \neq j$, allowing the interactions between different vehicle pairs to vary. However, in the present work, the same p, L and V are considered for all vehicle couples for simplicity. Moreover, in Karafyllis et al. (2025b) the potential function U was defined as U_i, $i = 1, ..., n$, meaning that the interaction between each vehicle i and the corridor boundaries can be different for each vehicle. For convenience, in the present work, the same potential U is considered for all vehicles.

Let $\tilde{\sigma} : \mathbb{R} \to (0, 1]$ be a non-increasing C^2 function that satisfies

$$\tilde{\sigma}(x) = 1 \text{ for } x \leq \varepsilon \text{ and } \tilde{\sigma}(x)x \leq M \text{ for } x \geq \varepsilon \tag{4.15}$$

$$\sup_{x\in\mathbb{R}} \left(|\tilde{\sigma}'(x)| + |\tilde{\sigma}''(x)|\right) < +\infty \tag{4.16}$$

where M and ε are positive constants. The function $\tilde{\sigma}$ is used in the controllers to adjust the desired speed of each vehicle based on the distance and the repulsive force produced by the potential function V from neighboring vehicles within the interaction area (see (4.20) below). Essentially, vehicles reduce their desired speed if there are more close vehicles interacting with them. It should be also noted that the function $\tilde{\sigma}$ induces and plays the role of viscosity as it will become clear from the macroscopic version of the GCC (Section 4.3).

The GCC, applied to each vehicle i, receives real-time information and produces the vehicle's control inputs F_i, δ_i. The required real-time information comprises: the state $(x_i, y_i, \theta_i, v_i)$ of the vehicle i, the relative positions and relative speeds of all vehicles given by $(x_j - x_i, y_j - y_i, \dot{x}_i - \dot{x}_j, \dot{y}_i - \dot{y}_j)$ that are in distance $d_{i,j} = \sqrt{(x_i - x_j)^2 + p(y_i - y_j)^2}$ less than λ, the values of its own boundary functions $\alpha_i(x)$, $\beta_i(x)$ and their derivatives $\alpha_i'(x)$, $\beta_i'(x)$ and $\alpha_i''(x)$, $\beta_i''(x)$ at the current x-coordinate of the position of the vehicle. The GCC equations are given as follows:

$$\begin{aligned} F_i = &-\frac{\left(\gamma\left(v_i \cos\left(\theta_i\right) - \zeta_i(\tilde{w})\right) + \Phi_i(\tilde{w}) + g_i(x_i, y_i)\Xi_i(\tilde{w})\right)}{\bar{q}(v_i, \theta_i, \zeta_i(\tilde{w}))} \\ &+ \frac{v_{\max}^2 \left(\tilde{Z}_i(\tilde{w}) + \sigma_i^{-1} v_i^2 \sin(\theta_i)\tan(\delta_i)\right)}{\bar{q}(v_i, \theta_i, \zeta_i(\tilde{w}))v_i(v_{\max} - v_i)} \end{aligned} \tag{4.17}$$

where

$$\Phi_i(\tilde{w}) = \sum_{j\neq i} V'(d_{i,j})\frac{(x_i - x_j)}{d_{i,j}}, \text{ for } \tilde{w} \in \Omega \tag{4.18}$$

$$\Xi_i(\tilde{w}) = \sum_{j\neq i} pV'(d_{i,j})\frac{(y_i - y_j)}{d_{i,j}}, \text{ for } \tilde{w} \in \Omega \tag{4.19}$$

$$\zeta_i\left(\tilde{w}\right) = v_i^* \tilde{\sigma}\left(\Phi_i\left(\tilde{w}\right) + g_i\left(x_i, y_i\right)\Xi_i\left(\tilde{w}\right)\right) \tag{4.20}$$

for $i = 1, ..., n$, and

$$\begin{aligned} \delta_i = \arctan\Bigg(&\frac{2\sigma_i\left(\cos\left(\theta_i\right) - \cos\left(\varphi\right)\right)^2}{\bar{b}v_{\max}^2 v_i h_i\left(x_i, y_i, \theta_i\right)} \Bigg(-\Gamma v_i^2\left(\sin(\theta_i)g_i(x_i, y_i)\cos(\theta_i)\right) \\ &+ \bar{b}v_{\max}^2 \frac{\sigma_i \cos(\theta_i)k_i(x_i, y_i, \theta_i)}{\cos(\theta_i) - \cos(\varphi)} - \sigma_i\Xi_i(\tilde{w}) - U'\left(\frac{2y_i - (\beta_i(x_i) + \alpha_i(x_i))}{\beta_i(x_i) - \alpha_i(x_i)}\right) \\ &\times \frac{2\sigma_i}{\beta_i(x_i) - \alpha_i(x_i)}\Bigg)\Bigg) \end{aligned} \tag{4.21}$$

where $\bar{b}, \gamma, \Gamma > 0$ are constants and $\tilde{w} \in \Omega$

$$g_i(x,y) := \frac{(\beta_i(x) - y)\alpha_i'(\xi) + (y - \alpha_i(x))\beta_i'(x)}{\beta_i(x) - \alpha_i(x)} \tag{4.22}$$

for all $(x,y) \in Y_i$,

$$\tilde{Z}_i(\tilde{w}) := v_i^* \tilde{\sigma}' \left(\Phi_i(\tilde{w}) + g_i(x_i,y_i)\Xi_i(\tilde{w})\right) \frac{d}{dt} \left(\Phi_i(\tilde{w}) + g_i(x_i,y_i)\Xi_i(\tilde{w})\right) \tag{4.23}$$

for all $\tilde{w} \in \Omega$, $i = 1,...,n$

$$\bar{q}(v,\theta,\zeta) = v_{\max}^2 \frac{v_{\max} v \cos(\theta) + \zeta v_{\max} - 2\zeta v}{2\left(v_{\max} - v\right)^2 v^2} \tag{4.24}$$

for all $v \in (0, v_{\max})$, $\theta \in (-\varphi,\varphi)$, $\zeta \in \mathbb{R}$

$$\begin{aligned} h_i(x,y,\theta) &= 2\cos(\theta)\left(\cos(\theta) - \cos(\varphi)\right) + \sin^2(\theta) \\ &\quad + \sin(\theta) g_i(x,y)(\cos(\theta) - 2\cos(\varphi)) \end{aligned} \tag{4.25}$$

for all $(x,y) \in Y_i$, $\theta \in (-\varphi,\varphi)$, $i = 1,...,n$

$$\begin{aligned} k_i(x_i,y_i,\theta) &= \cos(\theta)\left(\frac{y_i - \alpha_i(x_i)}{\beta_i(x_i) - \alpha_i(x_i)}\beta_i''(x_i) + \left(1 - \frac{y_i - \alpha_i(x_i)}{\beta_i(x_i) - \alpha_i(x_i)}\right)\alpha_i''(x_i)\right) \\ &\quad + \left((\beta_i(x_i) - \alpha_i(x_i))\sin(\theta) - g_i(x_i,y_i)\cos(\theta)\right)\frac{\beta_i'(x_i) - \alpha_i'(x_i)}{(\beta_i(x_i) - \alpha_i(x_i))^2} \end{aligned} \tag{4.26}$$

for all $(x_i,y_i) \in Y_i$, $\theta \in (-\varphi,\varphi)$, $i = 1,...,n$.

In controller (4.17), the term $\gamma\left(v_i \cos\left(\theta_i\right) - \zeta_i(\tilde{w})\right)$ is used to regulate the speed of the vehicle i towards its desired speed while the term $\Phi_i(\tilde{w})$ is used for collision avoidance, the term $g_i(x_i,y_i)\Xi_i(\tilde{w})$ counteracts the change of the vehicle's angular movement, and finally, the term $\tilde{Z}_i(\tilde{w})$ considers the relative speeds of neighboring vehicles. Similarly, for the steering angle (4.21), the term $\Gamma v_i^2\left(\sin(\theta_i) - g_i(x_i,y_i)\cos(\theta_i)\right)$ regulates the vehicle's lateral speed relative to the rate of change of the corridor boundaries, the potential U' is responsible for the vehicle i to stay within the corridor boundaries, while the remaining terms of (4.21) affect the vehicle's steering angle based on the corridor boundaries. From a fluid-like perspective, each of the terms included in (4.17) has specific meaning, as it will become clear from the macroscopic version of the GCC (Section 4.3). More specifically, $\gamma\left(v_i \cos\left(\theta_i\right) - \zeta_i(\tilde{w})\right)$ is a friction term, $\Phi_i(\tilde{w})$ is a pressure term, and $\tilde{Z}_i(\tilde{w}) + \sigma_i^{-1} v_i^2 \sin(\theta_i)\tan(\delta_i)$ is a viscous term.

The feedback control laws (4.17), (4.21) were designed in Karafyllis et al. (2025b) following a Lyapunov based methodology (using a pseudo-relativistic mechanical energy function as a Lyapunov function (see (A.5))) and ensure the following property: For any $\tilde{w}(0) \in \Omega$, we have $\tilde{w}(t) \in \Omega$ for all $t \geq 0$, which (recall definition (4.10)) rigorously guarantees that:

- there are no collisions between vehicles (i.e., $d_{i,j}(t) > L$ for $t \geq 0$, $i,j = 1,...,n$, $j \neq i$);
- no vehicle will exit its corridor set (i.e., $(x_i(t), y_i(t)) \in Y_i$ for $t \geq 0$);
- no vehicle will exceed the road speed limit or move in the upstream direction (i.e., $v_i(t) \in (0, v_{\max})$ for $t \geq 0$);

- the orientation of each vehicle is always bounded by the given value $\varphi \in \left(0, \frac{\pi}{2}\right)$ (i.e., $\left|\theta_i(t)\right| < \varphi$ for $t \geq 0$).

4.3.2 Sampled-data model

A common approach to using a continuous-time cruise controller in practical frameworks is to implement it as a digital controller (see Theodosis et al. (2022), Naderi et al. (2024), Hetel et al. (2017)). More specifically, by using the sampled version of the system's state $\tilde{w}(k)$ at each sampling instant kT , $k = 0, 1, 2, ...$, with T being the sampling period, the control inputs F_i, δ_i given by (4.17), and (4.21), respectively, can be digitalized and produce a sequence of control values $F_i(k)$, $\delta_i(k)$. This way, a discrete-time version of the bicycle kinematic model can be obtained through analytically integrating (4.1), while considering that the control inputs F_i, δ_i are constant on the time interval $[kT, (k+1)T)$, $k = 0, 1, 2, ...$

Defining

$$\omega_i(k) := \sigma_i^{-1} \tan(\delta_i(k)), \text{ for } i = 1, ..., n, \tag{4.27}$$

the discrete-time bicycle kinematic model is derived as follows:

If $\omega_i(k) \neq 0$:

$$\begin{aligned} x_i(k+1) = x_i(k) + \frac{1}{\omega_i(k)} \Bigg(& \sin\left(\theta_i(k) + \left(v_i(k) + F_i(k)\frac{T}{2}\right)\omega_i(k)T\right) \\ & - \sin(\theta_i(k))\Bigg) \end{aligned} \tag{4.28}$$

$$\begin{aligned} y_i(k+1) = y_i(k) - \frac{1}{\omega_i(k)} \Bigg(& \cos\left(\theta_i(k) + \left(v_i(k) + F_i(k)\frac{T}{2}\right)\omega_i(k)T\right) \\ & - \cos(\theta_i(k))\Bigg) \end{aligned} \tag{4.29}$$

$$\theta_i(k+1) = \theta_i(k) + \left(v_i(k) + F_i(k)\frac{T}{2}\right)\omega_i(k)T \tag{4.30}$$

$$v_i(k+1) = v_i(k) + F_i(k)T \tag{4.31}$$

and if $\omega_i(k) = 0$:

$$x_i(k+1) = x_i(k) + \left(v_i(k) + F_i(k)\frac{T}{2}\right)\cos(\theta_i(k))T \tag{4.32}$$

$$y_i(k+1) = y_i(k) + \left(v_i(k) + F_i(k)\frac{T}{2}\right)\sin(\theta_i(k))T \tag{4.33}$$

$$\theta_i(k+1) = \theta_i(k) \tag{4.34}$$

$$v_i(k+1) = v_i(k) + F_i(k)T \tag{4.35}$$

where the states $x_i(k)$, $y_i(k)$, $\theta_i(k)$, $v_i(k)$ denote the longitudinal position, the lateral position, the orientation, and the speed of the vehicle i at the time instant kT, $k = 0, 1, 2, ...$, while the control input values $F_i(k)$, $\delta_i(k)$ denote the acceleration and the steering angle of the vehicle i at the time period $[kT, (k+1)T)$. The acceleration F_i is saturated and is limited to stay within the range $[F_{\min}, F_{\max}]$, where $F_{\min}$, $F_{\max}$ are the lower and upper acceleration limits, respectively. More specifically, with a slight abuse of notation, we consider that $F_i(k) = sat(F_i(k))$ where

$$sat(F_i(k)) = \begin{cases} F_{\max}, & F_i(k) \geq F_{\max} \\ F_i(k), & F_i(k) \in (F_{\min}, F_{\max}) \\ F_{\min}, & F_i(k) \leq F_{\min} \end{cases} \tag{4.36}$$

4.4 Macroscopic model

4.4.1 Continuous macro-GCC model

In the literature, various methods have been used for the formal derivation of macroscopic traffic flow models from microscopic models (see Aw et al. (2002), Di Francesco and Rosini (2015), Helbing (2009), Helbing (2001), Holden and Risebro (2018a)). In the present work, the employed macroscopic traffic flow model has been formally derived from the microscopic model (4.1) based on a particle method (see Karafyllis et al. (2025a)), by adopting a methodology that is inspired by Di Francesco and Rosini (2015), Holden and Risebro (2018a), Holden and Risebro (2018b). The particle method provides the link between the macroscopic model and the microscopic model (4.1) under the control inputs (4.17), (4.21). More specifically, following the same derivation process that was first given in Karafyllis et al. (2022b) and neglecting the lateral movement of vehicles, the macro-GCC model is obtained

$$\tilde{\rho}_\tau + (\tilde{\rho}\tilde{v})_\xi = 0 \tag{4.37}$$

$$\tilde{Q}(\tilde{v},\tilde{r})\left(\tilde{v}_\tau + \tilde{v}\tilde{v}_\xi\right) + \frac{\tilde{P}'(\tilde{\rho})}{\tilde{\rho}}\tilde{\rho}_\xi = -\frac{v_{\max}^2 v^* \tilde{\sigma}'(\tilde{r})}{\tilde{\rho}(v_{\max}-\tilde{v})\tilde{v}}\left(\tilde{\rho}\tilde{P}'(\tilde{\rho})\,\tilde{v}_\xi\right)_\xi - \gamma\left(\tilde{v} - v^*\tilde{\sigma}(\tilde{r})\right) \tag{4.38}$$

$$\tilde{r} := \frac{\tilde{P}'(\tilde{\rho})}{\tilde{\rho}}\tilde{\rho}_\xi \tag{4.39}$$

for $\tau > 0$ and $\xi \in I(\tau)$, where $I(\tau) \subseteq \mathbb{R}$ is an appropriate interval. The macroscopic model (4.37)-(4.39) is to be considered with state constraints $0 < \tilde{\rho}(\tau,\xi) < \rho_{\max}$, $0 < \tilde{v}(\tau,\xi) < v_{\max}$ for all $\tau > 0$ and $\xi \in I(\tau)$, where $\tilde{\rho}(\tau,\xi)$, $\tilde{v}(\tau,\xi)$ are the traffic density and mean speed, respectively, at position $\xi \in I(\tau)$ on a highway, with $\rho_{\max}$ being the maximum density, and $v_{\max}$ being the maximum speed limit of the road; v^* is the speed set-point and $\gamma > 0$ is a constant.

In addition, the function $\tilde{P} : (0,\rho_{\max}) \to \mathbb{R}_+$ is $C^1((0,\rho_{\max}))$ and satisfies

$$\lim_{\tilde{\rho}\to\rho_{\max}^-} \tilde{P}(\tilde{\rho}) = +\infty \tag{4.40}$$

$$\tilde{P}(\tilde{\rho}) > 0 \text{ for } \tilde{\rho} \in (\bar{\rho},\rho_{\max}) \text{ and } \tilde{P}(\tilde{\rho}) = 0 \text{ for } \tilde{\rho} \in (0,\bar{\rho}] \tag{4.41}$$

where $\bar{\rho}$ is a constant that is called "interaction density", since for $\tilde{\rho} \in (0,\bar{\rho}]$, it follows from (4.41) that $\tilde{P}(\tilde{\rho}) = 0$ which reflects the fact that there is no interaction among vehicles (see Table 4.1 below). Indeed, at the microscopic level, when the distance between vehicles is greater than λ, there is no vehicle repulsion (see (4.12)). Furthermore, the function $\tilde{\sigma}(\tilde{r})$ is the same function used in the control input F_i (see (4.17), (4.23)) and satisfies the properties (4.15), (4.16). Finally, the function $\tilde{Q}(\tilde{v},\tilde{r})$ corresponds to the function (4.24), involved in the control input F_i and given by

$$\tilde{Q}(\tilde{v},\tilde{r}) := v_{\max}^2 \frac{v_{\max}\tilde{v} + (v_{\max} - 2\tilde{v})\,v^*\tilde{\sigma}(\tilde{r})}{2(v_{\max}-\tilde{v})^2\tilde{v}^2}. \tag{4.42}$$

The continuity equation (4.37) describes the mass (vehicle) conservation law, while equation (4.38) resembles the momentum equation for 1-D polytropic compressible fluid flow since it contains a density-dependent viscosity term $-\frac{v_{\max}^2 v^* \tilde{\sigma}'(\tilde{r})}{\bar{\rho}(v_{\max}-\tilde{v})\tilde{v}}\left(\tilde{\rho}\tilde{P}'\left(\tilde{\rho}\right)\tilde{v}_{\xi}\right)_{\xi}$ that affects the change of speed according to density; a pressure term $\frac{\tilde{P}'(\tilde{\rho})}{\tilde{\rho}}\tilde{\rho}_{\xi}$ that describes the tendency of vehicles to accelerate or decelerate based on the (local) density; and a friction term $-\gamma\left(\tilde{v}-v^*\tilde{\sigma}\left(\tilde{r}\right)\right)$ (by analogy with the relaxation term involved in the macroscopic traffic flow models for human drivers Aw and Rascle (2000), Zhang (2002)) that expresses the tendency of vehicles to adjust their speed to the given speed set-point.

The parameters $\rho_{\max}$, $\bar{\rho}$, ε, γ involved in the viscosity, pressure, and friction terms will play a significant role in the calibration procedure (see Section 4.6), since they have the potential to affect the density and speed solutions of the macro-GCC model. More specifically, the impact of the maximum density $\rho_{\max}$ follows from the fact that the pressure function $\tilde{P}\left(\tilde{\rho}\right)$ increases as the density solution approaches $\rho_{\max}$ (see (4.40)), reflecting the tendency of vehicles to accelerate and causing an increase in speed. The interaction density $\bar{\rho}$ determines the required level of density for which the vehicles start to interact with each other. If the value of $\bar{\rho}$ is not exceeded by the density solution, then there is no interaction among vehicles (see (4.41)) and consequently there is no change in speed, since the viscosity and pressure terms are not activated. The constant ε has also the potential to activate or disactivate the viscosity term affecting the speed solution, since for $\tilde{r}\leq\varepsilon$ it follows that $\tilde{\sigma}'\left(\tilde{r}\right)=0$ (see (4.15)), and therefore the viscosity term becomes zero. Finally, the constant γ involved in the friction term, reflects the tendency of vehicles to adjust their speed to the speed set-point, and can also affect the produced speed solution.

The fact that the macroscopic model (4.37)-(4.39) and the microscopic model (4.1) under the GCC are linked through the particle method (see Karafyllis et al. (2025b)), provides certain relations between the microscopic and the macroscopic quantities and parameters as shown in Table 4.1, where $m>0$ is the total "mass" of all vehicles which may not be the real physical mass of vehicles and its units may be veh (see Karafyllis et al. (2025b) for details). In particular, the interaction density $\bar{\rho}$ equals the mass m divided by the interaction distance λ, while the maximum density $\rho_{\max}$ equals the mass m divided by the safety distance L. Therefore, the macroscopic parameters $\bar{\rho}$, $\rho_{\max}$ are inversely proportional to the microscopic parameters λ, L, and we have $\frac{\rho_{\max}}{\bar{\rho}}=\frac{\lambda}{L}$. Moreover, the pressure function $\tilde{P}\left(\tilde{\rho}\right)$ of the macro-GCC model is linked with the potential function $V\left(d\right)$ used in the GCC through the relation

Macroscopic	**Microscopic**
$\bar{\rho}$	$\frac{m}{\lambda}$
$\rho_{\max}$	$\frac{m}{L}$
$v_{\max}$	$v_{\max}$
γ	γ
$\tilde{P}\left(\tilde{\rho}\right)$	$-mV'\left(\frac{m}{\tilde{\rho}}\right)$

Table 4.1: Relations between macroscopic and microscopic quantities and parameters.

$\tilde{P}(\tilde{\rho})=-mV'\left(\frac{m}{\tilde{\rho}}\right)$. These relations imply that by changing parameter values or functions included in GCC, e.g. the potential function, we can affect the physical properties of the emerging "traffic fluid", e.g. the pressure function. In this sense, we may talk about an engineered or artificial designed traffic fluid that approximates the actual emerging traffic flow. The parameters $v_{\max}$,γ are the same for both the microscopic and the macroscopic models.

It should be noted that the macroscopic model (4.37)-(4.39) cannot explicitly consider the case of width-varying roads, since its derivation is based on a string of vehicles moving on a single lane. This issue can be addressed by defining $\hat{\rho}$ as the number of vehicles per road-surface unit, e.g. measured in veh/(km·m) (vehicles per kilometer length and meter width), and introducing the changing road width $w(x)$ at location x through the change of variable

$$\tilde{\rho} = \hat{\rho} w \tag{4.43}$$

in equations (4.37)-(4.39). This modification is also used for the discretized version of the macro-GCC model in the following Section 4.4.2 to enable consideration of roads with variable width.

4.4.2 Discretized macro-GCC model

Before proceeding with the calibration procedure, we first need to discretize the macro-GCC model in space and time. For the discretization, a finite volume method is employed, that was initially used in Gunawan (2014) to approximate the solutions of the Saint-Venant equations; and modified in Chapter 3 (see (3.51)-(3.62)) to approximate the solutions of the macro-PRCC. In order to apply the finite volume method, an appropriate modification of equation (4.38) is needed, such that its resulting form be similar to the conservative form of the momentum equation included in the Saint-Venant equations (see Gunawan (2014)). To this end, the following functions are defined:

$$A\left(\tilde{v}\right) = \int_{v^*}^{\tilde{v}} a(s)ds, \tilde{v} \in \left(0, v_{\max}\right) \tag{4.44}$$

$$B\left(\tilde{v}\right) = \int_{v^*}^{\tilde{v}} b(s)ds, \tilde{v} \in \left(0, v_{\max}\right) \tag{4.45}$$

$$\beta\left(\tilde{v}, \tilde{r}\right) = A\left(\tilde{v}\right) + B\left(\tilde{v}\right)\tilde{\sigma}\left(\tilde{r}\right) \tag{4.46}$$

where

$$a\left(\tilde{v}\right) = \frac{v_{\max}^3}{2\left(v_{\max} - \tilde{v}\right)^2 \tilde{v}}, \tilde{v} \in \left(0, v_{\max}\right) \tag{4.47}$$

and

$$b\left(\tilde{v}\right) = \frac{v_{\max}^2\left(v_{\max} - 2\tilde{v}\right)v^*}{2\left(v_{\max} - \tilde{v}\right)^2 \tilde{v}^2}, \tilde{v} \in \left(0, v_{\max}\right). \tag{4.48}$$

Then, the function (4.42) can be written as follows

$$\tilde{Q}(\tilde{v}, \tilde{r}) := A'\left(\tilde{v}\right) + B'\left(\tilde{v}\right)\tilde{\sigma}\left(\tilde{r}\right). \tag{4.49}$$

Using (4.37), (4.49) and adding and subtracting the terms $\tilde{\rho}_t A\left(\tilde{v}\right)$ and $\tilde{\sigma}\left(\tilde{r}\right)\tilde{\rho}_t B\left(\tilde{v}\right)$, equation (4.38) takes the following form:

$$\begin{aligned} &\left(\tilde{\rho}A\left(\tilde{v}\right)\right)_\tau + \left(\tilde{\rho}\tilde{v}A\left(\tilde{v}\right)\right)_\xi + \tilde{\sigma}\left(\tilde{r}\right)\left(\tilde{\rho}B\left(\tilde{v}\right)\right)_\tau + \tilde{\sigma}\left(\tilde{r}\right)\left(\tilde{\rho}\tilde{v}B\left(\tilde{v}\right)\right)_\xi + \left(\tilde{P}\left(\tilde{\rho}\right)\right)_\xi = \\ &-\frac{v_{\max}^2 v^* \tilde{\sigma}'\left(\tilde{r}\right)}{\left(v_{\max} - \tilde{v}\right)\tilde{v}}\left(\tilde{\rho}\tilde{P}'\left(\tilde{\rho}\right)\tilde{v}_\xi\right)_\xi - \gamma\tilde{\rho}\left(\tilde{v} - v^*\tilde{\sigma}\left(\tilde{r}\right)\right). \end{aligned} \tag{4.50}$$

Equations (4.37), (4.50) are discretized in the sense of the finite volume method used in Gunawan (2014) and Chapter 3. The obtained discretized macro-GCC model considers, apart from the discretization in time, the discretization of the highway in a finite number n of sections having equal length $\delta\xi$. Each section i (where $i = 1, ..., n$) of the highway may have an on-ramp (Fig. 4.3) or an off-ramp at its upstream boundary. The on-ramp flow (if any) of section i is denoted by $u_{i-1/2}\left(k\right)$, while the off-ramp flow (if any) of section i is denoted by $s_{i-1/2}\left(k\right)$. The time is also discretized with uniform intervals $\delta\tau$. For each discrete time $k\delta\tau$, where $k = 0, 1, 2, ...$ is the discrete time index, the discretized macro-GCC model calculates

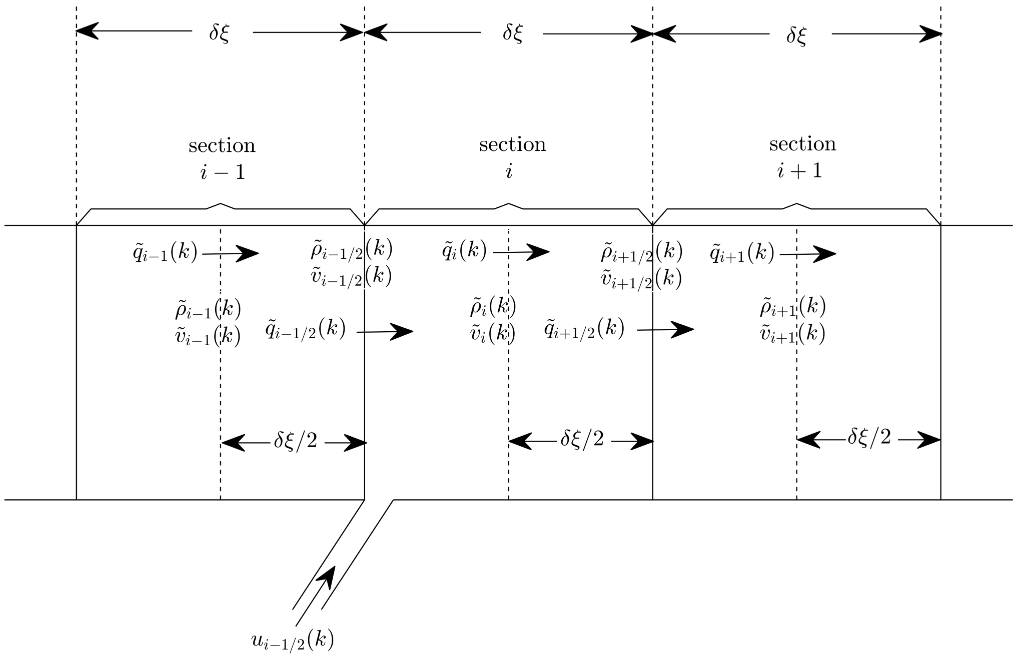

Figure 4.3: Discretization of a highway with an on-ramp within the discretized macro-GCC model.

at each section i its density $\tilde{\rho}_i(k)$ and the mean speed $\tilde{v}_i(k)$. Moreover, it calculates the exit flow $\tilde{q}_{i+1/2}(k)$ crossing the boundary between sections i and $i+1$ during the time interval $(k\delta\tau, (k+1)\,\delta\tau]$ (see Fig. 4.3). In the following discretization, the variables $\tilde{\rho}_{i+1/2}(k)$, $\tilde{v}_{i+1/2}(k)$, $\tilde{q}_i(k)$ are also used for the calculation of the section's density, mean speed, and flow, where $\tilde{v}_{i+1/2}(k)$ and $\tilde{\rho}_{i+1/2}(k)$ are the average speed and average density, respectively, of the sections i and $i+1$ at time $k\delta\tau$ (see the respective equations (4.56) and (4.60)), while $\tilde{q}_i(k)$ is the flow at the center of section i during the time interval $(k\delta\tau, (k+1)\,\delta\tau]$ (see (4.72) and Fig. 4.3). The equations of the space-time discretized macro-GCC model are given as follows:

$$\tilde{\rho}_i(k+1) = \tilde{\rho}_i(k) + \frac{\delta\tau}{\delta\xi}\left(\tilde{q}_{i-1/2}(k) - \tilde{q}_{i+1/2}(k) + u_{i-1/2}(k) - s_{i-1/2}(k)\right), \quad i = 1, ..., n \tag{4.51}$$

$$\tilde{q}_{i-1/2}(k) = \tilde{v}_{i-1/2}(k)\,\tilde{\rho}_{i-1}(k), \ i = 1, ..., n+1 \tag{4.52}$$

$$\tilde{q}_{i+1/2}(k) = \tilde{v}_{i+1/2}(k)\,\tilde{\rho}_i(k), \ i = 0, ..., n \tag{4.53}$$

$$\tilde{v}_{-1/2}(k) = \frac{3\tilde{v}_0(k) - \tilde{v}_1(k)}{2} \tag{4.54}$$

$$\tilde{v}_{i-1/2}(k) = \frac{\tilde{v}_{i-1}(k) + \tilde{v}_i(k)}{2}, \ i = 1, ..., n \tag{4.55}$$

$$\tilde{v}_{i+1/2}(k) = \frac{\tilde{v}_i(k) + \tilde{v}_{i+1}(k)}{2}, \ i = 0, ..., n-1 \tag{4.56}$$

$$\tilde{v}_{n+1/2}(k) = \frac{3\tilde{v}_n(k) - \tilde{v}_{n-1}(k)}{2} \tag{4.57}$$

$$\tilde{v}_{n+3/2}(k) = 3\tilde{v}_{n+1/2}(k) - 2\tilde{v}_n(k) \tag{4.58}$$

$$\tilde{\rho}_{i-1/2}\left(k\right)=\frac{\tilde{\rho}_{i-1}\left(k\right)+\tilde{\rho}_{i}\left(k\right)}{2},\ i=1,...,n \tag{4.59}$$

$$\tilde{\rho}_{i+1/2}\left(k\right)=\frac{\tilde{\rho}_{i}\left(k\right)+\tilde{\rho}_{i+1}\left(k\right)}{2},\ i=0,...,n-1 \tag{4.60}$$

$$\tilde{\rho}_{n+1/2}\left(k\right)=\frac{3\tilde{\rho}_{n}\left(k\right)-\tilde{\rho}_{n-1}\left(k\right)}{2} \tag{4.61}$$

$$\tilde{\rho}_{n+1}\left(k\right)=2\tilde{\rho}_{n+1/2}\left(k\right)-\tilde{\rho}_{n}\left(k\right) \tag{4.62}$$

$$\tilde{\rho}_{n+3/2}\left(k\right)=3\tilde{\rho}_{n+1/2}\left(k\right)-2\tilde{\rho}_{n}\left(k\right) \tag{4.63}$$

$$A_{i-1/2}\left(k\right)=A\left(\tilde{v}_{i-1/2}\left(k\right)\right),\ i=0,...,n+1 \tag{4.64}$$

$$A_{i+1/2}\left(k\right)=A\left(\tilde{v}_{i+1/2}\left(k\right)\right),\ i=0,...,n \tag{4.65}$$

$$B_{i-1/2}\left(k\right)=B\left(\tilde{v}_{i-1/2}\left(k\right)\right),\ i=0,...,n+1 \tag{4.66}$$

$$B_{i+1/2}\left(k\right)=B\left(\tilde{v}_{i+1/2}\left(k\right)\right),\ i=0,...,n \tag{4.67}$$

$$\tilde{r}_{i+1/2}\left(k\right)=\frac{\tilde{P}\left(\tilde{\rho}_{i+3/2}\left(k\right)\right)-\tilde{P}\left(\tilde{\rho}_{i+1/2}\left(k\right)\right)}{\delta\xi\,\tilde{\rho}_{i+1/2}\left(k\right)},\ i=0,...,n \tag{4.68}$$

$$\tilde{r}_{i}\left(k\right)=\frac{\tilde{P}\left(\tilde{\rho}_{i+1}\left(k\right)\right)-\tilde{P}\left(\tilde{\rho}_{i}\left(k\right)\right)}{\delta\xi\,\tilde{\rho}_{i}\left(k\right)},\ i=0,...,n \tag{4.69}$$

$$\begin{aligned}&\tilde{\beta}_{i+1/2}\left(k\right)=\beta\left(\tilde{v}_{i+1/2}\left(k\right),\tilde{r}_{i+1/2}\left(k\right)\right)=A_{i+1/2}\left(k\right)+B_{i+1/2}\left(k\right)\tilde{\sigma}\left(\tilde{r}_{i+1/2}\left(k\right)\right),\\&i=0,...,n\end{aligned} \tag{4.70}$$

$$\begin{aligned}\beta_{i+1/2}\left(k+1\right)&=\left(A_{i+1/2}\left(k\right)+B_{i+1/2}\left(k\right)\tilde{\sigma}\left(\tilde{r}_{i+1/2}\left(k+1\right)\right)\right)\frac{\tilde{\rho}_{i+1/2}\left(k\right)}{\tilde{\rho}_{i+1/2}\left(k+1\right)}\\
&+\frac{\delta\tau}{\delta\xi}\left(A_{i-1/2}\left(k\right)+B_{i-1/2}\left(k\right)\tilde{\sigma}\left(\tilde{r}_{i}\left(k+1\right)\right)\right)\frac{\tilde{q}_{i}\left(k\right)}{\tilde{\rho}_{i+1/2}\left(k+1\right)}\\
&-\frac{\delta\tau}{\delta\xi}\left(A_{i+1/2}\left(k\right)+B_{i+1/2}\left(k\right)\tilde{\sigma}\left(\tilde{r}_{i}\left(k+1\right)\right)\right)\frac{\tilde{q}_{i+1}\left(k\right)}{\tilde{\rho}_{i+1/2}\left(k+1\right)}\\
&-\delta\tau\tilde{r}_{i}\left(k+1\right)\frac{\tilde{\rho}_{i}\left(k+1\right)}{\tilde{\rho}_{i+1/2}\left(k+1\right)}\\
&-\frac{v_{\max}^{2}v^{*}\tilde{\sigma}'\left(\tilde{r}_{i}\left(k+1\right)\right)}{\tilde{\rho}_{i+1/2}\left(k+1\right)\left(v_{\max}-\tilde{v}_{i+1/2}\left(k\right)\right)\tilde{v}_{i+1/2}\left(k\right)}\frac{\delta\tau}{\delta\xi}\Bigg(\tilde{\rho}_{i+1}\left(k+1\right)\tilde{P}'\left(\tilde{\rho}_{i+1}\left(k+1\right)\right)\\
&\times\frac{\tilde{v}_{i+3/2}\left(k\right)-\tilde{v}_{i+1/2}\left(k\right)}{\delta\xi}-\tilde{\rho}_{i}\left(k+1\right)\tilde{P}'\left(\tilde{\rho}_{i}\left(k+1\right)\right)\frac{\tilde{v}_{i+1/2}\left(k\right)-\tilde{v}_{i-1/2}\left(k\right)}{\delta\xi}\Bigg)\\
&-\gamma\delta\tau\frac{\tilde{\rho}_{i}\left(k+1\right)}{\tilde{\rho}_{i+1/2}\left(k+1\right)}\left(\tilde{v}_{i+1/2}\left(k\right)-v^{*}\tilde{\sigma}\left(\tilde{r}_{i}\left(k+1\right)\right)\right),\ i=0,...,n\end{aligned} \tag{4.71}$$

$$\tilde{q}_{i}(k)=\frac{\tilde{v}_{i-1/2}\left(k\right)\tilde{\rho}_{i-1}\left(k\right)+\tilde{v}_{i+1/2}\left(k\right)\tilde{\rho}_{i}\left(k\right)}{2},\ i=0,...,n+1 \tag{4.72}$$

$$\tilde{v}_{i+1/2}\left(k+1\right)=\tilde{\beta}^{-1}\left(\beta_{i+1/2}\left(k+1\right)\right),\ i=0,...,n \tag{4.73}$$

$$\tilde{\beta}\left(\tilde{v}\right)=\beta\left(\tilde{v},\tilde{r}_{i+1/2}\left(k+1\right)\right),\ i=0,...,n,\ \tilde{v}\in\left(0,v_{\max}\right) \tag{4.74}$$

$$\tilde{v}_{i}\left(k+1\right)=\frac{\tilde{v}_{i-1/2}\left(k+1\right)+\tilde{v}_{i+1/2}\left(k+1\right)}{2},\ i=1,...,n \tag{4.75}$$

Symbol	**Name**	**Unit**
$\delta\tau$	Discrete time-step	h
$\delta\xi$	Length of each section i	km
k	Discrete time index	$0, 1, 2, ...$
$\tilde{\rho}_i(k), \hat{\rho}_i(k)$	Density, density per width unit of the $i-$th section at time $k\delta\tau$	veh/km, veh/(km·m)
$\tilde{v}_i(k)$	Mean speed of the $i-$th section at time $k\delta\tau$	km/h
$\tilde{\rho}_{i+1/2}(k)$, $\hat{\rho}_{i+1/2}(k)$	Average density, average density per width unit of the sections i and $i+1$ at time $k\delta\tau$	veh/km, veh/(km·m)
$\tilde{v}_{i+1/2}(k)$	Average speed of the sections i and $i+1$ at time $k\delta\tau$	km/h
$\tilde{q}_{i+1/2}(k)$	Exit flow of the $i-$th section during $(k\delta\tau, (k+1)\delta\tau]$	veh/h
$\tilde{q}_i(k)$	Flow at the center of the $i-$th section during $(k\delta\tau, (k+1)\delta\tau]$	veh/h
$u_{i-1/2}(k)$	On-ramp flow of the $i-$th section during $(k\delta\tau, (k+1)\delta\tau]$	veh/h
$s_{i-1/2}(k)$	Off-ramp flow of the $i-$th section during $(k\delta\tau, (k+1)\delta\tau]$	veh/h
w_i	Width of the $i-$th section	m
$\rho_{\max}$	Maximum density	veh/km
$\bar{\rho}$	Interaction density	veh/km
$v_{\max}$	Maximum speed limit of the road	km/h
v^*	Mean speed set-point	km/h
γ	Friction term constant	1/h
ε	Viscosity term constant	dimensionless

Table 4.2: Variables and parameters involved in the discretized macro-GCC model.

where (4.51) is the discretized version of the continuity equation (4.37) and (4.71) is the discretized version of the momentum equation (4.50). Moreover, $\tilde{q}_{1/2}(k)$ is the mainstream demand, while $\tilde{v}_0(k), \tilde{\rho}_0(k)$ are the given origin speed and density. The variables $\tilde{v}_{-1/2}(k)$, $\tilde{\rho}_{n+1}(k)$, $\tilde{\rho}_{n+3/2}(k)$, $\tilde{v}_{n+3/2}(k)$, given by (4.54), (4.62), (4.63), (4.58), are used for the mean speed calculation of the most upstream and downstream sections, i.e. $\tilde{v}_1(k+1)$ and $\tilde{v}_n(k+1)$, through equations (4.71)-(4.75), while the function $\beta(\tilde{v}, \tilde{r})$ is given by (4.46). Note that this is essentially an explicit numerical scheme, since some variables with discrete-time argument $(k+1)$, appearing on the right-hand side of some equations, may be replaced via a corresponding equation involving only variables with argument (k).

In equation (4.71), the terms

$$-\frac{v_{\max}^2 v^* \tilde{\sigma}'\left(\tilde{r}_i\left(k+1\right)\right)}{\tilde{\rho}_{i+1/2}\left(k+1\right)\left(v_{\max}-\tilde{v}_{i+1/2}\left(k\right)\right)\tilde{v}_{i+1/2}\left(k\right)}\frac{\delta\tau}{\delta\xi}\Bigg(\tilde{\rho}_{i+1}\left(k+1\right)\tilde{P}'\left(\tilde{\rho}_{i+1}\left(k+1\right)\right)$$
$$\times\frac{\tilde{v}_{i+3/2}\left(k\right)-\tilde{v}_{i+1/2}\left(k\right)}{\delta\xi}-\tilde{\rho}_i\left(k+1\right)\tilde{P}'\left(\tilde{\rho}_i\left(k+1\right)\right)\frac{\tilde{v}_{i+1/2}\left(k\right)-\tilde{v}_{i-1/2}\left(k\right)}{\delta\xi}\Bigg)$$

$$\delta\tau\tilde{r}_i\left(k+1\right)\frac{\tilde{\rho}_i\left(k+1\right)}{\tilde{\rho}_{i+1/2}\left(k+1\right)}$$

$$-\gamma\delta\tau\frac{\tilde{\rho}_i\left(k+1\right)}{\tilde{\rho}_{i+1/2}\left(k+1\right)}\left(\tilde{v}_{i+1/2}\left(k\right)-v^*\tilde{\sigma}\left(\tilde{r}_i\left(k+1\right)\right)\right)$$

are the discretized versions of the viscosity term, the pressure term, and the friction term, respectively, included in equation (4.50). Starting with the discretized viscosity term, apart from the parameters $v_{\max}$, v^* that are explicitly used, the parameters $\rho_{\max}$, $\bar{\rho}$, and ε are also included through the functions $\tilde{P}'\left(\tilde{\rho}_i\left(k+1\right)\right)$ (see (4.40), (4.41)) and $\tilde{\sigma}'\left(\tilde{r}_i\left(k+1\right)\right)$ (see (4.15)), respectively. The discretized pressure term includes the parameters $\rho_{\max}$, $\bar{\rho}$ through the discrete values $\tilde{r}_i\left(k+1\right)$ (see (4.69) and (4.70), (4.71)), and finally the discretized friction term includes the constant ε through the function $\tilde{\sigma}\left(\tilde{r}_i\left(k+1\right)\right)$ (see (4.15)), and the parameters γ, v^*.

To cover the case of width-varying roads, the following variable changes

$$\tilde{\rho}_0\left(k\right)=\hat{\rho}_0\left(k\right)w_1,\ \tilde{\rho}_{1/2}\left(k\right)=\hat{\rho}_{1/2}\left(k\right)w_1,$$

$$\tilde{\rho}_{n+1}\left(k\right)=\hat{\rho}_{n+1}\left(k\right)w_n,\ \tilde{\rho}_{n+3/2}\left(k\right)=\hat{\rho}_{n+3/2}\left(k\right)w_n,$$

$$\tilde{\rho}_i\left(k\right)=\hat{\rho}_i\left(k\right)w_i,\ \tilde{\rho}_{i+1/2}\left(k\right)=\hat{\rho}_{i+1/2}\left(k\right)w_i,\ i=1,...,n$$

are used in equations (4.71)-(4.75), where all $\hat{\rho}$ variables are densities per road width unit at the corresponding sections and times, and w_i is the width of the i−th section. In case section i has changing width (e.g. being a funnel section), the parameter w_i equals its average width. The variables and parameters involved in the discretized macro-GCC model are summarized in Table 4.2.

4.5 Model calibration procedure

Given ground-truth traffic data from a highway, the calibration (or parameter estimation or model identification) of a macroscopic traffic flow model aims at specifying the free model parameters such that the macroscopic model, fed with appropriate initial conditions and boundary and external data, reproduces the available traffic data of the highway with the highest possible accuracy (see Papamichail et al. (2023), Spiliopoulou et al. (2017)). It is noted that, apart from macroscopic traffic flow models, also microscopic or micro-macro traffic models may undergo a calibration procedure (see Papathanasopoulou et al. (2016), Tang et al. (2024), Punzo et al. (2021), Punzo et al. (2014), Monteil et al. (2014), Pasquale et al. (2018)) to improve their modelling accuracy. In lack of real traffic data and according to the aims of this study, the discrete-time GCC is applied to individual vehicles within microscopic simulation of two traffic scenarios, described in Section 4.6, to produce two corresponding sets of ground-truth data to be used in the calibration procedure.

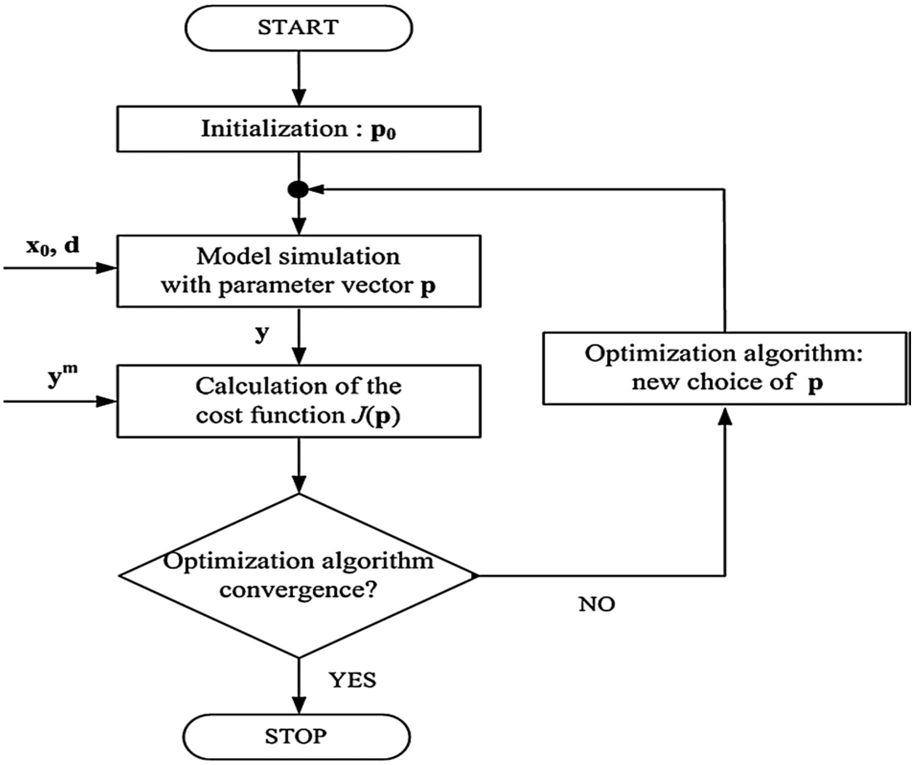

Figure 4.4: Calibration procedure.

The discretized macro-GCC model equations presented in Section 4.4.2 may be summarized and expressed in the following general discrete-time state-space form

$$\begin{aligned} \mathbf{x}(k+1) &= f\left[\mathbf{x}(k), \mathbf{d}(k), \mathbf{p}\right], \; k = 0, 1, ..., K-1 \\ \mathbf{x}(0) &= \mathbf{x}_0 \end{aligned} \tag{4.76}$$

where $\mathbf{x}$ stands for the state vector, $\mathbf{d}$ is the external variable vector, and $\mathbf{p}$ is the free-parameter vector. In particular, for the discretized macro-GCC model, the state vector $\mathbf{x}$ includes the section densities $\tilde{\rho}_1(k), ..., \tilde{\rho}_n(k)$ and mean speeds $\tilde{v}_1(k), ..., \tilde{v}_n(k)$; the external variable vector $\mathbf{d}$ consists of the origin speeds $\tilde{v}_0(k)$ and densities $\tilde{\rho}_0(k)$, the mainstream and on-ramp inflows denoted by $\tilde{q}_{1/2}(k)$ and $u_{i-1/2}(k)$, respectively, and the off-ramp flow $s_{i-1/2}(k)$; while $\mathbf{p}$ holds the unknown model parameters $\rho_{\max}$, $\bar{\rho}$, ε,γ that need to be specified. Note that $\mathbf{p}$ may also include a design parameter $\bar{c}$ used in the expression of the pressure function $\tilde{P}(\tilde{\rho})$ (see Section 4.6).

If the initial state $\mathbf{x}_0$ is given and the external vector $\mathbf{d}(k)$ is known over the time horizon $k = 0, 1, ..., K-1$, then the parameter estimation problem can be formulated as a nonlinear least-squares output error problem which aims at the minimization of the discrepancy between the model estimations and the ground-truth data by use of the following quadratic cost function

$$J(\mathbf{p}) = \sum_{k \in M} \left\| \mathbf{y}(k) - \mathbf{y}^m(k) \right\|_{\mathbf{Q}}^2 \tag{4.77}$$

subject to (4.76), where $\mathbf{Q}$ is a positive definite diagonal weighting matrix, and $\mathbf{y}(k) = \mathbf{g}(\mathbf{x}(k))$ is the model output vector. In the present study, the output vector $\mathbf{y}(k)$ includes the flows and mean speeds of all sections of the highway. Accordingly, the ground-truth vector $\mathbf{y}^m(k)$ includes the flows and speeds of all highway sections, resulting from the microscopic simulation with the discrete-time GCC. Finally, $M \subseteq \{1, 2, ..., K\}$.

Since the parameters of the macroscopic model are linked with the parameters of the microscopic GCC through the relations of Table 4.1, the parameter values of the discretized macro-GCC model may be searched for in a region around the values of the corresponding microscopic parameters. The described parameter estimation problem is a non-convex least-squares optimization problem that has multiple local minima, hence gradient-based algorithms are not appropriate. Therefore, to calibrate the discretized macro-GCC model, the Nelder-Mead algorithm is used (see Lagarias et al. (1998), Nelder and Mead (1965)), which is a derivative-free optimization algorithm that is more likely to locate a good local minimum. The model calibration procedure is carried out by use of the CALISTO software tool (Spiliopoulou et al. (2014)). Thus, as the Nelder-Mead algorithm requires, for any choice of the parameter vector **p**, the value of the cost function is computed as illustrated in Fig. 4.4. The routine attempts to improve the value of the cost function in subsequent iterations, until a local minimum is reached.

4.6 Macro-GCC model calibration results

4.6.1 Microscopic simulation settings

In this section, two infrastructure scenarios are presented for which the discretized macro-GCC model is calibrated to fit macroscopic traffic data (section flows, densities, and mean speeds) collected from microscopic simulation using the sampled-data model (4.27)-(4.36) under the control inputs (4.17), (4.21) provided by the GCC for each individual vehicle. In the first scenario, a highway with an on-ramp and an off-ramp is considered, while in the second scenario a highway that includes a width-reducing funnel is considered.

For both scenarios, the time horizon of the microscopic simulation was 1 h. The length of each vehicle is set to $\sigma_i = 4$ m and the width equals 1.93 m. Moreover, the desired speed of each vehicle is chosen randomly (with uniform distribution) within the range $[25, 32]$ m/s $=$ $[90, 115.2]$ km/h. For both scenarios (ramps case and funnel case), the sampled-data model (4.27)-(4.36) was applied with $F_{\min} = -3$ m/s^2 and $F_{\max} = 2$ m/s^2 for the acceleration limits, the values of the parameters shown in Table 4.3, and the functions:

Parameters	**Values**
L (m)	5
$v_{\max}$ (m/s)	35
φ (rad)	0.45
γ (1/s)	0.05
λ (m)	100
ε	10^{-3}
$\bar{c}$	3×10^{-4}
p	5.3
Γ	1
$\bar{b}$	0.9
c	1.6

Table 4.3: Values of the microscopic parameters used for both calibration scenarios (ramps case and funnel case).

$$V(d) = \begin{cases} \bar{c}\Big((\lambda - L)\,(3\lambda - 3L - 2)\ln\left(\frac{\lambda-L}{d-L}\right) \\ +\,(1 - 6\lambda + 3L)\,(\lambda - d) \\ +\frac{3}{2}\left(\lambda^2 - d^2\right) + \frac{(\lambda-L)(\lambda-d)}{d-L}\Big),\ L < d \leq \lambda \\ \qquad 0,\ d > \lambda \end{cases} \tag{4.78}$$

$$U(y) = \begin{cases} \left(\frac{1}{1-y^2} - c\right)^2, \ y \in \left(-1, -\frac{\sqrt{c-1}}{c}\right) \cup \left(\frac{\sqrt{c-1}}{c}, 1\right) \\ 0, \ y \in \left[-\frac{\sqrt{c-1}}{c}, \frac{\sqrt{c-1}}{c}\right] \end{cases} \tag{4.79}$$

$$\tilde{\sigma}(\tilde{r}) = \begin{cases} 1, \ \tilde{r} \leq \varepsilon \\ \exp\left(-(\tilde{r}-\varepsilon)^3\right), \ \tilde{r} > \varepsilon \end{cases} \tag{4.80}$$

The functions (4.78), (4.80) are involved in the control input F_i (4.17), while the function (4.79) is used in the control input δ_i (4.21). Recall that the potential function (4.78) is used for avoiding collisions and satisfies (4.11), (4.12), while the potential function (4.79) is used for preventing road boundary violation and satisfies (4.13), (4.14). Moreover, the constant $\bar{c}$ included in (4.78) is a design parameter that allows to increase or decrease the repulsion strength between vehicles.

The highway in both scenarios has a length of 3 km and is subdivided into 10 sections of 300 m length each. Outflow, mean speed, and density measurements were collected every 10 s for each section as ground-truth data for the calibration procedure and for further assessment. More specifically, the outflow is measured as the number of vehicles that crossed the downstream edge of each section within every time interval of 10 s, the mean speed is the average of the vehicle speeds inside each section at the time instants $t_k = 10k$ (s), $k = 0, 1, ..., 360$, while the density is measured as the number of vehicles inside each section at the time instants $t_k = 10k$ (s), $k = 0, 1, ..., 360$, divided by the length of the section.

4.6.2 Macroscopic simulation settings

Using the relations $\tilde{P}(\tilde{\rho}) = -mV'\left(\frac{m}{\tilde{\rho}}\right)$ and $\bar{\rho} = \frac{m}{\lambda}$ (see Table 4.1), it follows that the pressure function of the discretized macro-GCC model is given by

$$\tilde{P}(\tilde{\rho}) = -\lambda\bar{\rho}V'\left(\lambda\frac{\bar{\rho}}{\tilde{\rho}}\right) \tag{4.81}$$

where λ is the interaction distance used in the microscopic GCC (see Table 4.3), $\bar{\rho}$ is the interaction density, and $V : (L, +\infty) \to \mathbb{R}_+$ is the potential function used in the control input (4.17), given by (4.78). Notice that the design parameter $\bar{c}$ is also included in (4.81) through (4.78). Therefore, a link between the potential function (4.78) used for the microscopic GCC and the pressure function (4.81) of the discretized macro-GCC model is provided. By changing the values of the microscopic parameters included in (4.78) or even the entire function, we can influence the produced model estimations through the pressure function (4.81). In real conditions, parameter values or functions included in the GCC for vehicle movement may be leveraged to 'create' a traffic fluid with desired properties.

The parameters $\rho_{\max}$, $\bar{\rho}$, ε, γ, $\bar{c}$ are chosen to be calibrated, while the constant λ and the maximum speed limit of the road $v_{\max}$ are fixed and take the same values used for the microscopic simulation (see Table 4.3). The speed set-point v^* is also fixed and is set to be equal to 102 km/h, i.e., the average of the range of vehicle desired speeds used in the microscopic simulation. The parameters $\rho_{\max}$, $\bar{\rho}$ used in the discretized macro-GCC model and the microscopic parameters λ, L are linked through the relations $\rho_{\max} = \frac{m}{L}$ and $\bar{\rho} = \frac{m}{\lambda}$ (see Table 4.1). However, it is not possible to know in advance the total mass m of vehicles, and for this reason the parameters $\rho_{\max}$, $\bar{\rho}$ are included in the calibration. Moreover, the constant ε, has the potential to activate or disactivate the discretized viscosity term (see Section 4.4.2), affecting the model's speeds. Thus, it needs to be optimized to capture a possible speed reduction in the merging area. Since the design parameter $\bar{c}$ is involved in both the potential function (4.78) and the pressure function (4.81), the value shown in Table 4.3 could be used.

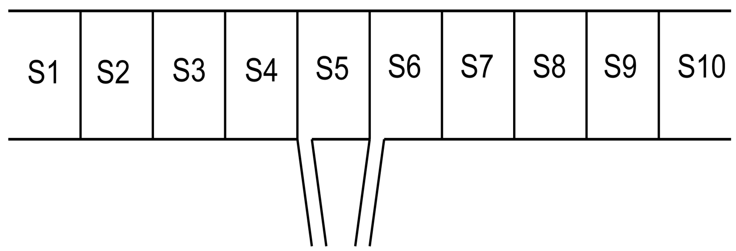

Figure 4.5: Sketch of the highway stretch for the ramps case.

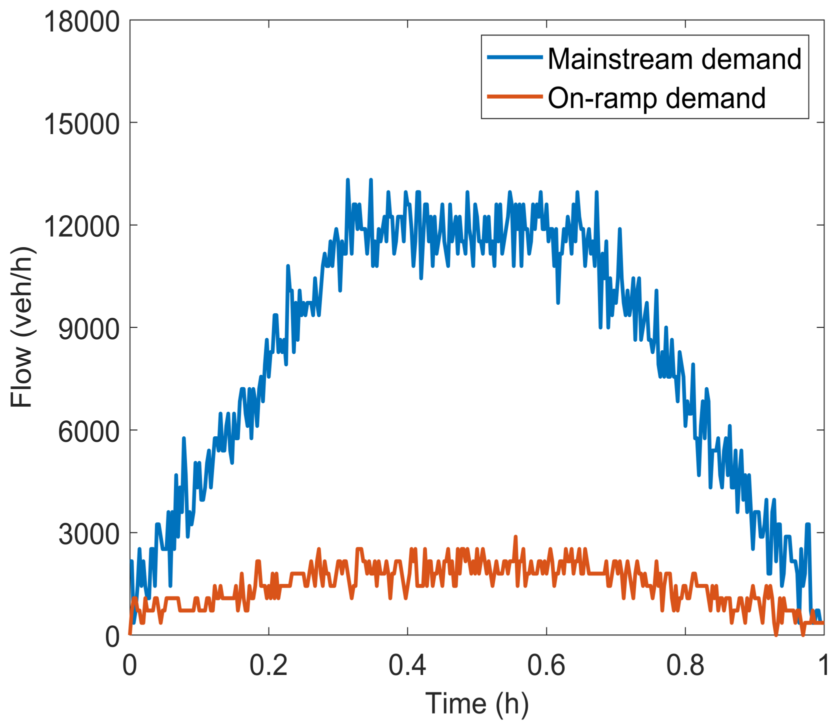

Figure 4.6: Mainstream and on-ramp demands.

However, for the pressure function, the parameter $\bar{c}$ may need a different value than that of the microscopic simulation (Table 4.3), to reflect the tendency of vehicles to accelerate or decelerate and therefore it is chosen to be calibrated.

For the resulting optimal values of the parameters $\rho_{\max}, \bar{\rho}$, it is expected that $\frac{\rho_{\max}}{\bar{\rho}} = \frac{\lambda}{L}$, as follows from the relations of Table 4.1. In addition, it is expected that the parameter γ should be close to the value used for the microscopic simulation (Table 4.3). For the time step, the value $\delta\tau = 2.8 \times 10^{-4}$ h is used.

For the calibration procedure, the diagonal elements of the diagonal weighting matrix $\mathbf{Q}$, used in the cost function (4.77), that correspond to speeds are set to 1, while those that correspond to flows are set to 0.01 due to higher flow values. These values, as well as the values used for the parameters of the Nelder-Mead algorithm were selected based on previous works (see Papamichail et al. (2023), Spiliopoulou et al. (2017)).

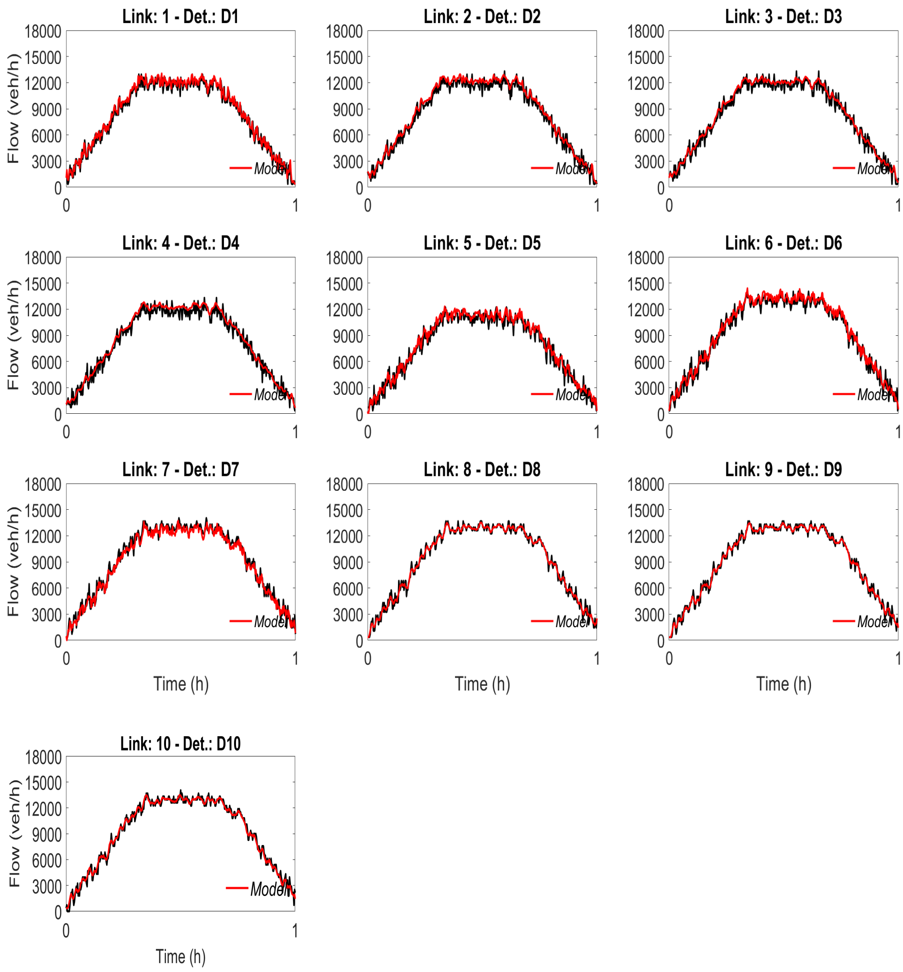

Figure 4.7: Traffic flows of highway links (sections): Ground truth (black) versus macroscopic model estimations (red) – Ramps case.

4.6.3 Ramps case

In the ramps case, the highway stretch of 3 km in length features a constant width of 10.2 m (corresponding to the width of 3 conventional lanes) and includes an on-ramp and an off-ramp. A sketch of the highway stretch is presented in Fig. 4.5. The stretch is divided into 10 sections (S1-S10), with a length of 300 m each, that match the sections used for the macroscopic model. Section 5 includes an off-ramp while section 6 includes an on-ramp. The demand trajectories at the highway entrance and the on-ramp feature a trapezoid profile and are illustrated in Fig. 4.6.

After calibrating the discretized macro-GCC model, the resulting optimal values of the parameters $\rho_{\max}, \bar{\rho}, \gamma$ were 498 veh/km, 24.8 veh/km, and 181 1/h, respectively. Thus, $\frac{\rho_{\max}}{\bar{\rho}} = \frac{498}{24.8} \approx 20 = \frac{\lambda}{L}$ which means that the resulting optimal values of $\rho_{\max}$, $\bar{\rho}$ were close to the expected ones. Also, the optimal value of the parameter γ was expected, since 181 $1/\mathrm{h} \approx 0.05$ $1/\mathrm{s}$, showing that it is roughly the same as the value used for the microscopic simulation (see Table 4.3). The optimal values for the rest of the calibration parameters, namely $\bar{c}$, ε, were 2×10^{-4}, and 10^{-2}, respectively, which are also close enough to the corresponding values of the microscopic simulation (see Table 4.3).

The calibration of the discretized macro-GCC model for fitting the ground-truth traffic

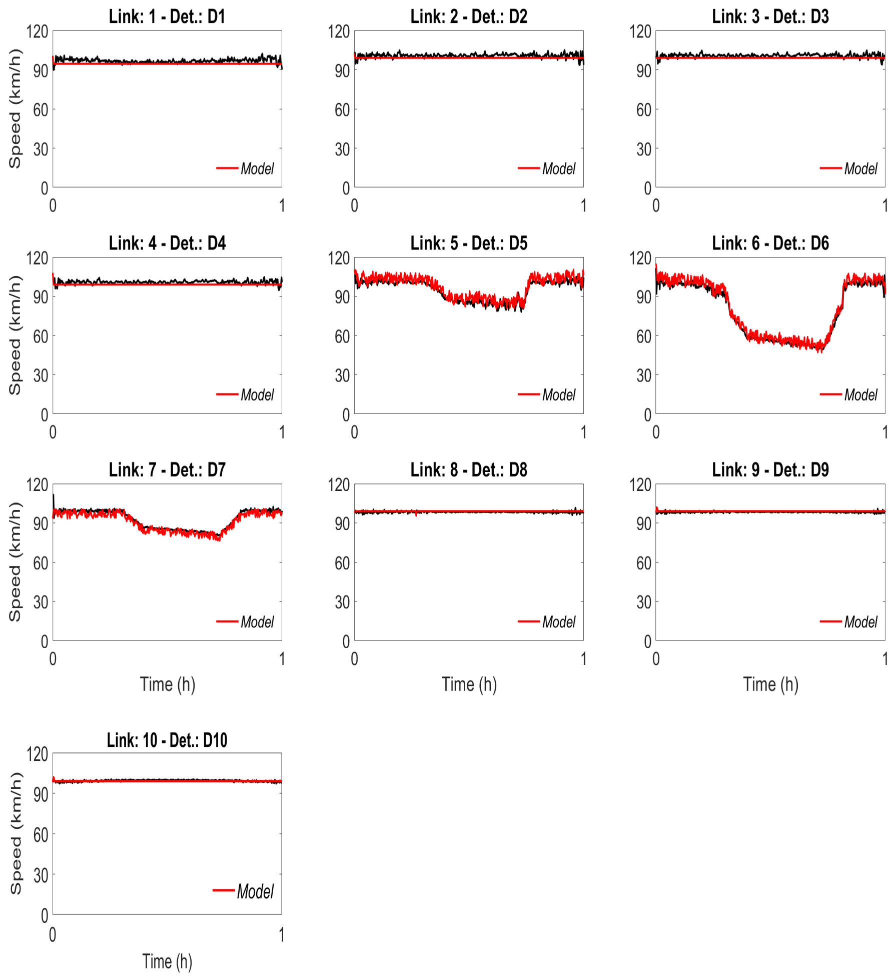

Figure 4.8: Mean speeds of highway links (sections): Ground truth (black) versus macroscopic model estimations (red) – Ramps case.

data produced via the microscopic (4.27) - (4.36) vehicle model, yields the trajectories illustrated in Figs. 4.7 - 4.9. It may be seen that, during the pick of the mainstream and on-ramp demand, from around 0.33 h to 0.67 h (see Fig. 4.6), congestion is created in the merging area (section 6), due to the on-ramp inflow, and the congestion spills back on section 5. In section 7, the vehicles start to accelerate and obtain again the free flow speed when they reach section 8. A small capacity drop can be observed in the flow diagram of section 6 during congestion (Fig. 4.7), particularly when speed decreases and density increases more strongly.

The Figs. 4.7 - 4.10 show that the calibrated macroscopic model reproduces with high accuracy the traffic conditions that appear in the microscopic simulation of lane-free traffic for automated vehicles using GCC. More specifically, the discretized macro-GCC model reproduces the speed reduction in section 6, the occurring spillback onto section 5, as well as the acceleration of the vehicles in section 7. Moreover, it reproduces the slight capacity drop observed in section 6 (Fig. 4.7).

The fundamental diagrams (flow versus density) that arise from the microscopically produced data for each section of the highway are presented in Fig. 4.11. Interesting hysteresis phenomena can be observed in the fundamental diagram of section 6 implying that the vehicle spacing is different under acceleration conditions. The hysteresis phenomena are reproduced

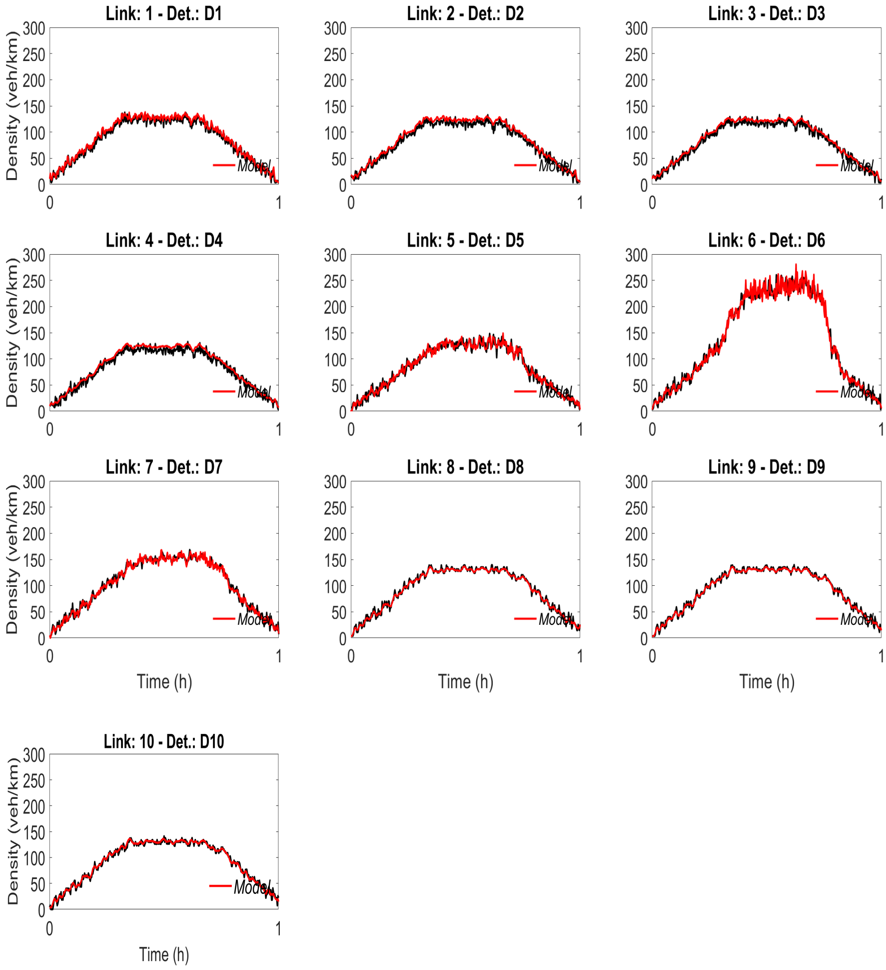

Figure 4.9: Densities of highway links (sections): Ground truth (black) versus macroscopic model estimations (red) – Ramps case.

by the calibrated macroscopic model as shown in Figs. 4.7 - 4.10.

Figure 4.12 shows how the value of the cost function (4.77) is affected by using a range of different values for one parameter at a time, while optimal values are used for the rest of the parameters. Starting with the sensitivity diagram of $\bar{\rho}$, it is observed that the value of the cost function increases for values much different than the optimal one. Using small values for the interaction density $\bar{\rho}$ (e.g. 5 to 15 veh/km), implies that the viscosity and pressure terms are activated at low density, which microscopically means that there is interaction even between very distant vehicles. As a result, the vehicles start slowing down even in cases where there is enough space to accelerate. Therefore, a huge difference between the model's speed outcomes and the microscopically produced speeds is observed, especially in the highway sections where free flow conditions hold, causing an increase in the cost function value. As we approach the optimal value 24.8 veh/km, the actual level of density for which the vehicles interact is reached and consequently the model's estimations match better the measured traffic data, as shown in the obtained small value of the cost function. In the case of using higher values than the optimal one (e.g. 30 to 50 veh/km), the viscosity and pressure terms are not activated even at high densities, which microscopically implies that a vehicle does not interact with its surrounding vehicles even when they are close enough. As a consequence, there is no sufficient reduction in speed, failing to reproduce the congestion

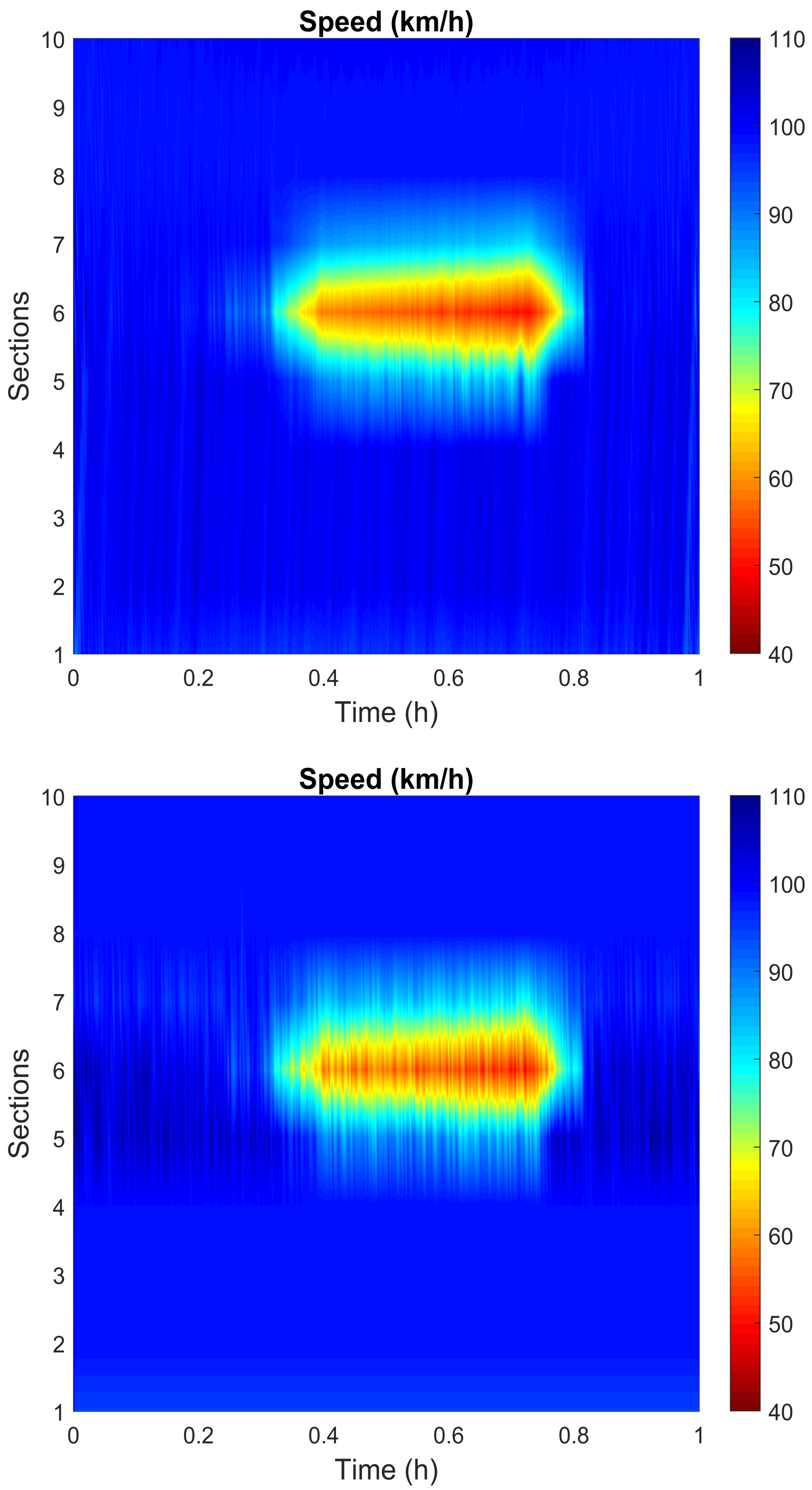

Figure 4.10: Space-time diagrams of microscopically produced speed (top) versus macroscopic model's speed estimations (bottom) – Ramps case.

observed in the merging area (section 6). This is also reflected in the increased value of the cost function.

In the sensitivity diagram of $\rho_{\max}$, using values lower than the optimal one (e.g. 410 to 450 veh/km) indicates that the value of $\rho_{\max}$ is approached at lower densities and therefore the pressure function $\tilde{P}(\tilde{\rho})$ goes fast to infinity (see (4.40)). At the microscopic level, this

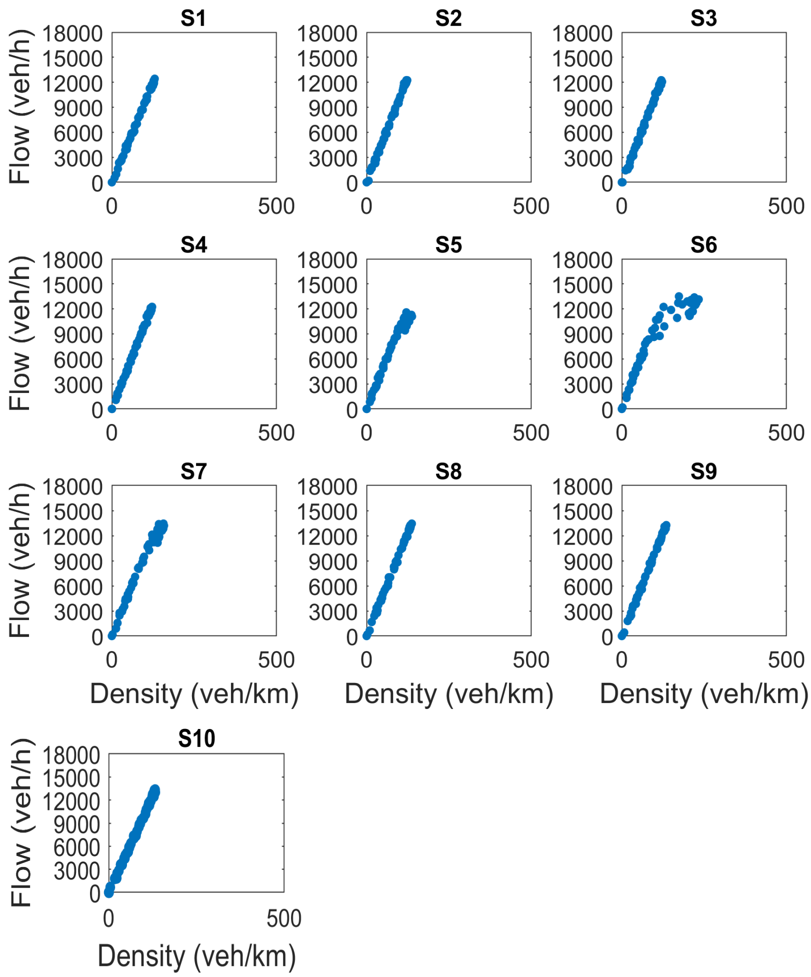

Figure 4.11: Fundamental diagrams with the microscopic simulation data – Ramps case.

means that the vehicles start accelerating earlier than the time observed in the microscopically produced speed. Consequently, the model cannot predict the right place and time and the right duration and extent of the occurring congestion in section 6, causing an increase in the cost function value. As we get closer to the optimal value of 498 veh/km, the improvement of the cost function reflects the model's ability to reproduce the occurring congestion in the right place and time. For higher values than the optimal one (e.g. 510 to 590 veh/km), the value of $\rho_{\max}$ is never approached enough by the model's density outcomes, causing longer duration of the congestion in the merging area, since the pressure function $\tilde{P}\left(\tilde{\rho}\right)$ goes slower to infinity (see (4.40)). Microscopically, this means that the acceleration rate of the vehicles becomes slower, making the duration of the congestion longer. Therefore, the discrepancy between the model's outcomes and the measured traffic data is increased as reflected in the increased cost function value.

Apart from the interaction density $\bar{\rho}$ included in the pressure function $\tilde{P}\left(\tilde{\rho}\right)$, the viscosity term can be activated or disactivated based on the values used for the constant ε. If ε is small enough (e.g., 10^{-6} to 10^{-3}), as shown in the sensitivity diagram of ε (Fig. 4.12), it can be easily exceeded by the values $\tilde{r}_i\left(k+1\right)$ (4.69) making the value of $\tilde{\sigma}'\left(\tilde{r}_i\left(k+1\right)\right)$ nonzero and activating the viscosity term. Note that the viscosity term can be activated only if the pressure term is nonzero. In a different case, $\tilde{r}_i\left(k+1\right)$ becomes zero, meaning that it

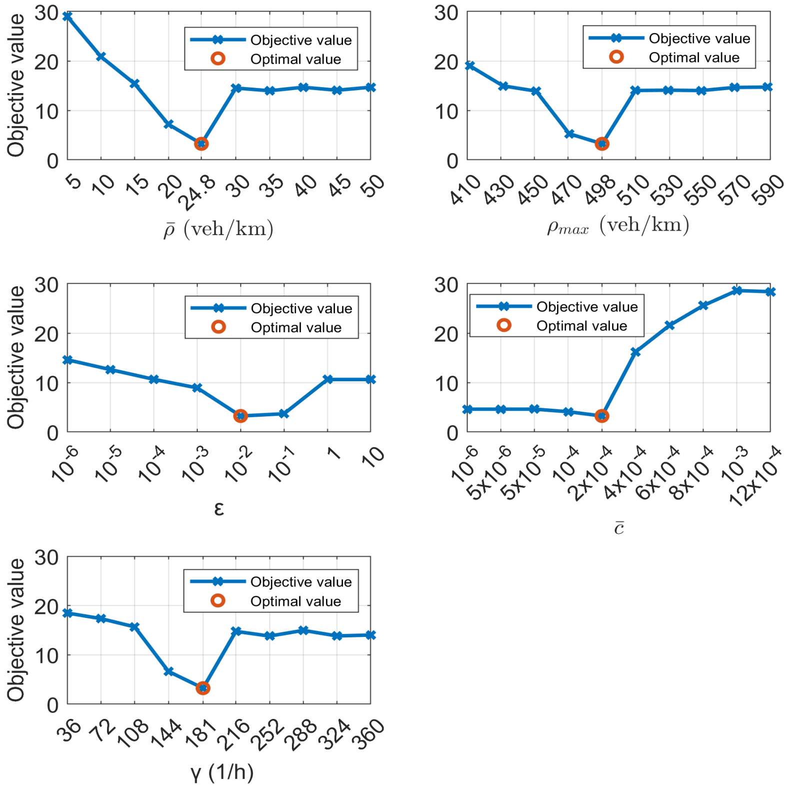

Figure 4.12: Sensitivity diagrams for the calibration parameters – Ramps case.

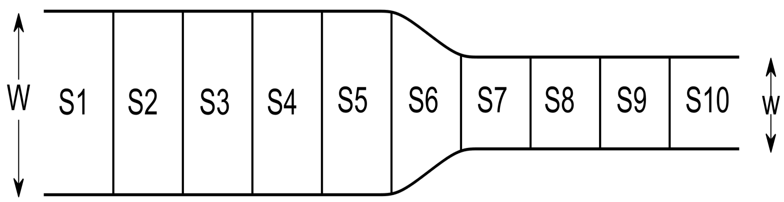

Figure 4.13: Sketch of the highway stretch for the funnel case.

is always smaller than the positive constant ε. Hence, $\tilde{\sigma}'\left(\tilde{r}_i\left(k+1\right)\right) = 0$ as follows from (4.15), and the viscosity term is never activated. Therefore, using very small values for ε implies that there are no times that only the pressure term is activated, since almost always $\tilde{r}_i\left(k+1\right)$ exceeds ε. Thus, the viscosity and pressure terms are simultaneously activated causing a stronger speed reduction in the merging area (section 6) than that of the measured traffic data, and consequently an increase of the cost function. As we get closer to the optimal value 10^{-2}, the activation of the viscosity and pressure terms is adjusted according to the conditions in the microscopically produced data, improving the cost function. For higher values, the opposite case is observed, where it is more difficult to have the value of ε exceeded

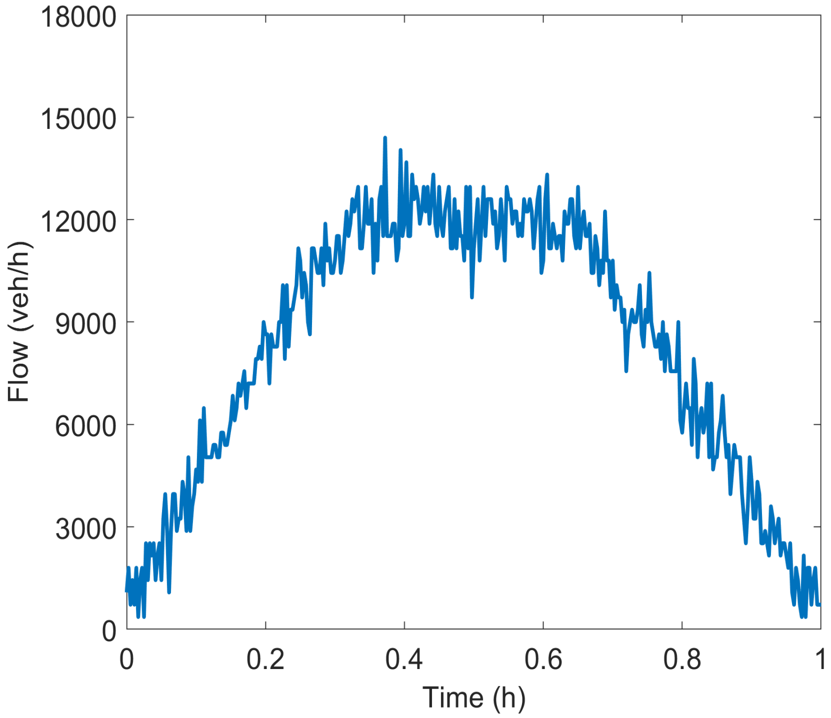

Figure 4.14: Mainstream demand for the funnel case.

by $\tilde{r}_i\,(k+1)$ and therefore the viscosity term is not activated as many times as previously. This causes a weaker speed reduction in the merging area (section 6) and hence an increase in the cost function value.

In the sensitivity diagram of the design parameter $\bar{c}$, there is a low sensitivity area from 10^{-6} to 2×10^{-4}, where 2×10^{-4} is the obtained optimal value. The small increase in the cost function value observed in this area is due to weaker reduction in speed in the merging area, which is less than the speed reduction in the measured traffic data. It should be noted that zero value cannot be used for $\bar{c}$, because then the viscosity and pressure terms would be completely dropped and a constant speed solution would result for all highway sections, which obviously contradicts the dynamic conditions appearing in the traffic data. Microscopically, the use of $\bar{c}=0$ implies that the potential function (4.78) used for avoiding collisions is completely omitted and therefore the collision occurrence is inevitable. For higher values than the optimal one, the pressure function increases, meaning at the microscopic level that the vehicles start accelerating earlier at the congestion head than the time observed in the microscopically produced speed. Consequently, the actual duration of the congestion cannot be reproduced accurately by the macroscopic model, and the value of the cost function increases.

Finally, the parameter γ is included in the friction term and describes the tendency of vehicles to adjust their speed to the given speed set-point v^*. Using lower values than the optimal one (e.g., 36 to 108 1/h), microscopically means that the vehicles have the tendency to adjust their speed to the speed set-point very fast, failing to reproduce the speed reduction observed in sections 5, 6, and 7 of the measured traffic data. This is reflected in the increased value of the cost function. As the optimal value 181 1/h is approached, the tendency of vehicles to obtain the speed set-point is adjusted according to the conditions that appear in the microscopically produced data, and therefore the cost function value is improved. For higher values than the optimal one, the vehicles are more sluggish in approaching the speed set-point, and as a result there is a delay in obtaining again the free flow speed after the

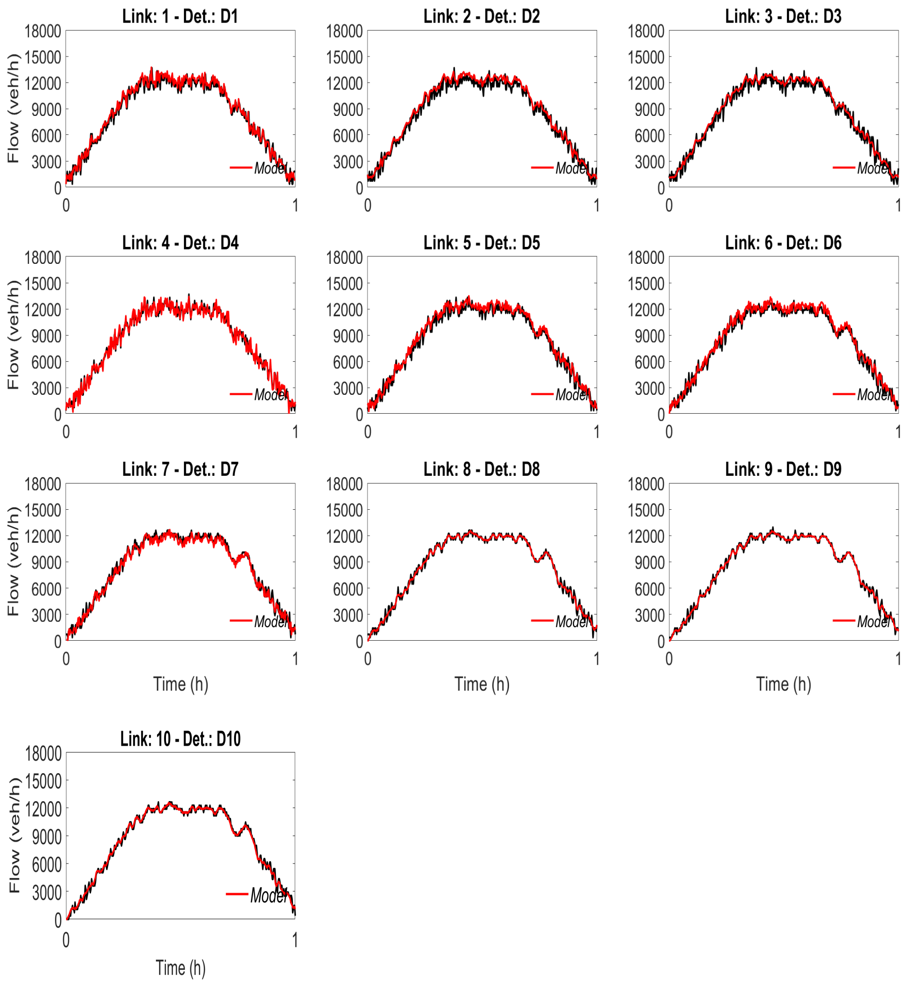

Figure 4.15: Traffic flows of highway links (sections): Ground truth (black) versus macroscopic model estimations (red) – Funnel case.

congestion in section 6. Hence, the model is less accurate in reproducing the microscopically produced speed of sections 7 - 10 causing a worse value for the cost function.

4.6.4 Funnel case

In this scenario, a funnel-like narrowing of the road is considered. Specifically, the highway stretch consists of 3 parts with different widths. The first part is the longest and widest part having length 1500 m and width $W = 13.6$ m (corresponding to the width of 4 conventional lanes); followed by a width-reducing funnel of length 300 m, that leads to the narrower part of the highway that has length 1200 m and width $w = 6.8$ m (corresponding to the width of 2 conventional lanes). A sketch of the highway stretch is presented in Fig. 4.13. The stretch is divided into 10 sections (S1 - S10), with a length of 300 m each, that match the sections used for the macroscopic model. Moreover, the demand trajectory is illustrated in Fig. 4.14.

After calibrating the discretized macro-GCC model, the resulting optimal values of the parameters $\rho_{\max}$, $\bar{\rho}$, γ were 500 veh/km, 25.1 veh/km, and 178 1/h, respectively. Hence, $\frac{\rho_{\max}}{\bar{\rho}} = \frac{500}{25.1} \approx 20 = \frac{\lambda}{L}$, meaning that the resulting optimal values of $\rho_{\max}$, $\bar{\rho}$ were very close to the expected ones and practically the same as in the ramps case. Also, the optimal value of the parameter γ is very close to its corresponding value used for the microscopic simulation (Table 4.3), since 178 $1/\text{h} \approx 0.05$ $1/\text{s}$. The optimal values for the rest of the calibrated

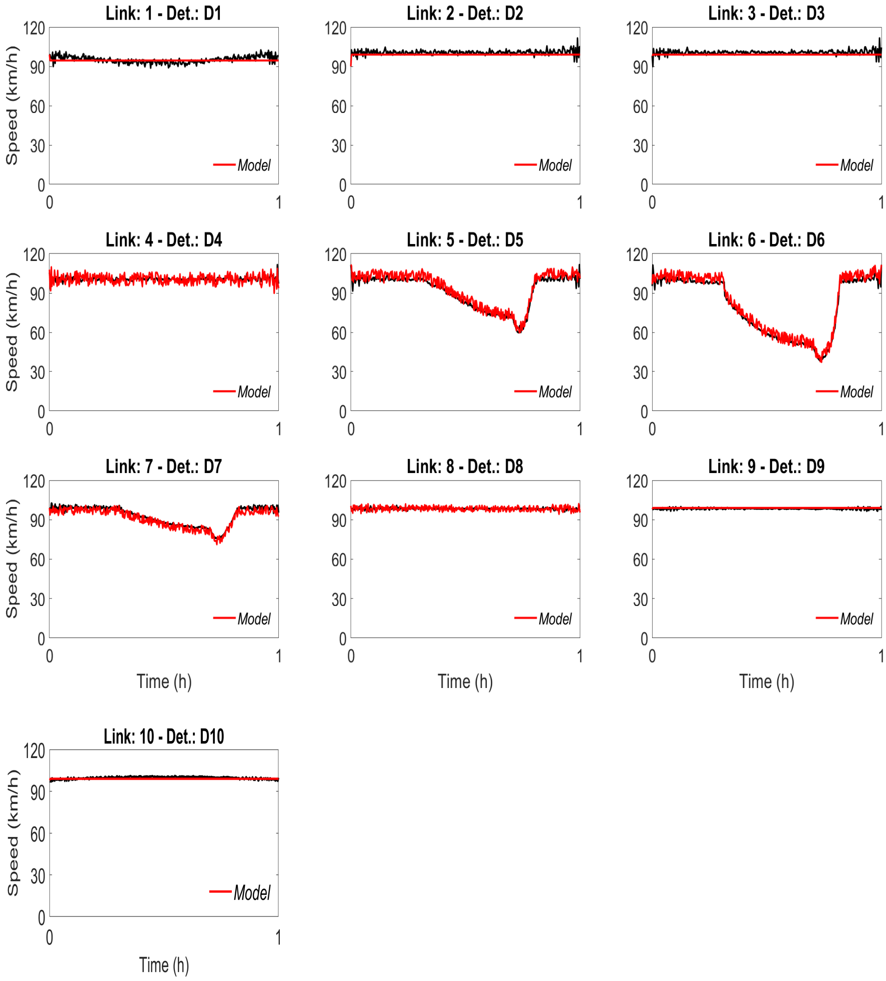

Figure 4.16: Mean speeds of highway links (sections): Ground truth (black) versus macroscopic model estimations (red) – Funnel case.

parameters, namely $\bar{c}$, ε, were 2×10^{-4}, and 10^{-2}, respectively, again close enough to the corresponding values of the microscopic simulation (see Table 4.3) and of the ramps case (Section 4.6.3).

The calibration of the discretized macro-GCC model for fitting the traffic data collected by using the sampled-data model (4.27) - (4.36), yields the trajectories illustrated in Figures 4.15 - 4.17. It is seen that during the pick of the mainstream demand, from around 0.33 h to 0.67 h (see Fig. 4.14), congestion is created at the funnel (section 6), due to the narrowing of the road, and spillback occurs onto section 5. In section 7, the vehicles start to accelerate and obtain again the free flow speed in section 8. In addition, a capacity drop can be observed in the flow diagram of section 6 during congestion (Fig. 4.15), particularly when speed falls below 45 km/h.

In Figures 4.15 - 4.18 it is shown that the calibrated macroscopic model reproduces with high accuracy the traffic conditions that appear in the microscopic simulation of lane-free traffic for automated vehicles. More specifically, the discretized macro-GCC model reproduces the speed reduction of section 6, the occurring spillback onto section 5, as well as the acceleration of the vehicles in section 7. Moreover, it also reproduces the capacity drop observed in section 6 (Fig. 4.15).

Fig. 4.19 depicts the fundamental diagrams of the highway sections that arise from the

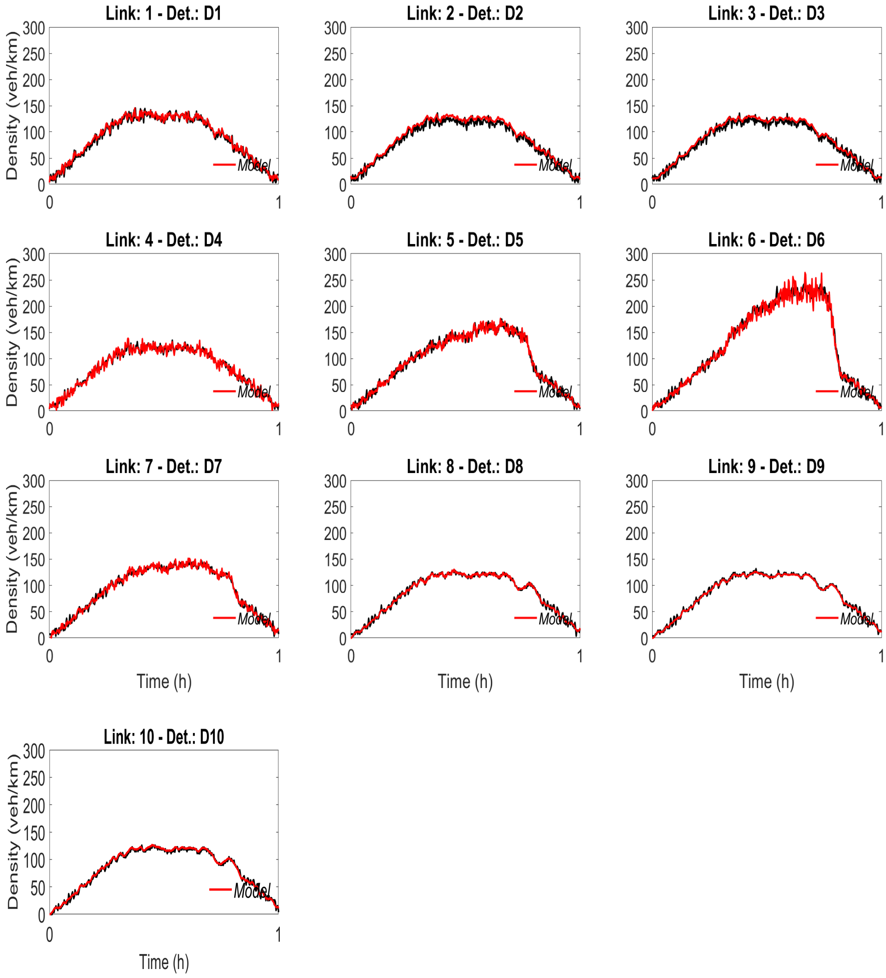

Figure 4.17: Densities of highway links (sections): Ground truth (black) versus macroscopic model estimations (red) – Funnel case.

traffic data of the microscopic simulation. Interesting hysteresis phenomena can be observed in the fundamental diagram of sections 5, 6 and 7, implying that the vehicle spacing is different under acceleration conditions. The hysteresis phenomena are reproduced by the calibrated macroscopic model as shown in Figures 4.15 - 4.18.

Finally, it should be noted that parameter sensitivity properties in the funnel case are similar as in Figure 4.12 and are omitted. More generally, the parameters obtained through independent calibration for the two scenarios, addressing two different infrastructures (ramps case and funnel case), are practically identical, something that highlights the consistency and robustness of the macro-GCC model that may in fact be used in future works even without calibration.

4.7 Conclusions

Lane-free automated-vehicle traffic has been recently proposed and studied using a variety of vehicle movement strategies. In this chapter, a vehicle movement strategy based on nonlinear feedback control is used. More specifically, a class of cruise controllers was used, namely the GCC, that allows the consideration of many real complex driving situations, including

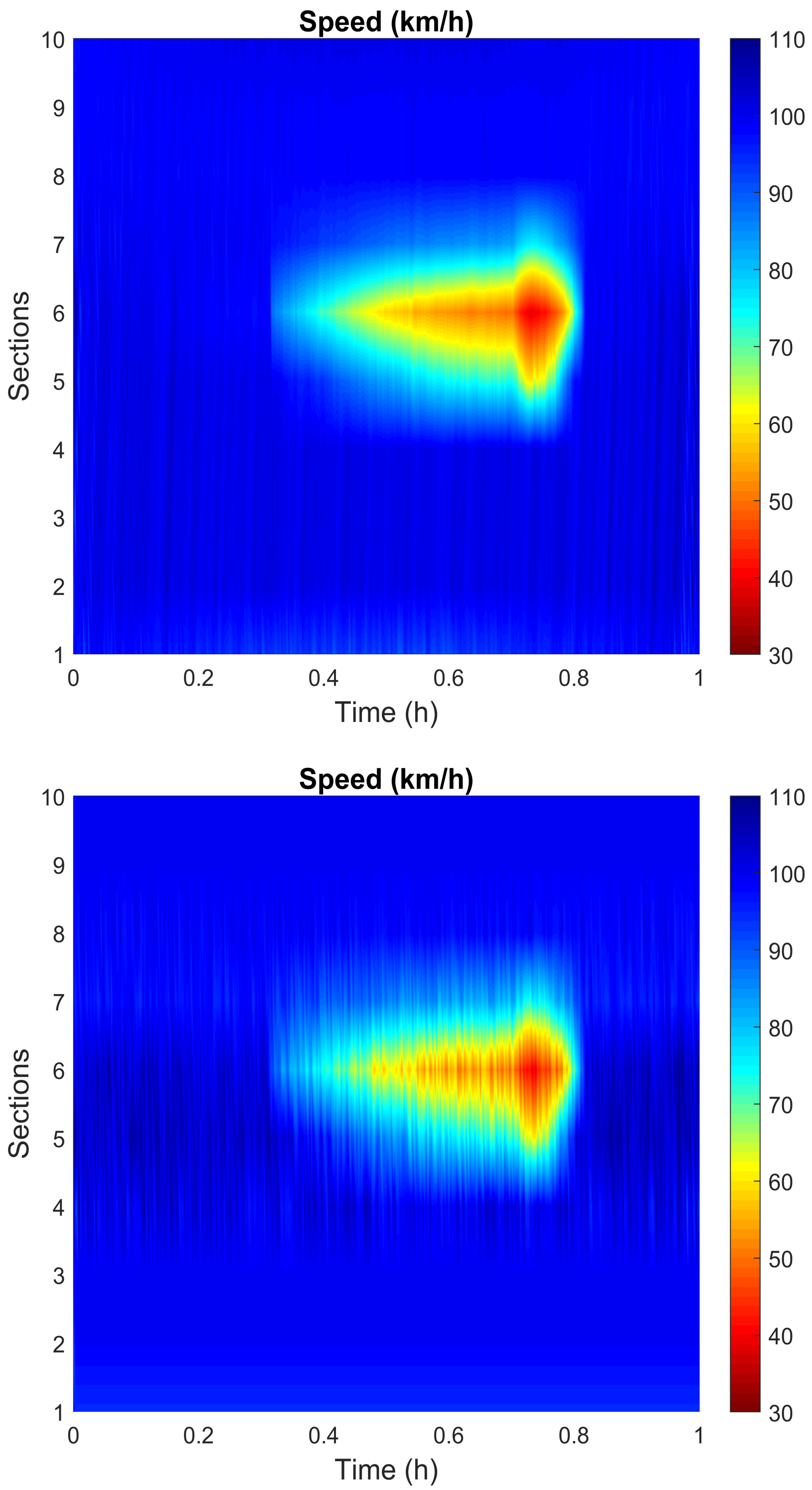

Figure 4.18: Space-time diagrams of microscopically produced speed (top) versus macroscopic model's speed estimations (bottom) – Funnel case.

the presence of on-ramps and off-ramps, the consideration of variable-width roads, the possibility of each vehicle to move within its own corridor, and the potential to have different individual desired speeds for each vehicle. The GCC was applied in microscopic simulation to produce macroscopic traffic data, by adopting a methodology that enables the discretization of the continuous-time bicycle kinematic model. Subsequently, the macro-GCC was

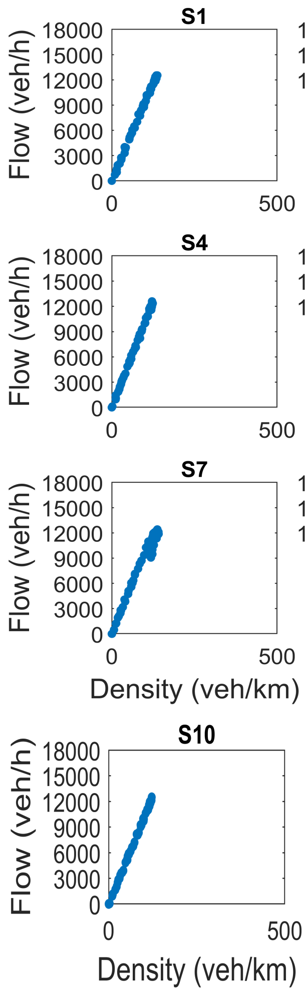

Figure 4.19: Fundamental diagrams with the microscopic simulation data – Funnel case.

discretized and calibrated to fit these data. The macro-GCC has been directly derived from the bicycle kinematic model under the GCC, which provided for certain relations between the microscopic and the macroscopic quantities and parameters.

To evaluate the accuracy of the calibrated macroscopic model, two distinct infrastructure scenarios were considered: first a highway stretch with an off-ramp and an on-ramp; and, second, a highway stretch with a funnel-like narrowing of its width. In both cases, it was shown that the macroscopic model reproduces with high accuracy all the traffic conditions that appear in the microscopically produced traffic data. In particular, the macroscopic model could reproduce the speed reduction caused by the on-ramp inflow and by the narrowing of the road in the respective scenarios, as well as the occurring spillback upstream. In addition, the calibrated macro-GCC model estimates properly the acceleration of vehicles downstream of the congestion area as well as the capacity drop and the hysteresis phenomena observed in both scenarios. Finally, the resulting optimal values for the calibrated parameters of the macroscopic model verified the existing relations between the microscopic and the macroscopic parameters i.e. the optimal values were very close to each other and to the values of the corresponding microscopic parameters used for the microscopic simulation. This highlights the consistency and robustness of the macro-GCC model that may in fact be used in future works even without calibration.

Chapter 5

Conclusions and future work

5.1 Conclusions

The revolution of lane-free AV traffic has already begun with the design and use of many related vehicle movement strategies. In this thesis, the traffic flow emerging from recently proposed decentralized CCs (i.e. the PRCC, and GCC) that can describe the 2-D lane-free movement of CAVs, has been studied. The CCs have been designed using nonlinear feedback control, i.e a control Lyapunov methodology with the Lyapunov function expressed on measures of the total energy of the system. The emerging traffic flow is investigated through macroscopic models that have been formally derived from the bicycle kinematic model (Polack et al. (2017), Rajamani (2012)) under the PRCC, and GCC, respectively. The derived macroscopic models involve the continuity equation and an additional PDE for the mean speed. The speed PDE is strongly reminiscent of the momentum equation for 1-D polytropic compressible fluid flow since it contains an inertial term, a viscosity term with density-dependent viscosity, a pressure term, and a friction term (the analogue of the relaxation term in macroscopic traffic flow models for human drivers). Therefore, it is justified to say that the derived macroscopic models are "fluid-like" models. The presence of many characteristics of the compressible fluid flow (including isotropy) in the obtained macroscopic models stems from the fact that lane-free movement and nudging are allowed by the respective CCs. The derivation is based on particle methods, in which the vehicles are considered as "self-driven" particles of a fluid ("the traffic fluid"). The particle methods link the proposed macroscopic models with the CCs since certain relations between the CC microscopic parameters and the physical properties of the "traffic fluid" are provided. In this sense, by changing the microscopic parameters, an artificial traffic fluid can be constructed , with specific physical properties, that can approximate the actual emerging traffic flow.

Based on that, specific selections for the functions included in the PRCC enabled a model reduction (Chapter 2), which is the analogue of the human-driven vehicles case, where the ARZ reduces to the LWR. The reduced model consists of a single PDE that has the form of a nonlinear heat equation and approximates the solutions of the macro-PRCC. The properties of the reduced model's solution were studied in Chapter 2 by introducing the appropriate notion of a weak solution, which is more demanding than the typical definition, since it requires mass conservation and certain entropy-like conditions to be hold. Moreover, a first-order finite difference numerical scheme was constructed to approximate the solutions of the reduced model. For the employed numerical scheme, a CFL-type condition was derived to ensure numerical stability. In addition, certain links between the weak solution and the numerical solution were established which imply that the employed numerical scheme provides high resolution approximations for the solutions of the reduced model. Furthermore, a realistic traffic scenario was considered to compare the mean flow produced by CAVs with that of human drivers by using the proposed reduced model for CAVs and the LWR model. It was shown that the mean flow produced by CAVs is much higher than that of human-driven vehicles.

The particle method used for the formal derivation of the macro-PRCC can be also used as a numerical scheme for approximating its solutions. This is justified, since the particle method under consideration is a modified version of the particle method for 1-D compressible fluid flow presented in Karafyllis and Papageorgiou (2023), which can be used both as a numerical method and as a tool for proving existence of solutions. In Chapter 3, the resulting numerical approximations were compared with those of other numerical methods for viscous compressible fluids, as well as with the numerical approximations provided for the solutions of the reduced model. Although a small difference between the numerical solutions was observed, the employed particle method requires much less computational cost compared to the other numerical methods and produces sharper accuracy in the numerical solutions, as it better preserves a differential inequality for energy conservation that holds for the macro-PRCC. In addition, by analogy with the traffic example used in Chapter 2, the macro-PRCC was compared with the ARZ model showing that the density obtained with the use of the macro-PRCC converges towards an equilibrium near the critical density as time increases and the vehicles are spread in a small space interval. Therefore, it follows that the mean flow produced by CAVs is much higher than that of human-driven vehicles.

The main concern with the proposed macroscopic models is whether they can sufficiently and accurately capture traffic phenomena involving automated vehicles on lane-free roads under the 2-D CCs, since their derivation assumes lane-based (i.e., 1-D movement). Nevertheless, Chapter 4 provided evidence that they perform successfully even in complex traffic situations. More specifically, the macro-GCC was calibrated to fit macroscopic traffic data collected from microscopic simulations using the GCC. For the microscopic simulations, two distinct traffic scenarios were considered, each involving a different kind of bottleneck. In the first scenario, a highway stretch with an off-ramp and an on-ramp was used, while in the second scenario a funnel-like narrowing of the road was considered. In both cases, it was shown that the calibrated macro-GCC reproduces with high accuracy all the dynamically changing traffic conditions that appear in the microscopically produced traffic data.

5.2 Future work

Since the microscopic and macroscopic models studied in this thesis are linked through particle methods, a natural and promising direction for future research is to further explore the performance, applicability, and robustness of the proposed macroscopic models in a wider range of traffic environments. Several directions are detailed below:

1. The fact that the macroscopic models follow directly from CCs whose design has multiple degrees of freedom offers significant flexibility, since there is a wide range of selectable functions and parameters that may lead to very different behaviors at the microscopic and macroscopic levels. As demonstrated in Chapter 2, specific selections for the functions embedded in the PRCC lead to a reduced macroscopic model. Moreover, in Chapter 3, Figures 3.21, 3.22 show that modifying the viscosity function directly affects the produced density.

   In future work, a more systematic exploration of different functional forms and parameterizations in the CCs could lead to a broader class of artificial designed traffic fluids with tunable macroscopic properties. This offers a unique opportunity to design traffic flow by shaping microscopic interactions.

2. The general setting and derivation of the CCs is not limited to the 2-D lane-free movement of CAVs, but it can be further extended to other types of agents operating in different spatial domains. For instance, autonomous aerial vehicles (e.g. drones) in 3-D environments (e.g. She and Ouyang (2021), She and Ouyang (2024)) or marine

vessels (e.g. Yip (2013), Wen et al. (2022)) navigating in congested waters may benefit from the employed decentralized feedback laws. In these contexts, the lane-free paradigm is not only natural but also essential.

Future research could therefore focus on adapting the proposed CCs and macroscopic derivation techniques to these domains, and evaluating whether the resulting PDE models can accurately capture the aggregate behavior of such agent systems. This could also include identifying new macroscopic observables (e.g. altitude layers in aerial traffic) and verifying model validity through simulations or experimental data.

3. One of the key transitional stages towards fully automated traffic systems is the coexistence of human-driven and "self-driven" vehicles. The decentralized nature of the NCC, PRCC, and GCC makes them suitable candidates for deployment on the CAVs into such mixed traffic scenarios, as these CCs do not rely on centralized coordination and can function effectively in heterogeneous settings.

   However, the proposed macroscopic models assume a homogeneous population of CAVs. Extending the derivation to heterogeneous agents with different dynamics, reaction delays, or behavioral characteristics remains an open and practically relevant problem. Therefore, future work could focus on:

   - Developing multi-class macroscopic traffic models that can explicitly capture the dynamics of both CAVs and human-driven vehicles (see e.g. Ciaramaglia et al. (2025), Imran et al. (2024)).
   - Investigating stability and interaction effects between classes. In the multi-class macroscopic traffic models, each vehicle class (CAVs or human-driven vehicles) would be described by its own density and speed fields. Moreover, interaction terms could be used in the PDEs accounting for cross-class influence (e.g. the impact of CAVs on human-driven vehicles and vice versa). This would allow for the investigation of how the proportion of CAVs, their control parameters, and the interaction dynamics affect overall traffic performance, stability, and flow capacity.

4. Urban traffic environments present additional challenges due to the presence of pedestrians, cyclists, and other dynamically moving obstacles. While decentralized CCs may still guide CAV motion effectively in such settings, they must incorporate uncertainty and reactivity to spontaneous pedestrian behavior or occlusions.

   At the macroscopic level, this motivates the development of models that may:

   - Represent non-conserved flows due to pedestrian interaction. In classical macroscopic traffic flow models (like the LWR), the vehicle number is conserved. However, in urban settings, vehicle flow is disrupted by e.g. pedestrians crossing streets unexpectedly, vehicles yielding at crosswalks or intersections, and temporary halts or detours caused by non-vehicular agents. These events break the conservation assumption locally and the number of vehicles may decrease temporarily in a segment (as they stop or slow down) without necessarily moving elsewhere. Therefore, there is a need for macroscopic models that allow for local non-conservation e.g. by modifying the continuity equation to include loss terms representing interruptions due to human activity.
   - Include source/sink terms (see e.g. Pereira et al. (2024)) to account for unexpected disruptions. “Source” and “sink” terms in PDEs represent inflow and outflow not accounted for by simple vehicle motion. More specifically, source

terms represent vehicles entering from side streets or parking areas and sink terms represent vehicles stopping for deliveries, parking, or yielding to pedestrians. Without these terms, the macroscopic dynamics will lack realism in urban environments.

5. The macroscopic traffic flow models presented in this thesis are formally derived from the bicycle kinematic model under the proposed CCs, using particle methods. While the formal derivation provides valuable intuition and enables consistent numerical approximations (see Chapter 4), the rigorous mathematical justification remains an open and significant research question.

   This is in line with a long-standing challenge in applied mathematics: establishing the exact relationship between microscopic particle-based descriptions and continuum-level PDE models, a challenge famously posed in Hilbert's 6^{th} problem. However, recent progress has been made in rigorously justifying macroscopic models using particle methods, particularly in the context of 1-D compressible fluid flows. In this regard, the work by Karafyllis and Papageorgiou (2023) provides an important milestone, offering rigorous convergence results of the particle methods for 1-D compressible fluid flows. These developments support the broader feasibility of establishing links between particle methods and macroscopic models in traffic flow.

   Nevertheless, extending such rigorous results to the lane-free traffic setting addressed in this thesis, which includes two-dimensional movement, introduces new theoretical difficulties. Future research could aim to solve this problem, ultimately leading to a mathematically sound foundation for the continuum modeling of controlled, automated traffic flow.

Bibliography

Agrawal, S., Kanagaraj, V. and Treiber, M. (2023). “Two-dimensional LWR model for lane-free traffic”. *Physica A: Statistical Mechanics and its Applications* 625, p. 128990.

Al-Taki, B., Atsou, K., Casanova, J., Goudon, T., Lafitte, P., Lagoutière, F. and Minjeaud, S. (2021). “Numerical Investigations of the Compressible Navier-Stokes System”. *ESAIM: Proceedings and Surveys* 70, pp. 1–13.

Ansanay-Alex, G., Babik, F., Latché, J. C. and Vola, D. (2011). “An L2-Stable Approximation of the Navier–Stokes Convection Operator for Low-Order Non-Conforming Finite Elements”. *International Journal for Numerical Methods in Fluids* 66, pp. 555–580.

Aronson, D. G. (1986). *The Porous Medium Equation, in: A. Fasano, M. Primicerio (eds), Nonlinear Diffusion Problems in: Lecture Notes in Mathematics*. Vol. 1224. Springer, pp. 1–46.

Artuñedo, A., Moreno-Gonzalez, M. and Villagra, J. (2024). “Lateral Control for Autonomous Vehicles: A Comparative Evaluation”. *Annual Reviews in Control* 57, p. 100910.

Aw, A., Klar, A., Rascle, M. and Materne, T. (2002). “Derivation of Continuum Traffic Flow Models from Microscopic Follow-the-Leader Models”. *SIAM Journal on Applied Mathematics* 64, pp. 259–278.

Aw, A. and Rascle, M. (2000). “Resurrection of “Second Order” Models of Traffic Flow”. *SIAM Journal on Applied Mathematics* 60, pp. 916–938.

Baines, M. J. and Sarahs, N. (2018). “A Moving-Mesh Finite Difference Scheme that Preserves Scaling Symmetry for a Class of Nonlinear Diffusion Problems”. *Journal of Computational and Applied Mathematics* 340, pp. 380–389.

Ballerini, M. et al. (2008). “Interaction Ruling Animal Collective Behavior Depends on Topological Rather Than Metric Distance: Evidence from a Field Study”. *Proceedings of the National Academy of Sciences* 105, pp. 1232–1237.

Bayen, A., Delle Monache, M. L., Garavello, M., Goatin, P. and Piccoli, B. (2022). *Control Problems for Conservation Laws with Traffic Applications: Modeling, Analysis, and Numerical methods*. Springer Nature.

Beale, J. T. (2009). “Smoothing Properties of Implicit Finite Difference Methods for a Diffusion Equation in Maximum Norm”. *SIAM Journal on Numerical Analysis* 47, pp. 2476–2495.

Bresch, D., Desjardins, B. and Gérard-Varet, D. (2007). “On Compressible Navier–Stokes Equations with Density Dependent Viscosities in Bounded Domains”. *Journal de Mathématiques Pures et Appliquées* 87, pp. 227–235.

Brezis, H. (2010). *Functional Analysis, Sobolev Spaces and Partial Differential Equations*. Springer.

Buckmire, R., McMurtry, K. and Mickens, R. (2009). “Numerical Studies of a Nonlinear Heat Equation with Square Root Reaction Term”. *Numerical Methods for Partial Differential Equations* 25, pp. 598–609.

Burger, M., Göttlich, S. and Jung, T. (2019). “Derivation of Second Order Traffic Flow Models with Time Delays”. *Networks & Heterogeneous Media* 14, pp. 265–288.

Caggio, M. and Donatelli, D. (2021). “High Mach Number Limit for Korteweg Fluids with Density Dependent Viscosity”. *Journal of Differential Equations* 277, pp. 1–37.

Chertock, A. and Levy, D. (2001). "Particle Methods for Dispersive Equations". *Journal of Computational Physics* 171, pp. 708–730.

Cho, C. H. (2013). "On the Finite Difference Approximation for Blow-up Solutions of the Porous Medium Equation with a Source". *Applied Numerical Mathematics* 65, pp. 1–26.

Christou, M. A., Sophocleous, C. and Christov, C. I. (2008). "Numerical Investigation of the Nonlinear Heat Diffusion Equation with High Nonlinearity on the Boundary". *Applied Mathematics and Computation* 201, pp. 729–738.

Ciaramaglia, I., Goatin, P. and Puppo, G. (2025). "A Multi-Class Non-Local Macroscopic Model with Time Delay for Mixed Autonomous/Human-Driven Traffic". *arXiv:2501.09440*.

Dafermos, C. M. (2010). *Hyperbolic Conservation Laws in Continuum Physics, Dynamical Systems and Differential Equations*. Springer.

Daganzo, C. F. (1995). "Requiem for Second-Order Fluid Approximations of Traffic Flow". *Transportation Research Part B: Methodological* 29, pp. 277–286.

Daganzo, C. F, Lin, W. H and Castillo, J. del (1997). "A Simple Physical Principle for the Simulation of Freeways with Special Lanes and Priority Vehicles". *Transportation Research Part B: Methodological* 31, pp. 103–125.

Di Francesco, M. and Rosini, M. D. (2015). "Rigorous Derivation of Nonlinear Scalar Conservation Laws from Follow-the-Leader Type Models via Many Particle Limit". *Archive for Rational Mechanics and Analysis* 217, pp. 831–871.

Dratman, E. (2013). "Efficient Approximation of the Solution of Certain Nonlinear Reaction–Diffusion Equations with Large Absorption". *Journal of Computational and Applied Mathematics* 238, pp. 180–202.

Ferrara, A., Sacone, S. and Siri, S. (2018). *Freeway traffic modelling and control*. Springer.

Filho, C. (2019). *Smoothed Particle Hydrodynamics: Fundamentals and Basic Applications in Continuum Mechanics*. Springer.

Gallouët, T., Maltese, D. and Novotny, A. (2019). "Error Estimates for the Implicit MAC Scheme for the Compressible Navier–Stokes Equations". *Numerische Mathematik* 141, pp. 495–567.

Goatin, P. and Laurent-Brouty, N. (2019). "The Zero Relaxation Limit for the Aw–Rascle–Zhang Traffic Flow Model". *Zeitschrift Für Angewandte Mathematik Und Physik* 70, p. 31.

Gunawan, P. (2014). "Numerical Study of Staggered Scheme for Viscous Saint-Venant Equations". *Applied Mathematical Sciences* 8, pp. 5349–5359.

Guo, N., Jiang, R., Wong, S., Hao, Q.-Y., Xue, S.-Q. and Hu, M.-B. (2021). "Bicycle Flow Dynamics on Wide Roads: Experiments and Simulation". *Transportation Research Part C: Emerging Technologies* 125, p. 103012.

Guo, Z. and Zhu, C. (2010). "Global Weak Solutions and Asymptotic Behavior to 1D Compressible Navier–Stokes Equations with Density-Dependent Viscosity and Vacuum". *Journal of Differential Equations* 248, pp. 2768–2799.

Haack, J., Jin, S. and Liu, J. G. (2012). "An All-Speed Asymptotic-Preserving Method for the Isentropic Euler and Navier-Stokes equations". *Communications in Computational Physics* 12, pp. 955–980.

Hairer, E., Nørsett, S. P. and Wanner, G. (1993). *Solving Ordinary Differential Equations. I Nonstiff Problems, second edition*. Springer.

Hajipour, M., Jajarmi, A., Malek, A. and Baleanu, D. (2018). "Positivity-Preserving Sixth-Order Implicit Finite Difference Weighted Essentially Non-Oscillatory Scheme for the Nonlinear Heat Equation". *Applied Mathematics and Computation* 325, pp. 146–158.

Helbing, D. (2001). "Traffic and Related Self-Driven Many-Particle Systems". *Reviews of Modern Physics* 73, pp. 1067–1141.

— (2009). "Derivation of Non-Local Macroscopic Traffic Equations and Consistent Traffic Pressures from Microscopic Car-Following Models". *The European Physics Journal B* 69, pp. 539–548.

Helbing, D., Schweitzer, F., Keltsch, J. and Molnar, P. (1997). "Active Walker Model for the Formation of Human and Animal Trail Systems". *Physical Review E* 56, pp. 2527–2539.

Hetel, L., Fiter, C., Omran, H., Seuret, A., Fridman, E., Richard, J. P. and Niculescu, S. I. (2017). "Recent Developments on the Stability of Systems with Aperiodic Sampling: An Overview". *Automatica* 76, pp. 309–335.

Hilbert, D. (2000). "Mathematical Problems". *Bulletin of the American Mathematical Society* 37, pp. 407–436.

Holden, H. and Risebro, N. H. (2018a). "Follow-the-Leader Models Can be Viewed as a Numerical Approximation to the Lighthill-Whitham-Richards Model for Traffic Flow". *Networks and Heterogeneous Media* 13, pp. 409–421.

— (2018b). "The Continuum Limit of Follow-the-Leader Models – A Short Proof". *Discrete and Continuous Dynamical Systems* 38, pp. 715–722.

Hošek, R. and She, B. (2018). "Stability and Consistency of a Finite Difference Scheme for Compressible Viscous Isentropic Flow in Multi-Dimension". *Journal of Numerical Mathematics* 26, pp. 111–140.

Imran, W., Tettamanti, T., Varga, B., Bifulco, G. N. and Pariota, L. (2024). "Macroscopic Modeling of Connected, Autonomous and Human-Driven Vehicles: A Pragmatic Perspective". *Transportation research interdisciplinary perspectives* 24, p. 101058.

Ioannou, P. A. and Chien, C. C. (1993). "Autonomous Intelligent Cruise Control". *IEEE Transactions on Vehicular Technology* 42, pp. 657–672.

Jovanovic, B., Matus, P. and Shchehlik, V. (2000). "The Estimates of Accuracy of Difference Schemes for the Nonlinear Heat Equation with Weak Solution". *Mathematical Modelling and Analysis* 5, pp. 86–96.

Kanagaraj, V. and Treiber, M. (2018). "Self-driven particle model for mixed traffic and other disordered flows". *Physica A: Statistical Mechanics and its Applications* 509, pp. 1–11.

Karafyllis, I. and Krstic, M. (2022a). "Global Stabilization of Compressible Flow Between Two Moving Pistons". *SIAM Journal on Control and Optimization* 60, pp. 1117–1142.

— (2022b). "Global Stabilization of Compressible Flow Between Two Moving Pistons". *SIAM Journal on Control and Optimization* 60, pp. 1117–1142.

— (2022c). "Spill-Free Transfer and Stabilization of Viscous Liquid". *IEEE Transactions on Automatic Control* 67, pp. 4585–4597.

Karafyllis, I. and Papageorgiou, M. (2023). "A Particle Method for 1-D Compressible Fluid Flow". *Studies in Applied Mathematics* 151, pp. 1282–1331.

Karafyllis, I., Theodosis, D. and Papageorgiou, M. (2022a). "Lyapunov-Based Two-Dimensional Cruise Control of Autonomous Vehicles on Lane-Free Roads". *Automatica* 145, p. 110517.

— (2022b). "Stability Analysis of Nonlinear Inviscid Microscopic and Macroscopic Traffic Flow Models of Bidirectional Cruise-Controlled Vehicles". *IMA Journal of Mathematical Control and Information* 39, pp. 609–642.

Karafyllis, I., Vokos, F. and Krstic, M. (2022c). "Feedback Stabilization of Tank-Liquid System with Robustness to Wall Friction". *ESAIM Control, Optimisation and Calculus of Variations* 28, p. 81.

— (2023). "Output-Feedback Control of Viscous Liquid-Tank System and its Numerical Approximation". *Automatica* 149, p. 110827.

Karafyllis, I., Theodosis, D. and Papageorgiou, M. (2022d). "Constructing Artificial Traffic Fluids by Designing Cruise Controllers". *Systems & Control Letters* 167, p. 105317.

— (2025a). "Forward Completeness in Open Sets and Applications to Control of Automated Vehicles". *IEEE Transactions on Automatic Control* 70, pp. 2406–2421.

— (2025b). "From Road Congestion to Vehicle-Control Enabled Artificial Traffic Fluids". *Annual Reviews in Control* 59, p. 100989.

Karper, T. K. (2013). "A Convergent FEM-DG Method for the Compressible Navier–Stokes Equations". *Numerische Mathematik* 125, pp. 441–510.

Katsaounis, T. and Simeoni, C. (2002). "Second Order Approximation of the Viscous Saint-Venant System and Comparison with Experiments". *Proceedings of the Ninth International Conference on Hyperbolic Problems*, pp. 633–644.

Kazhikhov, A. V. and Shelukhin, V. V. (1977). "Unique Global Solution with Respect to Time of Initial-Boundary Value Problems for One-Dimensional Equations of a Viscous Gas". *Journal of Applied Mathematics and Mechanics* 41, pp. 273–282.

Kerner, B. S. (2023). "Physics of automated-driving vehicular traffic". *Physical Review E* 108, p. 014302.

Kotsialos, A., Papageorgiou, M., Diakaki, C., Pavlis, Y. and Middelham, F. (2002). "Traffic Flow Modeling of Large-scale Motorway Networks Using the Macroscopic Modeling Tool METANET". *IEEE Transactions on Intelligent Transportation Systems* 3, pp. 282–292.

Ladyzhenskaya, O. A., Solonnikov, V. A. and Ural'ceva, N. N. (1968). "Linear and Quasilinear Equations of Parabolic Type". *Translations of AMS* 23.

Lagarias, J. C., Reeds, J. A., Wright, M. H. and Wright, P. E. (1998). "Convergence Properties of the Nelder–Mead Simplex Method in Low Dimensions". *SIAM Journal on Optimization* 9, pp. 112–147.

Laval, J. A and Daganzo, C. F (2006). "Lane-Changing in Traffic Streams". *Transportation Research Part B: Methodological* 40, pp. 251–264.

Lebacque, J. P (2002). "A Two Phase Extension of the LWR model Based on the Boundedness of Traffic Acceleration. In: Taylor M (ed) Transportation and traffic theory in the 21st century". *Proceedings of the 15th international symposium on transportation and traffic theory*, 697—718.

Lebacque, J. P., Mammar, S. and Haj-Salem, H. (2007). "The Aw–Rascle and Zhang's Model: Vacuum Problems, Existence and Regularity of the Solutions of the Riemann Problem". *Transportation Research Part B: Methodological* 41, pp. 710–721.

Leclercq, L. (2007). "A New Numerical Scheme for Bounding Acceleration in the LWR model". *Proceedings of the 4th IMA international conference on mathematics in transport*, 279—292.

Leveque, R. (1992). *Numerical Methods for Conservation Laws*. Birkhäuser.

Li, T. (2003). "Global Solutions of Nonconcave Hyperbolic Conservation Laws with Relaxation Arising from Traffic Flow". *Journal of Differential Equations* 190, pp. 131–149.

Li, X., Xiao, Y., Zhao, X., Ma, X. and Wang, X. (2023). "Modeling mixed traffic flows of human-driving vehicles and connected and autonomous vehicles considering human drivers' cognitive characteristics and driving behavior interaction". *Physica A: Statistical Mechanics and its Applications* 609, p. 128368.

Lighthill, M. H. and Whitham, G. B. (1955). "On Kinematic Waves II: A Theory of Traffic Flow on Long Crowded Roads". *Proceedings of the Royal Society of London. Series A. Mathematical and Physical Sciences* 229, pp. 317–345.

Lions, P. (1998). *Mathematical Topics in Fluid Dynamics, in: Compressible Models, vol.2*. Oxford Science Publication.

Liotta, S. F., Romano, V. and Russo, G. (2000). "Central Schemes for Balance Laws of Relaxation Type". *SIAM Journal on Numerical Analysis* 38, pp. 1337–1356.

Melo, C. A. H. (2014). "Existence and Stability of Equilibrium Solutions of a Nonlinear Heat Equation". *Applied Mathematics and Computation* 232, pp. 1025–1036.

Monteil, J., Billot, R., Sau, J., Buisson, C. and Faouzi, N. E. E (2014). "Calibration, estimation, and sampling issues of car-following parameters". *Transportation Research Record: Journal of the Transportation Research Board* 2422, pp. 131–140.

Naderi, M., Papageorgiou, M., Troullinos, D., Karafyllis, I. and Papamichail, I. (2024). "Controlling Automated Vehicles on Large Lane-Free Roundabouts". *IEEE Transactions on Intelligent Vehicle* 9, pp. 3061–3074.

Nelder, J. A. and Mead, R. (1965). "A Simplex Method for Function Minimization". *Computer Journal* 7, pp. 308–313.

Nessyahu, H. and Tadmor, E. (1990). "Non-Oscillatory Central Differencing for Hyperbolic Conservation Laws". *Journal of Computational Physics* 87, pp. 408–463.

N'Gohisse, F. and Boni, T. K (2011). "Numerical Blow-up for a Nonlinear Heat Equation". *Acta Mathematica Sinica,-English Series* 27, pp. 845–862.

Nilssen, T., Mannseth, T. and Tai, X. (2003). "Permeability Estimation with the Augmented Lagrangian Method for a Nonlinear Diffusion Equation". *Computational Geosciences* 7, pp. 27–47.

Nishida, T. (1986). "Equations of Motion of Compressible Viscous Fluids". *Studies in Mathematics and Its Applications* 18, pp. 97–128.

Papageorgiou, M., Mountakis, K. S., Karafyllis, I., Papamichail, I. and Wang, Y. (2021). "Lane-Free Artificial-Fluid Concept for Vehicular Traffic". *Proceedings of the IEEE* 109, pp. 114–121.

Papamichail, I., Schoenn-Anchling, N., Malekzadeh, M., Markantonakis, V. and Papageorgiou, M. (2023). "Macroscopic Traffic Flow Model Calibration for Lane-Free Automated Vehicle Traffic". *Proceedings of the IEEE 26th International Conference on Intelligent Transportation Systems (ITSC)*, pp. 3485–3492.

Papathanasopoulou, V., Markou, I. and Antoniou, C. (2016). "Online calibration for microscopic traffic simulation and dynamic multi-step prediction of traffic speed". *Transportation Research Part C: Emerging Technologies* 68, pp. 144–159.

Parrish, J. K., Viscido, S. V. and Grünbaum, D. (2002). "Self-Organized Fish Schools: An Examination of Emergent Properties". *The Biological Bulletin* 202, pp. 296–305.

Pasquale, C., Sacone, S., Siri, S. and Ferrara, A. (2018). "A new Micro-Macro METANET model for platoon control in freeway traffic networks". *Proceedings of the IEEE 21st International Conference on Intelligent Transportation Systems (ITSC)*, pp. 1481–1486.

Pereira, M., Kulcsar, B., Lipták, G., Kovács, M. and Szederkényi, G. (2024). "The Traffic Reaction Model: A Kinetic Compartmental Approach to Road Traffic Modeling". *Transportation Research Part C: Emerging Technologies* 158, p. 104435.

Polack, P., Altché, F., Novel, B. d'Andréa and La Fortelle, A. de (2017). "The Kinematic Bicycle Model: A Consistent Model for Planning Feasible Trajectories for Autonomous Vehicles?" *Proceedings of the 2017 IEEE Intelligent Vehicles Symposium (IV)*, pp. 812–818.

Popovych, R. O. and Ivanova, N. M (2005). "Potential Equivalence Transformations for Nonlinear Diffusion-Convection Equations". *Journal of Physics A: Mathematical and General* 38, pp. 3145–3155.

Price, D. J. (2012). "Smoothed Particle Hydrodynamics and Magnetohydrodynamics". *Journal of Computational Physics* 231, pp. 759–794.

Punzo, V., Montanino, M. and Ciuffo, B. (2014). "Do we really need to calibrate all the parameters? variance-based sensitivity analysis to simplify microscopic traffic flow models". *IEEE Transactions on Intelligent Transportation Systems* 16, pp. 184–193.

Punzo, V., Zheng, Z. and Montanino, M. (2021). "About calibration of car-following dynamics of automated and human-driven vehicles: Methodology, guidelines and codes". *Transportation Research Part C: Emerging Technologies* 128, p. 103165.

Rahman, M., Chowdhury, M., Xie, Y. and He, Y. (2013). "Review of Microscopic Lane-Changing Models and Future Research Opportunities". *IEEE Transactions on Intelligent Transportation Systems* 14, pp. 1942–1956.

Rajamani, R. (2012). *Vehicle Dynamics and Control*. Springer-Verlag.

Richards, P. I. (1956). "Shock Waves on the Highway". *Operations Research* 4, pp. 42–51.

Rincon, M., Límaco, J. and Liu, I. (2006). "A Nonlinear Heat Equation with Temperature-dependent Parameters". *Mathematical Physics Electronic Journal [electronic only]* 12, p. 21.

Rodriguez, A. and Vazquez, J. L. (1995). "Non-Uniqueness of Solutions of Nonlinear Heat Equations of Fast Diffusion Type". *Annales de l'Institut Henri Poincaré C, Analyse non linéaire* 12, pp. 173–200.

She, R. and Ouyang, Y. (2021). "Efficiency of UAV-Based Last-Mile Delivery Under Congestion in Low-Altitude Air". *Transportation Research Part C: Emerging Technologies* 122, p. 102878.

— (2024). "Hybrid Truck–Drone Delivery Under Aerial Traffic Congestion". *Transportation Research Part B: Methodological* 185, p. 102970.

Shelukhin, V. V. (1977). "The Unique Solvability of the Problem of Motion of a Piston in a Viscous Gas". *Dinamika Sploshnoi Sredy* 31, pp. 132–150.

— (1978). "Stabilization of the Solution of a Model Problem on the Motion of a Piston in a Viscous Gas". *Dinamika Sploshnoi Sredy* 173, pp. 134–146.

Smoller, J. (1994). *Shock Waves and Reaction-Diffusion Equations, second edition*. Springer-Verlag.

Spiliopoulou, A., Papamichail, I., Papageorgiou, M. and Chrysoulakis, J. (2014). *CALISTO user's manual, Deliverable 4.1*. Tech. rep. Athens: Technical Report for the Project SMOOTH, ARCHIMEDES III.

Spiliopoulou, A., Papamichail, I., Papageorgiou, M., Tyrinopoulos, Y. and Chrysoulakis, J. (2017). "Macroscopic Traffic Flow Model Calibration Using Different Optimization Algorithms". *Operational Research* 17, pp. 145–164.

Swaroop, D. and Hedrick, J. K. (1996). "String Stability of Interconnected Dynamic Systems". *IEEE Transactions on Automatic Control* 41, pp. 349–357.

Tang, L., Zhang, D., Han, Y., Fu, A., Zhang, H., Tian, Y., Yue, L., Wang, D. and Sun, J. (2024). "Parallel-computing-based calibration for microscopic traffic simulation model". *Transportation Research Record: Journal of the Transportation Research Board* 2678, pp. 279–294.

Theodosis, D., Karafyllis, I., Titakis, G., Papamichail, I. and Papageorgiou, M. (2024). "A Nonlinear Heat Equation Arising from Automated-Vehicle Traffic Flow Models". *Journal of Computational and Applied Mathematics* 437, p. 115443.

Theodosis, D., Tzortzoglou, F. N., Karafyllis, I., Papamichail, I. and Papageorgiou, M. (2022). "Sampled-Data Controllers for Autonomous Vehicles on Lane-Free Roads". *Proceedings of the 30th Mediterranean Conference on Control and Automation (MED 2022)*, pp. 103–108.

Thomas, J. (1995). *Numerical Partial Differential Equations: Finite Difference Methods*. Springer.

Troullinos, D., Chalkiadakis, G., Papamichail, I. and Papageorgiou, M. (2021). "Collaborative Multiagent Decision Making for Lane-Free Autonomous Driving". *Proceedings of the 20th International Conference on Autonomous Agents and MultiAgent Systems*, pp. 1335–1343.

Truong, L. X and Van Y, N. (2016). "On a Class of Nonlinear Heat Equations with Viscoelastic Term". *Computers & Mathematics with Applications* 72, pp. 216–232.

Varaiya, P. (1993). "Smart Cars on Smart Roads: Problems of Control". *IEEE Transactions on Automatic Control* 38, pp. 195–207.

Violeau, D. (2012). *Fluid Mechanics and the SPH method: Theory and Applications*. Oxford University Press.

Vranken, T. and Schreckenberg, M. (2022). "Modelling multi-lane heterogeneous traffic flow with human-driven, automated, and communicating automated vehicles". *Physica A: Statistical Mechanics and its Applications* 589, p. 126629.

Vranken, T., Sliwa, B., Wietfeld, C. and Schreckenberg, M. (2021). “Adapting a cellular automata model to describe heterogeneous traffic with human-driven, automated, and communicating automated vehicles”. *Physica A: Statistical Mechanics and its Applications* 570, p. 125792.

Wen, Y., Tao, W., Sui, Z., Piera, M. A. and Song, R. (2022). “Dynamic Model-Based Method for the Analysis of Ship Behavior in Marine Traffic Situation”. *Ocean Engineering* 257, p. 111578.

Wolf, M. T. and Burdick, J. W. (2008). “Artificial Potential Functions for Highway Driving with Collision Avoidance”. *Proceedings of the 2008 IEEE International Conference on Robotics and Automation*, pp. 3731–3736.

Wong, G. and Wong, S. (2002). “A Multi-Class Traffic Flow Model – An Extension of LWR Model with Heterogeneous Drivers”. *Transportation Research Part A: Policy and Practice* 36, pp. 827–841.

Y., F. and Seibold, B. (2009). “An Exactly Conservative Particle Method for one Dimensional Scalar Conservation Laws”. *Journal of Computational Physics* 228, pp. 5298–5315.

Yanumula, V. K., Typaldos, P., Troullinos, D., Malekzadeh, M., Papamichail, I. and Papageorgiou, M. (2023). “Optimal Trajectory Planning for Connected and Automated Vehicles in Lane-Free Traffic with Vehicle Nudging”. *IEEE Transactions on Intelligent Transportation Systems* 8, pp. 2385–2399.

Yao, Z., Gu, Q., Jiang, Y. and Ran, B. (2022). “Fundamental diagram and stability of mixed traffic flow considering platoon size and intensity of connected automated vehicles”. *Physica A: Statistical Mechanics and Its Applications* 604, p. 127857.

Yip, T. L. (2013). “A marine Traffic Flow Model”. *TransNav: International Journal on Marine Navigation and Safety of Sea Transportation* 7, pp. 109–113.

Yu, H., Amin, S. and Krstic, M. (2020). “Stability Analysis of Mixed-Autonomy Traffic with CAV Platoons Using Two-Class Aw-Rascle Model”. *Proceedings of the 59th IEEE conference on decision and control*, pp. 5659–5664.

Yu, H. and Krstic, M. (2022). *Traffic Congestion Control by PDE Backstepping*. Springer International Publishing.

Zhang, H. (2002). “A Non-Equilibrium Traffic Model Devoid of Gas-Like Behavior”. *Transportation Research Part B: Methodological* 36, pp. 275–290.

Appendix A

Cruise controllers for CAVs

A.1 Controller design

The family of CCs proposed in Karafyllis et al. (2022d) for vehicles operating on lane-free roads of constant width are constructed by means of Lyapunov functions expressed in terms of the mechanical energy of the vehicles and additional penalty terms that guarantee that all vehicle orientations remain within certain bounds. The constraints of the lane-free movement of CAVs on constant width roads are described by the following open set

$$\tilde{\Omega} := \left\{ \tilde{w} \in \mathbb{R}^{4n} : \begin{array}{c} (x_i, y_i) \in \mathbb{R} \times (-a, a),\ i = 1, ..., n \\ v_i \in (0, v_{\max}),\ |\theta_i| < \varphi,\ i = 1, ..., n \\ d_{i,j} > L,\ i, j = 1, ..., n\,,\ j \neq i \end{array} \right\} \tag{A.1}$$

where $\tilde{w} = (x_1, ..., x_n, y_1, ..., y_n, \theta_1, ..., \theta_n, v_1, ..., v_n)' \in \mathbb{R}^{4n}$ is the state vector, (x_i, y_i) is the vehicle's reference point with x_i being the longitudinal position and y_i being the lateral position of the vehicle in an inertial frame with Cartesian coordinates (X, Y) (see Fig. 4.1); a is the road width, v_i is the vehicle speed at the point (x_i, y_i), θ_i is the vehicle orientation with respect to the X-axis, $d_{i,j}$ is the inter-vehicle distance given by (4.8), U, V are potential functions that satisfy (4.11)-(4.14), $v_{\max}$ is the speed limit of the road, $\varphi \in \left(0, \frac{\pi}{2}\right)$, and L is the safety distance between the vehicles i, j.

Two main approaches can be considered for the construction of the Lyapunov function. The first one is based on Newtonian mechanics, and the Lyapunov function is given by the formula

$$\begin{aligned} H(\tilde{w}) :=& \frac{1}{2}\sum_{i=1}^{n} (v_i \cos(\theta_i) - v^*)^2 + \frac{\bar{b}}{2}\sum_{i=1}^{n} v_i^2 \sin^2(\theta_i) \\ &+ \sum_{i=1}^{n} U(y_i) + \frac{1}{2}\sum_{i=1}^{n}\sum_{j\neq i} V(d_{i,j}) \\ &+ A\sum_{i=1}^{n}\left(\frac{1}{\cos(\theta_i) - \cos(\varphi)} - \frac{1}{1 - \cos(\varphi)}\right) \end{aligned} \tag{A.2}$$

where $\bar{b}, A > 0$ are constants, $v^* \in (0, v_{\max})$ is the given desired longitudinal speed of all vehicles, and

$$\cos(\varphi) \geq \frac{v^*}{v_{\max}}. \tag{A.3}$$

The first two terms $\frac{1}{2}\sum_{i=1}^{n}(v_i \cos(\theta_i) - v^*)^2$, $\frac{b}{2}\sum_{i=1}^{n} v_i^2 \sin^2(\theta_i)$ are related to the kinetic energy of the system of n vehicles relative to an observer moving along the $x-$direction with speed v^* and zero, respectively. The third and fourth terms $\sum_{i=1}^{n} U(y_i)$, $\frac{1}{2}\sum_{i=1}^{n}\sum_{j\neq i} V(d_{i,j})$, are based on the potential functions involved in (4.11)-(4.14) and are related to the potential energy of the system. Finally, the last term of (A.2) $A\sum_{i=1}^{n}\left(\frac{1}{\cos(\theta_i)-\cos(\varphi)}-\frac{1}{1-\cos(\varphi)}\right)$ is a penalty term that blows up when $\theta_i \to \pm\varphi$.

In the second approach, the Lyapunov function is inspired by relativistic mechanics where the speed limits of relativistic mechanics (± the speed of light) are replaced by the two speed limits for vehicles (zero and the speed limit of the road $v_{\max}$, respectively). In this case, the Lyapunov function is given by the formula:

$$\begin{aligned} H_R(\tilde{w}) :=& \frac{v_{\max}^2}{2}\sum_{i=1}^{n}\frac{(v_i\cos(\theta_i)-v^*)^2+\bar{b}v_i^2\sin^2(\theta_i)}{(v_{max}-v_i)v_i} \\ &+\sum_{i=1}^{n}U(y_i)+\frac{1}{2}\sum_{i=1}^{n}\sum_{j\neq i}V(d_{i,j}) \\ &+A\sum_{i=1}^{n}\left(\frac{1}{\cos(\theta_i)-\cos(\varphi)}-\frac{1}{1-\cos(\varphi)}\right) \end{aligned} \tag{A.4}$$

For the design of the GCC (see Chapter 4) that allows the consideration of many real complex driving situations such as the presence of on-ramps and off-ramps, the consideration of variable-width roads, the potential of each vehicle to move within its own corridor Y_i given by (4.3), and the possibility to have different individual desired speeds for each vehicle, the following Lyapunov-like function is used

$$\begin{aligned} \tilde{H}(\tilde{w}) :=& \frac{v_{\max}^2}{2}\sum_{i=1}^{n}\frac{(v_i\cos(\theta_i)-\zeta_i(\tilde{w}))^2}{(v_{\max}-v_i)v_i} \\ &+\frac{\bar{b}v_{\max}^2}{2}\sum_{i=1}^{n}\frac{(sin(\theta_i)-g_i(x_i,y_i)\cos(\theta_i))^2}{cos(\theta_i)-cos(\varphi)} \\ &+\frac{1}{2}\sum_{i=1}^{n}\sum_{j\neq i}V(d_{i,j}) \\ &+\sum_{i=1}^{n}U\left(\frac{2y_i-(\beta_i(x_i)+\alpha_i(x_i))}{\beta_i(x_i)-\alpha_i(x_i)}\right) \end{aligned} \tag{A.5}$$

where $\alpha_i : \mathbb{R} \to \mathbb{R}$ and $\beta_i : \mathbb{R} \to \mathbb{R}$ are C^2 functions that satisfy (4.4)-(4.7), and the functions $\zeta_i(\tilde{w})$, $g_i(x_i, y_i)$ are given by (4.20) and (4.22), respectively. The function (A.5) has many differences from the Lyapunov function (A.4), since here the general case is considered where each vehicle has its own desired speed and its own corridor . Notice that the Lyapunov-like function (A.5) follows a pseudo-relativistic setting where the kinetic energy tends to infinity when the speed tends to zero or the speed limit $v_{\max}$.

It should be mentioned that in Karafyllis et al. (2022d), Karafyllis et al. (2025b) where the NCC, PRCC, and GCC were initially proposed, the constant p involved in (4.8), the safety distance L, the function $\tilde{\kappa} \in C^1((L,+\infty),\mathbb{R}_+)$ involved in the NCC and PRCC (see Sections A.2, A.3)), as well as the potential function V were defined for pairs of vehicles, i.e. $p_{i,j}$, $L_{i,j}$, $\tilde{\kappa}_{i,j}$, $V_{i,j}$, $i, j = 1,...,n$, $i \neq j$, allowing the interactions between different vehicle pairs to vary. However, here, the same p, L, $\tilde{\kappa}$ and V are considered for all vehicle couples for simplicity. Moreover, in Karafyllis et al. (2022d), Karafyllis et al. (2025b) the potential function U was defined as U_i, $i = 1,...,n$, meaning that the interaction between each vehicle i and the road/corridor boundaries can be different for each vehicle. For convenience, in the present work, the same potential U is considered for all vehicles.

A.2 Newtonian cruise controller (NCC)

The NCC obtained from the Lyapunov function (A.2) is given by

$$\delta_i = \arctan\left(\frac{\sigma_i}{v_i}\left(Z_i(\tilde{w}) - U'(y_i) - \sum_{j\neq i} V'(d_{i,j})\frac{(x_i - x_j)}{d_{i,j}} - bsin(\theta_i)F_i\right)\right.$$
$$\left.\times\left(v^* + \frac{A}{v_i(cos(\theta_i) - cos(\varphi))^2} + v_i cos(\theta_i)(b-1)\right)^{-1}\right) \tag{A.6}$$

$$F_i = -\frac{1}{cos(\theta i)}\left(\tilde{k}_i(\tilde{w})(v_i cos(\theta_i) - v^*) + \Lambda_i(\tilde{w})\right) \tag{A.7}$$

where

$$\tilde{k}_i(\tilde{w}) = \gamma + \frac{\Lambda_i(\tilde{w})}{v^*} + \frac{v_{\max} cos(\theta i)}{v^*(v_{\max} cos(\theta i) - v^*)}\ell(-\Lambda_i(\tilde{w})) \tag{A.8}$$

$$Z_i(\tilde{w}) = -\Gamma v_i sin(\theta_i) + \sum_{j\neq i}\tilde{\kappa}(d_{i,j})\left(\tilde{g}(v_j sin(\theta_j)) - \tilde{g}(v_j sin(\theta_j))\right) \tag{A.9}$$

$$\Lambda_i(\tilde{w}) = \sum_{j\neq i} V'(d_{i,j})\frac{(x_i - x_j)}{d_{i,j}} - \sum_{j\neq i}\tilde{\kappa}(d_{i,j})\left(\tilde{g}(v_j cos(\theta_j)) - \tilde{g}(v_i cos(\theta_j))\right) \tag{A.10}$$

where σ_i is the vehicle length, $\gamma, \Gamma > 0$ are constants, $\ell \in C^1(\mathbb{R})$, $\tilde{g} \in C^1(\mathbb{R})$, $\tilde{\kappa} \in C^1((L, +\infty), \mathbb{R}_+)$ for $i, j = 1, ..., n$, $j \neq i$ are functions that satisfy

$$\max(0, x) \leq \ell(x) \text{ for all } x \in \mathbb{R} \tag{A.11}$$

$$\tilde{g}'(x) > 0 \text{ for all } x \in \mathbb{R} \tag{A.12}$$

$$\tilde{\kappa}(d) = 0 \text{ for all } d \geq \lambda. \tag{A.13}$$

Moreover, δ_i and F_i are the control inputs of the i-th vehicle, where δ_i is the steering angle of the front wheels relative to the orientation θ_i and F_i is the acceleration. It should be noted that $\tilde{k}_i(\tilde{w})$ is a state-dependent controller gain, appropriately designed to guarantee that $v_i(t) \in (0, v_{\max})$. The feedback control laws (A.6), (A.7) were designed in Karafyllis et al. (2022d) following a Lyapunov based methodology (using the Lyapunov function (A.2)) and ensure the following property: For any $\tilde{w}(0) \in \tilde{\Omega}$ (recall (A.1)), we have $\tilde{w}(t) \in \tilde{\Omega}$ for all $t \geq 0$ (for more details see Karafyllis et al. (2022d)).

A.3 Pseudo-relativistic cruise controller (PRCC)

The PRCC obtained from the Lyapunov function (A.3) is given by

$$\delta_i = \arctan\left(\frac{\sigma_i}{\beta(v_i, \theta_i)}\left(\bar{G}_i(\tilde{w}) - U'(y_i) - \bar{\alpha}(v_i, \theta_i)F_i - \sum_{j\neq i} pV'(d_{i,j})\frac{(y_i - y_j)}{d_{i,j}}\right)\right) \tag{A.14}$$

$$F_i = \frac{1}{q(v_i, \theta_i)}\left(R_i(\tilde{w}) - \sum_{j\neq i} V'(d_{i,j})\frac{(x_i - x_j)}{d_{i,j}}\right) \tag{A.15}$$

where

$$\bar{G}_i(\tilde{w}) = -\bar{f}(v_i sin(\theta_i)) + \sum_{j \neq i} \tilde{\kappa}(d_{i,j}) \left(\tilde{g}(v_j sin(\theta_j)) - \tilde{g}(v_i sin(\theta_i))\right) \tag{A.16}$$

$$R_i(\tilde{w}) = -\tilde{f}(v_i cos(\theta_i) - v^*) + \sum_{j \neq i} \tilde{\kappa}(d_{i,j}) \left(\tilde{g}(v_j cos(\theta_j)) - \tilde{g}(v_i cos(\theta_i))\right) \tag{A.17}$$

and

$$q(v,\theta) := v_{\max}^2 \frac{v_{\max} v\, cos(\theta) - 2vv^* + v^* v_{\max}}{2(v_{\max} - v)^2 v^2} \tag{A.18}$$

$$\beta(v,\theta) = \frac{A}{(cos(\theta) - cos(\varphi))^2} + v_{\max}^2 \frac{(b-1)v\, cos(\theta) + v^*}{v_{\max} - v} \tag{A.19}$$

$$\bar{\alpha}(v,\theta) = \frac{b v_{\max}^3 sin(\theta)}{2(v_{\max} - v)^2 v}. \tag{A.20}$$

The C^1 functions $\tilde{f} : (-v^*, v_{\max} - v^*) \to \mathbb{R}$, $\bar{f} : (-v_{\max}, v_{\max}) \to \mathbb{R}$ involved in (A.16), (A.17) satisfy

$$x\tilde{f}(x) > 0 \text{ and } x\bar{f}(x) > 0 \text{ for } x \neq 0 \tag{A.21}$$

and $\tilde{g} \in C^1(\mathbb{R})$ satisfies (A.12). Moreover, δ_i and F_i are the control inputs of the i-th vehicle, where δ_i is the steering angle of the front wheels relative to the orientation θ_i and F_i is the acceleration. The feedback control laws (A.14), (A.15) were designed in Karafyllis et al. (2022d) following a Lyapunov based methodology (using the Lyapunov function (A.4)) and ensure the following property: For any $\tilde{w}(0) \in \tilde{\Omega}$ (recall (A.1)), we have $\tilde{w}(t) \in \tilde{\Omega}$ for all $t \geq 0$ (for more details see Karafyllis et al. (2022d)).

Appendix B

The formally derived macroscopic model for the NCC

The macro-NCC has been formally derived from the microscopic model (4.1) under the control inputs (A.6), (A.7), based on a particle method (see Karafyllis et al. (2022d), Karafyllis et al. (2025a)), by adopting a methodology that is inspired by Di Francesco and Rosini (2015), Holden and Risebro (2018a), Holden and Risebro (2018b). The particle method provides the link between the macroscopic model and the microscopic model (4.1) under the control inputs (A.6), (A.7). More specifically, following the same derivation process that was first given in Karafyllis et al. (2022b) and neglecting the lateral movement of vehicles, the macro-NCC model is obtained

$$\tilde{\rho}_\tau + (\tilde{\rho}\tilde{v})_\xi = 0 \tag{B.1}$$

$$\tilde{v}_\tau + \tilde{v}\tilde{v}_\xi + \frac{\tilde{P}'(\tilde{\rho})}{\tilde{\rho}}\tilde{\rho}_\xi = \frac{1}{\tilde{\rho}}\left(\tilde{g}'(\tilde{v})\tilde{\mu}(\tilde{\rho})\tilde{v}_\xi\right)_\xi - \tilde{J}(\tilde{G})\left(\tilde{v} - v^*\right) \tag{B.2}$$

$$\tilde{G} := -\frac{\tilde{P}'(\tilde{\rho})}{\tilde{\rho}}\tilde{\rho}_\xi + \frac{1}{\tilde{\rho}}\left(\tilde{g}'(\tilde{v})\tilde{\mu}(\tilde{\rho})\tilde{v}_\xi\right)_\xi \tag{B.3}$$

for $\tau > 0$ and $\xi \in I(\tau)$, where $I(\tau) \subseteq \mathbb{R}$ is an appropriate interval. The macroscopic model (B.1)-(B.3) is to be considered with state constraints $0 < \tilde{\rho}(\tau,\xi) < \rho_{\max}$, $0 < \tilde{v}(\tau,\xi) < v_{\max}$ for all $\tau > 0$ and $\xi \in I(\tau)$, where $\tilde{\rho}(\tau,\xi)$, $\tilde{v}(\tau,\xi)$ are the traffic density and mean speed, respectively, at position $\xi \in I(\tau)$ on a highway, with $\rho_{\max}$ being the maximum density, and $v_{\max}$ being the maximum speed limit of the road; v^* is the speed set-point and $\gamma > 0$ is a constant. The functions $\tilde{\mu} : (0,\rho_{\max}) \to \mathbb{R}_+$, $\tilde{P} : (0,\rho_{\max}) \to \mathbb{R}_+$ are $C^1\left((0,\rho_{\max})\right)$ and satisfy (1.4), (1.5). Moreover, the function $\tilde{g} \in C^1(\mathbb{R})$ satisfies (A.12), while $\tilde{J}(\tilde{G})$ is given by

$$\tilde{J}(\tilde{G}) = \gamma + \frac{v_{\max}\ell(\tilde{G})}{v^*(v_{\max} - v^*)} - \frac{\tilde{G}}{v^*} \tag{B.4}$$

where $\gamma > 0$ is a constant and the function $\ell \in C^1(\mathbb{R})$ satisfies (A.11).